POLITECNICO
MILANO 1863

POLITECNICO DI MILANO
DIPARTIMENTO SCIENZE E TECNOLOGIE AEROSPAZILALI
DOCTORAL PROGRAMME IN XXIX CYCLE

MODELING AND CONTROL OF ADAPTIVE GEOMETRICALLY NONLINEAR THIN-WALLED BEAMS WITH PIEZO-COMPOSITE: APPLICATIONS FOR ROTARY AND FIXED AIRCRAFT WINGS

Doctoral Dissertation of:
Xiao Wang

Supervisor:
Prof. Pierangelo Masarati

2017

Abstract

A Geometrically nonlinear composite thin-walled beam theory with fiber-reinforced and piezo-composite is developed. Some non-classical effects such as anisotropy, warping inhibition and three-dimensional (3-D) strain are accounted for in the beam model. The governing equations and the corresponding boundary conditions are derived using the Hamilton's principle. The Extended Galerkin's Method is used for the numerical study. The static and dynamical characteristics of the adaptive thin-walled structure are investigated by studying anisotropic properties of piezo-actuators, considered in conjunction with that of the structural tailoring of the fiber-reinforced host structure. Furthermore, the beneficial effects of the implementation of the active feedback control and tailoring technology on advanced adaptive aircraft wings or rotor blades, that can be modeled as the thin-walled beam developed in this dissertation, are highlighted.

Dedicated to my wife Xinghua and my son Di

whose love supports me through
all my panic and happiness

Acknowledgements

First of all, I wish to thank my supervisor, Professor Pierangelo Masarati, for his resourceful help and constant encouragement. I also wish to thank Professor Marco Morandini, for his help, patience and for devoting time from their busy schedule to discussing about my work.

I also to express my gratitude to Prof. Xiaoting Rui of Nanjing University of Science and Technology and Prof. Giovanni Bernardini of Università Degli Studi Roma Tre, for their constructive advice on this dissertation.

I would like to express my most profound thanks and gratitude to my parents for their sustaining love, dedication and support at all their possible levels. High appreciations are also expressed to my wife and my son, for their constant encouragement during the past years.

Contents

CHAPTER 1

Introduction

Composite materials and structures, due to their vast advantages, such as light weight, specific high stiffness, and elastic couplings, have been increasingly used in aerospace industry and other fields of advanced technology. They have even been identified as a major thrust for designing high-performance aerospace structures (see e.g., [26, 30]). Anisotropic composite thin-walled structures are expected to meet the increasingly aggressive missions of the next generation of high-performance flight vehicles. In recent years, some further refinements are conducted to the modeling of open or closed cross-section thin-walled composite beam structures (see e.g., [13, 20, 35, 93, 94, 102]). Among these efforts, Cortinez et al. [20] and Vo and Lee [94] introduced warping shear to try to improve the model's accuracy; and together with a geometrically exact, intrinsic theory of anisotropic beams developed by Hodges [33], the variational-asymptotic beam sectional analysis [102] can be used for arbitrarily large deflections and rotations (see e.g., [72]). More generally, any geometrically exact, intrinsic theory of anisotropic beams can be used provided the beam constitutive equation are computed correctly. Many similar approaches, based on a semi-analytical discretization of the beam section displacement field, have been proposed to compute the stiffness matrix of arbitrarily complex beam sections, see e.g. [28, 60, 102]. Basically the same approach can be used for the characterization of composite beams with piezo-electric patches [10, 57]. That said, simplified models such as the one used in this dissertation are still interesting, as they allow to get a better inside into the dependence of the elastic solution of the beam section parameters.

The design of advanced aircraft wings or rotor blades characterized by thin-walled structures was significantly influenced by the incorporation of composite material technology. As compared to their metallic counterparts, composite design of thin-walled structures offers considerable advantages with respect to strength and weight criteria, in

addition to providing adequate means of efficiently controlling static and dynamic response via implementation of structural tailoring [14,17,21,32,38,68,69,79,82,87,88]. Although elastic tailoring is a powerful technology that can offer a beneficial influence on the dynamic response characteristics, this technique is passive in nature in the sense that, once implemented, the structure cannot respond to the variety of factors under which it must operate. As a complementary option, the active control via the implementation of the smart materials system technology can be applied [11, 27, 29, 57]. Since piezoelectric materials have a lot desirable characteristics, such as self-sensing, structure embeddability, fast response and covering a broad range of frequency, they are well suited for the active control of deformable beams [16, 48, 49, 61, 62]. Due to the brittle nature of ceramics, they are however vulnerable to damage and can hardly conform to a curved surface. These drawbacks are overcame by piezo-composite materials such as the Active Fiber Composite (AFC) [6] and the Macro-Fiber Composite (MFC) [100]. Piezo-composite materials can be shaped and bonded to surfaces or embedded into structures.

In the existing literature, a lot publications on modeling or studying adaptive thin-walled structure are based on the assumption of fiber orientation of piezo-composite along the spanwise missing the discussion of the isotropic properties [16, 19, 48, 49, 61, 62, 78, 89]. Thus the system can only be controlled by the piezoelectrically induced bending moments. Thus a comprehensive study allowing to get a better insight into the influence of piezoelectrically induced extension, transverse shear, twist, bimoment and bendings is still interesting.

Figure 1.1 presents the construction of this dissertation. In Chapter 2, a geometrical nonlinear rotating thin-walled beam theory incorporating fiber-reinforced and piezo-composite is developed. Transverse shear strain, warping inhibitions and three-dimensional strain are accounted for. The governing equations and the associated boundary conditions are derived via Hamilton's principle.

In Chapter 3, active control of pretwisted rotating blades that modeled as thin-walled beam structures is investigated. The adaptive capabilities provided by a system of piezo-actuators bonded or embedded into the structure are also implemented in the system. The effects induced by high speed rotation, e.g., centrifugal stiffening, tennis-racket effect, that are essential for a reliable prediction of free-vibration characteristics of rotating blades are highlighted. Based on the classical feedback control and linear quadratic regular (LQR) control, the control authority of the implementation of piezo-actuators with different ply-angles, considered in conjunction with that of the structural tailoring, are highlighted. In addition, the rotating thin-walled beam model developed in this dissertation can also serve as the basic model of flexible spacecraft. Problems related to active vibration suppression of piezo-actuated spacecraft during attitude maneuvers are discussed in Chapter 4.

The model developed in Chapter 2 can also serve as the basic model of advanced adaptive aircraft wings when ignoring the rotating effects, see Chapters 5, 6 and 7. In Chapter 5, the effective damping performance of piezo-actuated aircraft wings is investigated by studying lay-up configurations of piezo-composite, in conjunction with elastic tailoring of the fiber-reinforced host structure. Problems related to nonlinear dynamics of advanced aircraft wings are discussed in Chapter 6. Modal interactions of swept aircraft wings carrying heavy external stores in the presence of simultaneous

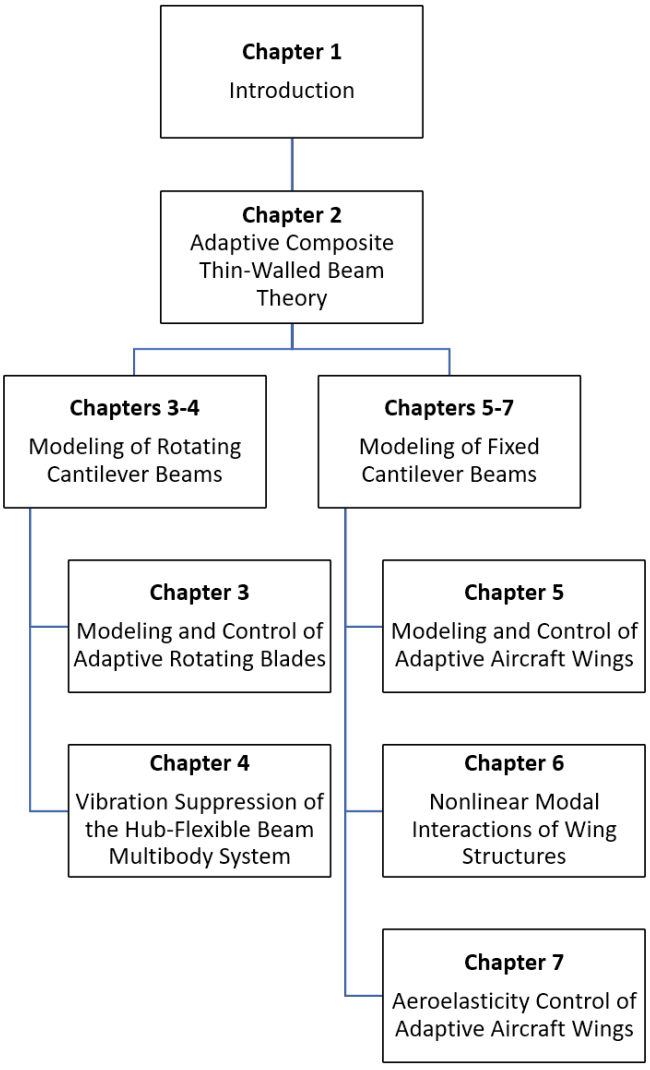

Figure 1.1: *Flow chart of the dissertation*

internal and external resonance are investigated. Moreover, the conditions for mode saturation and jump phenomena during modal interactions are highlighted. The objective of Chapter 7 is to study the active control effect on flutter suppression and dynamic aeroelastic response enhancement of a smart aircraft wing. The unsteady aerodynamic loads in subsonic compressible flows are based on 2-D indicial functions considered in conjunction with aerodynamic strip theory extended to 3-D wing model.

CHAPTER 2

Modeling of Geometrically Nonlinear Rotating Thin-Walled Beam Structures with Piezo-composite

2.1 Introduction

Beams are three dimensional (3D) bodies in which one dimension is large compared to the other two. The models based on 3D Finite Element Analysis (FEA) possess significant computational advantages. However, beam or one-dimensional (1D) models play an important role in structural analysis because they have smaller dimensionality and provide the designer with simple tools to analyze numerous problems.

2.2 Basic Assumptions

A single-cell, closed cross-section, rotating fiber-reinforced composite thin-walled structure with piezo-composite materials is considered here, see Fig. 2.1. The inertial reference system (X, Y, Z) is attached to the center of the hub O (considered to be rigid), while the rotating axis system (x, y, z) is located at the blade root with an offset R_0 from the rotation axis O. The unit vectors associated with the frame coordinates (X, Y, Z) and (x, y, z) are defined as $(\mathbf{I}, \mathbf{J}, \mathbf{K})$ and $(\mathbf{i}, \mathbf{j}, \mathbf{k})$, respectively. In addition, the local frame (s, y, n) attached on the mid-line contour of the cross-section is also considered, which s denotes the circumferential coordinate while n denotes the normal coordinate.

The geometrically nonlinear beam theory is based on the following assumptions [7, 18, 46, 98]:

1. The projection of the cross-section on a plane normal to the y-axis does not distort during deformation. This implies that the beam cross-sections are assumed rigid

in their own planes, but are allowed to warp out of their original planes. For thin-walled beam structures, i.e., aircraft wings and fuselage and ship hulls, the original cross-sectional shape is maintained by a system of transverse stiffening members (ribs or bulkheads). These are considered rigid within their plane but perfectly flexible with regard to deformation normal to their own plane, so that the adoption of this assumption leads to a reasonable mathematical model for the actual physical behavior [47, 78].

2. The transverse shear strains γ_{xy} and γ_{zy} are uniform over the entire cross-section.
3. Products of the derivatives of v can be neglected in the Green-Lagrange strain relations, since the axial displacement v is much smaller than displacement components on the cross-section plane u or w in the x and z direction, respectively.
4. The normal stress σ_{nn} (see Fig. 2.1 for its direction) can be neglected in deriving the constitutive relations, and the stress resultants N_{ss} and N_{sn} can also be neglected when compared with the remaining ones [7].
5. Warping displacement along the mid-line contour (referred to as primary warping) and off mid-line contour warping (referred to as the secondary warping) are both considered.
6. We assume that the rotation solely takes place in the plane (X, Y), viz., angular velocity $\dot{\mathbf{\Lambda}} = \dot{\Lambda}\mathbf{K} = \dot{\Lambda}\mathbf{k}$.

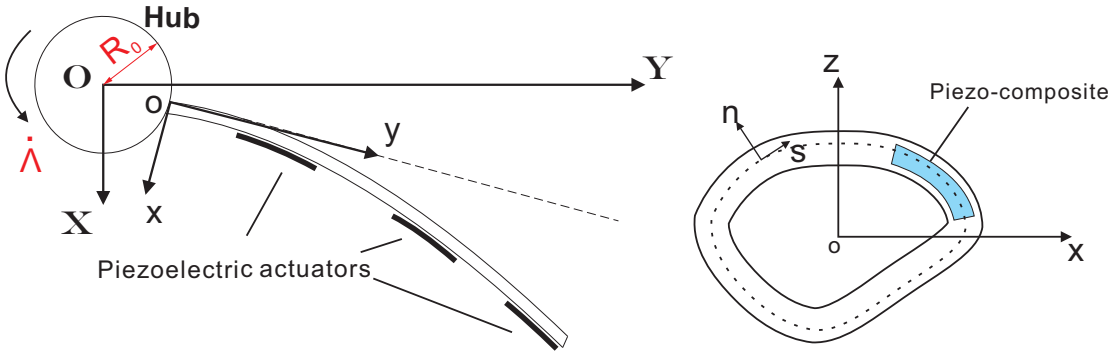

Figure 2.1: *A closed cross section of the thin-walled structure*

2.3 Kinematics

It is useful to express the position vector $\mathbf{R}$ of an arbitrary point $M(x, y, z)$ belonging to the deformed beam, measured from a fixed origin O (coinciding with the center of the hub), described in the rotating coordinate system (x, y, z). In the sense we have

$$\mathbf{R} = \mathbf{R}_0 + \mathbf{r} + \mathbf{\Delta}, \tag{2.1}$$

where $\mathbf{R}_0$, $\mathbf{r}$ and $\mathbf{\Delta}$ denote the position vector of the beam root point o (hub periphery), the undeformed position vector of point $M(x, y, z)$, and its displacement vector, respectively. Their expressions are

$$\mathbf{R}_0 = R_0\mathbf{j}, \quad \mathbf{r} = x\mathbf{i} + y\mathbf{j} + z\mathbf{k}, \quad \mathbf{\Delta} = u\mathbf{i} + v\mathbf{j} + w\mathbf{k}. \tag{2.2}$$

For arbitrary large rotation ϕ, the components of the 3-D displacements $u(x,y,z,t)$, $v(x,y,z,t)$, $w(x,y,z,t)$ in the displacement vector $\mathbf{\Delta}$ can be postulated as [96, 98]:

$$u = u_0 + (z + n\frac{\mathrm{d}\,x}{\mathrm{d}\,s})\sin\phi - (x - n\frac{\mathrm{d}\,z}{\mathrm{d}\,s})(1-\cos\phi), \tag{2.3a}$$

$$v = v_0 + (x - n\frac{\mathrm{d}\,z}{\mathrm{d}\,s})\theta_z + (z + n\frac{\mathrm{d}\,x}{\mathrm{d}\,s})\theta_x - [F_w + na]\phi', \tag{2.3b}$$

$$w = w_0 - (x - n\frac{\mathrm{d}\,z}{\mathrm{d}\,s})\sin\phi - (z + n\frac{\mathrm{d}\,x}{\mathrm{d}\,s})(1-\cos\phi), \tag{2.3c}$$

where

$$\theta_x = \gamma_{yz} - w_0'\cos\phi - u_0'\sin\phi, \quad \theta_z = \gamma_{xy} - u_0'\cos\phi + w_0'\sin\phi. \tag{2.4a}$$

The primary warping function F_w and secondary warping function a in Eq. (2.3b) are expressed as

$$F_w = \int_0^s [r_n(s) - \psi(s)]ds, \quad a = -(z\frac{\mathrm{d}\,z}{\mathrm{d}\,s} + x\frac{\mathrm{d}\,x}{\mathrm{d}\,s}), \tag{2.5}$$

here, the torsional function $\psi(s)$ and the quantity $r_n(s)$ (for its geometric significance, see Fig 2.2) are defined as

$$\psi(s) = \frac{\oint_c r_n(s)\,\mathrm{d}\,s}{h(s)G_{sy}(s)\oint_c \dfrac{\mathrm{d}\,s}{h(s)G_{sy}(s)}}, \quad r_n = z\frac{\mathrm{d}\,x}{\mathrm{d}\,s} - x\frac{\mathrm{d}\,z}{\mathrm{d}\,s}, \tag{2.6}$$

where $G_{sy}(s)$ is the effective membrane shear stiffness, which is defined as [7]:

$$G_{sy}(s) = \frac{N_{sy}}{h(s)\gamma_{sy}^0(s)}. \tag{2.7}$$

For the thin-walled beam theory considered herein, the six kinematic variables, $u_0(y,t)$, $v_0(y,t)$, $w_0(y,t)$, $\phi(y,t)$, $\theta_x(y,t)$, $\theta_z(y,t)$, which represent the 1-D displacement measures, constitute the basic unknowns of the problem. As will be shown in the sequel, the original 3-D elasticity problem will be reduced to a 1-D problem. Note that, when the transverse shear effect is ignored, Eqs. 2.3 degenerate to $\theta_x = -w_0'$, $\theta_z = -u_0'$, and as a result, the number of basic unknown quantities reduces to four. Such a case leads to the Bernoulli-Euler beam model, referred also to as the unshearble one.

2.4 Green-Lagrange strain

Based on the assumption 3, the non-zero normal Green-Lagrange strain component is:

$$\varepsilon_{yy} = \frac{\partial v}{\partial y} + \frac{1}{2}\left[\left(\frac{\partial u}{\partial y}\right)^2 + \left(\frac{\partial v}{\partial y}\right)^2 + \left(\frac{\partial w}{\partial y}\right)^2\right] \approx \frac{\partial v}{\partial y} + \frac{1}{2}\left[\left(\frac{\partial u}{\partial y}\right)^2 + \left(\frac{\partial w}{\partial y}\right)^2\right]. \tag{2.8}$$

Taking Eqs. 2.3 into above Eq. 2.8, we obtain that

$$\varepsilon_{yy} = \varepsilon_{yy}^0 + n\varepsilon_{yy}^1, \tag{2.9}$$

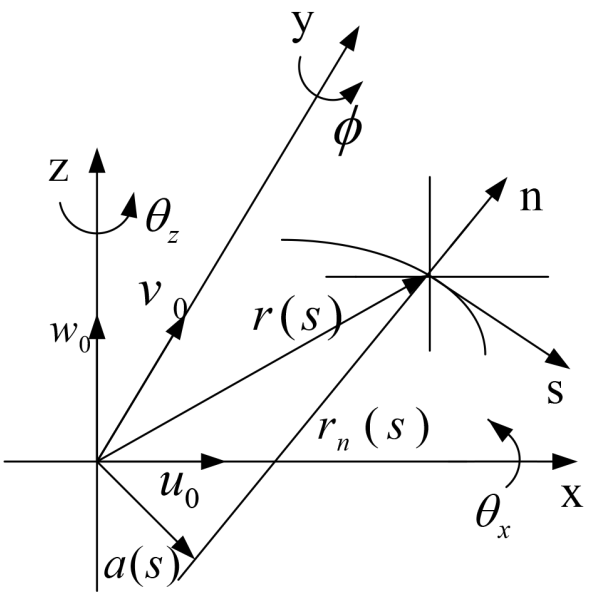

Figure 2.2: *Coordinate system and displacement field for the beam model.*

where

$$\begin{aligned}\varepsilon_{yy}^{0} =&[v_0' + x\theta_z' + z\theta_x' - F_w\phi''] + \frac{1}{2}\left[(u_0')^2 + (w_0')^2 + (\phi')^2(x^2+z^2)\right] \\ &+ u_0'\phi'(z\cos\phi - x\sin\phi) - w_0'\phi'(x\cos\phi + z\sin\phi),\end{aligned} \tag{2.10a}$$

$$\begin{aligned}\varepsilon_{yy}^{1} =& -\frac{\mathrm{d}\,z}{\mathrm{d}\,s}\theta_z' + \frac{\mathrm{d}\,x}{\mathrm{d}\,s}\theta_x' - a\phi'' + u_0'\left[\frac{\mathrm{d}\,x}{\mathrm{d}\,s}\cos\phi + \frac{\mathrm{d}\,z}{\mathrm{d}\,s}\sin\phi\right]\phi' \\ &+ w_0'\left[\frac{\mathrm{d}\,z}{\mathrm{d}\,s}\cos\phi - \frac{\mathrm{d}\,x}{\mathrm{d}\,s}\sin\phi\right]\phi' + r_n(\phi')^2,\end{aligned} \tag{2.10b}$$

in which, ε_{yy}^{0} denotes the axial strain associated with the primary warping, while ε_{yy}^{1} denotes a measure of curvature associated with the secondary warping. The non-zero transverse shear strain components are:

$$\gamma_{xy} = \frac{\partial u}{\partial y} + \frac{\partial v}{\partial x} + \frac{\partial u}{\partial x}\frac{\partial u}{\partial y} + \frac{\partial v}{\partial x}\frac{\partial v}{\partial y} + \frac{\partial w}{\partial x}\frac{\partial w}{\partial y} \approx \frac{\partial u}{\partial y} + \frac{\partial v}{\partial x} + \frac{\partial u}{\partial x}\frac{\partial u}{\partial y} + \frac{\partial w}{\partial x}\frac{\partial w}{\partial y}, \tag{2.11a}$$

$$\gamma_{yz} = \frac{\partial v}{\partial z} + \frac{\partial w}{\partial y} + \frac{\partial u}{\partial y}\frac{\partial u}{\partial z} + \frac{\partial v}{\partial y}\frac{\partial v}{\partial z} + \frac{\partial w}{\partial y}\frac{\partial w}{\partial z} \approx \frac{\partial v}{\partial z} + \frac{\partial w}{\partial y} + \frac{\partial u}{\partial y}\frac{\partial u}{\partial z} + \frac{\partial w}{\partial y}\frac{\partial w}{\partial z}. \tag{2.11b}$$

In the local coordinates (s, y, n), the non-zero transverse shear components can be represented as,
Tangential shear strain:

$$\gamma_{ys} = \gamma_{ys}^{0} + \psi(s)\phi' + 2n\phi', \tag{2.12a}$$

where

$$\begin{aligned}\gamma_{ys}^{0} =&\gamma_{xy}\frac{\mathrm{d}\,x}{\mathrm{d}\,s}+\gamma_{yz}\frac{\mathrm{d}\,z}{\mathrm{d}\,s}\\ =&\frac{\mathrm{d}\,x}{\mathrm{d}\,s}(\theta_z+u_0'\cos\phi-w_0'\sin\phi)+\frac{\mathrm{d}\,z}{\mathrm{d}\,s}(\theta_x+u_0'\sin\phi+w_0'\cos\phi),\end{aligned} \tag{2.12b}$$

Transverse shear strain:

$$\begin{aligned}\gamma_{ny} =&-\gamma_{xy}\frac{\mathrm{d}\,z}{\mathrm{d}\,s}+\gamma_{yz}\frac{\mathrm{d}\,x}{\mathrm{d}\,s}\\ =&-\frac{\mathrm{d}\,z}{\mathrm{d}\,s}(\theta_z+u_0'\cos\phi-w_0'\sin\phi)+\frac{\mathrm{d}\,x}{\mathrm{d}\,s}(\theta_x+u_0'\sin\phi+w_0'\cos\phi).\end{aligned} \tag{2.12c}$$

2.5 Constitutive Relations

The thin-walled beam structure consists of the passive material which is master (host) structure and the active material which is sensors and actuators. We assume that both passive material and active material can be modeled with the linear piezoelectric constitutive relationships. The constitutive equations of a 3-D piezoelectric continuum are [101]

$$\sigma_{ij} = c_{ijkl}^{E}\varepsilon_{kl} - e_{kij}E_k, \tag{2.13a}$$

$$D_i = e_{ikl}\varepsilon_{kl} + \kappa_{ik}^{\varepsilon}E_k, \tag{2.13b}$$

where, c_{ijkl}^{E}, e_{kij}, and $\kappa_{ik}^{\varepsilon}$ denote the elastic stiffness coefficients, the piezoelectric stress tensor and dielectric constant tensor, respectively. The superscripts E and ε denote constant electric field and constant strain, respectively. σ_{ij} and ε_{kl} denote the stress and strain components, while E_k and D_i denote the electric field intensity and electric displacement vector, respectively. Eq. (2.13a) describes *converse piezoelectric effect* which is used for distributed sensing while Eq. (2.13b) describes *direct piezoelectric effect* that is used for the active distributed control.

2.5.1 3-D Piezoelectric Constitutive Equations

In matrix form, the 3-D linear piezoelectric constitutive equation for a *generally orthotropic* fiber-reinforced composite material [36] and AFC or MFC piezo-composite material [6] can be given as

$$\begin{Bmatrix}\sigma_{11}\\ \sigma_{22}\\ \sigma_{33}\\ \tau_{23}\\ \tau_{31}\\ \tau_{12}\end{Bmatrix} = \begin{bmatrix}C_{11} & C_{12} & C_{13} & 0 & 0 & 0\\ C_{12} & C_{22} & C_{23} & 0 & 0 & 0\\ C_{13} & C_{23} & C_{33} & 0 & 0 & 0\\ 0 & 0 & 0 & C_{44} & 0 & 0\\ 0 & 0 & 0 & 0 & C_{55} & 0\\ 0 & 0 & 0 & 0 & 0 & C_{66}\end{bmatrix}\begin{Bmatrix}\varepsilon_{11}\\ \varepsilon_{22}\\ \varepsilon_{33}\\ \gamma_{23}\\ \gamma_{31}\\ \gamma_{12}\end{Bmatrix} - \begin{Bmatrix}e_{11}\\ e_{12}\\ e_{13}\\ 0\\ 0\\ 0\end{Bmatrix}E_1 \tag{2.14}$$

We assume the electric filed intensity is constant across the actuator thickness, i.e., $E_1 = -(V/\hat{h})$, where V and $\hat{h}$ are the applied voltage and electrode spacing of the interdigitated electrode for the actuator layer, respectively.

Note also that the stiffness matrix, $\mathbf{C}_{ij}$, in terms of the engineering constants are shown in [36, p. 66]. Moreover, electroelastic constant matrices of piezoelectric crystals vested in 20 kinds of groups are list in [25, pp. 88-92].

Then the constitutive equations referred to the primed coordinate system (s, y, n) for kth layer can be expressed as the form

$$\begin{Bmatrix} \sigma_{ss} \\ \sigma_{yy} \\ \sigma_{nn} \\ \tau_{yn} \\ \tau_{sn} \\ \tau_{sy} \end{Bmatrix}_{(k)} = \begin{bmatrix} \bar{C}_{11} & \bar{C}_{12} & \bar{C}_{13} & 0 & 0 & \bar{C}_{16} \\ \bar{C}_{12} & \bar{C}_{22} & \bar{C}_{23} & 0 & 0 & \bar{C}_{26} \\ \bar{C}_{13} & \bar{C}_{23} & \bar{C}_{33} & 0 & 0 & \bar{C}_{36} \\ 0 & 0 & 0 & \bar{C}_{44} & \bar{C}_{45} & 0 \\ 0 & 0 & 0 & \bar{C}_{45} & \bar{C}_{55} & 0 \\ \bar{C}_{16} & \bar{C}_{26} & \bar{C}_{36} & 0 & 0 & \bar{C}_{66} \end{bmatrix}_{(k)} \begin{Bmatrix} \varepsilon_{ss} \\ \varepsilon_{yy} \\ \varepsilon_{nn} \\ \gamma_{yn} \\ \gamma_{sn} \\ \gamma_{sz} \end{Bmatrix}_{(k)} - \begin{Bmatrix} \bar{e}_{11} \\ \bar{e}_{12} \\ \bar{e}_{13} \\ 0 \\ 0 \\ \bar{e}_{16} \end{Bmatrix}_{(k)} E_{1(k)} \tag{2.15}$$

where the transformed stiffness matrix $[\bar{\mathbf{C}}]$ can be found in [47, p. 567], and the transformed piezoelectric stress vector is given as

$$\bar{e}_{11} = m^2 e_{11} + n^2 e_{12}, \quad \bar{e}_{12} = n^2 e_{11} + m^2 e_{12}, \quad \bar{e}_{13} = e_{13}, \quad \bar{e}_{16} = mn\left(e_{11} - e_{12}\right). \tag{2.16}$$

where $m \equiv \cos\theta$ and $n \equiv \sin\theta$, $\theta \in [0,\ 2\pi]$. Based on the assumption 4, $\sigma_{nn} = 0$, leads Eq. 2.15 reduced to

$$\begin{Bmatrix} \sigma_{ss} \\ \sigma_{yy} \\ \tau_{yn} \\ \tau_{sn} \\ \tau_{sy} \end{Bmatrix}_{(k)} = \begin{bmatrix} \bar{Q}_{11} & \bar{Q}_{12} & 0 & 0 & \bar{Q}_{16} \\ \bar{Q}_{12} & \bar{Q}_{22} & 0 & 0 & \bar{Q}_{26} \\ 0 & 0 & \bar{Q}_{44} & \bar{Q}_{45} & 0 \\ 0 & 0 & \bar{Q}_{45} & \bar{Q}_{55} & 0 \\ \bar{Q}_{16} & \bar{Q}_{26} & 0 & 0 & \bar{Q}_{66} \end{bmatrix}_{(k)} \begin{Bmatrix} \varepsilon_{ss} \\ \varepsilon_{yy} \\ \gamma_{yn} \\ \gamma_{sn} \\ \gamma_{sz} \end{Bmatrix}_{(k)} - \begin{Bmatrix} e_{ss} \\ e_{yy} \\ 0 \\ 0 \\ e_{sy} \end{Bmatrix}_{(k)} E_{1(k)}. \tag{2.17}$$

where $[\bar{\mathbf{Q}}]$ is the matrix of the reduced elastic coefficients can be found in [47, p. 575], while the reduced piezoelectric stress coefficients are given as

$$e_{ss} = \bar{e}_{11} - \frac{\bar{C}_{13}}{\bar{C}_{33}}\bar{e}_{13}, \quad e_{yy} = \bar{e}_{12} - \frac{\bar{C}_{23}}{\bar{C}_{33}}\bar{e}_{13}, \quad e_{sy} = \bar{e}_{16} - \frac{\bar{C}_{36}}{\bar{C}_{33}}\bar{e}_{13}. \tag{2.18}$$

2.5.2 2-D Piezoelectric Constitutive Equations

The master (or host) structure is assumed composed of N_h layers, while the actuator is composed of N_p piezoelectric layers. Thus the total number of layer denotes as $N_{hp} = N_h + N_p$. The distribution function $P(\cdot)$ of actuators can be given (see Fig. 2.3):

$$P_k(n) = H(n - n_{k-1}) - H(n - n_k), \tag{2.19a}$$

$$P_k(s) = H(s - s_{k1}) - H(s - s_{k2}), \tag{2.19b}$$

$$P_k(y) = H(y - y_{k1}) - H(y - y_{k2}), \tag{2.19c}$$

where $H(\cdot)$ denotes Heaviside's distribution, while (n_k, n_{k-1}), (s_{k1}, s_{k2}) and (y_{k1}, y_{k2}) denote, respectively, the top and bottom heights of the actuator measured across the beam thickness, and its location along the beam circumference and span.

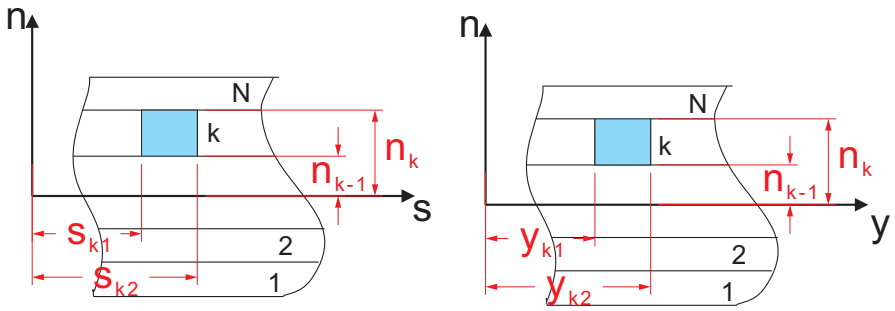

Figure 2.3: *Piezopatch locaton.*

The membrane stress resultants, the transverse shear stress resultants and stress couples are, respectively, given as

$$\begin{Bmatrix} N_{ss} \\ N_{yy} \\ N_{sy} \end{Bmatrix} = \sum_{k=1}^{N_{hp}} \int_{n_{(k-1)}}^{n_{(k)}} \begin{Bmatrix} \sigma_{ss} \\ \sigma_{yy} \\ \sigma_{sy} \end{Bmatrix}_k \mathrm{d}\, n, \quad \begin{Bmatrix} N_{yn} \\ N_{sn} \end{Bmatrix} = \sum_{k=1}^{N_{hp}} \int_{n_{(k-1)}}^{n_{(k)}} \begin{Bmatrix} \sigma_{yn} \\ \sigma_{sn} \end{Bmatrix}_k \mathrm{d}\, n, \tag{2.20}$$

$$\begin{Bmatrix} L_{yy} \\ L_{sy} \end{Bmatrix} = \sum_{k=1}^{N_{hp}} \int_{n_{(k-1)}}^{n_{(k)}} \begin{Bmatrix} \sigma_{yy} \\ \sigma_{sy} \end{Bmatrix}_k n \, \mathrm{d}\, n, \tag{2.21}$$

where $n_{(k)}$ and $n_{(k-1)}$ denote the distances from the middle surface of the cross-section to the upper and lower surface of the kth layer, respectively. With the definition of stretching quantity A_{ij}, bending-stretching coupling stiffness quantity B_{ij} and thermal and hygric moments D_{ij},

$$(A_{ij},\ B_{ij},\ D_{ij}) = \sum_{k=1}^{N_{hp}} \int_{n_{(k-1)}}^{n_{(k)}} \bar{Q}_{ij}^{(k)} (1,\ n,\ n^2)\, \mathrm{d}\, n, \tag{2.22}$$

as well as the assumption 4, $N_{ss} = 0$ and $N_{sn} = 0$, we obtain

$$\begin{Bmatrix} N_{yy} \\ N_{ys} \\ L_{yy} \\ L_{sy} \end{Bmatrix} = \begin{bmatrix} K_{11} & K_{12} & K_{13} & K_{14} \\ K_{21} & K_{22} & K_{23} & K_{24} \\ K_{41} & K_{42} & K_{43} & K_{44} \\ K_{51} & K_{52} & K_{53} & K_{54} \end{bmatrix} \begin{Bmatrix} \epsilon_{yy}^0 \\ \gamma_{ys}^0 \\ \phi' \\ \epsilon_{yy}^1 \end{Bmatrix} - \begin{Bmatrix} \tilde{N}_{yy} \\ \tilde{N}_{sy} \\ \tilde{L}_{yy} \\ \tilde{L}_{sy} \end{Bmatrix}, \tag{2.23}$$

and

$$N_{yn} = \left(A_{44} - \frac{{A_{45}}^2}{A_{55}} \right) \gamma_{yn}. \tag{2.24}$$

In these equations K_{ij} denote the modified local stiffness coefficients of the adaptive structure defined in Appendix A.1. While $\tilde{N}_{yy}$, $\tilde{N}_{sy}$ and $\tilde{L}_{yy}$, $\tilde{L}_{sy}$ denote the piezoelec-

trically induced stress resultant and stress couple,

$$\begin{cases} \tilde{N}_{yy} = \sum_{k=1}^{N_p} \left(e_{yy} - \dfrac{A_{12}}{A_{11}} e_{ss} \right) E_{1(k)} (n_2 - n_1) P_{(k)}(s) P_{(k)}(y) \\ \tilde{N}_{sy} = \sum_{k=1}^{N_p} \left(e_{sy} - \dfrac{A_{16}}{A_{11}} e_{ss} \right) E_{1(k)} (n_2 - n_1) P_{(k)}(s) P_{(k)}(y) \\ \tilde{L}_{yy} = \sum_{k=1}^{N_p} \left[\dfrac{1}{2} e_{yy}(n_1 + n_2) - \dfrac{B_{12}}{A_{11}} e_{ss} \right] E_{1(k)} (n_2 - n_1) P_{(k)}(s) P_{(k)}(y) \\ \tilde{L}_{sy} = \sum_{k=1}^{N_p} \left[\dfrac{1}{2} e_{sy}(n_1 + n_2) - \dfrac{B_{16}}{A_{11}} e_{ss} \right] E_{1(k)} (n_2 - n_1) P_{(k)}(s) P_{(k)}(y) \end{cases} \tag{2.25}$$

2.6 Formulation of the Governing System

In order to formulate the equations of motion and the associated boundary conditions, Hamilton's principle [58, pp. 82-86] is used. It states that the true path of motion renders the following variational form stationary:

$$\int_{t_1}^{t_2} \left(\delta T + \delta V - \overline{\delta W_e} \right) \mathrm{d}\, t = 0, \tag{2.26a}$$

with (at $t = t_1, t_2$)

$$\delta u_0 = \delta v_0 = \delta w_0 = \delta \theta_x = \delta \theta_z = \delta \phi = 0, \tag{2.26b}$$

where the kinetic energy T, the strain energy V and the virtual work due to unsteady aerodynamic and gust loads W_e are defined as [98]

$$T = \frac{1}{2} J_h \dot{\theta}^2 + \frac{1}{2} \int_0^L \oint_c \sum_{k=1}^{N_{hp}} \int_{h_{(k)}} \rho_{(k)} \left(\dot{\mathbf{R}} \cdot \dot{\mathbf{R}} \right) \mathrm{d}\, n \, \mathrm{d}\, s \, \mathrm{d}\, y, \tag{2.27a}$$

$$V = \frac{1}{2} \int_0^L \oint_c \left[N_{yy} \varepsilon_{yy}^0 + N_{ys} \gamma_{sy}^0 + L_{yy} \varepsilon_{yy}^1 + L_{sy} \phi' + N_{ny} \gamma_{ny} \right] \mathrm{d}\, s \, \mathrm{d}\, y, \tag{2.27b}$$

$$\begin{aligned} \delta W_e = & \tau_\Lambda \delta \Lambda + \int_0^L \left[p_x \delta u_0 + p_y \delta v_0 + p_z \delta w_0 + m_y \delta \phi - b_w \delta \phi' + m_x \delta \theta_x + m_z \delta \theta_z \right] \mathrm{d}\, y \\ & \left[\bar{Q}_x \delta u_0 + \bar{Q}_z \delta w_o + \bar{T}_y \delta v_0 + \bar{M}_x \delta \theta_x + \bar{M}_z \delta \theta_z + \bar{M}_y \delta \phi + \bar{B}_w \delta \phi' \right] \Big|_0^L . \end{aligned} \tag{2.27c}$$

In Eqs. (2.26) and (2.27), t_1 and t_2 denote two arbitrary motions of time; J_h is the rotary inertia of the hub; ρ is the mass density; δ denotes the variation operator; p_x, p_y and p_z are the external forces while m_x, m_y and m_z are the moments about $x-$, $y-$ and z-axes per unit span length, respectively; b_w is the bimoment of the surface tractions; the terms with over-bar $\bar{(\,)}$ denotes the external loads at beam tip.

Thus, after a lengthy derivative manipulation, the governing equation of rigid hub and flexible thin-walled beam system can be derived as

$$\delta \Lambda \ : \ J_H + \int_0^L I_0 \, \mathrm{d}\, y = \tau_\Lambda, \tag{2.28a}$$

$$\delta u_0 : [T_y u_0' - M_z \phi' \sin\phi + M_x \phi' \cos\phi + Q_x \cos\phi + Q_z \sin\phi]' + p_x - I_1 = 0, \tag{2.28b}$$

$$\delta v_0 : T_y' + p_y - I_2 = 0, \tag{2.28c}$$

$$\delta w_0 : [T_y w_0' - M_z \phi' \cos\phi - M_x \phi' \sin\phi - Q_x \sin\phi + Q_z \cos\phi]' + p_z - I_3 = 0, \tag{2.28d}$$

$$\begin{aligned}\delta\phi : {} & M_y' - B_w'' + [M_x(u_0' \cos\phi - w_0' \sin\phi) - M_z(w_0' \cos\phi + u_0' \sin\phi) + \Gamma_t \phi']' \\ & + M_x(u_0' \phi' \sin\phi + w_0' \phi' \cos\phi) - M_z(w_0' \phi' \sin\phi - u_0' \phi' \cos\phi) \\ & + Q_x(u_0' \sin\phi + w_0' \cos\phi) - Q_z(u_0' \cos\phi - w_0' \sin\phi) + m_y + b_w' - I_4 + I_9' = 0,\end{aligned} \tag{2.28e}$$

$$\delta\theta_x : M_x' - Q_z + m_x - I_5 = 0, \tag{2.28f}$$

$$\delta\theta_z : M_z' - Q_x + m_z - I_6 = 0. \tag{2.28g}$$

For cantilevered beams the boundary conditions at the root are entirely static, while at the tip entirely kinematic. As a result, the boundary conditions are
at beam root $y = 0$,

$$u_0 = v_0 = w_0 = \phi = \phi' = \theta_x = \theta_z = 0, \tag{2.29}$$

at beam tip $y = L$,

$$\delta u_0 : T_y u_0' - M_z \phi' \sin\phi + M_x \phi' \cos\phi + Q_x \cos\phi + Q_z \sin\phi = 0, \tag{2.30a}$$

$$\delta v_0 : \quad T_y = 0, \tag{2.30b}$$

$$\delta w_0 : T_y w_0' - M_z \phi' \cos\phi - M_x \phi' \sin\phi - Q_x \sin\phi + Q_z \cos\phi = 0, \tag{2.30c}$$

$$\begin{aligned}\delta\phi : {} & - B_w' + M_y + M_x(u_0' \cos\phi - w_0' \sin\phi) - M_z(w_0' \cos\phi + u_0' \sin\phi) \\ & + \Gamma_t \phi' + I_9 = 0,\end{aligned} \tag{2.30d}$$

$$\delta\phi' : B_w = 0, \quad \delta\theta_x : M_x = 0, \quad \delta\theta_z : M_z = 0. \tag{2.30e}$$

In governing equations (2.28), the inertial terms I_i ($i = 0, 1, 2, 3, 4, 5, 6, 9$) are given as

$$\begin{aligned}I_0 = {} & \ddot{\Lambda}\Big[b_1(R_0 + y)^2 + b_5 + 2b_1(R_0 + y)v_0 + b_1 {u_0}^2 + b_1 {v_0}^2 \\ & + (b_4 + b_{14}){\theta_x}^2 + (b_5 + b_{15}){\theta_z}^2 + (b_{10} + b_{18}){\phi'}^2 + (b_4 - b_5)\sin^2\phi\Big] \\ & - b_1(R_0 + y + v_0)\ddot{u}_0 + b_1 u_0 \ddot{v}_0 + (b_5 + b_{15})\cos\phi\ddot{\theta}_z \\ & - (b_4\theta_x \cos\phi - b_5\theta_z \sin\phi)\ddot{\phi} + (b_4 + b_{14})\sin\phi\ddot{\theta}_x \\ & + 2\dot{\Lambda}\Big[b_1 u_0 \dot{u}_0 + b_1(R_0 + y + v_0)\dot{v}_0 + (b_{10} + b_{18})\phi'\dot{\phi}' \\ & + (b_4 + b_{14})\theta_x\dot{\theta}_x + (b_5 + b_{15})\theta_z\dot{\theta}_z + (b_4 - b_5)\sin\phi\cos\phi\dot{\phi}\Big] \\ & + \Big[b_4\theta_x \sin\phi + b_5\theta_z \cos\phi\Big]\dot{\phi}^2,\end{aligned} \tag{2.31a}$$

$$I_1 = b_1[\ddot{u}_0 - \ddot{\Lambda}(R_0 + y + v_0) - \underset{\sim}{2\dot{\Lambda}\dot{v}_0} - \underline{\underline{\dot{\Lambda}^2 u_0}}], \tag{2.31b}$$

$$I_2 = b_1[\ddot{v}_0 + \ddot{\Lambda}u_0 + \underset{\sim}{2\dot{\Lambda}\dot{u}_0} - \underline{\underline{\dot{\Lambda}^2(R_0 + y + v_0)}}], \tag{2.31c}$$

$$I_3 = b_1\ddot{w}_0, \tag{2.31d}$$

$$\begin{aligned} I_4 =& (b_4 + b_5)\ddot{\phi} - (b_4\theta_x\cos\phi - b_5\theta_z\sin\phi)\ddot{\Lambda} - \underset{\sim}{2\dot{\Lambda}(b_4\dot{\theta}_x\cos\phi - b_5\dot{\theta}_z\sin\phi)} \\ & - \underset{\cdots}{\dot{\Lambda}^2(b_4 - b_5)\sin\phi\cos\phi}, \end{aligned} \tag{2.31e}$$

$$I_9' = (b_{10} + b_{18})(\ddot{\phi}'' - \underline{\underline{\dot{\Lambda}^2\phi''}}), \tag{2.31f}$$

$$I_5 = (b_4 + b_{14})(\ddot{\theta}_x + \sin\phi\ddot{\Lambda} - \underline{\underline{\dot{\Lambda}^2\theta_x}}) + \underset{\sim}{2\dot{\Lambda}b_4\cos\phi\dot{\phi}}, \tag{2.31g}$$

$$I_6 = (b_5 + b_{15})(\ddot{\theta}_z + \cos\phi\ddot{\Lambda} - \underline{\underline{\dot{\Lambda}^2\theta_z}}) - \underset{\sim}{2\dot{\Lambda}b_5\sin\phi\dot{\phi}}, \tag{2.31h}$$

in which, the mass coefficients b_{ij} are give in A.2, while the terms associated with wavy lines, double underlines, and dot lines denote the Coriolis forces, the centrifugral forces and the Tennis-Racket effect.

As for the 1-D stress resultants and stress couples appearing in the equations of motion and the boundary conditions (Eqs. (2.28) and (2.30)) are defined as:

$$\begin{aligned} T_y(y,t) &= \oint_C N_{yy}\,\mathrm{d}\,s, \quad M_z(y,t) = \oint_C (xN_{yy} - L_{yy}\frac{\mathrm{d}\,z}{\mathrm{d}\,s})\,\mathrm{d}\,s, \\ M_x(y,t) &= \oint_C (zN_{yy} + L_{yy}\frac{\mathrm{d}\,x}{\mathrm{d}\,s})\,\mathrm{d}\,s, \quad Q_x(y,t) = \oint_C (N_{sy}\frac{\mathrm{d}\,x}{\mathrm{d}\,s} - N_{ny}\frac{\mathrm{d}\,z}{\mathrm{d}\,s})\,\mathrm{d}\,s, \\ Q_z(y,t) &= \oint_C (N_{sy}\frac{\mathrm{d}\,z}{\mathrm{d}\,s} + N_{ny}\frac{\mathrm{d}\,x}{\mathrm{d}\,s})\,\mathrm{d}\,s, \quad B_w(y,t) = -\oint_C (F_wN_{yy} + aL_{yy})\,\mathrm{d}\,s, \\ M_y(y,t) &= \oint_C [N_{sy}\psi(s) + 2L_{sy}]\,\mathrm{d}\,s, \quad \Gamma_t(y,t) = \oint_C \left[(x^2 + z^2)N_{yy} + 2r_nL_{yy}\right]\mathrm{d}\,s. \end{aligned} \tag{2.32}$$

Actually in Eqs. (2.32), the one dimension axial force T_y, transverse shear forces Q_x, Q_z, bending moments M_x, M_z, torque M_y, bimoment B_w, and nonlinear stress couple Γ_t consist of two parts, e.g., $T_y = \hat{T}_y + \tilde{T}_y$, over-hat $(\hat{\cdot})$ and over-tilde $(\tilde{\cdot})$ identifying the pure mechanical and piezo-actuator contributions, respectively.

For the pure mechanical contribution, their expressions in terms of the basic 1-D

displacement measures can be written as:

$$\begin{Bmatrix} \hat{T}_y \\ \hat{M}_z \\ \hat{M}_x \\ \hat{Q}_x \\ \hat{Q}_z \\ \hat{B}_w \\ \hat{M}_y \\ \hat{\Gamma}_t \end{Bmatrix} = \begin{bmatrix} a_{11} & a_{12} & a_{13} & a_{14} & a_{15} & a_{16} & a_{17} & a_{18} \\ a_{12} & a_{22} & a_{23} & a_{24} & a_{25} & a_{26} & a_{27} & a_{28} \\ a_{13} & a_{23} & a_{33} & a_{34} & a_{35} & a_{36} & a_{37} & a_{38} \\ a_{14} & a_{24} & a_{34} & a_{44} & a_{45} & a_{46} & a_{47} & a_{48} \\ a_{15} & a_{25} & a_{35} & a_{45} & a_{55} & a_{56} & a_{57} & a_{58} \\ a_{16} & a_{26} & a_{36} & a_{46} & a_{56} & a_{66} & a_{67} & a_{68} \\ a_{17} & a_{27} & a_{37} & a_{47} & a_{57} & a_{67} & a_{77} & a_{78} \\ a_{18} & a_{28} & a_{38} & a_{48} & a_{58} & a_{68} & a_{78} & a_{88} \end{bmatrix} \begin{Bmatrix} v_0' + \frac{1}{2}(u_0')^2 + \frac{1}{2}(w_0')^2 \\ \theta_z' - w_0'\phi' \cos\phi - u_0'\phi' \sin\phi \\ \theta_x' + u_0'\phi' \cos\phi - w_0'\phi' \sin\phi \\ \theta_z + u_0' \cos\phi - w_0' \sin\phi \\ \theta_x + u_0' \sin\phi + w_0' \cos\phi \\ \phi'' \\ \phi' \\ \frac{1}{2}(\phi')^2 \end{Bmatrix}, \tag{2.33}$$

in which the global stiffness quantities a_{ij} are defined in Appendix A.3. For general anisotropic materials, the stiffness matrix in Eq. (2.33) is fully populated. In such a case, the governing system and the associated BCs would exhibit a complete coupling between the various modes, i.e., warping (primary and secondary), bending (vertical and lateral), twist and transverse shearing. However toward the goal of meeting the needs of various problems, such as eliminating a chronic aeroelastic instability featured by forward wing aircraft [50], improving twisting motion of turbine rotor blades at different rotor speeds [12], particular lay-ups are used to induce specific types of elastic couplings. The explicit discussion will be given in the following chapters.

As for pure piezo-actuator contribution, the piezoelectrically induced actuation coupling are the functions of external voltages, and it can be expressed in the form as

$$\tilde{\mathbf{F}} = [\mathcal{A}_i^F] P(y) \mathbf{V}, \tag{2.34}$$

where $P(y)$ of Eq. (2.19c) denotes the locations along span of the actuator. For the case of a rectangular cross-section as shown in Fig. 2.4, the actuators can be grouped as two actuator-pairs, i.e., flange-actuator-pair (top and bottom walls) and web-actuator-pair (left and right walls). Thus the pure piezo-actuator contribution of Eqs. (2.32) can be

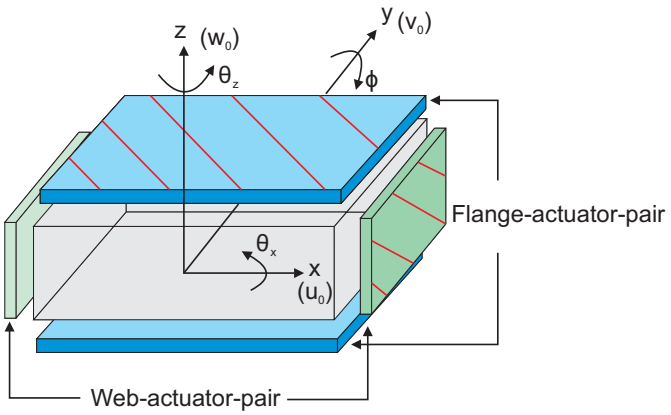

Figure 2.4: *Piezo-actuator-pairs for a rectangular cross-section*

expressed as

$$\begin{Bmatrix} \tilde{T}_y(y,t) \\ \tilde{M}_y(y,t) \\ \tilde{B}_w(y,t) \\ \tilde{\Gamma}_t(y,t) \\ \tilde{M}_z(y,t) \\ \tilde{M}_x(y,t) \\ \tilde{Q}_x(y,t) \\ \tilde{Q}_z(y,t) \end{Bmatrix} = \begin{bmatrix} \mathcal{A}_1^{Ty} & \mathcal{A}_2^{Ty} & \mathcal{A}_3^{Ty} & \mathcal{A}_4^{Ty} \\ \mathcal{A}_1^{My} & \mathcal{A}_2^{My} & \mathcal{A}_3^{My} & \mathcal{A}_4^{My} \\ \mathcal{A}_1^{Bw} & \mathcal{A}_2^{Bw} & \mathcal{A}_3^{Bw} & \mathcal{A}_4^{Bw} \\ \mathcal{A}_1^{\Gamma t} & \mathcal{A}_2^{\Gamma t} & \mathcal{A}_3^{\Gamma t} & \mathcal{A}_4^{\Gamma t} \\ \mathcal{A}_1^{Mz} & \mathcal{A}_2^{Mz} & \mathcal{A}_3^{Mz} & \mathcal{A}_4^{Mz} \\ \mathcal{A}_1^{Mx} & \mathcal{A}_2^{Mx} & \mathcal{A}_3^{Mx} & \mathcal{A}_4^{Mx} \\ \mathcal{A}_1^{Qx} & \mathcal{A}_2^{Qx} & \mathcal{A}_3^{Qx} & \mathcal{A}_4^{Qx} \\ \mathcal{A}_1^{Qz} & \mathcal{A}_2^{Qz} & \mathcal{A}_3^{Qz} & \mathcal{A}_4^{Qz} \end{bmatrix} \begin{Bmatrix} P^F(y)V_1(t) \\ P^F(y)V_2(t) \\ P^W(y)V_3(t) \\ P^W(y)V_4(t) \end{Bmatrix}, \tag{2.35}$$

where $P^F(y)$ and $P^W(y)$ of Eq. (2.19c) denote the locations along span for flange-actuator-pair and web-actuator-pair, respectively; the piezo-actuator coefficients $\mathcal{A}_i^X$ ($i = 1,2,3,4$) are defined in Appendix A.4, and the voltage parameters V_i ($i = 1,2,3,4$) are defined as

$$V_1(t) = \frac{1}{2}\left[V_T(t) - V_B(t)\right], \quad V_2(t) = \frac{1}{2}\left[V_T(t) + V_B(t)\right], \tag{2.36a}$$

$$V_3(t) = \frac{1}{2}\left[V_L(t) - V_R(t)\right], \quad V_4(t) = \frac{1}{2}\left[V_L(t) + V_R(t)\right], \tag{2.36b}$$

where V_T, V_B, V_L and V_R denote the voltages applied on the actuators located at the top, bottom, left and right plates of the beam.

CHAPTER 3

Active Control of Adaptive Pretwisted Rotating Blades

3.1 Introduction

In this chapter, a rotating thin-walled blade theory incorporating fiber-reinforced and piezo-composite is developed and used to study the active control for vibration suppression, see Fig. 3.1. The structural model accounts for transverse shear strain, primary and secondary warpings, pretwist and presetting angles, centrifugal stiffening effect and tennis-racket effect. The adaptive capabilities are provided by the actuators manufactured by anisotropic piezo-composite layers embedded into the structure. In addition, the elastic tailoring technology is applied to optimal the rotating blade structure. Specifically, circumferentially uniform stiffness (CUS) lay-up configuration is adopted to decouple the system into two independent elastic couplings, viz., flapping-lagging-transverse shear and extension-twist elastic couplings. Based on the negative velocity feedback control and lienar quadratic regular (LQR) control, the control authority of the implementation of piezo-actuators with different ply-angles, considered in conjunction with that of the structural tailoring, are highlighted. Moreover, the influences of design factors, such as rotor speed, presetting and pretwist angles are also investigated in detailed.

3.2 Dynamical model

Besides the rotating coordinate system (x, y, z), a local coordinate system (x^p, y, z^p) is also defined, where x^p and z^p are the principal axes of an arbitrary beam cross-section, see Fig. 3.2. Coordinate systems (x, y, z) and (x^p, y, z^p) are related by the following

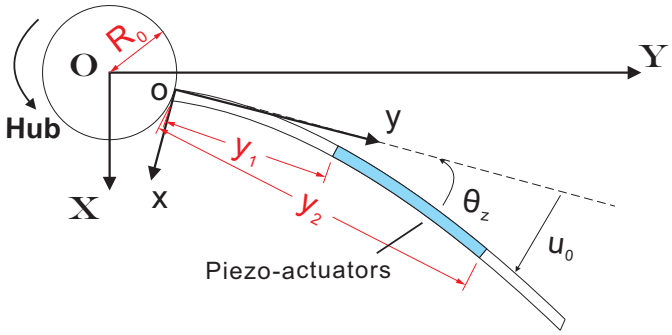

Figure 3.1: *Adaptive rotating blade model*

transformation

$$\begin{cases} x(s,y) = x^p(s)\cos\beta(y) + z^p(s)\sin\beta(y), \\ z(s,y) = -x^p(s)\sin\beta(y) + z^p(s)\cos\beta(y), \end{cases} \tag{3.1}$$

where the linear pretwist angle $\beta(y)$ can be assumed as

$$\beta(y) = \gamma_0 + \beta_0 y/L, \tag{3.2}$$

in which γ_0, β_0 and L denote the presetting angle, the pretwist angle of the cross-section at the beam tip and the length of the beam, respectively.

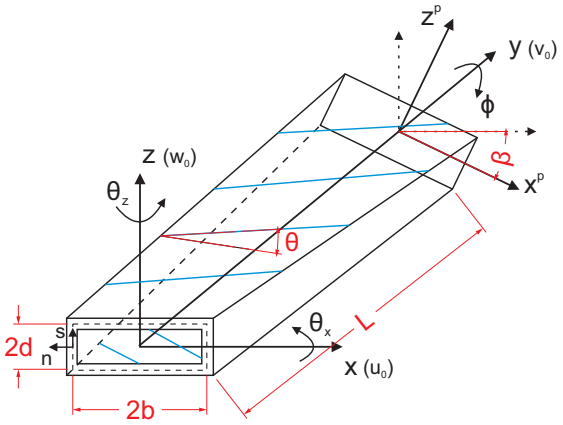

Figure 3.2: *A pretwisted thin-walled beam with the rectangular cross-section*

The governing equations and associated boundary conditions of the adaptive rotating blade are based on the theory developed in Chapter 2. Although the governing equations are valid for a thin-walled beam with an arbitrary closed cross-section, for the sake of illustration, the beam with a typical rectangular cross-section of Fig. 3.2 is solely considered in the following discussions.

3.2.1 Circumferentially uniform stiffness (CUS) lay-up configuration

A special structural configuration, viz., *circumferentially uniform stiffness* (CUS) configuration was firstly proposed by Rehfield and Atilgan [81] and is considered here. For the thin-walled beam with rectangular cross-section as shown in Fig. 3.2, a CUS

configuration implies the ply-angle distribution $\theta(z) = \theta(-z)$ of the top and bottom walls and $\theta(x) = \theta(-x)$ of the left and right walls, see Fig. 3.3.

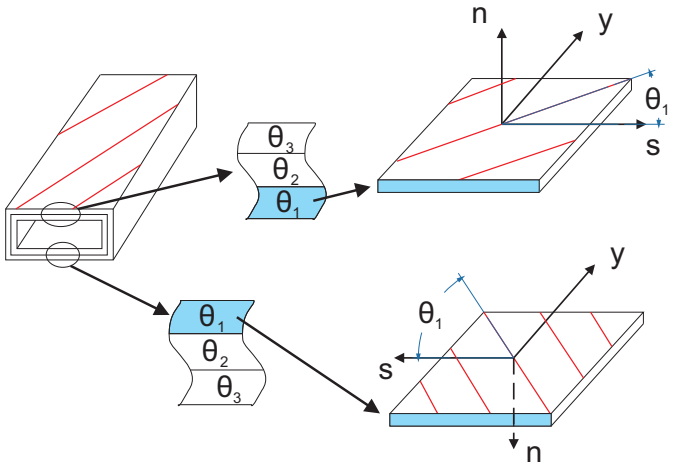

Figure 3.3: *Circumferentially uniform stiffness (CUS) configuration*

Applying circumferentially uniform stiffness (CUS) lay-up configuration will yield $[a_{ij}(y)]$ in Eq. (2.33) decoupling into two, viz, extension-twist elastic coupling,

$$\begin{Bmatrix} \hat{T}_y \\ \hat{M}_y \\ \hat{B}_w \\ \hat{\Gamma}_t \end{Bmatrix} = \begin{bmatrix} a_{11} & a_{17} & 0 & a_{18} \\ a_{17} & a_{77} & 0 & a_{78} \\ 0 & 0 & a_{66} & 0 \\ a_{18} & a_{78} & 0 & a_{88} \end{bmatrix} \begin{Bmatrix} v_0' + \frac{1}{2}(u_0')^2 + \frac{1}{2}(w_0')^2 \\ \phi' \\ \phi'' \\ \frac{1}{2}(\phi')^2 \end{Bmatrix}, \tag{3.3}$$

and bending-transverse shear elastic coupling,

$$\begin{Bmatrix} \hat{M}_z \\ \hat{M}_x \\ \hat{Q}_x \\ \hat{Q}_z \end{Bmatrix} = \begin{bmatrix} a_{22}(y) & a_{23}(y) & a_{24}(y) & a_{25}(y) \\ a_{23}(y) & a_{33}(y) & a_{34}(y) & a_{35}(y) \\ a_{24}(y) & a_{34}(y) & a_{44}(y) & a_{45}(y) \\ a_{25}(y) & a_{35}(y) & a_{45}(y) & a_{55}(y) \end{bmatrix} \begin{Bmatrix} \theta_z' - w_0'\phi' \cos\phi - u_0'\phi' \sin\phi \\ \theta_x' + u_0'\phi' \cos\phi - w_0'\phi' \sin\phi \\ \theta_z + u_0' \cos\phi - w_0' \sin\phi \\ \theta_x + u_0' \sin\phi + w_0' \cos\phi \end{Bmatrix}. \tag{3.4}$$

Note that, a_{ij} in Eq. (3.3) are independent of spanwise coordinate, i.e., $a_{ij}(y) = a_{ij}^p$. a_{ij}^p is the stiffness coefficients describe in the local coordinate system (x^p, y, z^p). As for the explicit expressions of $a_{ij}(y)$ in Eq. (3.4), they are given in Appendix A.5. Note that, a_{23}^p, a_{24}^p, a_{35}^p and a_{45}^p, these four local stiffness quantities are all zero in the expressions of $a_{ij}(y)$.

Applying CUS lay-up configuration and being described in the rotating coordinate system (x, y, z), Eq. (2.35) will be reduced as two actuating groups, viz., extension-

twist actuating coupling

$$\begin{Bmatrix} \tilde{T}_y(y,t) \\ \tilde{M}_y(y,t) \\ \tilde{B}_w(y,t) \\ \tilde{\Gamma}_t(y,t) \end{Bmatrix} = \begin{bmatrix} \mathcal{A}_2^{Ty} & \mathcal{A}_4^{Ty} \\ \mathcal{A}_2^{My} & \mathcal{A}_4^{My} \\ 0 & 0 \\ \mathcal{A}_2^{\Gamma t} & \mathcal{A}_4^{\Gamma t} \end{bmatrix} \begin{Bmatrix} V_2(t) \\ V_4(t) \end{Bmatrix} P(y), \tag{3.5}$$

and bending-transverse shear actuating coupling

$$\begin{Bmatrix} \tilde{M}_z(y,t) \\ \tilde{M}_x(y,t) \\ \tilde{Q}_x(y,t) \\ \tilde{Q}_z(y,t) \end{Bmatrix} = \begin{bmatrix} \mathcal{A}_1^{Mx}\sin\beta(y) & \mathcal{A}_3^{Mz}\cos\beta(y) \\ \mathcal{A}_1^{Mx}\cos\beta(y) & -\mathcal{A}_3^{Mz}\sin\beta(y) \\ \mathcal{A}_1^{Qx}\cos\beta(y) & \mathcal{A}_3^{Qz}\sin\beta(y) \\ -\mathcal{A}_1^{Qx}\sin\beta(y) & \mathcal{A}_3^{Qz}\cos\beta(y) \end{bmatrix} \begin{Bmatrix} V_1(t) \\ V_3(t) \end{Bmatrix} P(y). \tag{3.6}$$

3.2.2 Governing equations and boundary conditions

In this chapter we assume that the angular speed is constant, i.e., $\dot{\Lambda} = \Omega$. In order to study the eigen-frequencies of the rotating blade in a general may, a linear blade structural dynamics model is derived. Note that, in order to capture the high rotating speed induced effects, i.e., dynamic stiffening, tennis-racket effect, the nonlinear terms that yield linear contributions should be kept. In view of physically evidence fact that the blade is much stiffer in the longitudinal direction than in the flapping and lagging ones, the effect of the axial inertia is much smaller than the others. Thus discarding axial inertial term $b_1\ddot{v}_0$ and Coriolis effect term $2b_1\Omega\dot{v}_0$ (which is negligibly small for this particular blade orientation [24]), the direct integration of Eq. (2.28c) in conjunction with boundary condition at the free end, stipulating zero external forces ($p_y = 0$, $\tilde{T}_y = 0$) yields

$$T_y(y,t) \approx -\int_y^L \left\{-b_1\Omega^2(R_0 + y + v_0)\right\} \mathrm{d}\, y = b_1\Omega^2 R(y) = \hat{\hat{T}}_y(y,t), \tag{3.7}$$

where double over-hat $\hat{\hat{(\cdot)}}$ denotes the force induced by dynamical (centrifugal) stiffening effect and

$$R(y) = R_0(L-y) + \frac{1}{2}(L^2 - y^2). \tag{3.8}$$

Note that, for high angular speed Ω, this dynamic stiffening effect will be significant and should be included in the linear system. In addition, as concerns Eq. (2.28e) governing the twist-extension motion, $\hat{\Gamma}_t$ which plays the role of a torsional stiffness induced by the centrifugal force field should also be considered [88],

$$\hat{\hat{\Gamma}}_t = (b_4 + b_5)\Omega^2 R(y). \tag{3.9}$$

Taking Eqs. (3.3), (3.4), (3.5) and (3.6) into the governing equations and the associated boundary conditions (Eqs. (2.28)-(2.30)) in conjunction with Eqs. (3.7) and (3.9), the system can be linearized in the CUS lay-up configuration. Actually the linear system can be split into two subsystems, one governs the lateral bending-vertical bending coupling motion (flap-lag) and the other governs the twist-extension coupling motion.

BB-subsystem (Lateral Bending-Vertical Bending coupling)

$$\begin{aligned}\delta u_0 \,:\, & [a_{24}\theta_z' + a_{34}\theta_x' + a_{44}(u_0' + \theta_z) + a_{45}(w_0' + \theta_x)]' + p_x + \underline{b_1\Omega^2[R(y)u_0']'} \\ & - b_1[\ddot{u}_0 - \underbrace{2\Omega\dot{v}_0}_{} - \underline{\Omega^2 u_0}] + \delta_p P'(y)\left[\mathcal{A}_1^{Qx}V_1\cos\beta + \mathcal{A}_3^{Qz}V_3\sin\beta\right] \\ & + \beta' P(y)\left[-\mathcal{A}_1^{Qx}V_1\sin\beta + \mathcal{A}_3^{Qz}V_3\cos\beta\right] = 0,\end{aligned} \tag{3.10a}$$

$$\begin{aligned}\delta w_0 \,:\, & [a_{25}\theta_z' + a_{35}\theta_x' + a_{45}(u_0' + \theta_z) + a_{55}(w_0' + \theta_x)]' + \underline{b_1\Omega^2[R(y)w_0']'} \\ & - b_1\ddot{w}_0 + p_z + \delta_p P'(y)\left[\mathcal{A}_3^{Qz}V_3\cos\beta - \mathcal{A}_1^{Qx}V_1\sin\beta\right] \\ & - \beta' P(y)\left[\mathcal{A}_3^{Qz}V_3\sin\beta + \mathcal{A}_1^{Qx}V_1\cos\beta\right] = 0,\end{aligned} \tag{3.10b}$$

$$\begin{aligned}\delta\theta_x \,:\, & \left[a_{23}\theta_z' + a_{33}\theta_x' + a_{34}(u_0' + \theta_z) + a_{35}(w_0' + \theta_x)\right]' - \left[a_{25}\theta_z' + a_{35}\theta_x'\right. \\ & \left. + a_{45}(u_0' + \theta_z) + a_{55}(w_0' + \theta_x)\right] + m_x - b_4\ddot{\theta}_x - b_6\ddot{\theta}_z - \underbrace{2\Omega b_4\dot{\phi}}_{} \\ & + \underline{\underline{\Omega^2(b_4\theta_x + b_6\theta_z)}} + \delta_p P'(y)\left[\mathcal{A}_1^{Mx}V_1\cos\beta - \mathcal{A}_3^{Mz}V_3\sin\beta\right] \\ & + P(y)\left[(-\mathcal{A}_1^{Mx}\beta' + \mathcal{A}_1^{Qx})V_1\sin\beta - (\mathcal{A}_3^{Mz}\beta' + \mathcal{A}_3^{Qz})V_3\cos\beta\right] = 0,\end{aligned} \tag{3.10c}$$

$$\begin{aligned}\delta\theta_z \,:\, & \left[a_{22}\theta_z' + a_{23}\theta_x' + a_{24}(u_0' + \theta_z) + a_{25}(w_0' + \theta_x)\right]' - \left[a_{24}\theta_z' + a_{34}\theta_x'\right. \\ & \left. + a_{44}(u_0' + \theta_z) + a_{45}(w_0' + \theta_x)\right] + m_z - b_5\ddot{\theta}_z - b_6\ddot{\theta}_x - \underbrace{2\Omega b_6\dot{\phi}}_{} \\ & + \underline{\underline{\Omega^2(b_5\theta_z + b_6\theta_x)}} + \delta_p P'(y)\left[\mathcal{A}_3^{Mz}V_3\cos\beta + \mathcal{A}_1^{Mx}V_1\sin\beta\right] \\ & - P(y)\left[(\mathcal{A}_3^{Mz}\beta' + \mathcal{A}_3^{Qz})V_3\sin\beta - (\mathcal{A}_1^{Mx}\beta' - \mathcal{A}_1^{Qx})V_1\cos\beta\right] = 0,\end{aligned} \tag{3.10d}$$

the boundary conditions are
at $y = 0$:

$$u_0 = w_0 = \theta_x = \theta_z = 0, \tag{3.11}$$

and at $y = L$:

$$\begin{aligned}\delta u_0 \,:\, & a_{24}(L)\theta_z' + a_{34}(L)\theta_x' + a_{44}(L)(u_0' + \theta_z) + a_{45}(L)(w_0' + \theta_x) \\ & + \delta_s\left[\mathcal{A}_1^{Qx}V_1\cos\beta(L) + \mathcal{A}_3^{Qz}V_3\sin\beta(L)\right] = \bar{Q}_x,\end{aligned} \tag{3.12a}$$

$$\begin{aligned}\delta w_0 \,:\, & a_{25}(L)\theta_z' + a_{35}(L)\theta_x' + a_{45}(L)(u_0' + \theta_z) + a_{55}(L)(w_0' + \theta_x) \\ & + \delta_s\left[\mathcal{A}_3^{Qz}V_3\cos\beta(L) - \mathcal{A}_1^{Qx}V_1\sin\beta(L)\right] = \bar{Q}_z,\end{aligned} \tag{3.12b}$$

$$\begin{aligned}\delta\theta_x \,:\, & a_{23}(L)\theta_z' + a_{33}(L)\theta_x' + a_{34}(L)(u_0' + \theta_z) + a_{35}(L)(w_0' + \theta_x) \\ & + \delta_s\left[\mathcal{A}_1^{Mx}V_1\cos\beta(L) - \mathcal{A}_3^{Mz}V_3\sin\beta(L)\right] = \bar{M}_x,\end{aligned} \tag{3.12c}$$

$$\begin{aligned}\delta\theta_z \,:\, & a_{22}(L)\theta_z' + a_{23}(L)\theta_x' + a_{24}(L)(u_0' + \theta_z) + a_{25}(L)(w_0' + \theta_x) \\ & + \delta_s\left[\mathcal{A}_3^{Mz}V_3\cos\beta(L) + \mathcal{A}_1^{Mx}V_1\sin\beta(L)\right] = \bar{M}_z.\end{aligned} \tag{3.12d}$$

TE-subsystem (Twist-Extension coupling)

$$\begin{aligned}\delta v_0 \; : a_{11}v_0'' + a_{17}\phi'' + p_y + \delta_p P'(y)[\mathcal{A}_2^{Ty}V_2 + \mathcal{A}_4^{Ty}V_4] \\ - b_1[\ddot{v}_0 + \underbrace{2\Omega\dot{u}_0}_{\sim\sim\sim} - \underline{\Omega^2(R_0 + y + v_0)}] = 0,\end{aligned} \tag{3.13a}$$

$$\begin{aligned}\delta\phi \; : a_{17}v_0'' + a_{77}\phi'' - a_{66}\phi^{(iv)} + m_y + b_w' + \delta_p P'(y)[\mathcal{A}_2^{My}V_2 + \mathcal{A}_4^{My}V_4] \\ - (b_4 + b_5)\ddot{\phi} + b_{10}\ddot{\phi}'' + \underbrace{2\Omega(b_4\dot{\theta}_x + b_6\dot{\theta}_z)}_{\sim\sim\sim} + \underbrace{\Omega^2\,[b_6 + (b_4 - b_5 - b_6)\phi]}_{\cdots\cdots\cdots} \\ + \underline{\Omega^2[(b4 + b5)R(y)\phi']'} - \underbrace{b_{10}\Omega^2\phi''}_{- - - - -} = 0,\end{aligned} \tag{3.13b}$$

the boundary conditions are
at $y = 0$:

$$v_0 = \phi = \phi' = 0, \tag{3.14}$$

and at $y = L$:

$$\delta v_0 \; : a_{11}v_0' + a_{17}\phi' + \delta_s[\mathcal{A}_2^{Ty}V_2 + \; \mathcal{A}_4^{Ty}V_4] = \bar{T}_y, \tag{3.15a}$$

$$\delta\phi \; : a_{17}v_0' + a_{77}\phi' - a_{66}'''\phi + b_{10}(\ddot{\phi}' - \underbrace{\Omega^2\phi'}_{- - -}) + \delta_s[\mathcal{A}_2^{My}V_2 + \delta_s\mathcal{A}_4^{My}V_4] = \bar{M}_y, \tag{3.15b}$$

$$\delta\phi' \; : \; a_{66}\phi'' = \bar{B}_w, \tag{3.15c}$$

In these equations, the terms associated with (1) the centrifugal acceleration, (2) the Coriolis, (3) the tennis-racket, (4) the centrifugal warping and (5) the centrifugal-rotatory effects are underscored by (1) a solid line (____), (2) a wavy line ($\sim\sim\sim$), (3) a dotted line ($\cdots\cdots$), (4) a dashed line ($- - -$) and (5) two superposed solid lines ($\equiv\equiv\equiv$) respectively. More details about these high rotating speed induced effects can be found e.g. in Refs. [40,47,88]. For the cases (a) the actuator is spread over the entire beam span (b) the actuator is a single patch, the traces have to be taken as (a) $\delta_p = 0$ and $\delta_s = 1$ (b) $\delta_p = 1$ and $\delta_s = 0$, respectively. Note that, the two subsystems are independent when Coriolis effects are discarded.

3.3 Solution methodology

3.3.1 The Extend Galerkin's Method

The Extend Galerkin's Method (EGM) [45, 70, 75] is applied to discretize the system for numerical study. The underlying idea of EGM is to select weighting (or shape) functions that exactly satisfy only the geometric boundary conditions ($y = 0$). The terms arising as a result of the non-fulfillment of natural boundary conditions ($y = L$) remain as residual terms in the energy functional itself, which are then minimized in the Galerkin sense [44], thus yielding excellent accuracy and rapid convergence [70]. Let

$$\begin{aligned}u_0(y,t) = \mathbf{\Psi}_u^T(y)\mathbf{q}_u(t), \quad v_0(y,t) = \mathbf{\Psi}_v^T(y)\mathbf{q}_v(t), \quad w_0(y,t) = \mathbf{\Psi}_w^T(y)\mathbf{q}_w(t), \\ \phi_(y,t) = \mathbf{\Psi}_\phi^T(y)\mathbf{q}_\phi(t), \quad \theta_x(y,t) = \mathbf{\Psi}_x^T(y)\mathbf{q}_x(t), \quad \theta z(y,t) = \mathbf{\Psi}_z^T(y)\mathbf{q}_z(t),\end{aligned} \tag{3.16}$$

where the shape functions $\mathbf{\Psi}_u^T(y)$, $\mathbf{\Psi}_v^T(y)$, $\mathbf{\Psi}_w^T(y)$, $\mathbf{\Psi}_\phi^T(y)$, $\mathbf{\Psi}_x^T(y)$ and $\mathbf{\Psi}_z^T(y)$ are required to fulfill the geometric boundary conditions. Thus the discretized forms of the BB- and TE-subsystems follow as

$$\mathbf{M}_{B/T}\ddot{\mathbf{q}}_{B/T} + [\mathbf{K}_{B/T} + \Omega^2\hat{\mathbf{K}}_{B/T}]\mathbf{q}_{B/T} + \mathcal{A}_{B/T}\mathbf{V}_{B/T} = \mathbf{Q}_{B/T}, \tag{3.17}$$

where

$$\mathbf{q}_B = \begin{Bmatrix}\mathbf{q}_u^T & \mathbf{q}_w^T & \mathbf{q}_x^T & \mathbf{q}_z^T\end{Bmatrix}^T, \quad \mathbf{q}_T = \begin{Bmatrix}\mathbf{q}_v^T & \mathbf{q}_\phi^T\end{Bmatrix}^T, \tag{3.18}$$

$$\mathbf{V}_B = \begin{Bmatrix}V_1 & V_3\end{Bmatrix}^T, \quad \mathbf{V}_T = \begin{Bmatrix}V_2 & V_4\end{Bmatrix}^T. \tag{3.19}$$

The subscript B and T denote the matrix/vector of BB- and TE-subsystems, respectively. The expressions for mass matrix $\mathbf{M}_{B/T}$, stiffness matrix $\mathbf{K}_{B/T}$, additional stiffness matrix $\hat{\mathbf{K}}_{B/T}$, actuating matrix $\mathcal{A}_{B/T}$ and external excitation vector $\mathbf{Q}_{B/T}$ are given in Appendix A.6.

3.3.2 Negative velocity feedback control

We assume the sensor can offer the velocity information at the beam span $y = Y_s$, then the actuating voltage vector $\mathbf{V}_{B/T}$ for the negative velocity feedback control algorithm [47, 63] can be rewritten as

$$\begin{aligned}\mathbf{V}_B &= \begin{Bmatrix}V_1\\V_3\end{Bmatrix} = \begin{Bmatrix}-k_1[-\dot{\theta}_x^p(Y_s,t)]\\-k_3[\dot{\theta}_z^p(Y_s,t)]\end{Bmatrix}\\ &= \begin{Bmatrix}k_1[\dot{\theta}_x(Y_s,t)\cos\beta + \dot{\theta}_z(Y_s,t)\sin\beta]\\-k_3[-\dot{\theta}_x(Y_s,t)\sin\beta + \dot{\theta}_z(Y_s,t)\cos\beta]\end{Bmatrix} = \mathbf{P}_B(Y_s)\dot{\mathbf{q}}_B(t),\end{aligned} \tag{3.20}$$

$$\mathbf{V}_T = \begin{Bmatrix}V_2\\V_4\end{Bmatrix} = \begin{Bmatrix}-k_2\dot{\phi}^p(Y_s,t)\\-k_4\dot{\phi}^p(Y_s,t)\end{Bmatrix} = \begin{Bmatrix}-k_2\dot{\phi}(Y_s,t)\\-k_4\dot{\phi}(Y_s,t)\end{Bmatrix} = \mathbf{P}_T(Y_s)\dot{\mathbf{q}}_T(t), \tag{3.21}$$

where, k_i ($i = 1, 2, 3, 4$) are defined as feedback control gains. The expressions of control matrices $\mathbf{P}_{B/T}$ are given in Appendix A.6. As a result, the closed-loop dicretized system Eq. (3.17) becomes

$$\mathbf{M}_{B/T}\ddot{\mathbf{q}}_{B/T}(t) + \mathcal{A}_{B/T}\mathbf{P}_{B/T}\dot{\mathbf{q}}_{B/T}(t) + [\mathbf{K}_{B/T} + \Omega^2\hat{\mathbf{K}}_{B/T}]\mathbf{q}_{B/T}(t) = \mathbf{Q}_{B/T}(t). \tag{3.22}$$

3.3.3 Linear Quadratic Regulator optimal control

One important target of the piezo-actuators is to suppress the vibration of the blade. To achieve this target, linear quadratic regulator (LQR) optimal control based on the use of a full state feedback scheme is adopted. Eq. (3.17) can be cast in state-space form as

$$\dot{\mathbf{x}}(t) = \mathbf{A}\mathbf{x}(t) + \mathbf{B}\mathbf{Q}(t) - \mathbf{B}\mathcal{A}_\mathbf{1}V_1(t) - \mathbf{B}\mathcal{A}_\mathbf{3}V_3(t) \tag{3.23}$$

where,

$$\mathbf{x}(t) = \begin{bmatrix}\mathbf{q}^T(t)\\\dot{\mathbf{q}}^T(t)\end{bmatrix}, \quad \mathbf{A} = \begin{bmatrix}\mathbf{0} & \mathbf{I}\\-\mathbf{M}^{-1}\mathbf{K} & \mathbf{0}\end{bmatrix}, \quad \mathbf{B} = \begin{Bmatrix}\mathbf{0}\\\mathbf{M}^{-1}\end{Bmatrix}. \tag{3.24}$$

Note that the LQR control provides sort of a benchmark, an ideal optimal value which cannot be obtained in practical applications because the state $\mathbf{x}$ is not available and needs to be reconstructed using a state estimator that degrades the quality of the regulator. Within the LQR control algorithm, we minimize the cost function (both the response of the closed-loop system and the control effort should be minimized simultaneously).

$$J = \frac{1}{2}\int_{t_0}^{t_f} \left(\mathbf{x}^T\mathbf{Z}\mathbf{x} + V_i R_i V_i\right) \mathrm{d}\, t, \tag{3.25}$$

where positive semidefinite matrix $\mathbf{Z}$ and positive definite scalar R_i denote the state weighting matrix and the control weighting scalar, respectively, while t_0 and t_f denote the present and the final time, respectively. Following Ref. [5], the weighting matrices $\mathbf{Z}$ and R_i proper to a trade off between control effectiveness and control energy consumption by taking

$$\mathbf{Z} = \begin{bmatrix} \alpha\mathbf{K} & \mathbf{0} \\ \mathbf{0} & \beta\mathbf{M} \end{bmatrix}, \quad R_i = \eta_i {\mathcal{A}_\mathbf{i}}^T \mathbf{K}^{-1} \mathcal{A}_\mathbf{i}, \quad (i = 1, 3) \tag{3.26}$$

where α and β are weighting coefficients, ($\alpha\beta \geq 0$ and $(\alpha + \beta) > 0$), where η_i is a positive scale factor. The matrix $\mathbf{Z}$ actually represents the sum of the system kinetic and potential energies in the sense of

$$\frac{1}{2}\int_{t_0}^{t_f} \mathbf{x}^T\mathbf{Z}\mathbf{x}\, \mathrm{d}\, t = \frac{1}{2}\int_{t_0}^{t_f} \left[\dot{\mathbf{q}}^T\beta\mathbf{M}\dot{\mathbf{q}} + \mathbf{q}^T\alpha\mathbf{K}\mathbf{q}\right] \mathrm{d}\, t. \tag{3.27}$$

On the perspective of vibration suppression, it is reasonable to just consider the system kinetic energy, i.e., weighting coefficients combination $\alpha = 0$ and $\beta = 1$ is adopted in the context. Thus, the LQR optimal feedback control law can be given as

$$V_i(t) = -\mathbf{G}_i\mathbf{x}(t), \tag{3.28}$$

where $\mathbf{G}_i$ is the optimal gain matrix,

$$\mathbf{G}_i = -\mathbf{R}^{-1} {\mathcal{A}_\mathbf{i}}^T \mathbf{B}^T \mathbf{P}_\mathbf{i}, \tag{3.29}$$

while $\mathbf{P}_\mathbf{i}$ is the positive-definite solution to the steady-state Riccati equation

$$\mathbf{Z} + \mathbf{P}_\mathbf{i}\mathbf{A} + \mathbf{A}^T\mathbf{P}_\mathbf{i} - R_i\mathbf{P}_\mathbf{i}\mathbf{B}\mathcal{A}_\mathbf{i}{\mathcal{A}_\mathbf{i}}^T\mathbf{B}^T\mathbf{P}_\mathbf{i} = 0. \tag{3.30}$$

3.4 Model validations

The model validation is implemented on two aspects, viz., frequency and actuating performance. At first, Table 3.1 compares the frequency predictions of an unpretwisted rotating beam with the FEM results in Ref. [91] and the experimental data in Ref. [17], showing good agreements. The geometry and material properties of the box beam used in this validation are shown in Table 3.2.

Table 3.3 further compares the frequency predictions of a pretwisted and unrotating beam. The characteristics of the beam are given as [47, p. 275]

$$a_{22}^p = 487.9\ \mathrm{N}\cdot\mathrm{m}^2, \quad a_{33}^p = 2.26\ \mathrm{N}\cdot\mathrm{m}^2, \quad a_{44}^p = a_{55}^p = 3.076\times10^6\ \mathrm{N}\cdot\mathrm{m}^2$$
$$a_{25}^p = a_{34}^p = 0, \quad b_1^p = 0.3447\ \mathrm{kg/m}, \quad b_4^p = 8.57\times10^{-8}\ \mathrm{kg}\cdot\mathrm{m},$$
$$b_5^p = 0.19\times10^{-4}\ \mathrm{kg}\cdot\mathrm{m}, \quad b_6^p = 0, \quad L = 0.1524\ \mathrm{m}.$$

The present displayed predictions are in good agreement with the results of Ref. [69].

Table 3.1: *Frequencies at $\Omega = 1002$ rpm for CUS lay-up configuration (Hz)* [a].

	$[75]_6$			$[90/60]_3$		
Mode	Exp. [17]	FEM [91]	Present	Exp. [17]	FEM [91]	Present
Flap 1	36.49	34.63	36.65	39.54	38.71	39.26
Lag 1	53.73	47.31	55.79	56.42	54.38	56.44
Flap 2	202.2	188.0	202.45	222.3	215.8	220.3

[a] $\gamma_0 = \beta_0 = 0$, $\Omega = 1002$ rpm, $R_0 = 0$

Table 3.2: *Details of thin-walled composite box beam for validation [17]*

E_{11}	1.42×10^{11} N/m^2	Density (ρ)	1.442×10^3 Kg/m^3
$E_{22} = E_{33}$	9.8×10^9 N/m^2	Width ($2b^a$)	2.268×10^{-2} m
$G_{12} = G_{13}$	6.0×10^9 N/m^2	Depth ($2d^a$)	1.212×10^{-2} m
G_{23}	4.83×10^9 N/m^2	Number of layers (N_h)	6
$\mu_{12} = \mu_{13}$	0.42	Layer thickness	1.270×10^{-4} m
μ_{23}	0.50	Length (L)	0.8446 m

[a] Inner dimensions of the cross section.

Table 3.3: *Comparison of coupled flapping-lagging frequencies of a pretwisted beam* [a] *(Hz).*

Mode	1BB	2BB	3BB	4BB
Ref. [69]	62.0	305.1	949.0	1206.1
Present	62.1	305.3	951.3	1209.2

[a] $\gamma_0 = 0$, $\beta_0 = 45^o$, $\Omega = 0$, $R_0 = 0$

Next, a $1/16$th scale blade with NACA 0012 airfoil cross-section of Fig. 3.4a is used for actuating performance validation. Material properties of E-glass and AFC layers are shown in Table 3.4. Fig. 3.4b plots the tip twist angle varying with applied voltage, showing a good agreement with Ref. [23].

3.5 Numerical study and discussion

Material properties and geometric specifications of the host structure are shown in Table 3.6. The piezo-actuator is manufactured by signal crystal MFC, whose material properties are given in Table 3.4. We assume the piezo-actuators are spread over the entire beam span and bonded outside the host structure. The lay-up configurations for the host structure and the piezo-actuator are listed in Table 3.5. The sensor is located at the beam tip, i.e., $Y_s = L$.

3.5.1 Study of piezo-actuator coefficients

The piezo-actuator coefficients $\mathcal{A}_i^X$ appearing in Eqs. (3.5) and (3.6) are plotted as a function of piezo-actuator ply-angle θ_p in Fig. 3.5. Note that, the piezo-actuator coefficients appearing in BB- and TE-subsystems are indicated by solid and dashed lines,

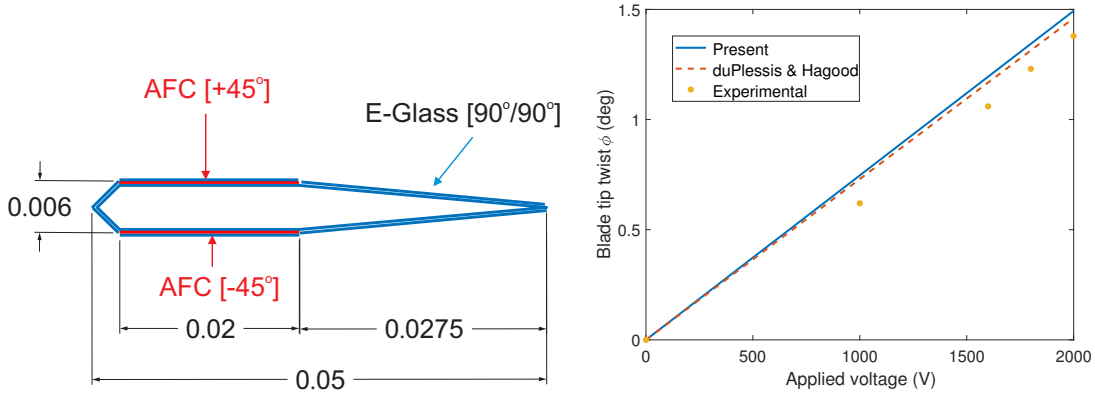

(a) *NACA0012 airfoil cross-section (unit:* m*)*

(b) *Tip deflection for NACA 0012 airfoil*

Figure 3.4: *Validations of NACA 0012 airfoil*

Table 3.4: *Material properties of E-glass, AFC, and single crystal MFC (S-MFC)*

Material property	E-Glass [23]	AFC [23]	S-MFC [71]
E_1 (Gpa)	14.8	30.54	6.23
E_2 (Gpa)	13.6	16.11	11.08
G_{12} (Gpa)	1.9	5.5	2.01
μ_{12}	0.19	0.36	0.229
d_{11} ($\times 10^{-12}$ m/V)	N/A	381	1896.5
d_{12} ($\times 10^{-12}$ m/V)	N/A	-160	-838.2
ρ (Kg m^{-3})	1700	4810	5338.3
Thickness ($\times 10^{-4}$ m)	2.032	1.689	17
Electrode spacing ($\times 10^{-3}$ m)	N/A	1.143	1.7

Table 3.5: *CUS lay-up configurations (deg)* [a]

		Flanges		Webs	
Layer	Material	Top	Bottom	Left	Right
CUS (7)	Piezo-actuator	$[\theta_p]$	$[\theta_p]$	$[\theta_p]$	$[\theta_p]$
CUS (1-6)	Host structure	$[\theta_h]_6$	$[\theta_h]_6$	$[\theta_h]_6$	$[\theta_h]_6$

[a] θ_p and θ_h denote the ply-angles in piezo-actuator and host structure.

Table 3.6: *Material properties (Graphite-Epoxy) and geometric specifications of the thin-walled box beam*

Material	**Value**	**Geometric**	**Value**
E_{11}	206.8×10^9 N/m^2	Width ($2b^a$)	0.254 m
$E_{22} = E_{33}$	5.17×10^9 N/m^2	Depth ($2d^a$)	0.0681 m
$G_{12} = G_{13}$	2.55×10^9 N/m^2	Wall thickness (h)	0.0102 m
G_{23}	3.10×10^9 N/m^2	Number of layers (N_h)	6
$\mu_{12} = \mu_{13} = \mu_{23}$	0.25	Layer thickness	0.0017 m
ρ	1.528×10^3 Kg/m^3	Length (L)	2.032 m

[a] The length is measured on the mid-line contour.

respectively. Two distinct trends can be concluded in the results of Fig. 3.5. One including bending coefficients ($\mathcal{A}_1^{Mx}$, $\mathcal{A}_3^{Mz}$) [1] and extension coefficients ($\mathcal{A}_2^{Ty}$, $\mathcal{A}_4^{Ty}$) shows a symmetric dependence centered around $\theta_p = 90^o$. The other characterizing transverse shear coefficients ($\mathcal{A}_1^{Qx}$, $\mathcal{A}_3^{Qz}$) and twist coefficients ($\mathcal{A}_2^{My}$ and $\mathcal{A}_4^{My}$), instead, presents an anti-symmetric trend. Moreover, their values equal to zero when $\theta_p = 0^o,\ 90^o, 180^o$, and their maximum absolute values reached for $\theta_p \approx 42,\ 138^o$.

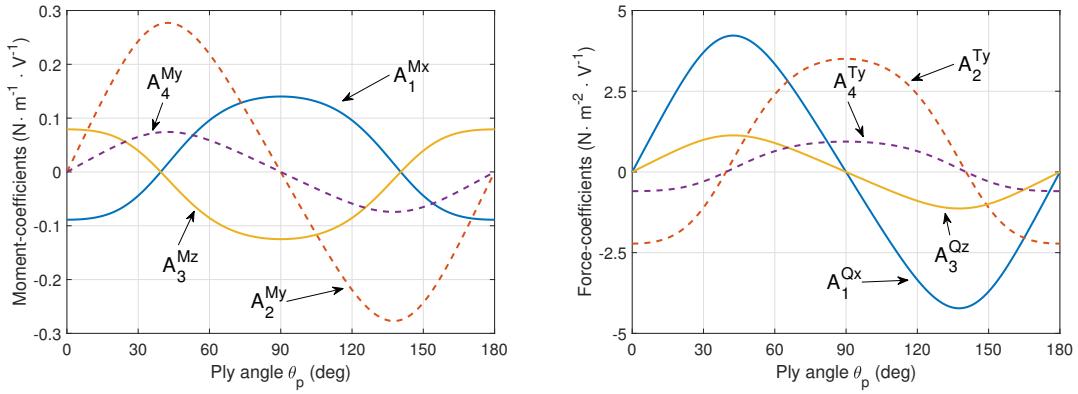

Figure 3.5: *Damping ratios of BB-subsystem as a function of piezo-actuator ply-angle θ_p; $k_1 = k_3 = 100$, $\Omega = 0$, $\gamma_0 = \beta_0 = 0$*

3.5.2 Study of anisotropic characteristic of piezo-composite

BB-subsystem

Considering that the lateral bending-vertical bending elastic coupling has a significant effect on flapping and lagging motions, the weak and strong elastic coupling cases should be investigated separately. For an unpretwisted beam, the elastic coupling is just related to stiffness coefficients $a_{25} = a_{25}^p$ and $a_{34} = a_{34}^p$ [75]. Fig. 3.6 depicts all non-zero stiffness coefficients a_{ij}^p in BB-subsystem as a function of host ply-angle θ_h. It can be seen that a_{25}^p and a_{34}^p are negligible during $0^o < \theta_h < 30^o$ or $150^o < \theta_h < 180^o$. Thus, $\theta_h = 15^o$ and $\theta_h = 75^o$ are selected to study the weak and strong elastic coupling cases, respectively.

Figures 3.7a and 3.7b plot damping ratios of the first four modes as a function of piezo-actuator ply-angle θ_p for the weak and strong elastic coupling cases, respectively. The damping ratios in Figs. 3.7a and 3.7b follow the trend of coefficients ($\mathcal{A}_1^{Mx}$, $\mathcal{A}_3^{Mz}$) in Fig. 3.5 and ($\mathcal{A}_1^{Qx}$, $\mathcal{A}_3^{Qz}$) in Fig. 3.5, respectively. This implies that bending moment actuation and transverse shear force actuation play the dominate role in weak and strong elastic coupling cases, respectively. As a result, the optimum piezo-actuator ply-angle for $\theta_h = 15^o$ and $\theta_h = 75^o$ cases are $\theta_p = 90^o$ and $\theta_p = 130^o$, respectively.

TE-subsystem

Figure 3.8 depicts damping ratios of the first three twist modes as a function of θ_p for selected two host structure cases, i.e., $\theta_h = 15^o$ and $\theta_h = 75^o$. It can been seen that

[1] The reason for $\mathcal{A}_1^{Mx}$ and $\mathcal{A}_3^{Mz}$ exhibiting the opposite trends is the reverse definition of θ_x in Fig. 2.2.

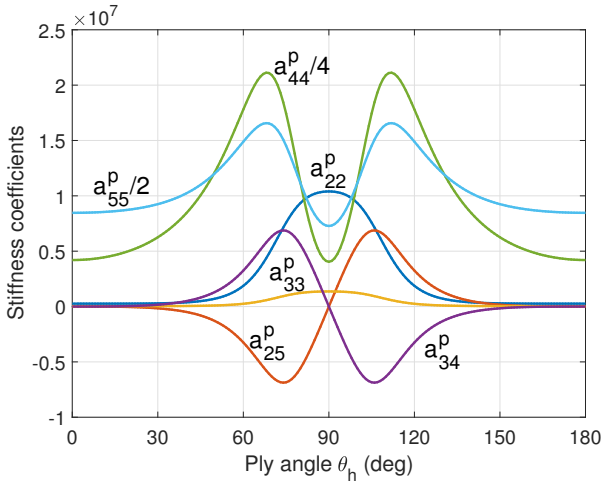

Figure 3.6: *Stiffness coefficients a^p_{ij} as a function of host structure ply-angle θ_h in BB-subsystem; units: a^p_{22} $(\mathrm{N}\cdot\mathrm{m}^2)$, a^p_{25} $(\mathrm{N}\cdot\mathrm{m})$, a^p_{33} $(\mathrm{N}\cdot\mathrm{m}^2)$, a^p_{34} $(\mathrm{N}\cdot\mathrm{m})$, a^p_{44} (N) and a^p_{55} (N).*

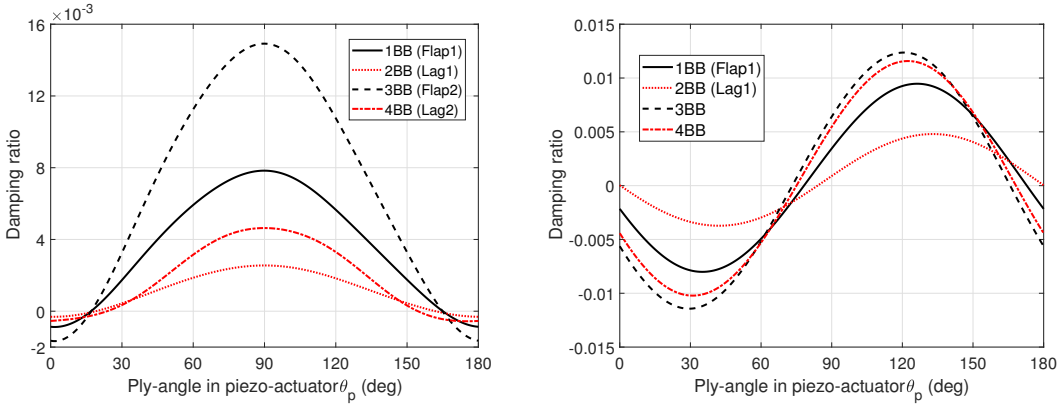

(a) $\theta_h = 15^o$ **(b)** $\theta_h = 75^o$

Figure 3.7: *Damping ratios of BB-subsystem as a function of piezo-actuator ply-angle θ_p; $k_1 = k_3 = 100$, $\Omega = 0$, $\gamma_0 = \beta_0 = 0$*

$\theta_p \approx 135^o$ yields the best twist control authority.

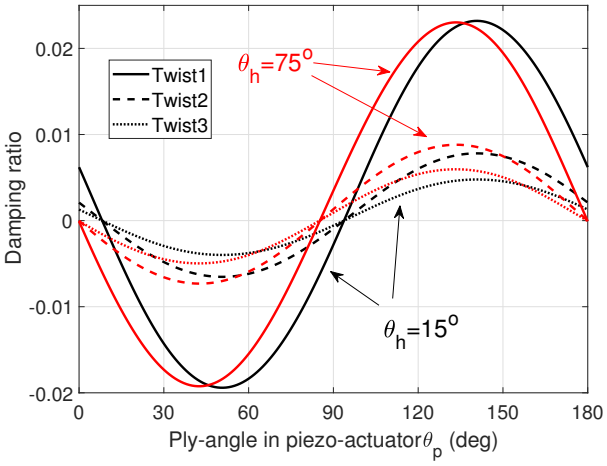

Figure 3.8: *Damping ratios of TE-subsystem as a function of piezo-actuator ply-angle θ_p; $k_2 = k_4 = 10$, $\Omega = 0$, $\gamma_0 = \beta_0 = 0$.*

3.5.3 Study of host structure tailoring

BB-subsystem

Figure 3.9 plots frequencies of the first four modes of BB-subsystem as a function of host ply-angle θ_h. According to the weak and strong elastic coupling cases, it is reasonable to split the domain of θ_h into "Decoupling" and "Couping" two parts, see Fig. 3.9. Note that, according to their mode shapes, the first four modes of BB-subsystem can also be denoted as Flap1, Lag1, Flap2 and Lag2 for weak elastic coupling cases. However, there will be no pure flapping or lagging modes for strong elastic coupling cases.

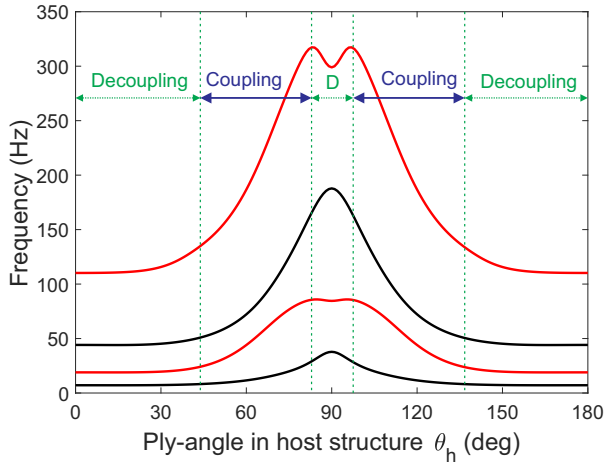

Figure 3.9: *Frequencies of BB-subsystem as a function of host structure ply-angle θ_h; $\Omega = 0$, $\gamma_0 = \beta_0 = 0$.*

Damping ratios of the first four modes of BB-subsystem are highlighted in Fig. 3.10 for selected two piezo-actuator ply-angle cases, viz., $\theta_p = 90^o$ (bending moment actuation dominated) and $\theta_p = 130^o$ (transverse shear force actuation dominated). It can be seen that host ply-angle θ_h has a significant effect on damping ratios. $\theta_p = 90^o$ and $\theta_p = 130^o$ would be the better choice for weak and strong elastic coupling cases, respectively.

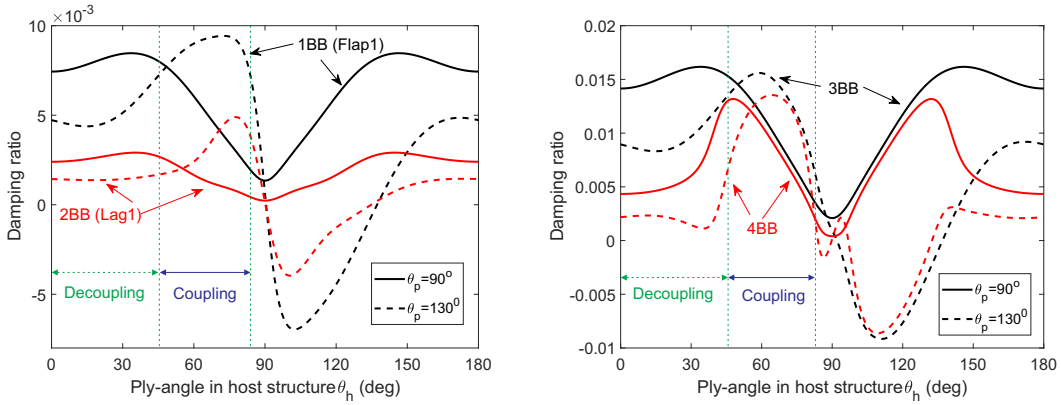

Figure 3.10: *Damping ratios of BB-subsystem as a function of host structure ply-angle θ_h; $k_1 = k_3 = 100$, $\Omega = 0$, $\gamma_0 = \beta_0 = 0$*

TE-subsystem

A typical extension mode cross phenomenon can be seen in Fig. 3.11, which depicts frequencies of TE-subsystem as a function of θ_h. The results of Fig. 3.12a show that host ply-angle θ_h has a significant effect on damping ratios of the twist modes. Note that, the damping ratios change suddenly during the mode cross regions in Fig. 3.12a, and this can be seen more clearly in Fig. 3.12b that depicts the damping ratios for $\theta_p = 90^o$ case. In $\theta_p = 90^o$ case, the direct twist actuations ($\mathcal{A}_2^{My}$, $\mathcal{A}_4^{My}$) are immaterial. Damping ratios of the twist modes are induced by the extension actuations ($\mathcal{A}_2^{Ty}$, $\mathcal{A}_4^{Ty}$) via the twist-extension elastic coupling.

3.5.4 Study of rotor speed and presetting angle

BB-subsytem

Figures 3.13a plots frequencies of the first three modes of BB-subsystem as a function of rotating speed Ω for the weak elastic coupling case. Since centrifugal stiffening effect is more significant in flapping modes than in lagging modes, a frequency crossing of fundamental lagging and flapping modes can be seen in Fig. 3.13a for the unpresetting beam ($\gamma_0 = 0$). In addition, both in Figs. 3.13a and 3.13b, it can be found that depending on the flapping and lagging modes, the increase of presetting angle γ_0 yields either an enhance or weaken effect on centrifugal stiffening effect, respectively. The results of Fig. 3.14 present that with the increase of Ω, damping ratios of the flapping modes decrease more significantly than the lagging mode does.

For the strong elastic coupling case, frequencies and damping ratios of the first three modes are shown in Figs. 3.15 and 3.16a, respectively. Since the elastic coupling will

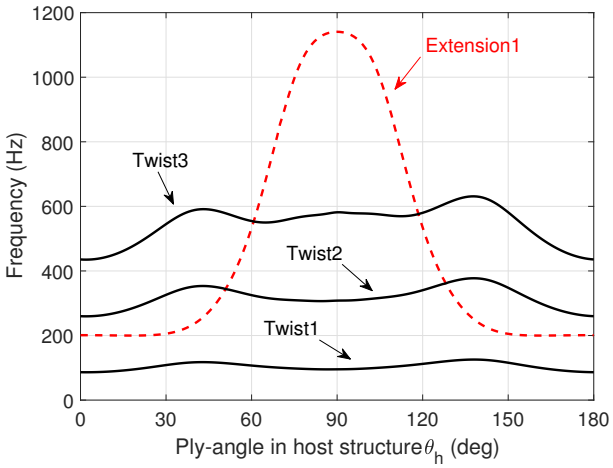

Figure 3.11: *Frequencies of TE-subsystem as a function of host structure ply-angle* θ_h*;* $\Omega = 0$*,* $\gamma_0 = \beta_0 = 0$

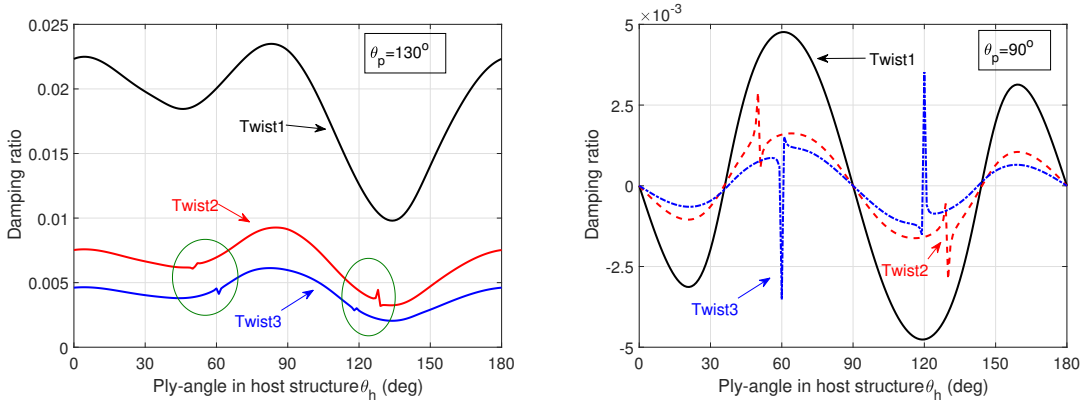

(a) $\theta_p = 130^o$ **(b)** $\theta_p = 90^o$

Figure 3.12: *Damping ratios of TE-subsystem as a function of host structure ply-angle* θ_h*;* $k_2 = k_4 = 10$*,* $\Omega = 0$*,* $\gamma_0 = \beta_0 = 0$*.*

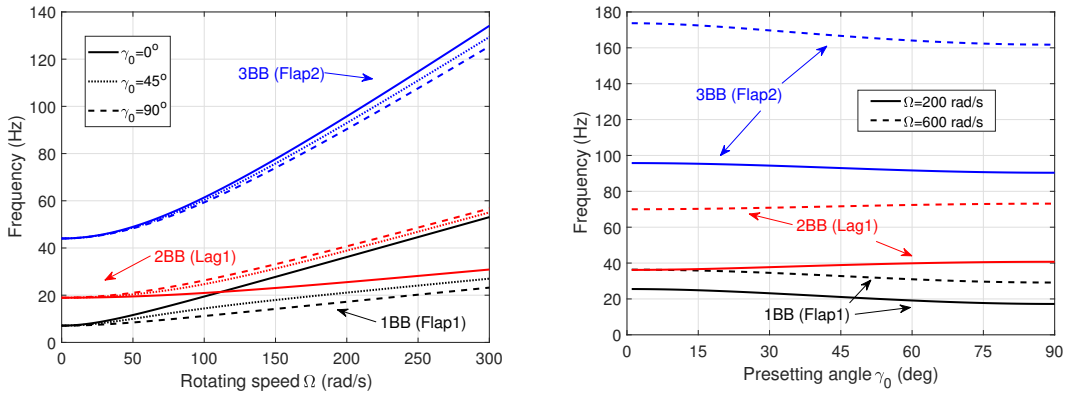

(a) *Rotating speed* Ω **(b)** *Presetting angle* γ_0

Figure 3.13: *Frequencies of BB-subsystem vs. rotating speed and presetting angle for selected presetting angles* γ_0*;* $\theta_h = 15^o$*,* $\theta_p = 90^o$*,* $k_1 = k_3 = 100$*,* $R_0 = 0.1L$*.*

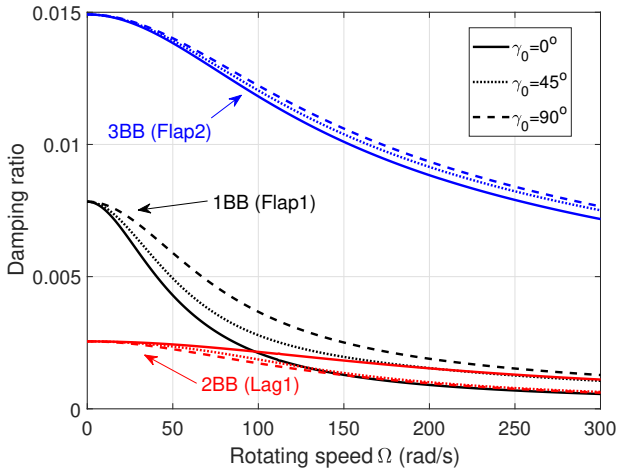

Figure 3.14: *Damping ratios of BB-subsystem vs. rotating speed* Ω *for selected presetting angles* γ_0*;* $\theta_h = 15^o$*,* $\theta_p = 90^o$*,* $k_1 = k_3 = 100$*,* $R_0 = 0.1L$*.*

be further enhanced by the centrifugal stiffening effect, in Fig. 3.15, there is no typical flapping-lagging frequency crossing phenomenon as shown in Fig. 3.13a. During the region near $\Omega \approx 500$ rad/s, the frequencies of 1BB and 2BB modes are very close but not cross for the un-presetting beam ($\gamma_0 = 0$). And their damping ratios present sudden changes during this region, see Fig. 3.16a. The influence of presetting angle γ_0 on the damping ratios for the strong elastic coupling case can be seen more clearly in Fig. 3.16b.

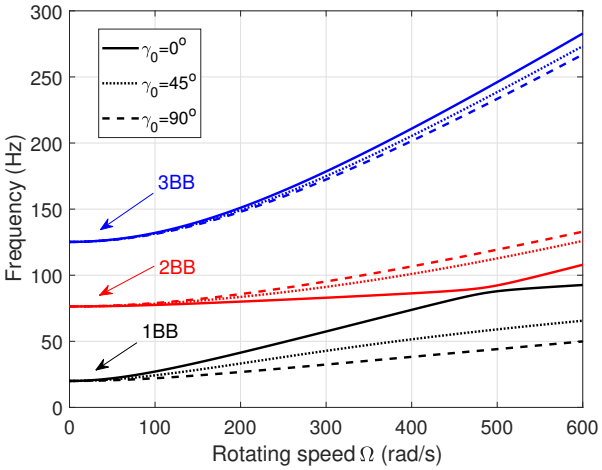

Figure 3.15: *Frequencies of BB-subsystem vs. rotating speed Ω for selected presetting angles γ_0; $\theta_h = 75^o$, $\theta_p = 130^o$, $k_1 = k_3 = 100$, $R_0 = 0.1L$.*

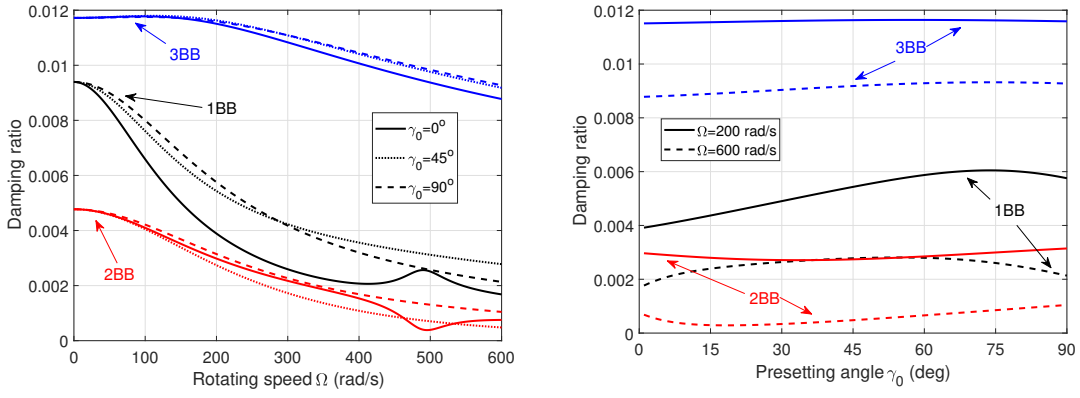

(a) *Rotating speed Ω*

(b) *Presetting angle γ_0*

Figure 3.16: *Damping ratios of BB-subsystem vs. rotating speed and presetting angle; $\theta_h = 75^o$, $\theta_p = 130^o$, $k_1 = k_3 = 100$, $R_0 = 0.1L$.*

TE-subsystem

Figures. 3.17a and 3.17b plot frequencies and damping ratios of the first three twist modes as a function of Ω, respectively. The additional torsional stiffness induced by centrifugal force yields an increase of frequency in Fig. 3.17a and a decrease of damp-

ing ratio in Fig. 3.17b. Since the increase of presetting angle γ_0 will yield an increase of the softening tennis-racket term, the fundamental twist frequency exhibits a significant decrease in Fig. 3.18a. However this destiffening effect is immaterial for higher twist modes. This conclusion can also be identified in Fig. 3.18b, which highlights the influence of γ_0 on the twist damping ratios. In Fig. 3.18b, with the increase of γ_0, damping ratio of the fundamental twist mode increases until $\gamma_0 \approx 75^o$, then slightly decreases.

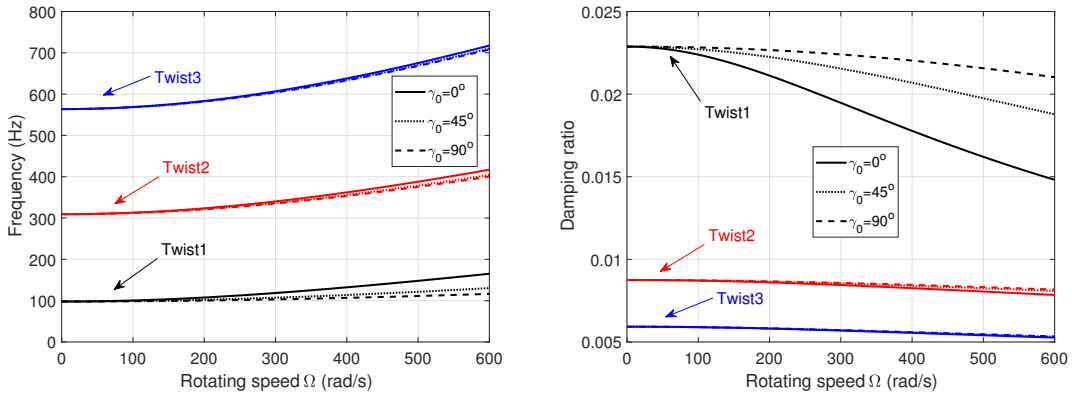

(a) *Frequencies* **(b)** *Damping ratios*

Figure 3.17: *Rotating speed Ω influence of TE-subsystem for selected presetting angles γ_0; $\theta_h = 75^o$, $\theta_p = 130^o$, $k_2 = k_4 = 10$, $R_0 = 0.1L$.*

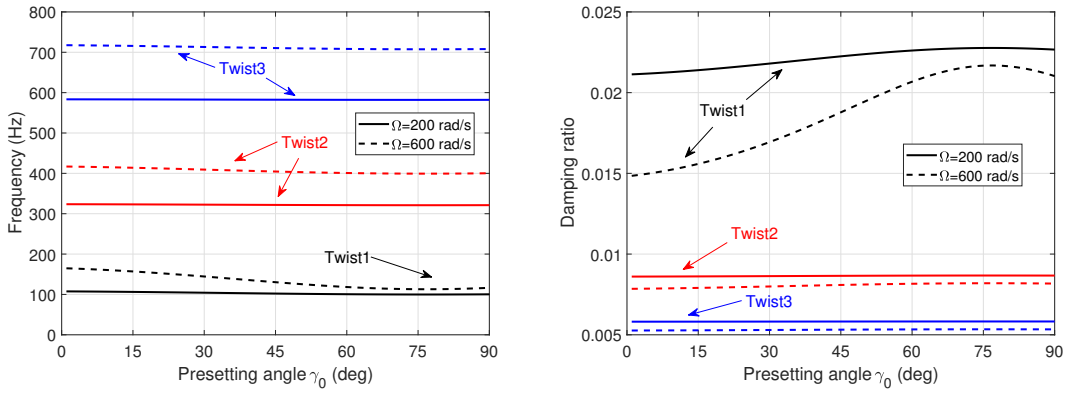

(a) *Frequencies* **(b)** *Damping ratios*

Figure 3.18: *Presetting angle γ_0 influence of TE-subsystem for selected presetting angles γ_0; $\theta_h = 75^o$, $\theta_p = 130^o$, $k_2 = k_4 = 10$, $R_0 = 0.1L$.*

3.5.5 Study of pretwist angle

In order to model helicopter and tilt rotor blades, a special case of Eq. (3.2) is assumed,

$$\beta(y) = \beta_0 - \beta_0 y/L. \tag{3.31}$$

This will make the pretwist angle at the beam tip equal to zero, i.e., $\beta(L) = 0$.

BB-subsystem

For fiber-reinforced blades, pretwist angle will make flapping and lagging motions coupled strongly, thus we just consider $\theta_h = 75^o$ this case here. Fig. 3.19 depicts frequencies of the first three modes of BB-subsystem as a function of pretwist angle β_0. For the unrotating case, the fundamental frequency (1BB) is not sensitive to pretwist angle β_0. However it decreases significantly with the increase of β_0 for the high speed rotating case ($\Omega = 600$ rad/s).

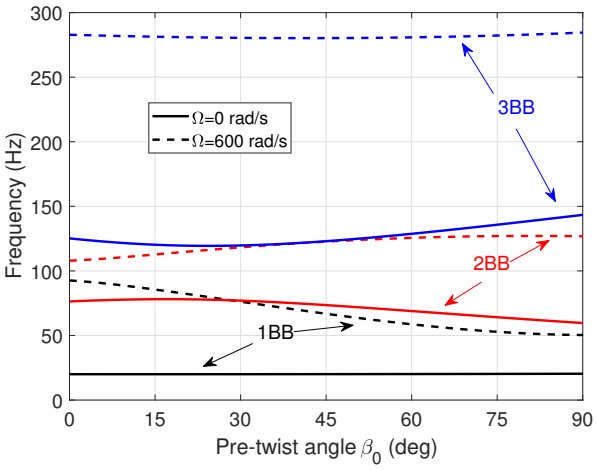

Figure 3.19: *Frequencies of BB-subsystem vs. pretwist angle β_0 for selected rotating speeds Ω; $\theta_h = 75^o$, $\theta_p = 130^o$, $k_1 = k_3 = 100$, $R_0 = 0.1L$.*

In order to study the relationship between damping ratios and pretwist angle β_0, two piezo-actuator cases, i.e., $\theta_p = 130^o$ (transverse shear force actuation dominated) in Fig. 3.20a and $\theta_p = 90^o$ (bending moment actuation dominated) in Fig. 3.20b are considered. According to the previous discussion, we know for the strong elastic coupling case, transverse shear force actuation is more efficient than bending moment actuation when the beam is unpretwisted. However for a pretwisted beam, transverse shear force actuation may lose control for 2BB mode, and even induce a negative damping ratio for the high speed rotating case, see Fig. 3.20a. On the other hand, bending moment actuation can guarantee the balanced positive damping ratios for an arbitrary pretwisted angle β_0, see Fig. 3.20b.

TE-subsystem

The influence of pretwist angle β_0 on frequencies and damping ratios of the twist modes are illustrated in Figs. 3.21a and 3.21b, respectively. It can be seen the influences of β_0 are negligible both in Figs. 3.21a and 3.21b.

3.6 LQR control for BB-subsystem

3.6.1 Study of damping ratios

Recalling the LQR control methodology, the control authority is solely related to control weighing factor η_i. Figs. 3.22a and 3.22b plot damping ratios of the first four modes

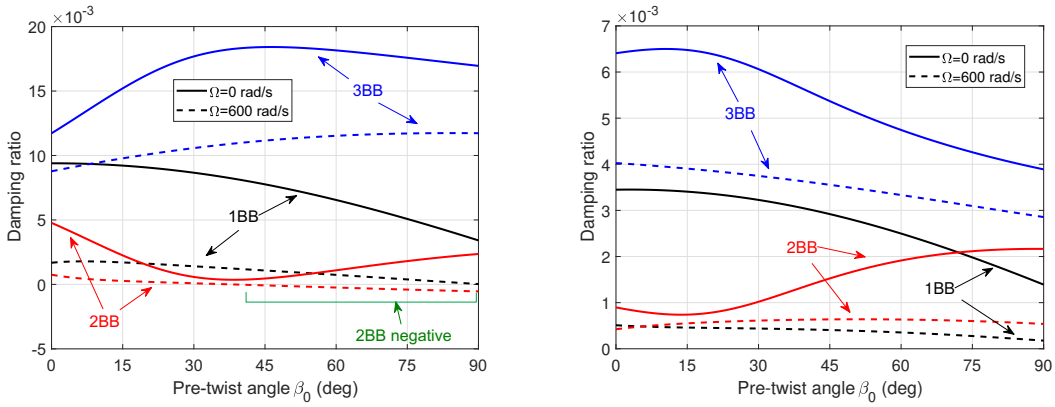

(a) $\theta_p = 130^o$ **(b)** $\theta_p = 90^o$

Figure 3.20: *Damping ratios of the first three modes of BB-subsystem vs. pretwist angle* β_0 *for selected rotating speeds* Ω*;* $\theta_h = 75^o$*,* $k_1 = k_3 = 100$*,* $R_0 = 0.1L$*.*

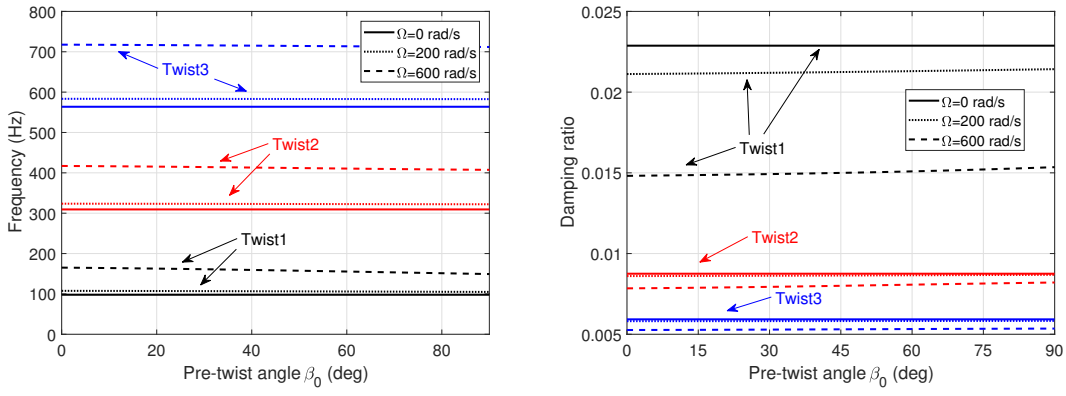

(a) *Frequencies* **(b)** *Damping ratios*

Figure 3.21: *Pretwist angle* β_0 *influence of TE-subsystem for selected rotating speeds* Ω*;* $\theta_h = 75^o$*,* $\theta_p = 130^o$*,* $k_2 = k_4 = 10$*,* $R_0 = 0.1L$*.*

as a function of η_i. It can be found damping ratios decrease with the increase of η_i.

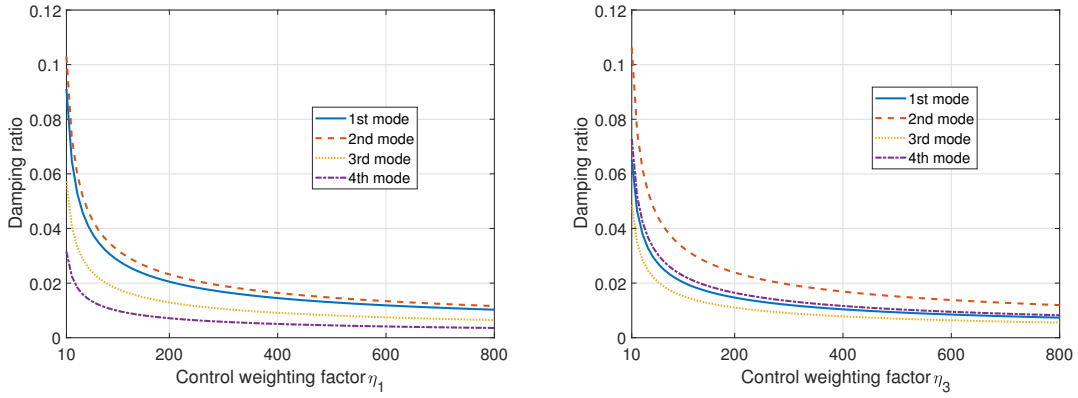

(a) η_1 **(b)** η_3

Figure 3.22: *Damping ratios of the first four modes versus control weighting factor;* $\beta_0 = 0^o$, $\theta_h = 90^o$, $\theta_p^F = 80^o$

For $\theta_h = 90^o$ case that the flapwise bending and chordwise bending are elastically decoupled, damping ratios of the first four modes plotted as a function of ply-angle are shown in Figs. 3.23a and 3.23b. In addition, the non-shear-actuation and non-bending-actuation points are indicated by black and red dots, respectively. According to mode shapes study, the 1st and 3rd are flapwise bending modes, while the 2nd and 4th are chordwise bending modes. The result of Fig. 3.23a presents that flange-actuator-pair can control chordwise bending modes by piezoelectrically induced chordwise transverse shear $\mathcal{A}_1^{Qx}$ while control flapwise bending modes by $\mathcal{A}_1^{Mx}$. Note that, $\mathcal{A}_1^{Qx}$ will offer a robust control authority on chordwise bending modes in the domain $10^o < \theta_p^F < 70^o$ or $110^o < \theta_p^F < 170^o$. Similar results can also be concluded for web-actuator-pair in Fig. 3.23b.

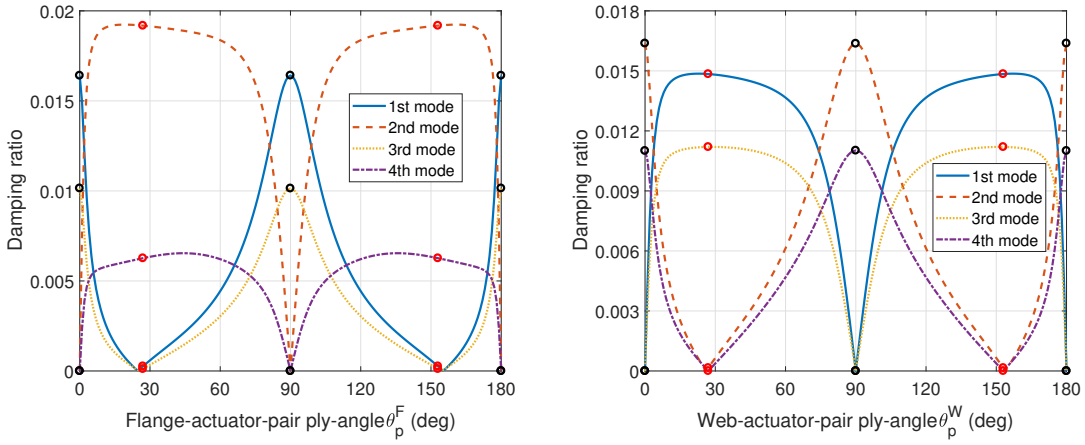

(a) *Flange-actuator-pair* **(b)** *Web-actuator-pair*

Figure 3.23: *Damping ratios of the first four modess versus actuator-pair ply-angle* θ_p*;* $\theta_h = 90^o$, $\eta_1 = \eta_3 = 600$, $\beta_0 = 0^o$

For the strong elastic couping case $\theta_p = 75^o$, Figs. 3.24a and 3.24b plot damping ratios of the first four modes as a function of flange-actuator-pair ply-angle θ_p^F and web-actuator-pair ply-angel θ_p^W, respectively. It can be found that the variations of damping ratios are complicated in Figs. 3.24a and 3.24b. In Fig. 3.24a, the flange-actuator-pair induced transverse shear force (indicated in red dots) or bending moment (indicated in black dots) can both control the flapwise and chordwise bending modes individually via elastic coupling. However in Fig. 3.24b, the influence of elastic coupling on web-actuator-pair control effect is not as significant as on that of flange-actuator-pair. In general, in the domain of $60^o < \theta_p < 90^o$, the damping ratios vary sharply, while the variations are relatively slow in the domain of $90^o < \theta_p < 150^o$. We denote the last domain as the robust ply-angle domain.

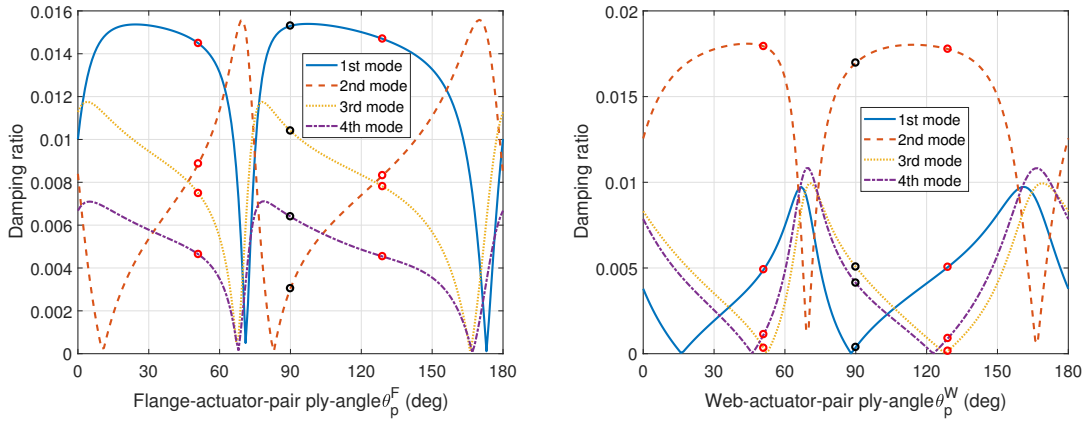

(a) *Flange-actuator-pair* **(b)** *Web-actuator-pair*

Figure 3.24: *Damping ratios of the first four modess versus actuator-pair ply-angle* θ_p*;* $\theta_h = 75^o$*,* $\eta_1 = \eta_3 = 600$*,* $\beta_0 = 0^o$

Due to the pretwist angle, the chordwise and flapwise bending modes of the system will be always coupled each other. Figs. 3.25a and 3.25b present damping ratios of a pretwisted rotary thin-walled beam. Compared Fig. 3.25a with 3.24a, the variations of damping ratios induced by flange-actuator-pair show the similarity. The significant influence of pretwisted angle can be seen on the 2nd mode which is indicated by dashed line. The variation similarity of damping ratios induced by web-actuator-pair can also be found in Figs. 3.25b and 3.24b. The significant influence of pretwist angle can be observed on the 3rd and 4th modes.

Figures 3.26 and 3.27 further highlight influence of pretwist angle on damping ratios induced by pure piezoelectric bending moment ($\theta_p = 90^o$) and transverse shear force ($\theta_p = 129^o$).

3.6.2 Dynamical simulation

A pretwisted rotary blade with strong elastic couplings is considered in this dynamic simulation. Piezo-actuator with $\theta_p = 135^o$ is implemented for the reason that on one hand this ply-angle is in the robust ply-angle domain, on the other hand it can yield a significant piezoelectrically induced torque on twist motion. Note that in the actual

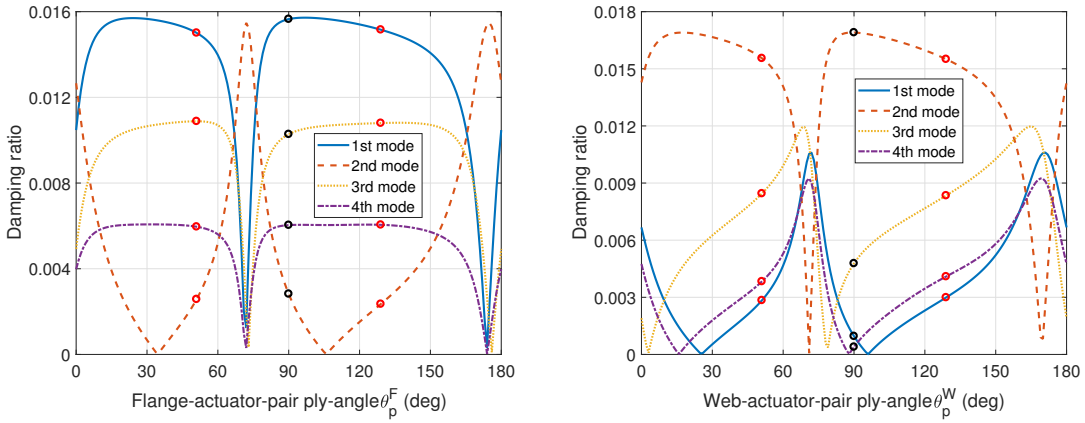

(a) *Flange-actuator-pair* **(b)** *Web-actuator-pair*

Figure 3.25: *Damping ratios of the first four modess versus actuator-pair ply-angle* θ_p*;* $\theta_h = 75^o$*,* $\eta_1 = \eta_3 = 600$*,* $\beta_0 = 45^o$

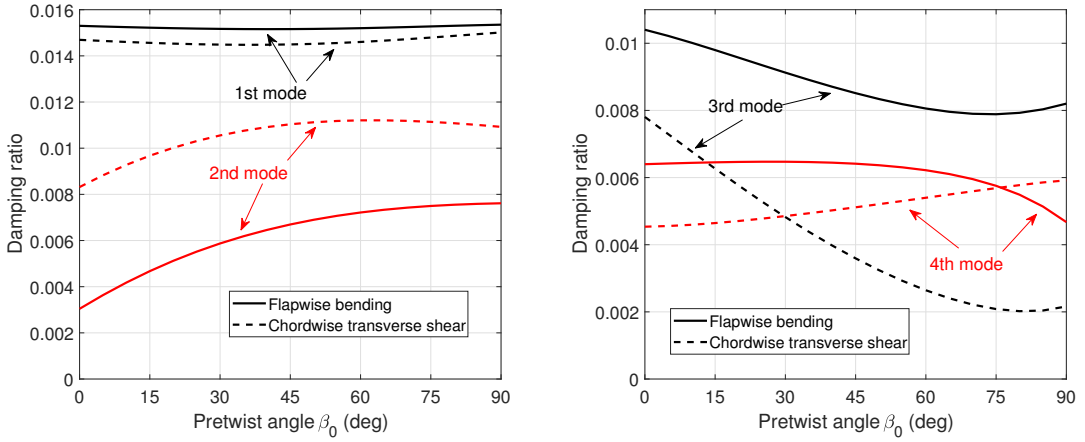

Figure 3.26: *Damping ratios of the first four modes versus pretwist angle* β_0*;* $\theta_h = 75^o$*,* $\eta_1 = \eta_3 = 600$*,* $\theta_p^F = 90^o$ *for flapwise bending,* $\theta_p^F = 129^o$ *for chordwise transverse shear*

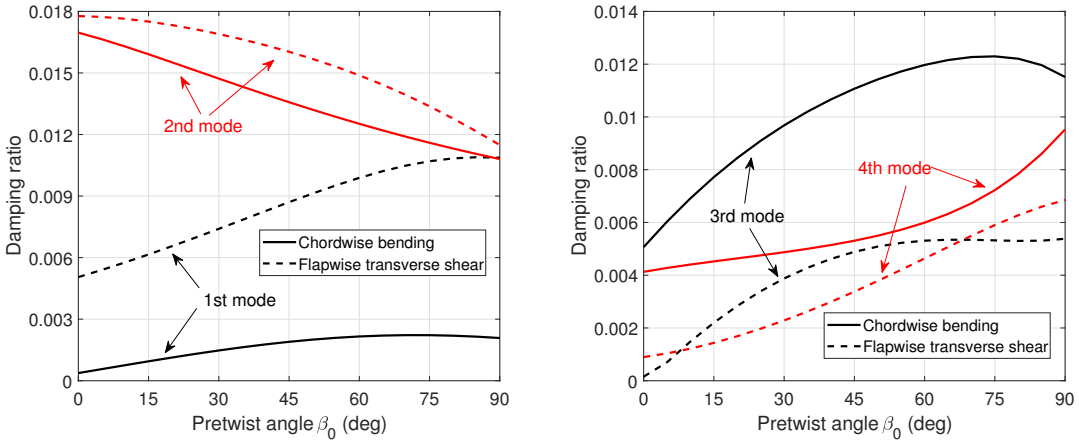

Figure 3.27: *Damping ratios of the first four modes versus pretwist angle* β_0*;* $\theta_h = 75^o$*,* $\eta_1 = \eta_3 = 600$*,* $\theta_p^W = 90^o$ *for chrodwise bending,* $\theta_p^W = 129^o$ *for flapwise transverse shear*

simulations, the first seven structural modes are used. The dynamic responses of the blade tip under the impulse load are presented in Fig.s 3.28a and 3.28b. The associate voltage parameters are shown in Fig. 3.28c. In order to make the output value of voltage V_1 and V_3 at the same level (see Fig. 3.28c), the control weighting factors $\eta_1 = 600$ and $\eta_3 = 24000$ are adopted. It can be found that flange-actuator-pair present significant better control effect than that of web-actuator-pair no matter on lateral or vertical directions.

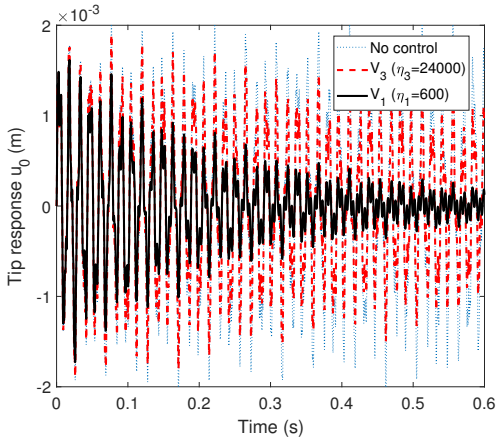

(a) *Lateral direction* $u_0(L,t)$

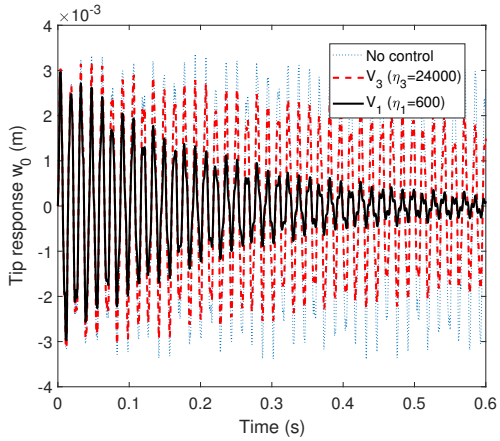

(b) *Vertical direction* $w_0(L,t)$

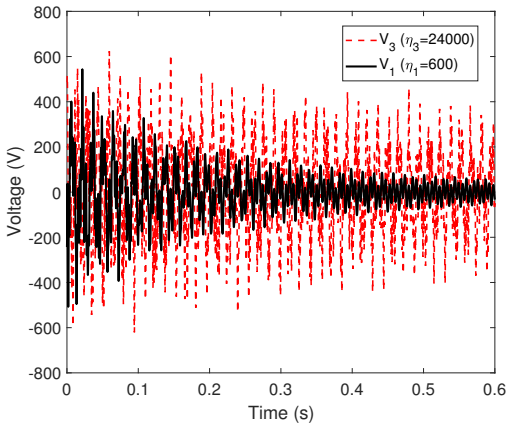

(c) *Voltages time history*

Figure 3.28: *Beam tip response to impulse load;* $p_x = p_z = 10\ \mathrm{N{\cdot}m^{-1}}$, $\theta_h = 75^o$, $\theta_p = 135^o$, $\beta_0 = 60^o$

CHAPTER 4

Active Control of Adaptive Rotating Hub-Beam Multibody System

4.1 Introduction

In this chapter, modeling and control of an adaptive rigid hub and flexible beam multibody system are implemented. The beam structure is modeled as a fiber-reinforced thin-walled composite beam with a typical rectangular cross-section, see Fig. 4.1. The adaptive capabilities are provided by the anisotropic piezo-actuators embedded into the structure. The hub-beam multibody model we developed here can serve as the basic model of adaptive flexible spacecraft. The main target of the adaptive capabilities of the system is to suppress the residual vibration during attitude maneuvers. Based on the linear quadratic regular (LQR) control methodology, the influences of lay-up configuration on control authority of vibration suppression are investigated.

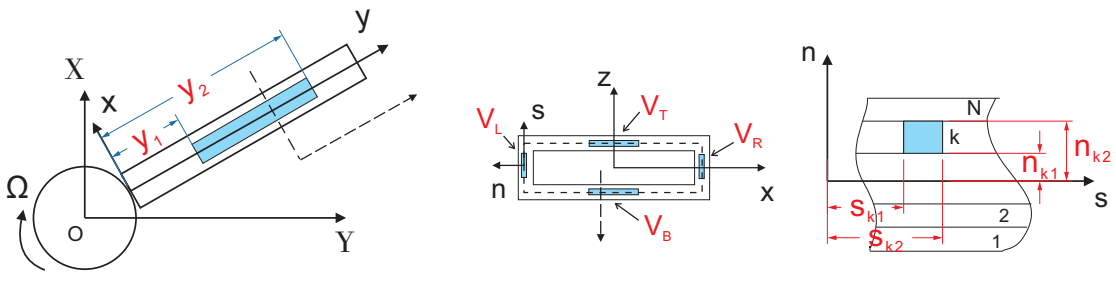

Figure 4.1: *Hub-beam multibody system*

4.2 Dynamical model

The dynamical model is based on the geometrically nonlinear thin-walled beam theory developed in Chapter 2. According to the governing equations (2.28) and the associated boundary conditions (2.29) and (2.30), in general, the seven degrees of freedom of the hub-beam system are fully coupled. In engineering applications, special lay-up configurations (e.g., cross-ply, CAS and CUS [75]) are usually adopted to design particular couplings meeting different working environment. Here *circumferentially asymmetric stiffness* (CAS) lay-up configuration (both for host structure θ_h and piezo-actuator θ_p) is considered.

For the thin-walled beam with rectangular cross-section as shown in Fig. 5.1, a CAS configuration implies the ply-angle distribution $\theta(z) = \theta(z)$ of the top and bottom walls and $\theta(x) = \theta(x)$ of the left and right walls, see Fig. 4.2. For a circumferential asym-

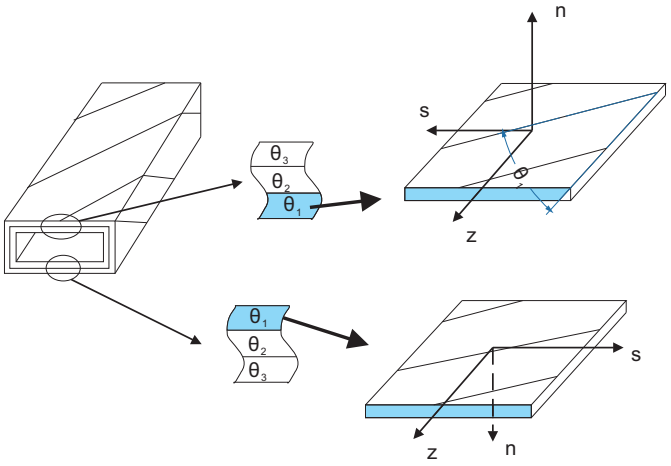

Figure 4.2: *CAS lay-up configuration*

metric stiffness (CAS) lay-up configuration the stiffness matrix $[a_{ij}]$ can be decoupled into two types of elastic coupling, viz, extension-transverse shear

$$\begin{Bmatrix} \hat{T}_y \\ \hat{Q}_x \\ \hat{Q}_z \\ \hat{\Gamma}_t \end{Bmatrix} = \begin{bmatrix} a_{11} & a_{14} & a_{15} & a_{18} \\ a_{14} & a_{44} & 0 & a_{48} \\ a_{15} & 0 & a_{55} & 0 \\ a_{18} & a_{48} & 0 & a_{88} \end{bmatrix} \begin{Bmatrix} v_0' + \frac{1}{2}(u_0')^2 + \frac{1}{2}(w_0')^2 \\ \theta_z + u_0' \cos\phi - w_0' \sin\phi \\ \theta_x + u_0' \sin\phi + w_0' \cos\phi \\ \frac{1}{2}(\phi')^2 \end{Bmatrix}, \tag{4.1a}$$

and bending-twist coupling,

$$\begin{Bmatrix} \hat{M}_z \\ \hat{M}_x \\ \hat{B}_w \\ \hat{M}_y \end{Bmatrix} = \begin{bmatrix} a_{22} & 0 & 0 & 0 \\ 0 & a_{33} & 0 & a_{37} \\ 0 & 0 & a_{66} & 0 \\ 0 & a_{37} & 0 & a_{77} \end{bmatrix} \begin{Bmatrix} \theta_z' - w_0'\phi' \cos\phi - u_0'\phi' \sin\phi \\ \theta_x' + u_0'\phi' \cos\phi - w_0'\phi' \sin\phi \\ \phi'' \\ \phi' \end{Bmatrix}, \tag{4.1b}$$

the stiffness coefficient a_{15} is equal to zero for balanced lay-ups on the left and right beam spars.

If the piezo-composite actuators are distributed in CAS configuration, Eq. (2.35) can be split in two, viz., extension-transverse coupling

$$\begin{Bmatrix} \tilde{T}_y(y,t) \\ \tilde{Q}_x(y,t) \\ \tilde{Q}_z(y,t) \\ \tilde{\Gamma}_t(y,t) \end{Bmatrix} = \begin{bmatrix} \mathcal{A}_2^{Ty} & \mathcal{A}_4^{Ty} \\ \mathcal{A}_2^{Qx} & 0 \\ 0 & \mathcal{A}_4^{Qz} \\ \mathcal{A}_2^{\Gamma t} & \mathcal{A}_4^{\Gamma t} \end{bmatrix} \begin{Bmatrix} V_2(t) \\ V_4(t) \end{Bmatrix} P(y), \tag{4.2a}$$

and bending-twist coupling

$$\begin{Bmatrix} \tilde{M}_z(y,t) \\ \tilde{M}_x(y,t) \\ \tilde{B}_w(y,t) \\ \tilde{M}_y(y,t) \end{Bmatrix} = \begin{bmatrix} 0 & \mathcal{A}_3^{Mz} \\ \mathcal{A}_1^{Mx} & 0 \\ 0 & 0 \\ \mathcal{A}_1^{My} & \mathcal{A}_3^{My} \end{bmatrix} \begin{Bmatrix} V_1(t) \\ V_3(t) \end{Bmatrix} P(y). \tag{4.2b}$$

As a result, taking Eqs. (4.1), (4.2) and (3.7), (3.9) into the governing equations 2.28 in conjunction with the boundary conditions 2.30, approximating the trigonometric functions with their Taylor series expansion ($\sin\phi \approx \phi$ and $\cos\phi \approx 1$), and dropping other nonlinear terms induced by beam deformation, the system can be split into two subsystems, one governs the hub, beam chordwise bending and extension coupling motion and the other governs the beam flapwise bending and twist coupling motion. The governing equations of the two subsystems are expressed as,

Hub-beam subsystem ($\Lambda - u_0 - v_0 - \theta_z$)

$$\begin{aligned} \delta\Lambda \;:\; & J_H\ddot{\Lambda} + \int_0^L \Big\{ \ddot{\Lambda}\big[b_1(R_0+y)^2 + b_5\big] - b_1(R_0+y)\ddot{u}_0 + (b_5+b_{15})\ddot{\theta}_z \\ & + 2\dot{\Lambda}b_1(R_0+y)\dot{v}_0 \Big\}\,\mathrm{d}\,y = \tau_\Lambda, \end{aligned} \tag{4.3a}$$

$$\begin{aligned} \delta u_0 \;:\; & a_{14}v_0'' + a_{44}(u_0'' + \theta_z') + p_x + \delta_p\mathcal{A}_2^{Qx}V_2P_2'(y) \\ & - b_1\big[\ddot{u}_0 - \ddot{\Lambda}(R_0+y) - \underbrace{2\dot{\Lambda}\dot{v}_0}_{} - \underline{\underline{\dot{\Lambda}^2 u_0}}\big] + \underline{b_1\dot{\Lambda}^2[R(y)u_0']'} = 0, \end{aligned} \tag{4.3b}$$

$$\begin{aligned} \delta v_0 \;:\; & a_{11}v_0'' + a_{14}(u_0'' + \theta_z') + p_y + \delta_p\mathcal{A}_2^{Ty}V_2P_2'(y) \\ & + \delta_p\mathcal{A}_4^{Ty}V_4P_2'(y) - b_1\big[\ddot{v}_0 - \underbrace{2\dot{\Lambda}\dot{u}_0}_{} + \underline{\underline{\dot{\Lambda}^2(R_0+y+v_0)}}\big] = 0, \end{aligned} \tag{4.3c}$$

$$\begin{aligned} \delta\theta_z \;:\; & a_{22}\theta_z'' - a_{14}v_0' + a_{44}(u_0' + \theta_z) + m_z + \delta_p\mathcal{A}_3^{Mz}V_3P_1'(y) \\ & - \mathcal{A}_2^{Qx}V_2P_2(y) - (b_5+b_{15})\big[\ddot{\theta}_z + \ddot{\Lambda} - \underline{\underline{\dot{\Lambda}^2\theta_z}}\big] = 0, \end{aligned} \tag{4.3d}$$

while the associated boundary conditions are
at $y = 0$,

$$u_0(0) = v_0(0) = \theta_z(0) = 0, \tag{4.4}$$

and at $y = L$,

$$\delta u_0 \;:\; a_{14}v_0'(L) + a_{44}(u_0'(L) + \theta_z(L)) + \delta_s\mathcal{A}_2^{Qx}V_2 = 0, \tag{4.5a}$$

$$\delta v_0 \;:\; a_{11}v_0'(L) + a_{14}(u_0'(L) + \theta_z(L)) + \delta_s\mathcal{A}_2^{Ty}V_2 + \delta_s\mathcal{A}_4^{Ty}V_4 = 0, \tag{4.5b}$$

$$\delta\theta_z \;:\; a_{22}\theta_z'(L) + \delta_s\mathcal{A}_3^{Mz}V_3 = 0. \tag{4.5c}$$

Beam subsystem ($w_0 - \phi - \theta_x$)

$$\delta w_0 \; : a_{55}(w_0'' + \theta_x') - b_1\ddot{w}_0 + \delta_p \mathcal{A}_4^{Qz} V_4 P_2'(y) + p_z + \underline{b_1 \dot{\Lambda}^2 [R(y) w_0']'} = 0, \tag{4.6a}$$

$$\begin{aligned}\delta\phi \; : a_{37}\theta_x'' + a_{77}\phi'' - a_{66}\phi^{(iv)} + m_y + b_w' + \delta_p \mathcal{A}_1^{My} V_1 P_1'(y) + \delta_p \mathcal{A}_3^{My} V_3 P_1'(y) \\ - (b_4 + b_5)\ddot{\phi} + \ddot{\Lambda} b_4 \theta_x + \underline{2\dot{\Lambda} b_4 \dot{\theta}_x} + \dot{\Lambda}^2 (b_4 - b_5)\phi + \underline{(b_4 + b_5)\dot{\Lambda}^2 [R(y)\phi']'} \\ + (b_{10} + b_{18})(\ddot{\phi}'' - \underline{\dot{\Lambda}^2 \phi''}) = 0,\end{aligned} \tag{4.6b}$$

$$\begin{aligned}\delta\theta_x \; : a_{33}\theta_x'' + a_{37}\phi'' - a_{55}(w_0' + \theta_x) + m_x + \delta_p \mathcal{A}_1^{Mx} V_1 P_1'(y) \\ - \mathcal{A}_4^{Qz} V_4 P_2(y) - \underline{2\dot{\Lambda} b_4 \dot{\phi}} - (b_4 + b_{14})(\ddot{\theta}_x + \phi\ddot{\Lambda} - \underline{\dot{\Lambda}^2 \theta_x}) = 0,\end{aligned} \tag{4.6c}$$

the associated boundary conditions
at $y = 0$,

$$w_0 = \phi = \phi' = \theta_x = 0, \tag{4.7}$$

and at $y = L$,

$$\delta w_0 \; : a_{55}(w_0' + \theta_x) + \delta_s \mathcal{A}_4^{Qz} V_4 = 0, \tag{4.8a}$$

$$\delta\phi \; : a_{37}\theta_x' + a_{77}\phi' - a_{66}'''\phi + (b_{10} + b_{18})\ddot{\phi}' + \delta_s \mathcal{A}_1^{My} V_1 + \delta_s \mathcal{A}_3^{My} V_3 = 0, \tag{4.8b}$$

$$\delta\phi' \; : \; a_{66}\phi'' = \bar{B}_w, \tag{4.8c}$$

$$\delta\theta_x \; : a_{33}\theta_x' + a_{37}\phi' + \delta_s \mathcal{A}_1^{Mx} V_1 = 0, \tag{4.8d}$$

If the actuator is spread over the entire beam span, the traces are $\delta_p = 0$ and $\delta_s = 1$; otherwise, if the actuator is a single patch, the traces assume the values $\delta_p = 1$ and $\delta_s = 0$.

Note that the two subsystems are actuated coupled via web-actuator-pair (voltage parameters V_3 and V_4). However, reported in Ref. [97], these coupling effects are immaterial in most cases and it is reasonable to treat these two subsystems as independent.

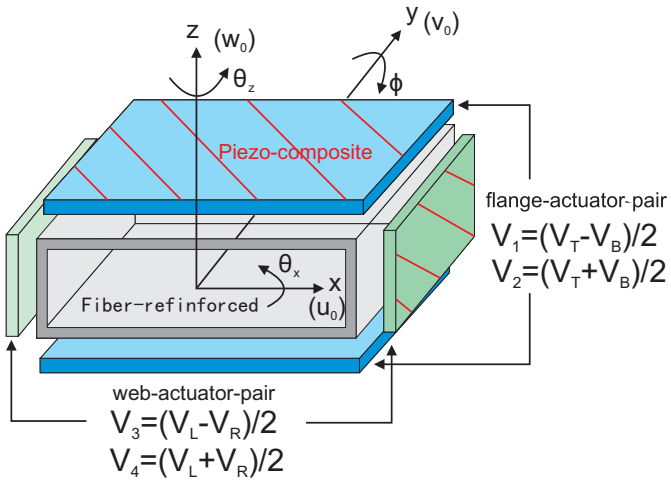

Figure 4.3: *Actuator-pairs bounded on the thin-walled box beam*

4.3 Discretization via the Extend Galerkin's Method

For numerical study, the Extend Galerkin's Method (EGM) [45,70] is used to discretize the system. In this chapter, we just focus on control of the hub-beam subsystem. Let

$$u_0(y,t) = \mathbf{\Psi}_u^T(y)\mathbf{q}_u(t), \quad v_0(y,t) = \mathbf{\Psi}_v^T(y)\mathbf{q}_v(t), \quad \theta z(y,t) = \mathbf{\Psi}_z^T(y)\mathbf{q}_z(t), \quad (4.9)$$

where the shape functions $\mathbf{\Psi}_u^T(y)$, $\mathbf{\Psi}_v^T(y)$ and $\mathbf{\Psi}_z^T(y)$ are required to fulfill only the essential boundary conditions, while $\mathbf{q}_u(t)$, $\mathbf{q}_v(t)$ and $\mathbf{q}_z(t)$ are $N \times 1$ generalized displacement vectors. Equations (4.3) and (4.5) lead to the following discretized equations of motion,

$$\begin{aligned} &\begin{bmatrix} J_H + M_\Lambda & \mathbf{M}_{\Lambda q} \\ \mathbf{M}_{\Lambda q}^T & \mathbf{M} \end{bmatrix} \begin{Bmatrix} \ddot{\Lambda} \\ \ddot{\mathbf{q}} \end{Bmatrix} + 2\dot{\Lambda} \begin{bmatrix} 0 & \mathbf{G}_{\Lambda q} \\ \mathbf{0} & \mathbf{G} \end{bmatrix} \begin{Bmatrix} \dot{\Lambda} \\ \dot{\mathbf{q}} \end{Bmatrix} \\ &+ \dot{\Lambda}^2 \begin{bmatrix} 0 & \mathbf{0} \\ \mathbf{0} & \mathcal{C} \end{bmatrix} \begin{Bmatrix} \Lambda \\ \mathbf{q} \end{Bmatrix} + \begin{bmatrix} 0 & \mathbf{0} \\ \mathbf{0} & \mathbf{K} \end{bmatrix} \begin{Bmatrix} \Lambda \\ \mathbf{q} \end{Bmatrix} + \begin{Bmatrix} \mathbf{0}_{1\times 3} \\ \mathcal{A} \end{Bmatrix} \mathbf{V} = \begin{Bmatrix} \tau_\Lambda \\ \mathbf{Q} \end{Bmatrix}, \end{aligned} \quad (4.10)$$

where

$$\mathbf{q} = \begin{Bmatrix} \mathbf{q}_u^T & \mathbf{q}_v^T & \mathbf{q}_z^T \end{Bmatrix}^T, \quad \mathbf{V} = \begin{Bmatrix} V_2 & V_3 & V_4 \end{Bmatrix}^T. \quad (4.11)$$

The rotary inertia of thin-walled beam M_Λ is given as

$$M_\Lambda = \int_0^L \left\{ b_1 (R_0 + y)^2 + b_5 \right\} \mathrm{d}\, y. \quad (4.12)$$

As for matrices of hub-beam inertia coupling $\mathbf{M}_{\Lambda q}$, beam mass $\mathbf{M}$, gyroscopic effect $\mathbf{G}_{\Lambda q}$, beam Corilos effect $\mathbf{G}$, beam centrifugal stiffening $\mathcal{C}$, beam stiffness $\mathbf{K}$, and additional excitation $\mathbf{Q}$, their expressions are given in Appendix A.8.

4.3.1 Dynamic model in non-inertial system

For dynamic problem of flexible hub-beam system in non-inertial system, the law of hub motion is usually assumed known and need not be solved. Thus dynamical model in non-inertial system can be obtained by neglecting the equations of hub in Eq. (4.10),

$$\mathbf{M}\ddot{\mathbf{q}} + 2\dot{\Lambda}\mathbf{G}\dot{\mathbf{q}} + (\mathbf{K} + \dot{\Lambda}^2\mathcal{C})\mathbf{q} + \mathcal{A}\mathbf{V} = \mathbf{Q}. \quad (4.13)$$

Note that, for the constant rotating speed case, the thin-walled beam system (4.13) is linear in natural.

4.3.2 Simplified linear model and controller design

For the low rotating speed case, the Coriolis and centrifugal effects are immaterial, thus the nonlinear flexible hub-beam system 4.10 can be reduced to the linear one,

$$\begin{bmatrix} J_H + M_\Lambda & \mathbf{M}_{\Lambda q} \\ \mathbf{M}_{\Lambda q}^T & \mathbf{M} \end{bmatrix} \begin{Bmatrix} \ddot{\Lambda} \\ \ddot{\mathbf{q}} \end{Bmatrix} + \begin{bmatrix} 0 & \mathbf{0} \\ \mathbf{0} & \mathbf{K} \end{bmatrix} \begin{Bmatrix} \Lambda \\ \mathbf{q} \end{Bmatrix} + \begin{Bmatrix} \mathbf{0} \\ \mathcal{A} \end{Bmatrix} \mathbf{V} = \begin{Bmatrix} \tau_\Lambda \\ \mathbf{Q} \end{Bmatrix}. \quad (4.14)$$

In order to suppress the vibration of the flexible thin-walled beam via the piezo-actuators, linear quadratic regular concept (LQR) that based on the use of a full state

feedback scheme is adopted. In state-space form, Eq. (4.14) becomes

$$\dot{\mathbf{x}}(t) = \mathbf{A}\mathbf{x}(t) + \mathbf{B}\begin{Bmatrix}\tau_\Lambda(t)\\ \mathbf{Q}(t)\end{Bmatrix} + \begin{bmatrix}\mathbf{W}_2 & \mathbf{W}_3 & \mathbf{W}_4\end{bmatrix}\begin{Bmatrix}V_2(t)\\ V_3(t)\\ V_4(t)\end{Bmatrix}, \tag{4.15}$$

where

$$\mathbf{x}(t) = \{\Lambda, \mathbf{q}^T(t), \dot{\Lambda}, \dot{\mathbf{q}}^T(t)\}^T, \tag{4.16a}$$

$$\mathbf{A} = \begin{bmatrix} \mathbf{0}_{(N+1)\times(N+1)} & \mathbf{I}_{(N+1)\times(N+1)} \\ -\begin{bmatrix} J_H + M_\Lambda & \mathbf{M}_{\Lambda q} \\ \mathbf{M}_{\Lambda q}^T & \mathbf{M}\end{bmatrix}^{-1}\begin{bmatrix}0 & \mathbf{0}\\ \mathbf{0} & \mathbf{K}\end{bmatrix} & \mathbf{0}_{(N+1)\times(N+1)}\end{bmatrix}, \tag{4.16b}$$

$$\mathbf{B} = \begin{Bmatrix} \mathbf{0}_{(N+1)\times 1} \\ \begin{bmatrix} J_H + M_\Lambda & \mathbf{M}_{\Lambda q} \\ \mathbf{M}_{\Lambda q}^T & \mathbf{M}\end{bmatrix}^{-1}\end{Bmatrix}, \tag{4.16c}$$

$$\mathbf{W_i} = \begin{Bmatrix} \mathbf{0}_{(N+1)\times 1} \\ -\begin{bmatrix} J_H + M_\Lambda & \mathbf{M}_{\Lambda q} \\ \mathbf{M}_{\Lambda q}^T & \mathbf{M}\end{bmatrix}^{-1}\begin{bmatrix}\mathbf{0}\\ \mathcal{A}_\mathbf{i}\end{bmatrix}\end{Bmatrix} \quad (i = 2, 3, 4), \tag{4.16d}$$

In engineering applications, active control via piezo-actuators embedded in the host structure of the thin-walled beam is normally used to suppress the vibration during hub motions. In other words, the major target of LQR control algorithm applied on the system (4.14) is to eliminate the residual vibrations on transverse direction, viz., making $\dot{u}_0 = 0$ or $\dot{\theta}_z = 0$. Recalling governing equations of hub-beam system (4.3), voltage parameter V_4 is solely related to piezoelectrically induced extension $\tilde{T}_y$. Although additional transverse response can be induced by extension $\tilde{T}_y$ via extension-transverse elastic coupling, indicated in Ref. [97], it is immaterial due to the high extensional stiffness for fiber-reinforced thin-walled beam. Thus we can omit the control terms associated to V_4 in Eq. (4.14). In addition, although voltage parameter V_2 is related both to extension $\tilde{T}_y$ and transverse shear $\tilde{Q}_x$, $\tilde{Q}_x$ will play the dominate role in transverse vibration suppression [97]. As for V_3, it is just related to bending $\tilde{M}_z$. Thus the controller of the hub-beam system can be split into two independent parts, i.e., transverse shear actuation offered by flange-actuator-pair (V_2) and bending actuation offered by web-actuator-pair (V_3).

Within the linear quadratic regulator control algorithm, we minimize the cost function (both the response of the closed-loop system and the control effort should be minimized simultaneously) for each control methodology.

$$J = \frac{1}{2}\int_{t_0}^{t_f}\left(\bar{\mathbf{x}}^T\mathbf{Z}\bar{\mathbf{x}} + V_i^T R_i V_i\right)\mathrm{d}\,t, \tag{4.17}$$

where the reduced beam state $\bar{\mathbf{x}}$ is given as $\bar{\mathbf{x}} = \{\mathbf{q}^T, \dot{\mathbf{q}}^T\}^T$. The positive semidefinite matrix $\mathbf{Z}$ and positive definite symmetric matrix $\mathbf{R}$ denote the state weighting matrix and the control weighting matrix, respectively. According to [5], the weighting matrices $\mathbf{Z}$ and $\mathbf{R}$ proper to a trade off between control effectiveness and control energy

consumption by taking

$$\mathbf{Z} = \begin{bmatrix} \alpha\mathbf{K} & \mathbf{0} \\ \mathbf{0} & \beta\mathbf{M} \end{bmatrix}, \quad \mathbf{R_i} = \eta {\mathcal{A}_\mathbf{i}}^T \mathbf{K}^{-1} \mathcal{A}_\mathbf{i}, \tag{4.18}$$

where α and β are weighting coefficients, ($\alpha\beta \geq 0$ and $(\alpha + \beta) > 0$), where η a scale factor. Actually, the matrix $\mathbf{Z}$ represents the combination of the thin-wall beam kinetic and potential energies in the sense of

$$\frac{1}{2}\int_{t_0}^{t_f} \bar{\mathbf{x}}^T \mathbf{Z} \bar{\mathbf{x}} \,\mathrm{d}\, t = \frac{1}{2}\int_{t_0}^{t_f} \left[\beta \dot{\mathbf{q}}^T \mathbf{M} \dot{\mathbf{q}} + \alpha \mathbf{q}^T \mathbf{K} \mathbf{q}\right] \mathrm{d}\, t. \tag{4.19}$$

For the problem of vibration suppression, it is reasonable to just consider the beam kinetic energy, i.e., weighting coefficients combination $\alpha = 0$ and $\beta = 1$ is adopted in this chapter.

Thus the optimal feedback control law is given by

$$V_i(t) = -\mathbf{G}_i \bar{\mathbf{x}}(t), \tag{4.20}$$

where G_i is the optimal gain matrix,

$$\mathbf{G}_i = \mathbf{R}^{-1} {\mathbf{W}_\mathbf{i}}^T \mathbf{P_i}, \tag{4.21}$$

while $\mathbf{P_i}$ is the positive-definite solution to the steady-state Riccati equation

$$\mathbf{Z} + \mathbf{P_i}\bar{\mathbf{A}} + \bar{\mathbf{A}}^T \mathbf{P_i} - \mathbf{P_i} \mathbf{W_i} {\mathbf{R_i}}^{-1} {\mathbf{W}_\mathbf{i}}^T \mathbf{P_i} = \mathbf{0}, \tag{4.22}$$

where the reduced matrix $\bar{\mathbf{A}}$ is

$$\bar{\mathbf{A}} = \begin{bmatrix} \mathbf{0}_{N\times N} & \mathbf{I}_{N\times N} \\ -\mathbf{M}^{-1}\mathbf{K} & \mathbf{0}_{N\times N} \end{bmatrix}. \tag{4.23}$$

Solution of the Riccati equations yields the control law which depends only on α, β and the structural mass, stiffness and centrifugal force matrices.

4.4 Numerical study

4.4.1 Model validation

Since the main part of the model validations have been implemented in the previous chapters, here we just validate the rotation induced dynamics stiffness effect for CAS lay-up configuration. The material property and geometry of the thin-walled box beam for validation are shown in Table 4.1. The details of the CAS lay-up configuration are given in Table. 4.2. Table 4.3 illustrates the eigen-frequencies of the rotating thin-walled beam (4.13) for selected constant rotating speeds. It can be found that our predicted frequencies have good agreements with those of experiment and FEM results.

Table 4.1: *Material property and geometry of the thin-walled box beam for validation [17]*

E_{11}	1.42×10^{11} N/m^2	Density (ρ)	1.442×10^3 Kg/m^3
$E_{22} = E_{33}$	9.8×10^9 N/m^2	Width ($2b^a$)	2.268×10^{-2} m
$G_{12} = G_{13}$	6.0×10^9 N/m^2	Depth ($2d^a$)	1.212×10^{-2} m
G_{23}	4.83×10^9 N/m^2	Number of layers (N_h)	6
$\mu_{12} = \mu_{13}$	0.42	Layer thickness	1.270×10^{-4} m
μ_{23}	0.50	Length (L)	0.8446 m

[a] Inner dimensions of the cross section.

Table 4.2: *CAS lay-up configurations for thin-walled box beam*[a]

	Flanges		Webs	
Material	Top	Bottom	Left	Right
Host structure	$[\theta_h]_6$	$[\theta_h]_6$	$[\theta_h/-\theta_h]_3$	$[\theta_h/-\theta_h]_3$
Piezo-actuator[b]	$[\theta_p^F]$	$[\theta_p^F]$	$[\theta_p^W]$	$[\theta_p^W]$

[a] θ_h, θ_p^F and θ_p^W denote the ply-angle for host structure, flange-actuator-pair and web-actuator-pair, respectively.

[b] The piezo-actuators are assumed positioned of the outer side of the laminate if they are adopted.

Table 4.3: *Frequencies validation for rotating thin-walled beam with CAS lay-up configuration* $\theta_h = 45°$.

Speed	Mode	Exp. [17]	FEM [1, 4]	Present
0 rpm	1st	16.67	14.69	15.19
	2nd	96.15	92.02	95.04
1008 rpm	1st	25.63	23.48	24.22
	2nd	118.3	102.1	108.2

Table 4.4: *Material property and geometric specification of the thin-walled beam with a rectangular cross-section [97]*

Material	**Value**	**Geometric**	**Value**
E_{11}	206.8×10^9 N $\cdot$ m^{-2}	Width ($2b^a$)	0.254 m
$E_{22} = E_{33}$	5.17×10^9 N $\cdot$ m^{-2}	Depth ($2d^a$)	0.0681 m
$G_{13} = G_{23}$	2.55×10^9 N $\cdot$ m^{-2}	Wall thickness (h)	0.0102 m
G_{12}	3.10×10^9 N $\cdot$ m^{-2}	Number of layers (m_h)	6
$\mu_{12} = \mu_{13} = \mu_{23}$	0.25	Layer thickness	0.0017 m
ρ	1528 Kg $\cdot$ m^{-3}	Length (L)	4.064 m

[a] The length is measured on the mid-line contour.

Table 4.5: *Material properties of piezo-actuator manufactured by MFC [71]*

E_{11}	$31.2.8 \times 10^9$ N $\cdot$ m^{-2}	d_{11}	386.63×10^{-12} m $\cdot$ V^{-1}
$E_{22} = E_{33}{}^*$	17.05×10^9 N $\cdot$ m^{-2}	$d_{12} = d_{13}{}^*$	-175.50×10^{-12} m $\cdot$ V^{-1}
$G_{12} = G_{13}{}^* = G_{23}{}^*$	5.12×10^9 N $\cdot$ m^{-2}	ρ	5115.9 Kg $\cdot$ m^{-3}
$\mu_{12} = \mu_{13}{}^* = \mu_{23}{}^*$	0.303	m_p	1
Electrode spacing	0.0017 m	Thickness	0.0017 m

* The value is assumed by the author.

4.4.2 Dynamic simulation

The material property and the geometric specification of the beam host structure used in simulation are shown in Table 4.4. While the material property of piezo-actuators are given in Table 4.5. We assume the piezo-actuators are spread over the entire beam span unless other stated. The lay-up configurations of the thin-walled beam are specified in Table 4.2.

Before the simulation, it is essential to identify the suitable host structure ply-angle θ_h, flange-actuator-pair ply-angle θ_p^F and web-actuator-pair ply-angle θ_p^W. The relationship between stiffness coefficients a_{ij} and host structure ply-angle θ_h has been discussed in Ref. [98]. According to the results of Ref. [98], $\theta_h = 75^\circ$ will induce a strong flapwise bending-twist elastic coupling that is beneficial for the dynamical response of the beam subsystem. Figs. 4.4a and 4.4b depict piezo-actuator coefficients of hub-beam subsystem, viz., $\mathcal{A}_2^{Qx}$ and $\mathcal{A}_3^{Mz}$, respectively. It can be found that host-structure configuration has a significant effect on piezo-actuators. For flange-actuator-pair induced chordwise transverse shear $\mathcal{A}_2^{Qx}$ in Fig. 4.4a, $\theta_p^F \approx 135^\circ$ will reach the maximum absolve value for $\theta_h = 75^\circ$ case. While for web-actuator-pair induced flapwise bending $\mathcal{A}_3^{Mz}$, generally, the maximum absolute value exists at $\theta_p^W = 90^\circ$. As a result, without other stated, the combination $\theta_h = 75^\circ$, $\theta_p^F = 135^\circ$ and $\theta_p^W = 75^\circ$ is adopted for the hub-beam subsystem in the simulation.

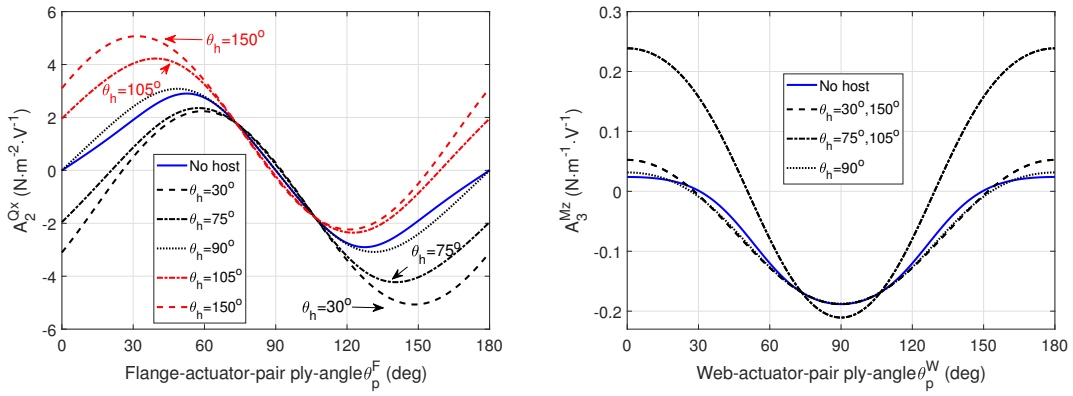

(a) $\mathcal{A}_2^{Qx}$ **(b)** $\mathcal{A}_3^{Mz}$

Figure 4.4: *Piezo=actuator coefficients*

In order to simulate the hub-beam system undergoing a rest-to-rest motion [85] that is widely used in spacecraft attitude maneuver, the optimal Bang-off-Bang switched rotating torque as shown in Fig. 4.5a is applied on the hub. Note that, the first 7 modes of the thin-walled beam are used in the simulation. And the LQR control parameters $\eta_2 = 300$ and $\eta_3 = 3000$ are adopted in default.

In engineering application, the rotary inertia of hub J_H is usually a variable parameter. For example, as the basic model of satellite, J_H will decrease with the consumption of fuel for attitude maneuver. Thus the following nondimensional parameter is defined

for the simple description of J_H,

$$\eta_{hub} = \frac{J_H}{\int_0^L [b_1(R_0 + y)^2 + b_5]\,\mathrm{d}\,y}, \tag{4.24}$$

where the denominator term denotes the rotary inertia of the beam. Fig. 4.5b highlights the influence of J_H on hub angular displacement during the rest-to-rest motion. The

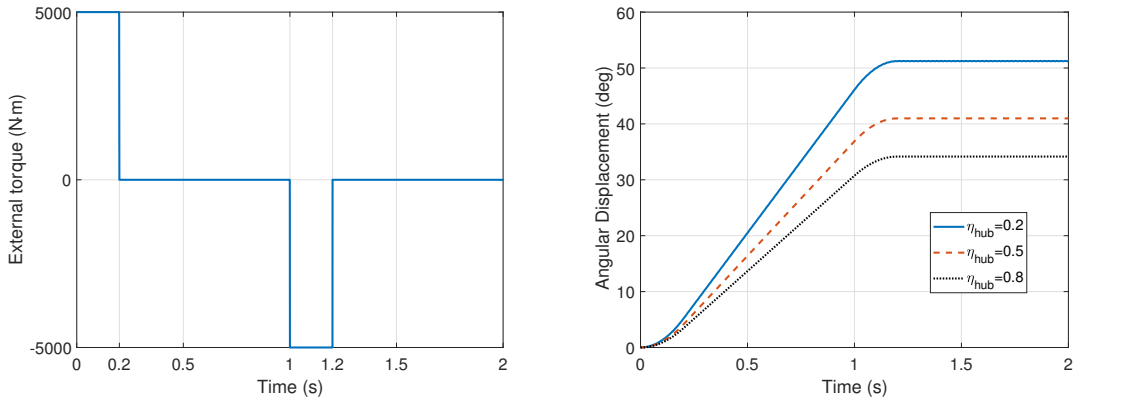

(a) *Time history of external torque*

(b) *Time history of angular displacement for selected rotary inertia of hub*

Figure 4.5: *Time history of external torque and angular displacement*

influence of J_H on active vibration suppression is further highlighted in Fig. 4.6, which plots damping ratios of the first three modes of the hub-beam system as a function of η_{hub}. In addition, the result of Fig. 4.6 illustrates that flange-actuator-pair induced shear control will offer the balanced damping performance for all three modes, however web-actuator-pair induced bending control will just have a significant damping effect on the first mode.

Figures 4.7a and 4.7b depict the associated displacement and velocity responses of the beam tip under the LQR vibration suppression control during the attitude maneuver, respectively. It can be found that bending control and shear control have similar control authority on chordwise vibration suppression. Fig. 4.8a further depicts the associated time history of angular velocity. The applied voltages history are illustrated in Fig. 4.8b. The result of Fig. 4.8b presents that the maximum value of voltage V_3 is about twice that of V_2, which implies shear control is more efficient than bending control in our case. Actually host structure configuration has a noticeable influence on damping performance of transverse shear control, see Fig. 4.9. On the other hand, the result of Fig. 4.9 shows that the influence of host structure on bending control induced damping ratios is immaterial.

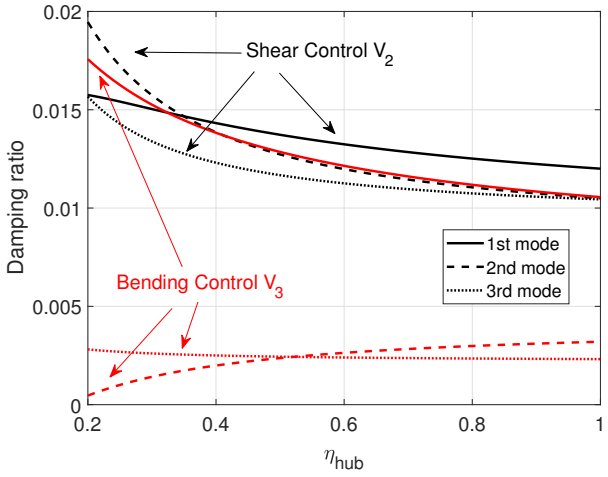

Figure 4.6: *Damping ratios of the first three modes vs. hub rotary inertia parameter* η_{hub}

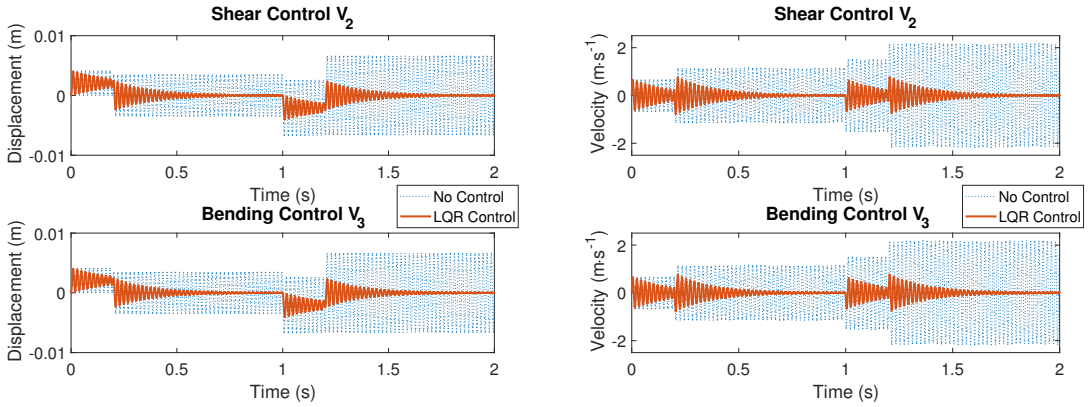

(a) *Displacement* **(b)** *Velocity*

Figure 4.7: *Tip displacement and velocity of the thin-walled beam;* $\eta_{hub} = 0.2$

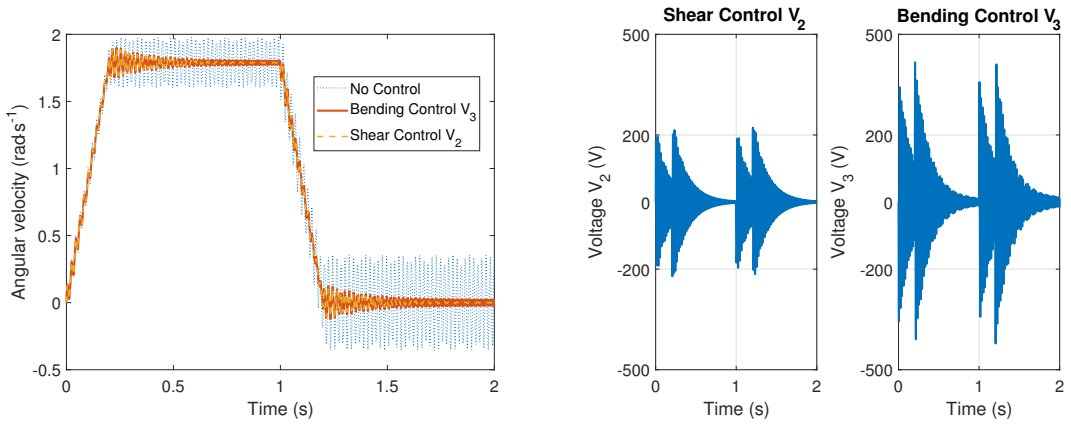

(a) *Angluar velocity* **(b)** *Voltages*

Figure 4.8: *Time history of angular velocity and the associated voltages;* $\eta_{hub} = 0.2$

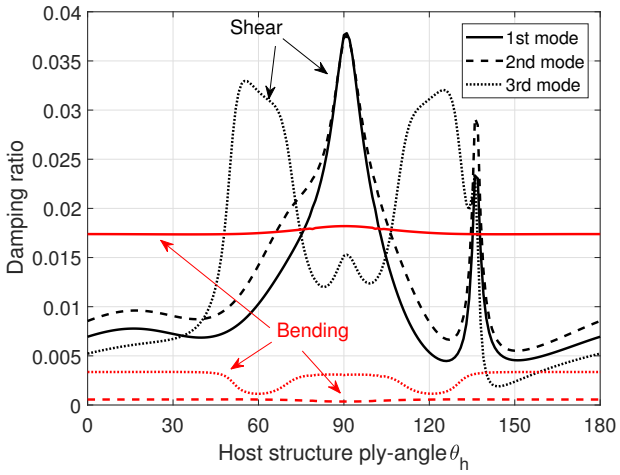

Figure 4.9: *Damping ratio of the first three modes vs. host structure ply-angle* θ_h*;* $\eta_{hub} = 0.2$

CHAPTER 5

Modeling and Control of Piezo-actuated Wings

5.1 Introduction

Problems related to mathematical modeling and optimal dynamic control of adaptive aircraft wings modeled as composite thin-walled structures are considered. Some non-classical effects such as warping inhibition and three-dimensional (3-D) strain are accounted for in the beam model. The adaptive capabilities are provided by the actuators manufactured by anisotropic piezo-composite layers embedded into the structure. The Extended Galerkin's Method is used for the numerical study. A negative velocity feedback control algorithm and the linear quadratic regulator (LQR) feedback control strategy are adopted to control the aircraft wing response. The effective damping performance is optimized by studying anisotropic characteristics of piezo-composite and elastic tailoring of the fiber-reinforced host structure. The relations between active vibration control effect and design factors, such as the size and position of piezo-actuator are investigated in detailed.

5.2 Dynamical model

The advanced aircraft wing is modeled as an adaptive composite thin-walled beam which is developed in Chapter 2. In order to model the fixed wing structure, we ignore the associated rotating terms in governing equations (2.28). A typical circumferential asymmetric stiffness (CAS) lay-up configuration is adopted to model the aircraft wing structure. The twist-bending elastic coupling induced by the CAS lay-up is beneficial for the aeroelastic response behavior [43, 46, 49], especially for the suppression of the flutter instability [76, 77, 86]. The elastic couplings and piezoelectrically induced actuating couplings of CAS lay-up configuration are discussed in Chapter 4. Approximating the trigonometric functions of Eqs. (2.28) with their Taylor series expansion,

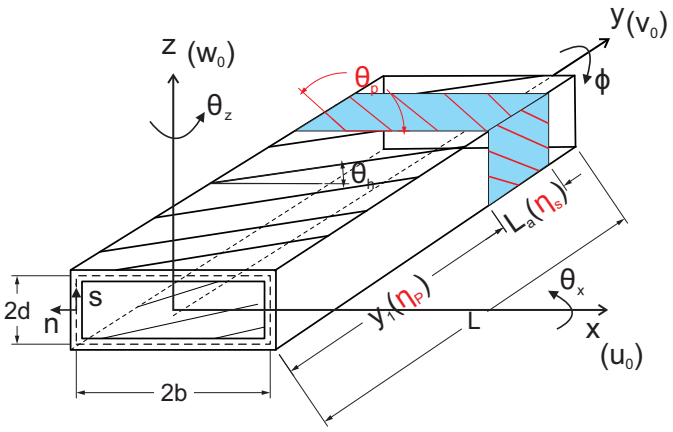

Figure 5.1: *Thin-walled box beam model*

i.e. $\sin\phi \approx \phi$ and $\cos\phi \approx 1$, the CAS lay-up configuration equations can be split into two subsystem, the *Lateral Bending-Extension coupling subsystem* $(u_0 - v_0 - \theta_z)$ and the *Twist-Vertical Bending coupling subsystem* $(w_0 - \phi - \theta_x)$.

BE-subsystem (Lateral Bending-Extension coupling subsystem)

$$\delta u_0 \; : \; a_{14}v_0'' + a_{44}(u_0'' + \theta_z') - b_1\ddot{u}_0 + p_x + \delta_p \mathcal{A}_2^{Qx} V_2 R'(y) = 0, \tag{5.1a}$$

$$\delta v_0 \; : \; a_{11}v_0'' + a_{14}(u_0'' + \theta_z') - b_1\ddot{v}_0 + p_y + \delta_p \mathcal{A}_2^{Ty} V_2 R'(y) + \delta_p \mathcal{A}_4^{Ty} V_4 R'(y) = 0, \tag{5.1b}$$

$$\begin{aligned}\delta\theta_z \; : & \, a_{22}\theta_z'' - a_{14}v_0' + a_{44}(u_0' + \theta_z) - (b_5 + b_{15})\ddot{\theta}_z + m_z + \delta_p \mathcal{A}_3^{Mz} V_3 R'(y) \\ & - (\delta_p + \delta_s)\mathcal{A}_2^{Qx} V_2 R(y) = 0.\end{aligned} \tag{5.1c}$$

The boundary conditions for cantilevered beams are
at $y = 0$:

$$u_0 = v_0 = \theta_z = 0, \tag{5.2}$$

and at $y = L$:

$$\delta u_0 \; : a_{14}v_0' + a_{44}(u_0' + \theta_z) + \delta_s \mathcal{A}_2^{Qx} V_2 = \bar{Q}_x, \tag{5.3a}$$

$$\delta v_0 \; : a_{11}v_0' + a_{14}(u_0' + \theta_z) + \delta_s \mathcal{A}_2^{Ty} V_2 + \delta_s \mathcal{A}_4^{Ty} V_4 = \bar{T}_y, \tag{5.3b}$$

$$\delta\theta_z \; : a_{22}\theta_z' + \delta_s \mathcal{A}_3^{Mz} V_3 = \bar{M}_z. \tag{5.3c}$$

TB-subsystem (Twist-Vertical Bending coupling subsystem)

$$\delta w_0 \; : \; a_{55}(w_0'' + \theta_x') - b_1\ddot{w}_0 + p_z + \delta_p \mathcal{A}_4^{Qz} V_4 R'(y) = 0, \tag{5.4a}$$

$$\begin{aligned}\delta\phi \; : & \, a_{37}\theta_x'' + a_{77}\phi'' - a_{66}\phi^{(iv)} - (b_4 + b_5)\ddot{\phi} + (b_{10} + b_{18})\ddot{\phi}'' + m_y + b_w' \\ & + \delta_p \mathcal{A}_1^{My} V_1 R'(y) + \delta_p \mathcal{A}_3^{My} V_3 R'(y) = 0,\end{aligned} \tag{5.4b}$$

$$\begin{aligned}\delta\theta_x \; : & \, a_{33}\theta_x'' + a_{37}\phi'' - a_{55}(w_0' + \theta_x) - (b_4 + b_{14})\ddot{\theta}_x + m_x + \delta_p \mathcal{A}_1^{Mx} V_1 R'(y) \\ & - (\delta_p + \delta_s)\mathcal{A}_4^{Qz} V_4 R(y) = 0,\end{aligned} \tag{5.4c}$$

The boundary conditions, for cantilevered beams are
at $y = 0$:

$$w_0 = \phi = \phi' = \theta_x = 0, \tag{5.5}$$

and at $y = L$:

$$\delta w_0 \ : a_{55}(w_0' + \theta_x) + \delta_s \mathcal{A}_4^{Qz} V_4 = \bar{Q}_z, \tag{5.6a}$$

$$\delta\phi \ : a_{37}\theta_x' + a_{77}\phi' - a_{66}'''\phi + (b_{10} + b_{18})\ddot{\phi}' + \delta_s \mathcal{A}_1^{My} V_1 + \delta_s \mathcal{A}_3^{My} V_3 = \bar{M}_y, \tag{5.6b}$$

$$\delta\phi' \ : \ a_{66}\phi'' = \bar{B}_w, \tag{5.6c}$$

$$\delta\theta_x \ : a_{33}\theta_x' + a_{37}\phi' + \delta_s \mathcal{A}_1^{Mx} V_1 = \bar{M}_x, \tag{5.6d}$$

If the actuator is spread over the entire beam span, the traces are $\delta_p = 0$ and $\delta_s = 1$; otherwise, if the actuator is a single patch, the traces assume the values $\delta_p = 1$ and $\delta_s = 0$. Note that the BE-subsystem and the TB-subsystem are not entirely independent, since they are coupled by the voltage parameters V_3 and V_4.

5.3 Solution methodology

The Extend Galerkin's Method (EGM) as used in Section 3.3 is adopted for numerical study. Then Eqs. (5.1)-(5.3) and (5.4)-(5.6) lead to the following discretized equations of motion,

$$[\mathbf{M}]_{(B,T)}\{\ddot{\mathbf{q}}\}_{(B,T)} + [\mathbf{K}]_{(B,T)}\{\mathbf{q}\}_{(B,T)} + [\mathcal{A}]_{(B,T)}\{\mathbf{V}\}_{(B,T)} = [\mathbf{Q}]_{(B,T)}, \tag{5.7}$$

where

$$\mathbf{q}_B = \left\{ \begin{array}{ccc} \mathbf{q}_u^T & \mathbf{q}_v^T & \mathbf{q}_z^T \end{array} \right\}^T, \quad \mathbf{q}_T = \left\{ \begin{array}{ccc} \mathbf{q}_w^T & \mathbf{q}_\phi^T & \mathbf{q}_x^T \end{array} \right\}^T, \tag{5.8}$$

$$\mathbf{V}_B = \left\{ V_2 \quad V_3 \quad V_4 \right\}^T, \quad \mathbf{V}_T = \left\{ V_1 \quad V_3 \quad V_4 \right\}^T. \tag{5.9}$$

In the above equations, subscripts B, T denote the BE-subsystem and TB-subsystem, respectively. The expressions for mass matrix $\mathbf{M}_{(B,T)}$, stiffness matrix $\mathbf{K}_{(B,T)}$, actuation matrix $\mathcal{A}_{(B,T)}$ and external excitation vector $\mathbf{Q}_{(B,T)}$ are given in Appendix A.7.

5.4 Model validation

The beam model developed here is validated by comparing the vibration frequency predicted for a composite thin-walled beam with the analytical results of Ref. [4] and the experimental data of Ref. [17]. The geometry and material properties of the cantilever thin-walled box beam of Fig. 5.1 are specified in Table 5.1. The results, reported in Table 5.2, show a better agreement of the present model with experimental data than that of Ref. [4].

5.5 Static study

The material property (Graphite-Epoxy) and geometric specification for the thin-walled box beam of Fig. 5.1 are shown in Table 5.3. In order to obtain better actuating performance, the piezo-actuators are manufactured by single crystal MFC [19, 71], whose material property is specified in Table 5.4. Moreover, the piezo-composite laminate is distributed over the entire cross-section. The lay-up configurations (both for host structure and piezo-actuator) can be found in Table 5.5.

Table 5.1: *Details of thin-walled composite box beam for validation [17]*

E_{11}	1.42×10^{11} N/m^2	Density (ρ)	1.442×10^3 Kg/m^3
$E_{22} = E_{33}$	9.8×10^9 N/m^2	Width ($2b^a$)	2.268×10^{-2} m
$G_{12} = G_{13}$	6.0×10^9 N/m^2	Depth ($2d^a$)	1.212×10^{-2} m
G_{23}	4.83×10^9 N/m^2	Number of layers (N_h)	6
$\mu_{12} = \mu_{13}$	0.42	Layer thickness	1.270×10^{-4} m
μ_{23}	0.50	Length (L)	0.8446 m

[a] Inner dimensions of the cross section.

Table 5.2: *Natural frequency (Hz) for* $[45]_6$ *CAS lay-up configuration*

Mode	Exp. [17]	Analytical [4]	Error (%)	Present	Error [a] (%)
1TB	16.67	14.69	-11.9	15.20	-8.8
2TB	96.15	92.02	-4.3	95.09	-1.1
1BE	29.48	25.13	-14.8	26.64	-9.6

[a] Relative error, (Present − Exp.)/Exp. × 100%.

5.5.1 Piezo-actuator coefficients study

The non-zero CAS configuration piezo-actuator coefficients of Eq.(4.2) are depicted in Fig. 5.2 as a function of the piezo-actuator ply-angle θ_p. Two distinct trends emerge from the results of Fig. 5.2.

The first trend characterizes the bending coefficients ($\mathcal{A}_1^{Mx}$, $\mathcal{A}_3^{Mz}$) and the extension coefficients ($\mathcal{A}_2^{Ty}$, $\mathcal{A}_4^{Ty}$). The coefficients increase from $\theta_p = 0^o$ to $\theta_p = 90^o$, then decrease until $\theta_p = 180^o$. Their values equal zero when $\theta_p \approx 40^o$ and $\approx 140^o$. Note that, because of the reverse definition of θ_x (see Fig. 5.1), coefficients $\mathcal{A}_1^{Mx}$ and $\mathcal{A}_3^{Mz}$ present the exactly opposite trends.

The second trend characterizes the transverse shear coefficients ($\mathcal{A}_2^{Qx}$, $\mathcal{A}_4^{Qz}$) and the twist coefficients ($\mathcal{A}_1^{My}$, $\mathcal{A}_3^{My}$). The previous groups of coefficients have a symmetric dependence centered around $\theta_p = 90^o$. These coefficients, instead, show an anti-symmetric trend around $\theta_p = 90^o$. They are equal to zero when $\theta_p = 0^o,\ 90^o, 180^o$, with the maximum absolute values reached for $\theta_p \approx 42^o$ and $\theta_p \approx 138^o$.

5.5.2 Actuation performance study

In this subsection, the relationship between actuation performance and voltage parameters (V_1, V_2, V_3, V_4) is specifically discussed.

Table 5.3: *Material property and geometric specification of the host structure [47, p. 131]*

E_{11}	206.8×10^9 N/m^2	Width ($2b^a$)	0.254 m
$E_{22} = E_{33}$	5.17×10^9 N/m^2	Depth ($2d^a$)	0.0681 m
$G_{12} = G_{13}$	2.55×10^9 N/m^2	Wall thickness (h)	0.0102 m
G_{23}	3.10×10^9 N/m^2	Number of layers (N_h)	6
$\mu_{12} = \mu_{13} = \mu_{23}$	0.25	Layer thickness	0.0017 m
ρ	1.528×10^3 Kg/m^3	Length (L)	2.032 m

[a] The length is measured on the mid-line contour.

Table 5.4: *Material properties of E-glass, AFC, MFC and single crystal MFC (S-MFC)*

	E-Glass [23]	AFC [23]	MFC [71]	S-MFC [71]
E_1 (Gpa)	14.8	30.54	31.2	6.23
E_2 (Gpa)	13.6	16.11	17.05	11.08
G_{12} (Gpa)	1.9	5.5	5.12	2.01
μ_{12}	0.19	0.36	0.303	0.229
d_{11} ($\times 10^{-12}$ m/V)	N/A	381	386.63	1896.5
d_{12} ($\times 10^{-12}$ m/V)	N/A	-160	-175.50	-838.2
ρ (Kg m^{-3})	1700	4810	5115.9	5338.3
Thickness ($\times 10^{-4}$ m)	2.032	1.689	17	17
Electrode spacing ($\times 10^{-3}$ m)	N/A	1.143	1.7	1.7

Table 5.5: *Lay-up configurations for beam with CAS lay-up [unit:deg].*

		Flanges		Webs	
Material	Layer	Top	Bottom	Left	Right
Piezo-actuator	CAS (7) [a]	$[\theta_p]$	$[\theta_p]$	$[\theta_p]$	$[\theta_p]$
Host structure	CAS (1-6)	$[\theta_h]_6$	$[\theta_h]_6$	$[\theta_h/-\theta_h]_3$	$[\theta_h/-\theta_h]_3$

[a] The piezo-actuator is positioned of the outer side of the laminate.

TB-subsystem

The equations governing the TB-subsystem in Eqs. (5.4), have the voltage vector $\mathbf{V}_T = [V_1, V_3, V_4]^T$ as forcing parameters. Specifically, the voltage parameter V_1 influences both twist and bending, while V_3 and V_4 work for twist and transverse shear, respectively. Note that the elastic coupling of the structure has a significant effect on the actuation performance. The twist-bending elastic coupling in Eq. (4.1b) is related to the stiffness coefficient a_{37}. Two typical host structure ply-angles, viz., $\theta_h = 15^o$ and $\theta_h = 75^o$, are considered here. The corresponding values for a_{37} were computed in Ref. [98], i.e., a_{37} equals -4.05×10^3 N.m^2 and 3.92×10^5 N.m^2, respectively. Thus, the elastic coupling can be ignored for $\theta_h = 15^o$, while it is significant for $\theta_h = 75^o$.

Figures 5.3a and 5.3b depict the tip deflections obtained from $V_1 = 1000$ V (black curve), $V_3 = 1000$ V (red curve) and $V_4 = 1000$ V (green curve) for weak and strong elastic coupling cases, respectively. The non-dimensional quantities are defined as

$$\hat{u}_0 = \frac{u_0}{2b}, \quad \hat{v}_0 = \frac{v_0}{L}, \quad \hat{w}_0 = \frac{w_0}{2b}, \quad \hat{\phi} = \phi, \quad \hat{\theta}_x = \theta_x, \quad \hat{\theta}_z = \theta_z. \tag{5.10}$$

It can be seen that the voltage parameter V_4, which is related to transverse-shear-actuation can be ignored in both cases. In addition, the voltage parameter V_1 dominates the TB-subsystem actuation performance. Note that, for strong elastic coupling case in Fig. 5.3b, twist-actuation shows better performance on bending deflection than direct bending-actuation.

BE-subsystem

According to the governing equations (5.1) of the BE-subsystem, voltage V_2 is related to both extension and transverse shear actuation, while V_3 and V_4 are related to bending

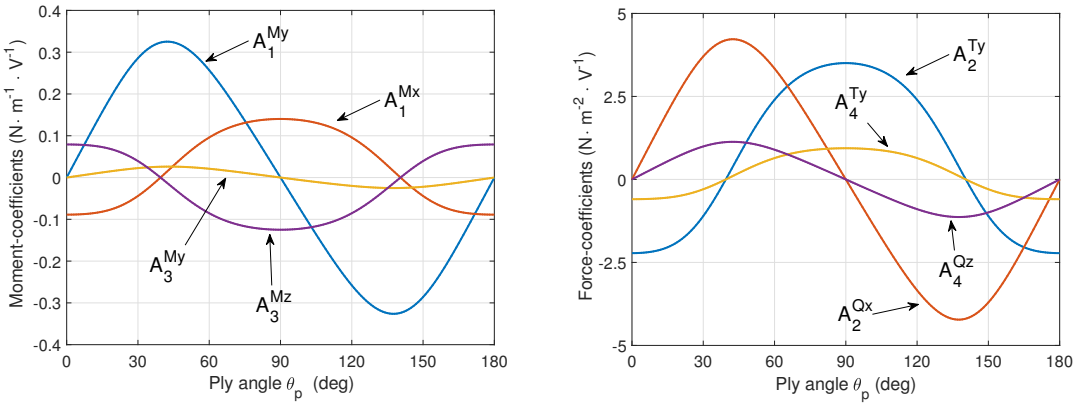

Figure 5.2: *Piezo-actuator coefficients with single crystal MFC as a function of the ply-angle θ_p in CAS lay-up configuration.*

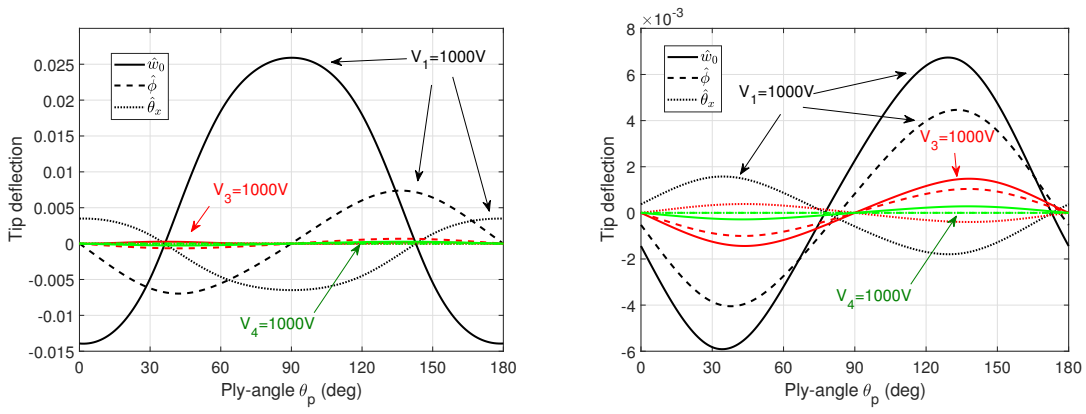

(a) $\theta_h = 15^o$ **(b)** $\theta_h = 75^o$

Figure 5.3: *Beam tip deflections of the TB-subsystem as a function of the piezo-actuator ply-angle θ_p.*

and extension actuation, respectively. The results obtained for two typical host structure cases, $\theta_h = 15^o$ and $\theta_h = 75^o$, are reported in Figs. 5.4a and 5.4b.

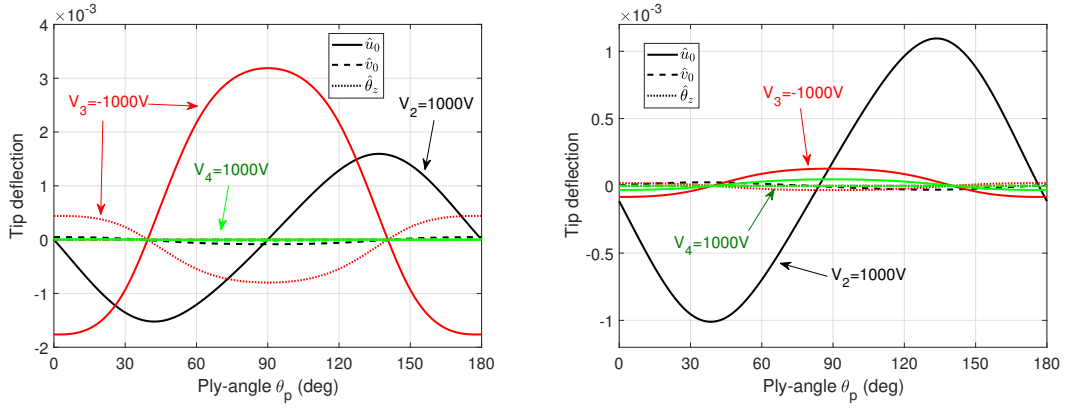

(a) $\theta_h = 15^o$ **(b)** $\theta_h = 75^o$

Figure 5.4: *Beam tip deflections of BE-subsystem as a function of the piezo-actuator ply-angle* θ_p.

The beam extension stiffness coefficient a_{11} is much higher than the other terms. Thus, the extension actuation induced by voltage parameter V_4 can be ignored, see both Figs. 5.4a and 5.4b. The voltage V_2 has a significant effect on actuation performance for both cases: the transverse-shear-actuation, weak in the TB-subsystem, is much stronger in the BE-subsystem. One reason for this is that the size of the flange-actuator-pair is almost four times than that of the web-actuator-pair. In addition, the direct bending actuation induced by voltage V_3 (red line) in the $\theta_h = 75^o$ case in Fig. 5.4b is much weaker than that in the $\theta_h = 15^o$ case in Fig. 5.4a.

Conclusion

In a nutshell, the TB-subsystem is dominated by V_1 for the weak elastic coupling case (see Fig. 5.3a), while the BE-subsystem is dominated by V_2 when the elastic coupling effect is strong (see Fig. 5.4b). As a result, although the TB-subsystem and the BE-system are actually coupled by V_3 and V_4, it is nonetheless reasonable to treat these two subsystems as independent.

5.5.3 The influence of piezo-composite material for actuating performance

The actuation performance of three typical piezo-composite materials, viz., AFC [6], standard MFC [100] and single crystal MFC [71] are compared in Fig. 5.5a and 5.5b. The corresponding material properties are reported in Table 5.4. It can be seen that, generally, no matter the bending performance $\hat{u}_0$ (dot lines), $\hat{w}_0$ (solid lines) or twist performance $\hat{\phi}$ (dashed line), the single crystal MFC shows the best actuating performance. This is in agreement with the conclusions of Park et al. [19, 71]. Note that different piezo-composite materials may need different ply-angles $\bar{\theta}_p$ to achieve the best actuation performance. For example, in the $\theta_h = 75^o$ case of Fig. 5.5b, $\bar{\theta}_p \approx 130^o$ for S-MFC and $\bar{\theta}_p \approx 110^o$ for standard MFC or AFC.

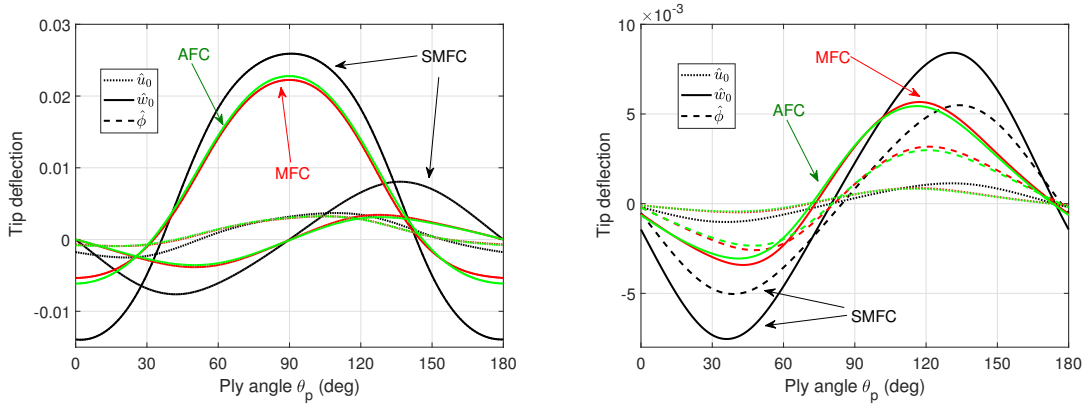

(a) $\theta_h = 15^o$ **(b)** $\theta_h = 75^o$

Figure 5.5: *The bending deflection $\hat{u}_0$, $\hat{w}_0$ and twist deflection $\hat{\phi}$ of the beam tip for AFC, standard MFC and single crystal MFC. ($V_1 = V_3 = V_4 = 1000$ V for TB-subsystem, $V_2 = -V_3 = V_4 = 1000$ V for BE-subsystem)*

5.6 Dynamic control of twist-bending (vertical) coupling subsystem

5.6.1 Governing equations including negative velocity feedback control

A negative velocity feedback control is considered here. In this section, we firstly investigated the torsion/bending (TB) subsystem that is important in the aeroelastic control of an aircraft wing. If we assume the sensor can offer the velocity information at $y = Y_s$, then actuating voltage vector $\mathbf{V}_T$ for the negative velocity feedback control can be computed

$$\mathbf{V}_T = \begin{Bmatrix} V_1 \\ V_3 \\ V_4 \end{Bmatrix} = \begin{Bmatrix} -k_1[\alpha_1^k \dot{\hat{\phi}}(Y_s,t) + \beta_1^k \dot{\hat{\theta}}_x(Y_s,t)] \\ -k_3 \dot{\hat{\phi}}(Y_s,t) \\ -k_4[\alpha_4^k \dot{\hat{w}}_0(Y_s,t) + \beta_4^k \dot{\hat{\theta}}_x(Y_s,t)] \end{Bmatrix} = \mathbf{P}(Y_s)\dot{\mathbf{q}}_T(t), \tag{5.11}$$

where, k_i ($i = 1, 3, 4$) are the feedback control gains, α_i^k and β_i^k are weighting coefficients of the control gains, and matrix $\mathbf{P}$ is defined in A.7. As a result, the closed-loop discretized system Eq. (5.7) becomes

$$\mathbf{M}_T \ddot{\mathbf{q}}_T(t) + \mathcal{A}_T \mathbf{P} \dot{\mathbf{q}}_T(t) + \mathbf{K}_T \mathbf{q}_T(t) = \mathbf{Q}_T(t). \tag{5.12}$$

5.6.2 Control gain weighting coefficients discussion

The first step in designing the controller is to choose suitable control weighting coefficients. Since the flapping and twisting motions usually have a significant phase difference, we can simplify the control system by considering only two cases for the voltage parameter V_1, i.e., the bending control ($\alpha_1^k = 0$, $\beta_1^k = -1$) and the twist control ($\alpha_1^k = 1$, $\beta_1^k = 0$). Furthermore, as evidenced by the static study, the shear force induced by V_4 is immaterial in the TB-subsystem. As a result, the velocity feedback Eq. (5.11) can be simplified to a combination of these two cases: the Bending Control

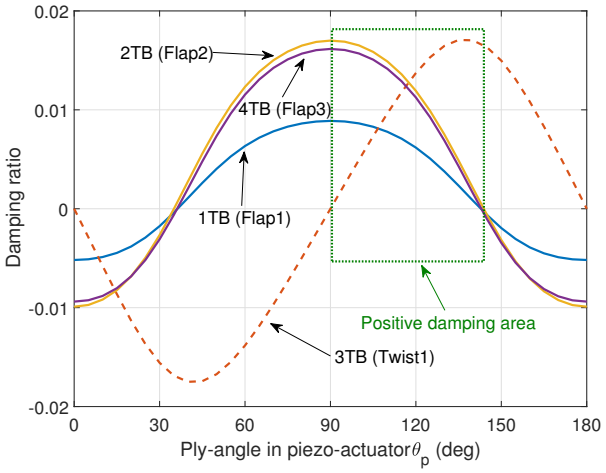

Figure 5.6: *Damping ratios as a function of piezo-composite ply-angle θ_p; bending control methodology, $k_i = 100$, $\theta_h = 15^o$.*

Methodology,

$$\mathbf{V}_T = \begin{Bmatrix} V_1 \\ V_3 \end{Bmatrix} = \begin{Bmatrix} k_1 \dot{\theta}_x \\ -k_3 \dot{\phi} \end{Bmatrix} \tag{5.13}$$

and the Twist Control Methodology

$$\mathbf{V}_T = \begin{Bmatrix} V_1 \\ V_3 \end{Bmatrix} = \begin{Bmatrix} -k_1 \dot{\phi} \\ -k_3 \dot{\phi} \end{Bmatrix} \tag{5.14}$$

The static study in Section 5.5.2 evidenced a significant effect of the twist-bending elastic coupling on the actuation performance. Thus, the weak and strong elastic coupling cases are separately investigated here. Bending control is considered first because twist control has a weak bending authority for the weak elastic coupling case. Fig. 5.6 depicts the damping ratios obtained for the first four modes of the weak elastic coupling case $\theta_h = 15^o$. The figure allows to easily identify the positive damping area $90^o \leqslant \theta_p \leqslant 138^o$. The first four modes are denoted as Flap1, Flap2, Twist1 and Flap3, respectively. Since the twist-bending coupling can be ignored in the first four modes, the damping ratios of the flapping and the twist modes follow the trend of coefficients $\mathcal{A}_1^{Mx}$ and $\mathcal{A}_3^{My}$ variation in Fig. 5.2, respectively.

Considering the strong twist-bending elastic coupling case of $\theta_h = 75^o$, the results obtained with the bending control methodology and the twist control methodology are shown in Figs. 5.7a and 5.7b, respectively. Note that, due to the strong elastic coupling, there will be no pure bending mode or twist mode for the TB-subsystem. The twist control methodology is more efficient, especially for the third mode (3TB), whose modal shape is dominated by the twist component. This is because the negative twist damping will be induced by direct bending actuation via twist-bending elastic coupling, see Fig. 5.7a.

In a nutshell, the optimal control strategy for the $\theta_h = 15^o$ case is the bending control methodology with $\theta_p \approx 120^o$, while for the $\theta_h = 75^o$ case is the twist control methodology with $\theta_p \approx 135^o$.

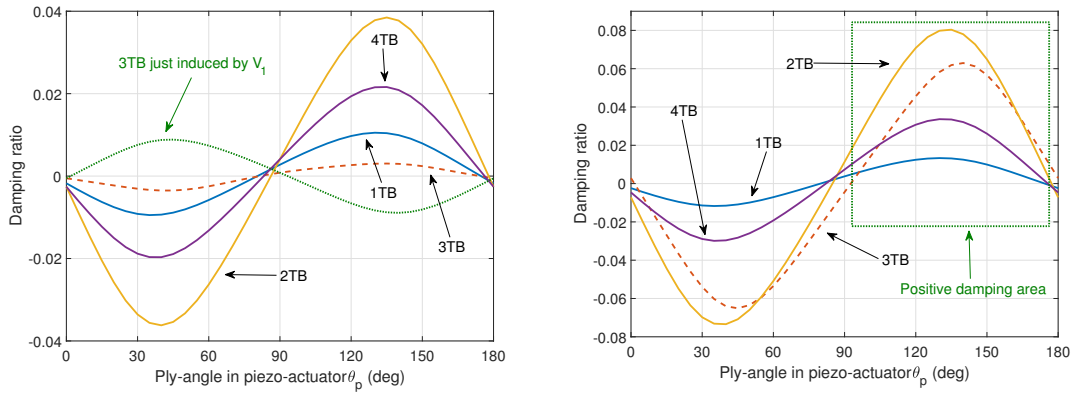

(a) *Bending control methodology* **(b)** *Twist control methodology*

Figure 5.7: *Damping ratios as a function of the piezo-composite ply-angle* θ_p*;* $k_i = 100$*,* $\theta_h = 75^o$

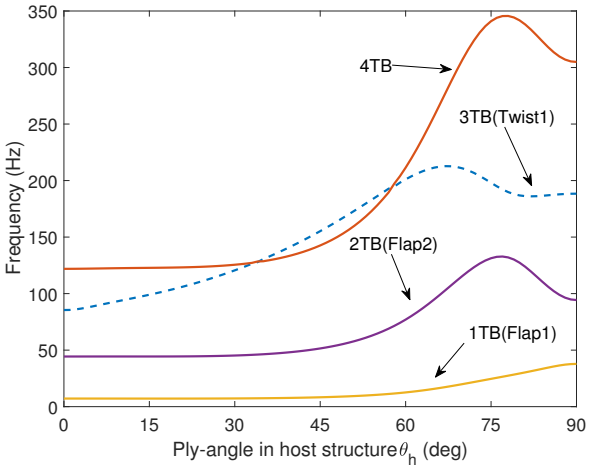

Figure 5.8: *First four modes frequencies as a function of host structure ply-angle* θ_h*;* $\theta_p = 120^o$ *and* $k_i = 100$*.*

5.6.3 Optimized by tailoring

It is clear that the twist-bending elastic coupling has a significant effect on control efficiency. Thus, in order to optimize the control performance by host structure tailoring, the effect of the ply-angle θ_h on the vibration control authority is investigated.

Figure 5.8 depicts the frequencies of the first four modes as a function of angle θ_h. A typical *mode cross* phenomenon between the third and fourth modes can be found in Fig. 5.8. In order to avoid misunderstanding in the following study, it states that the 4th mode is denoted 3TB and 3rd mode is denoted 4TB in the mode crossed range $33^o < \theta_h < 60^o$. The frequency of mode 1TB increases from $\theta_h = 0^o$ to $\theta_h = 90^o$; modes 2TB and 4TB reach their maximum frequency for $\theta_h \approx 80^o$.

In order to compare the bending and twist control methodologies, $\theta_p = 120^o$ in piezo-actuator is adopted here, since this angle allows to achieve comparable bending moment and twist authorities. The damping ratios obtained with the bending and the

twist control methodology are shown in Figs. 5.9a and 5.9b, respectively. A sudden

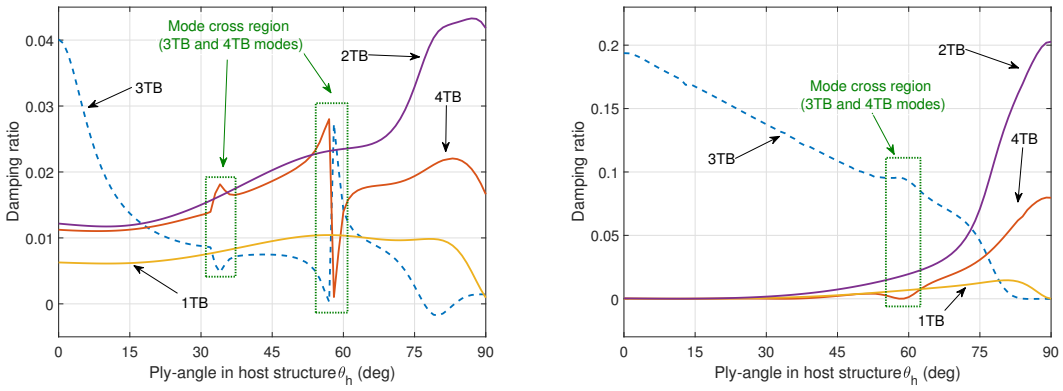

(a) *Bending control methodology* **(b)** *Twist control methodology*

Figure 5.9: *Damping ratio as a function of the host structure ply-angle θ_h; $\theta_p = 120^o$ and $k_i = 100$.*

change around the mode cross points $\theta_h \approx 33^o$ and $\theta_h \approx 58^o$ can be found in Figs. 5.9a and 5.9b. Especially near the point $\theta_h \approx 58^o$ in Fig. 5.9a, a jump phenomenon is observed. This is because near this point, not only the eigen-frequencies of the 3TB and 4TB modes are almost the same, but their mode shapes are similar as well. Outside of the mode cross regions, the damping ratios for both control methodologies increase for the 1TB, 2TB and 4TB modes, and decreases for the 3TB mode. Furthermore, for bending control methodology of Fig. 5.9a, mode 3TB has a negative damping above $\theta_h \approx 80^o$, and the damping ratios of modes 1TB, 2TB and 3TB significantly decrease near $\theta_h = 90^o$.

The absolute value of the first mode (1TB) eigenvalue real part is plotted as a function of θ_h in Fig. 5.10a. The corresponding curves for the 2TB, 3TB and 4TB modes are reported in Fig. 5.10b. The plots of Figs. 5.10a and 5.10b can be splitted into two different regions, i.e. Area 1 for $0 < \theta_h < 45^o$ and Area 2 for $69^0 < \theta_h < 87^o$; these regions are characterized by weak and strong twist-bending elastic coupling, respectively. In Area 1, the twist control methodology (red lines) has almost no flapping damping; thus, the bending control methodology (black lines) should be chosen. Within Area 2, instead, the flapping damping induced by the elastic coupling allows to achieve a damping that is higher than that of the direct flapping control; thus, the twist control methodology would be a better choice here.

5.6.4 Vibration control under an impulsive load

An impulsive load with coefficients $p_z = m_y = 1$, and $m_x = 0$ in Eqs. (5.4) is applied to the $\theta_h = 75^o$ structure. Figs. 5.11a and 5.11b depict the time responses of the tip flapping displacement $\hat{w}_0(L,t)$ and twist rotation $\hat{\phi}(L,t)$, respectively. Piezo-actuator $\theta_p = 90^o$ with bending control methodology, that was chosen in Refs. [16, 49, 86], is compared with the piezo-actuator $\theta_p = 135^o$ with twist control methodology. From the results of Figs. 5.11a and 5.11b, it can be seen that the twist control shows a significant advantage both for the flapping and twisting motions.

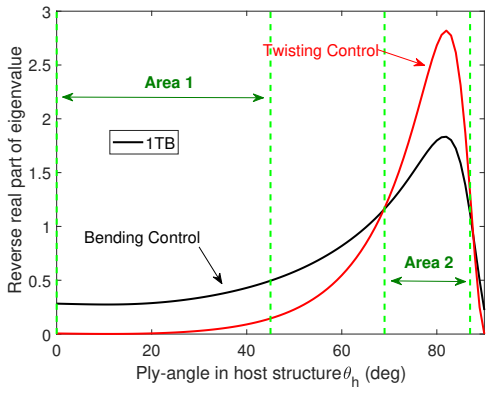

(a) *1st mode*

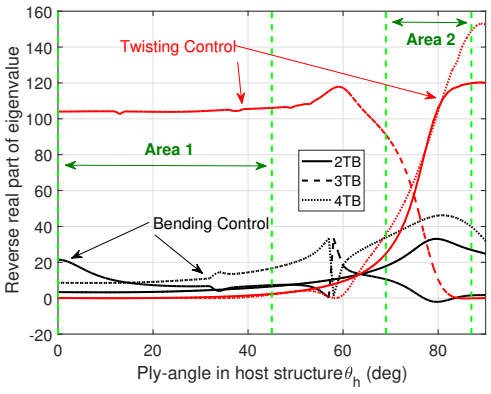

(b) *2nd,3rd and 4th modes*

Figure 5.10: *Absolute value of the real part of eigenvalue as a function of the host structure ply-angle θ_h; $\theta_p = 120^o$, $k_i = 100$.*

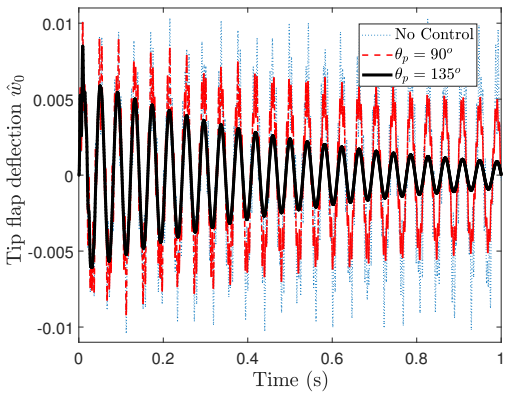

(a) *Flapping displacement $\hat{w}_0$*

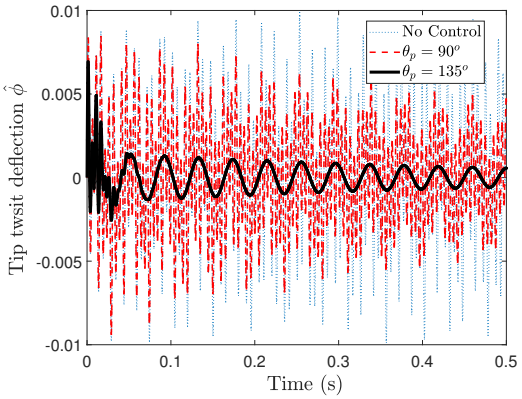

(b) *Twist rotation $\hat{\phi}$*

Figure 5.11: *Tip response in TB-subsystem ($\theta_h = 75^o$) subject to an impulse load; $k_i = 100$.*

5.6.5 The influence of position of piezo-actuator

Investigating the effect of size and position of piezo-actuators allows to strike a balance between their cost and efficiency. As reported by Librescu et al [43,46], twist-bending elastic coupling is beneficial for the aeroelastic response behavior. Thus the piezo-actuator $\theta_p = 135^o$ with twist control methodology and strong elastic coupling host structure $\theta_h = 75^o$ is considered here. The size of the piezo-actuator is first fixed at 10% of the beam span, and the sensors are applied at the outer end of the piezo-actuator, see Fig. 5.1. The resulting first four modes damping ratios are depicted in Fig. 5.12a as a function of the piezo-actuator position. When the piezo is positioned between 48% and 67% of the wing span, the 4TB mode damping is negative. A good compromise is achieved at 40% of the span. However, for a large size piezo-actuator, e.g., 70% length of span see Fig. 5.12b, the damping ratios of the first four modes are all positive. In a nutshell, the optimized position for piezo-actuator is around central point of the span.

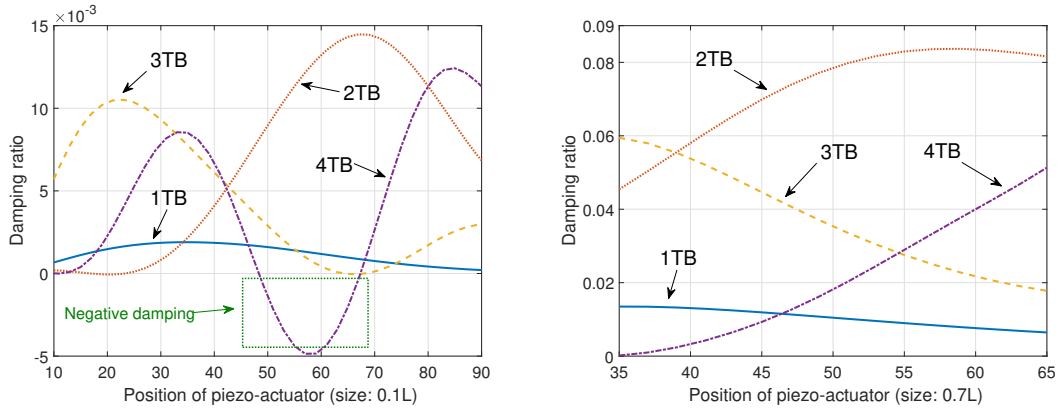

(a) *Size:* $0.1L$ **(b)** *Size:* $0.7L$

Figure 5.12: *Damping ratios as a function of the piezo-actuator position;* $\theta_h = 75^o$, $\theta_p = 135^o$, $k_i = 100$.

5.7 Dynamic control of lateral bending-extension coupling subsystem

5.7.1 Elastic coupling

Figure 5.13 depicts stiffness coefficients a_{ij} of BE-subsystem as a function of host structure ply-angle θ_h. Actually compared to the host structure stiffness, the additional stiffness of piezo-actuators is immaterial. From the results of Fig. 5.13, it can be found that, regardless of θ_h, the absolute value of extensional stiffness a_{11} is significantly greater than that of other stiffness coefficients, which implies that the idea of controlling beam system using piezoelectrically induced extension ($\tilde{T}_y$) seems unrealistic. As for bending stiffness a_{22} and transverse shear stiffness a_{44}, their maximum values exist at $\theta_h = 90^o$ and $\theta_h \approx 70^o(110^o)$, respectively.

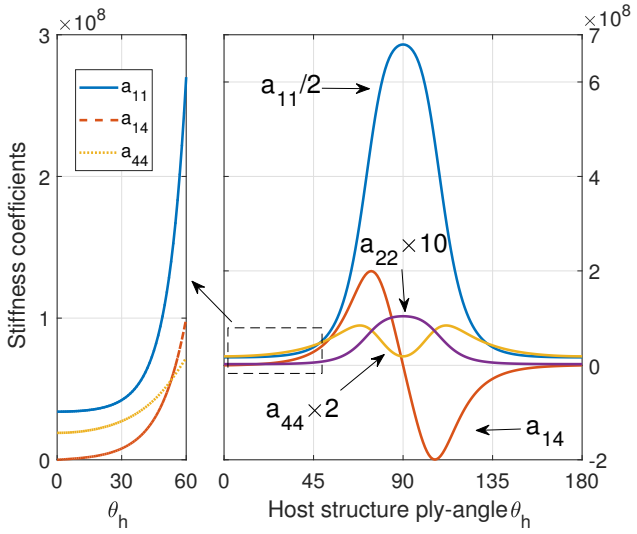

Figure 5.13: *Stiffness coefficients a_{ij} of BE-subsystem;* a_{11} (N), a_{14} (N), a_{22} ($\mathrm{N} \cdot m^{-2}$), a_{44} (N)

5.7.2 Dynamic control via velocity feedback control

In this section, damping ratios induced by piezo-actuators are studied based on the velocity feedback control. The control authorities between piezoelectric transverse shear force offered by flange-actuator-pair V_2 and piezoelectric bending moment offered by web-actuator-pair V_3 are compared. Figs. 5.14a and 5.14b illustrate damping ratios of the first three modes plotted as a function of host structure ply-angle θ_h. For bending control indicated in dashed lines, the system exhibits the expected positive damping ratios for all first three modes. Actually for the case that the piezo-actuator is spread over the entire beam span, voltage parameter V_3 will just produce a piezoelectric chordwise bending moment in the boundary conditions at the beam tip. This can also explain why the damping ratio curves (dashed lines in Figs. 5.14a and 5.14b) present the reverse variation trend as that of bending stiffness a_{22} in Fig. 5.13.

However, for transverse shear control indicated in solid lines, the system exhibits a negative damping ratio of 2nd mode in Fig. 5.14b. This means the idea of vibration suppression via transverse shear control based on the simple velocity feedback is unrealistic. This result can also be concluded in Figs. 5.15a and 5.15b, which plot damping ratios as a function of piezo-actuator ply-angle θ_p.

5.7.3 Dynamic control via LQR optimal control

Recalling Eq. (3.30), solution of Riccati equation yields the control law which depends only on the weighting coefficient η_i that making the balance on control effectiveness and energy consumption. Thus weighing coefficients for transverse shear control η_2 and bending control η_3 should be investigated firstly. Note that, host structure with ply-angle $\theta_h = 75^o$ is considered in the following numerical study, since this configuration can provide a strong twist-flapwise bending elastic couping [77, 97] that is benefit in various practical engineering applications. Relationships between weighting coefficients η_2, η_3 and system damping ratios are highlighted in Fig. 5.16. It can be found that the damping ratios decrease more and more slowly with the increase of η_i. In addition,

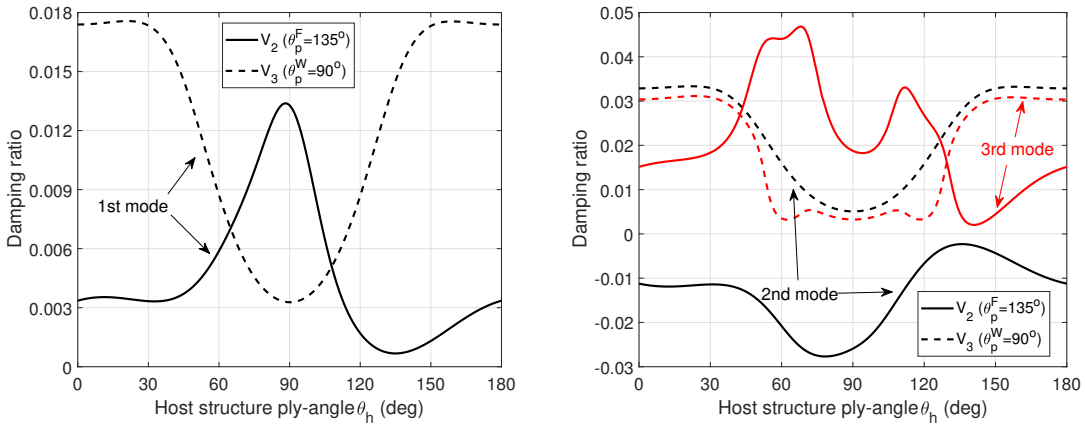

(a) *1st mode* **(b)** *2nd and 3thd modes*

Figure 5.14: *Damping ratio of the first three modes plotted as a function of host structure ply-angle* θ_h*;* $k_2 = k_3 = 1000$ V · s

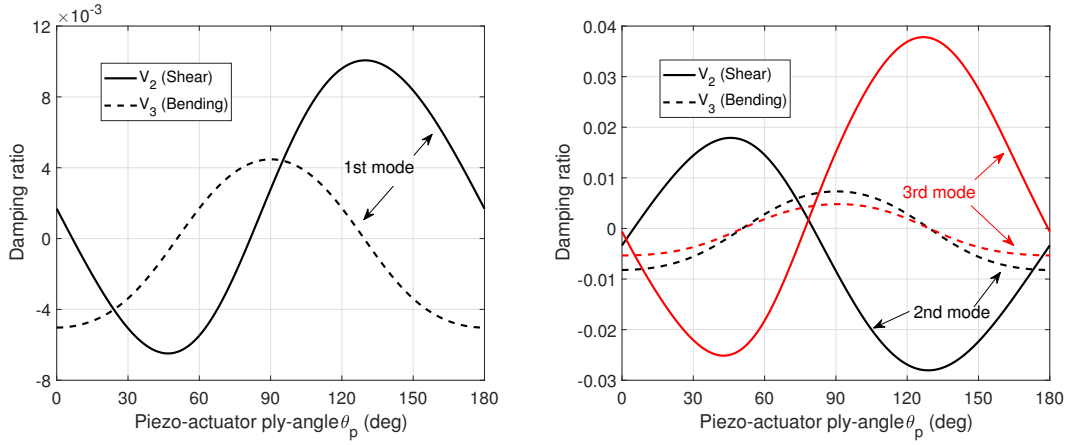

(a) *1st mode* **(b)** *2nd and 3rd modes*

Figure 5.15: *Damping ratio of the first three modes plotted as a function of piezo-actuator ply-angle* θ_p*;* $\theta_h = 75^o$*,* $k_2 = k_3 = 1000$ V · s

piezoelectric induced transverse shear force (V_2) will induce similar damping ratios for the first three modes when applying LQR control strategy. While piezoelectric bending moment (V_3) will induce greater damping ratios for lower modes.

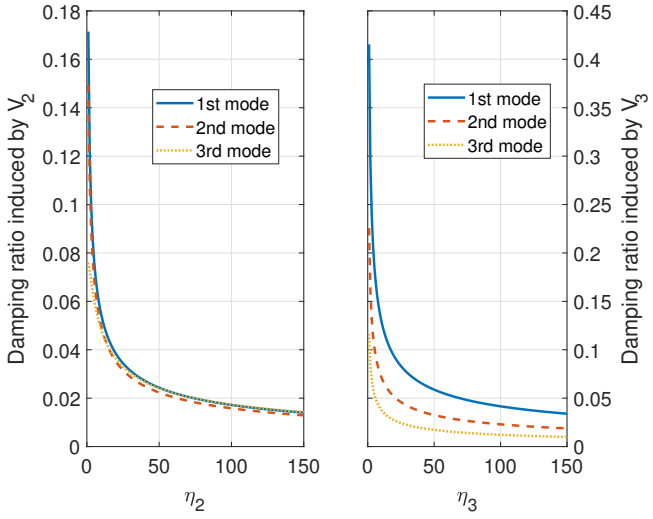

Figure 5.16: *Damping ratios of the first three modes vs. weighting coefficient η; $\theta_h = 75^o$, $\theta_p^F = 135^o$*

Figure 5.17a depicts the responses of beam tip under a lateral impulse load for selected control strategies. Note that, the first six structure modes are used in the simulation. The associated voltage time history are shown in Fig. 5.17b. It can be seen that within the same applied voltages level in Fig. 5.17b, as our expected, bending LQR optimal control (V_2) is more efficient than bending velocity feedback control, see Fig. 5.17a. Moreover, transverse shear LQR control presents a significantly better control authority than that of bending LQR control.

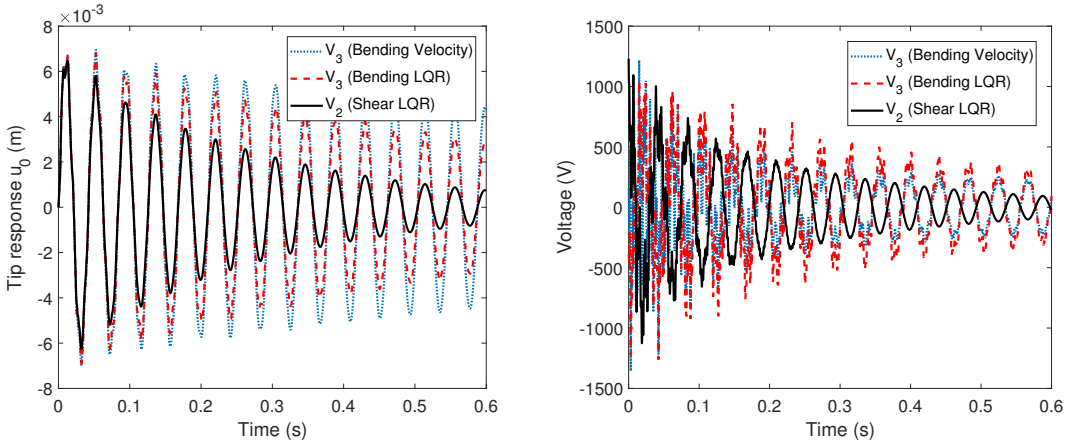

(a) *Beam tip response $u_0(L,t)$*

(b) *Voltages*

Figure 5.17: *Response time-history to a lateral impulse load; $p_x = 10\,\mathrm{N}\cdot\mathrm{m}^{-1}$, $\theta_h = 75^o$, $\theta_p^F = 135^o$, $\theta_p^W = 90^o$, $k_3 = 1000$ V·s, $\eta_2 = 50$, $\eta_3 = 2000$*

The relationships between control authority and piezo-actuator configuration on the

perspective of controller energy consumption are highlighted in Fig. 5.18, which plots damping ratios of the first three modes as a function of piezo-actuator ply-angle θ_p for the constant weighting coefficients $\eta_2 = 50$ and $\eta_3 = 2000$. Since piezoelectrically induced bending will always provide positive damping for all modes, the damping ratios presented in Fig. 5.18 are not sensitive to piezo-actuator ply-angle. On the contrary, in view of fact that transverse shear may provide positive and negative damping for different modes at the same time, additional energy will be consumed during the vibration suppression process. Thus we can observe the significant influence of piezo-actuator ply-angle on damping ratios in Fig. 5.18. Specifically, flange-actuator-pair with $\theta_p^F \approx 72^o$ or $\approx 170^o$ can produce the maximum balanced positive damping ratios. While flange-actuator-pair may lose control for the system when $\theta_p^F \approx 5^o$ and $\theta_p^F \approx 80^o$.

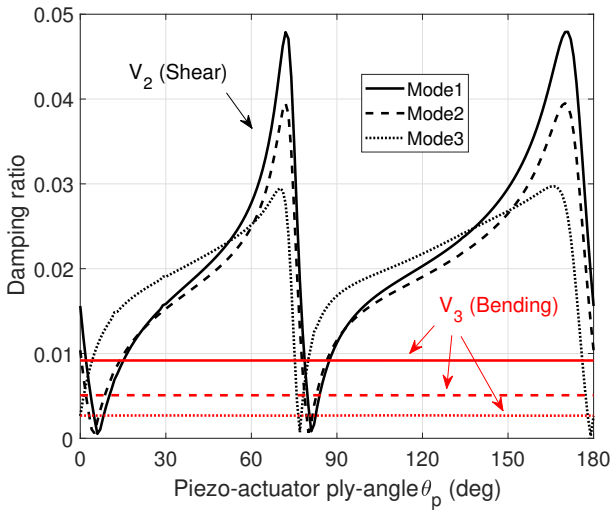

Figure 5.18: *Damping ratios of the first three modes vs. piezo-actuator ply-angle* θ_p*;* $\theta_h = 75^o$, $\eta_2 = 50$, $\eta_3 = 2000$

These results can be seen more clearly in Fig. 5.19a, which plots the beam tip response time-history under a lateral impulse load for selected flange-actuator-pair configurations. The associated voltage time-history are shown in Fig. 5.19b. On the aspect of ideal energy consumption, $\theta_p^F = 170^o$ is indeed more efficient than $\theta_p^F = 135^o$, see Fig. 5.19a. However, the average applied control voltage of $\theta_p^F = 170^o$ case is significantly greater than that of $\theta_p^F = 135^o$ case in Fig. 5.19b. This is because the maximum absolute value of transverse shear pizeo-actuator coefficient $\mathcal{A}_2^{Qx}$ exists at $\theta_p^F \approx 135^o$, see Fig. 5.2.

5.7.4 Piezo-actuator size and position study

Considering the high cost and high density of piezo-composite materials, the rational designs of piezo-actuators, such as the size and the position, should be investigated. Before discussions, the following nondimensionless parameters are defined,

$$\eta_s = \frac{L_a}{L}, \quad \eta_p = \frac{y_1}{L}, \tag{5.15}$$

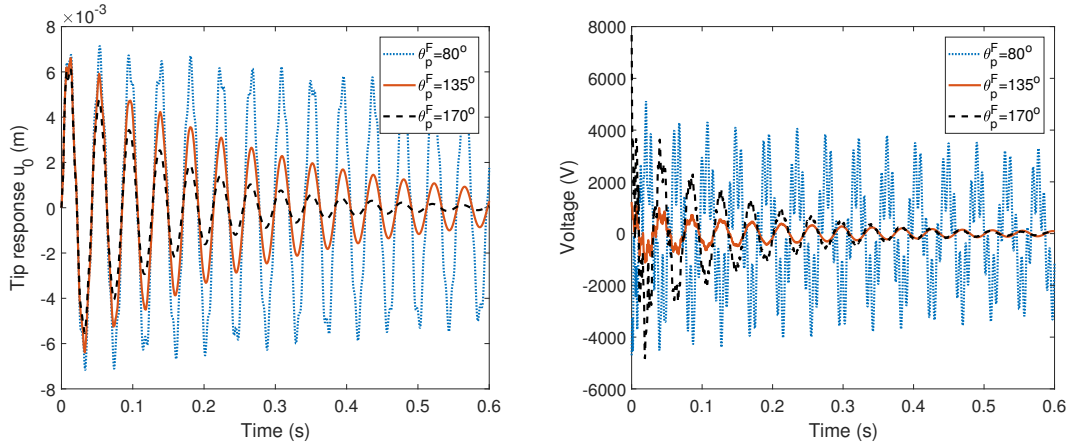

(a) *Beam tip response* $u_0(L,t)$ **(b)** *Voltages*

Figure 5.19: *Response time-history to a lateral impulse load;* $p_x = 10\,\mathrm{N}\cdot\mathrm{m}^{-1}$, $\theta_h = 75^o$, $\eta_2 = 50$

where η_s and η_p denote size and position of the piezo-actuator, see Fig. 5.1.

Since flange-actuator-pair with $\theta_p^F = 135^o$ can produce a maximum piezoelectric torque that is benefit for twist-flapwise bending coupling subsystem [97], this configuration is also adopted here for chrodwise bending-extension coupling subsystem. Figs. 5.20a and 5.20b plot damping ratios as a function of flange-actuator-pair position for small ($\eta_s = 0.3$) and large size ($\eta_s = 0.7$) cases, respectively. It can be found that damping ratio of the first mode is not sensitive to position. In general, flange-actuator-pair located near the root of the beam can produce the maximum damping ratios.

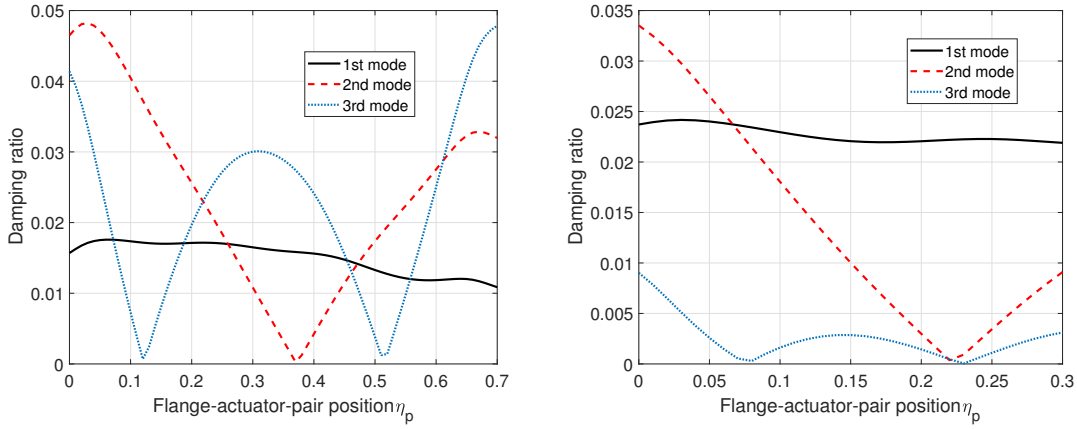

(a) *Size:* $\eta_s = 0.3$ **(b)** *Size:* $\eta_s = 0.7$

Figure 5.20: *Damping ratios of the first three modes plotted as a function of flange-actuator-pair position;* $\theta_h = 75^o$, $\theta_p^F = 135^o$, $\eta_2 = 50$

As for the web-actuator-pair, the influence of position on damping ratios are highlighted in Figs. 5.21a and 5.21b. It can be found that no matter the size of the actuator, damping ratio of the first mode decreases when the actuator position moves from beam root to the tip. In a nutshell, the ideal position for web-actuator-pair is around central

point of the span considering the balanced damping ratios for all modes.

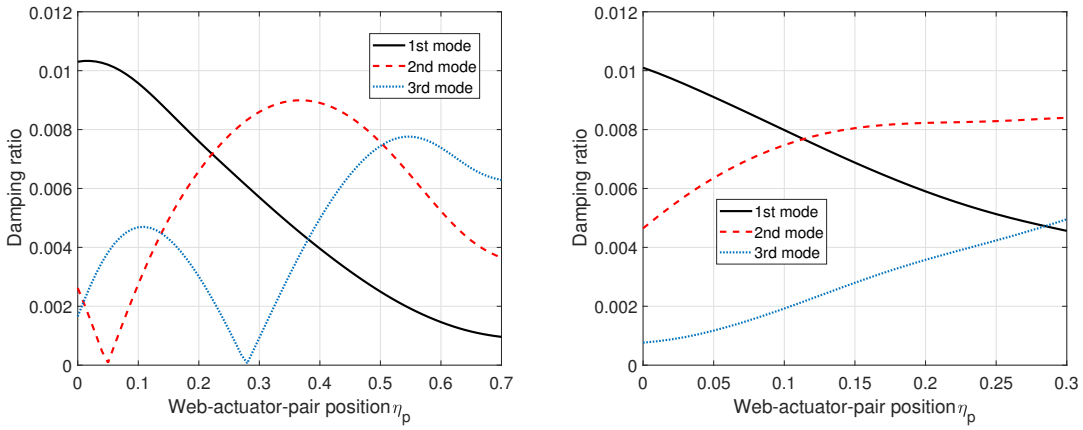

(a) *Size:* $\eta_s = 0.3$ **(b)** *Size:* $\eta_s = 0.7$

Figure 5.21: *Damping ratios of the first three modes plotted as a function of web-actuator-pair position;* $\theta_h = 75^o$, $\theta_p^W = 90^o$, $\eta_2 = 2000$

CHAPTER 6

Nonlinear Modal Interactions for Advanced Composite Aircraft Wings

6.1 Introduction

Nonlinear dynamic characteristics of a composite aircraft wing structure modeled by a geometrically nonlinear anisotropic thin-walled beam in the presence of simultaneous $1:2$ internal and $1:1$ external resonances are investigated in this chapter.

One necessary condition for the presence of modal interaction is that the linear natural frequencies ω_i are commensurate or nearly commensurate, i.e., $\sum_{i=1}^{n} k_i\omega_i \approx 0$, with k_i positive or negative integers [65, p. xvii]. For composite structures, this condition can be easily fulfilled and there may even exist numerous groups of linear modes which simultaneously fulfill this condition. As an example, for a flat sandwich panel as investigated by [80], $\omega_{21}(45.0) + \omega_{41}(133.0) = 178.0 \approx \omega_{42}(177.0)$, $\omega_{12}(69.0) + \omega_{42}(177.0) = 246.0 = \omega_{14}(246.0)$, $\omega_{22}(92.0) + \omega_{23}(169.0) = 261.0 \approx \omega_{24}(262.0)$, $2\omega_{21}(90.0) + \omega_{31}(78.0) = 168.0 \approx \omega_{23}(169.0)$, $\omega_{12}(69.0) + \omega_{32}(129.0) = 198.0 \approx \omega_{33}(199.0)$, $\omega_{21}(45.0) + \omega_{13}(152.0) = 197.0 \approx \omega_{33}(199.0)$. Although there have been extensive research work on this issue in solid structures, such as solid beam, plate, shell [53–56], in the context of aircraft composite wing structures modeled as thin-walled box beams, the issue of modal interactions has not yet been addressed.

In the present work, due to its beneficial aeroelastic response behavior, composite thin-walled box beams with geometric nonlinear deformations under circumferentially asymmetric stiffness (CAS) [46, 47] configuration is adopted to model the advanced wing structure. Bending-twist coupling induced both by the anisotropy of the constituent material and by the heavy external stores arbitrarily located along the wing span and chord is accounted as well. The equations of motion and compatible boundary conditions are derived from an extended Hamilton's principle [58, pp. 82-86]. Then, the

extended full-basis Galerkin's method [45, 70] and the method of multiple scales [64] are adopted to semi-discretize and solve the related nonlinear problems. Alternatively, the direct form with the multiple scales method [2] is also viable in the present case. As proved by Lacarbonara [41], full-basis discretization (e.g., Galerkin) approach yields the same resonant nonlinear normal modes with the direct approach. Next, based on the amplitude modulation equations, modal interactions in the presence of simultaneous internal and external resonances are analytically investigated. Actually, for the case of simultaneous $1:2$ internal and $1:1$ external resonances we considered in the present work, as demonstrated by Nayfeh [66] and Luongo [52], cubic and higher nonlinearities has no effect on the amplitude modulation equations. Finally, for the purpose of validating the preceding theoretical results, the commercial code ABAQUS [31] is used to simulate the nonlinear vibration responses of the thin-walled box beam subjected to primary-resonance excitation. The fast Fourier transform (FFT) [99] is further used for validating the preceding theoretical results.

6.2 Dynamical model

A fiber-reinforced composite thin-walled beam as shown in Fig. 6.1a is considered here to model the aircraft wing structure. In addition to the concentrate stores distributed

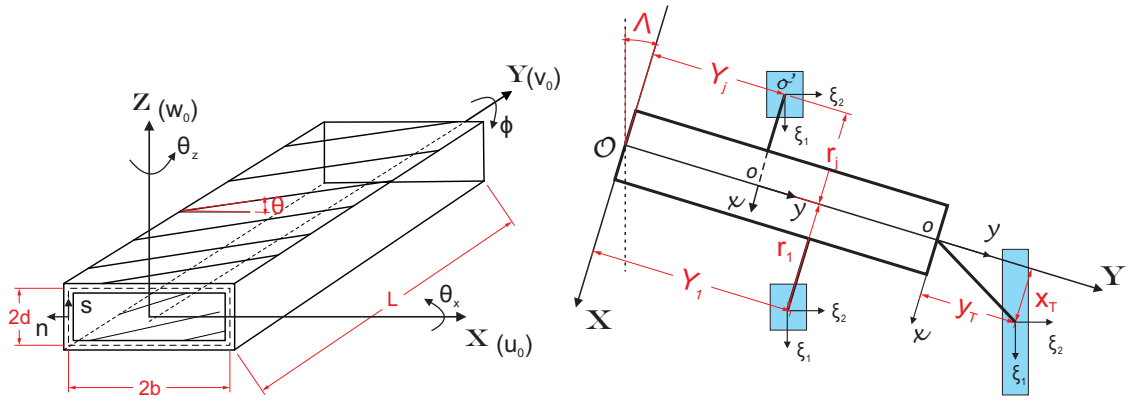

(a) *Geometry of an aircraft wing modeled as a thin-walled beam* **(b)** *A swept aircraft wing with external stores*

Figure 6.1: *Advanced aircraft wing structure model*

along the beam span, a tip store is also considered, see Fig. 6.1b. In order to describe the position of the store, besides the inertial frame $OXYZ$, another body-fixed frame $oxyz$ attached to the wing is considered, see Fig. 6.1b.

6.2.1 Kinetic energy of external stores

To derive the kinetic energy of external stores associated with the various components of the system, the centroid position of the jth external store described in the body-fixed coordinate system $oxyz$ should be expressed in terms of those of the global coordinate system $OXYZ$ via a rotation matrix $\mathbf{R}$. The expressions for the components of the rotation matrix $\mathbf{R}$ are related to the choice of technique for representing the rotation. In this investigation, an exponential of a skew-symmetric matrix $\mathbf{R} = \exp(\mathbf{\Theta})$ is

adopted [3, 74, 84]. It is reasonable to use the following truncated form of the rotation matrix [59, 73]

$$\mathbf{R} = \exp(\mathbf{\Theta}) \approx \mathbf{I} + \mathbf{\Theta} + \frac{1}{2}\mathbf{\Theta}^2, \quad \mathbf{\Theta} = \begin{bmatrix} 0 & -\theta_z & \phi \\ \theta_z & 0 & \theta_x \\ -\phi & -\theta_x & 0 \end{bmatrix}. \tag{6.1}$$

Note that the truncated rotation matrix (6.1) will characterize complete quadratic nonlinear terms induced by external stores but incomplete cubic nonlinear terms. However, only the quadratic nonlinear terms are specifically discussed in the context. As a result, the position vector $\mathbf{p}_j$ of the jth store after deformation measured from zero can be expressed as

$$\mathbf{p}_j = \begin{Bmatrix} u_0 & v_0 + Y_j & w_0 \end{Bmatrix}^T + \mathbf{R} \begin{Bmatrix} x_j & y_j & z_j \end{Bmatrix}^T, \tag{6.2}$$

in which for the span distributed store located at Y_j ($j = \overline{1, J}$), the local position components (x_j, y_j, z_j) is given as $(r_j, 0, 0)$. r_j is the chord location of the jth store, see Fig. 6.1b. As for the tip store ($Y_j = L$), (x_j, y_j, z_j) is given as $(x_T, y_T, 0)$, in which x_T and y_T denote chord and span offsets of the tip store, see Fig. 6.1b. Thus the translational kinetic energy of the stores can be expressed as:

$$T_s^{tr} = \frac{1}{2} m_T \left(\frac{\partial \mathbf{p}_T}{\partial t} \right)^2 + \sum_{j=1}^{J} \frac{1}{2} m_j \left(\frac{\partial \mathbf{p}_j}{\partial t} \right)^2, \tag{6.3}$$

where m_j and m_T denote mass of the jth span distributed store and mass of the tip store, respectively.

The external stores of the aircraft wing are usually associated with engines, fuel tanks or winglets. For the rotational kinetic energy of the external stores, described in the store attached inertial frame ($o'\xi_1\xi_2\xi_3$) (see Fig. 6.1b) can be expressed as:

$$T_s^{ro} = \frac{1}{2} \begin{Bmatrix} \Omega_1 \\ \Omega_2 \\ \Omega_3 \end{Bmatrix}^T \begin{bmatrix} I_T^{11} & 0 & 0 \\ 0 & I_T^{22} & 0 \\ 0 & 0 & I_T^{33} \end{bmatrix} \begin{Bmatrix} \Omega_1 \\ \Omega_2 \\ \Omega_3 \end{Bmatrix} + \sum_{j=1}^{J} \frac{1}{2} \begin{Bmatrix} \Omega_1 \\ \Omega_2 \\ \Omega_3 \end{Bmatrix}^T \begin{bmatrix} I_j^{11} & 0 & 0 \\ 0 & I_j^{22} & 0 \\ 0 & 0 & I_j^{33} \end{bmatrix} \begin{Bmatrix} \Omega_1 \\ \Omega_2 \\ \Omega_3 \end{Bmatrix}, \tag{6.4}$$

where I_j^{xx} and I_T^{xx} ($xx = 11, 22, 33$) are the principal moments of inertia of the jth span distributed store and of the tip store, respectively. The angular velocity components $(\Omega_1, \Omega_2, \Omega_3)$ can be computed of those of the global coordinate system $OXYZ$ as

$$\begin{Bmatrix} \Omega_1 \\ \Omega_2 \\ \Omega_3 \end{Bmatrix} = \begin{bmatrix} \cos(\Lambda) & \sin(\Lambda) & 0 \\ -\sin(\Lambda) & \cos(\Lambda) & 0 \\ 0 & 0 & 1 \end{bmatrix} \begin{Bmatrix} \dot{\theta}_1 \\ \dot{\theta}_2 \\ \dot{\theta}_3 \end{Bmatrix}, \tag{6.5}$$

where Λ is the sweep angle (positive backward), see Fig. 6.1b. The angular velocities $\{\dot{\theta}_1 \ \dot{\theta}_2 \ \dot{\theta}_3\}^T$ can be obtained from the truncated form of rotation matrix in Eq. (6.1) as [34, 59]

$$\begin{Bmatrix} \dot{\theta}_1 \\ \dot{\theta}_2 \\ \dot{\theta}_3 \end{Bmatrix} \approx [\mathbf{I} + \frac{1}{2}\mathbf{\Theta}] \begin{Bmatrix} -\dot{\theta}_x \\ \dot{\phi} \\ \dot{\theta}_z \end{Bmatrix}. \tag{6.6}$$

6.2.2 Governing equations and boundary conditions

In order to formulate the equations of motion, Hamilton's principle [58, pp. 82-86] is applied. The true path of motion renders the following variational form stationary:

$$\int_{t_1}^{t_2} \left(\delta T_b + \delta T_s^{tr} + \delta T_s^{ro} + \delta V_b - \overline{\delta W_e}\right) \mathrm{d}\, t = 0, \tag{6.7a}$$

with

$$\delta u_0 = \delta v_0 = \delta w_0 = \delta\theta_x = \delta\theta_z = \delta\phi = 0 \quad \text{at} \quad t = t_1, t_2, \tag{6.7b}$$

where T_b and V_b denote the kinetic energy and strain energy of the clear wing, respectively; while $\overline{\delta W_e}$ stands for the virtual work due to the external forces. Their explicit expressions can be known in Ref. [98]. After lengthy manipulations and collecting the terms associated with the same displacement variation, the governing equations expressed in terms of the basic unknowns, are:

$$\begin{aligned}\delta u_0 \ : & \, a_{14}v_0'' + a_{44}(u_0'' + \theta_z') - \sum_{j=1}^{J} \delta_D(y - Y_j) m_j \ddot{u}_0 + \underline{\left[N_u^2 + N_u^3\right]' - \bar{E}_u^2 - \bar{E}_u^3 + \mathcal{O}_u^4} \\ & + p_x - b_1 \ddot{u}_0 = 0,\end{aligned} \tag{6.8a}$$

$$\begin{aligned}\delta v_0 \ : & \, a_{11}v_0'' + a_{14}(u_0'' + \theta_z') - \sum_{j=1}^{J} \delta_D(y - Y_j) m_j (\ddot{v}_0 + r_j \ddot{\theta}_z) \\ & + \underline{\left[N_v^2 + N_v^3\right]' - \bar{E}_v^2 - \bar{E}_v^3 + \mathcal{O}_v^4} + p_y - b_1 \ddot{v}_0 = 0,\end{aligned} \tag{6.8b}$$

$$\begin{aligned}\delta w_0 \ : & \, a_{55}(w_0'' + \theta_x') - \sum_{j=1}^{J} \delta_D(y - Y_j) m_j (\ddot{w}_0 - r_j \ddot{\phi}) \\ & \underline{\left[N_w^2 + N_w^3\right]' - \bar{E}_w^2 - \bar{E}_w^3 + \mathcal{O}_w^4} + p_z - b_1 \ddot{w}_0 = 0,\end{aligned} \tag{6.8c}$$

$$\begin{aligned}\delta\phi \ : & \, a_{37}\theta_x'' + a_{77}\phi'' - a_{66}\phi^{(iv)} + \underline{\left[N_\phi^2 + N_\phi^3\right]' - \bar{E}_\phi^2 - \bar{E}_\phi^3 + \bar{N}_\phi^2 + \bar{N}_\phi^3 + \mathcal{O}_\phi^4} \\ & + m_y + b_w' - (b_4 + b_5)\ddot{\phi} + b_{10}\ddot{\phi}'' - \sum_{j=1}^{J} \delta_D(y - Y_j) \Big\{ m_j(-r_j \ddot{w}_0 + {r_j}^2 \ddot{\phi}) \\ & + \left[(I_j^{11}\sin^2\Lambda + I_j^{22}\cos^2\Lambda)\ddot{\phi} + (I_j^{22} - I_j^{11})\sin\Lambda\cos\Lambda\ddot{\theta}_x\right] \Big\} = 0,\end{aligned} \tag{6.8d}$$

$$\begin{aligned}\delta\theta_x \ : & \, a_{33}\theta_x'' + a_{37}\phi'' - a_{55}(w_0' + \theta_x) + \underline{\left[N_x^2 + N_x^3\right]' + \bar{N}_x^2 + \bar{N}_x^3 - \bar{E}_x^2 - \bar{E}_x^3 + \mathcal{O}_x^4} \\ & - \sum_{j=1}^{J} \delta_D(y - Y_j) \Big\{ \left[(I_j^{11}\cos^2\Lambda + I_j^{22}\sin^2\Lambda)\ddot{\theta}_x + (I_j^{22} - I_j^{11})\sin\Lambda\cos\Lambda\ddot{\phi}\right] \Big\} \\ & + m_x - b_4 \ddot{\theta}_x = 0,\end{aligned} \tag{6.8e}$$

$$\delta\theta_z : a_{22}\theta_z'' - a_{14}v_0' - a_{44}(u_0' + \theta_z) + \underline{\left[N_z^2 + N_z^3\right]' + \bar{N}_z^2 + \bar{N}_z^3 - \bar{E}_z^2 - \bar{E}_z^3 + \mathcal{O}_z^4} + m_z - b_5\ddot{\theta}_z - \sum_{j=1}^{J}\delta_D(y - Y_j)\Big\{m_j\left[r_j\ddot{v}_0 + {r_j}^2\ddot{\theta}_z\right] + I_j^{33}\ddot{\theta}_z\Big\} = 0, \tag{6.8f}$$

and the associate boundary conditions can be given as:
at $y = 0$,

$$u_0 = v_0 = w_0 = \phi = \phi' = \theta_x = \theta_z = 0, \tag{6.9}$$

at $y = L$,

$$\delta u_0 : a_{14}v_0' + a_{44}(u_0' + \theta_z) + m_M(\ddot{u}_0 - y_T\ddot{\theta}_z) + \underline{E_u^2 + N_u^2 + E_u^3 + N_u^3 + \mathcal{O}_u^4} = 0, \tag{6.10a}$$

$$\delta v_0 : a_{11}v_0' + a_{14}(u_0' + \theta_z) + m_T(\ddot{v}_0 + x_T\ddot{\theta}_z) + \underline{E_v^2 + N_v^2 + E_v^3 + N_v^3 + \mathcal{O}_v^4} = 0, \tag{6.10b}$$

$$\delta w_0 : a_{55}(w_0' + \theta_x) + m_T(\ddot{w}_0 - x_T\ddot{\phi} - y_T\ddot{\theta}_x) + \underline{E_w^2 + N_w^2 + E_w^3 + N_w^3 + \mathcal{O}_w^4} = 0, \tag{6.10c}$$

$$\begin{aligned}\delta\phi : {} & a_{37}\theta_x' + a_{77}\phi' - a_{66}\phi''' + m_T(-x_T\ddot{w}_0 + {x_T}^2\ddot{\phi} + x_T y_T\ddot{\theta}_x) \\ & + (I_T^{11}\sin^2\Lambda + I_T^{22}\cos^2\Lambda)\ddot{\phi} + (I_T^{22} - I_T^{11})\sin\Lambda\cos\Lambda\ddot{\theta}_x \\ & + \underline{E_\phi^2 + N_\phi^2 + E_\phi^3 + N_\phi^3 + \mathcal{O}_\phi^4} = 0,\end{aligned} \tag{6.10d}$$

$$\begin{aligned}\delta\theta_x : {} & a_{33}\theta_x' + a_{37}\phi' + m_T(-y_T\ddot{w}_0 + x_T y_T\ddot{\phi} + {y_T}^2\ddot{\theta}_x) + (I_T^{11}\cos^2\Lambda + I_T^{22}\sin^2\Lambda)\ddot{\theta}_x \\ & + (I_T^{22} - I_T^{11})\sin\Lambda\cos\Lambda\ddot{\phi} + \underline{E_x^2 + N_x^2 + E_x^3 + N_x^3 + \mathcal{O}_x^4} = 0,\end{aligned} \tag{6.10e}$$

$$\delta\theta_z : a_{22}\theta_z' + m_T(-y_T\ddot{u}_0 + x_T\ddot{v}_0 + {y_T}^2\ddot{\theta}_z) + I_T^{33}\ddot{\theta}_z + \underline{E_z^2 + N_z^2 + E_z^3 + N_z^3 + \mathcal{O}_z^4} = 0, \tag{6.10f}$$

In these equations, the a_{ij} and b_{ij} terms are associated with 1-D stiffness and mass terms of the clean wing, and their expressions can be found in the appendix of Ref. [98]. In Eqs. (6.8), p_x, p_y, p_z are the external forces per unit span; b_w is the bimoment of the surface tractions; m_x, m_y, m_z are the moments about $x-$, $y-$, $z-$axis, respectively; $(N_i^2, \bar{N}_i^2)$ and $(N_i^3, \bar{N}_i^3)$ $(i = u, v, w, \phi, x, z)$ are quadratic and cubic nonlinear terms that only related to the wing structure. Terms $\bar{E}_i^2$ and $\bar{E}_i^3$ $(i = u, v, w, \phi, x, z)$ appearing in the governing equations (6.8) denote the quadratic and cubic nonlinear terms induced by all J span distributed stores. While E_i^2 and E_i^3 that in the boundary conditions (6.10) denote the quadratic and cubic nonlinear terms induced by the tip store. The expressions of quadratic nonlinear terms are reported in appendix A.9.

6.3 Nonlinear analysis

6.3.1 Discretization via the Extended Galerkin's Method

For nonlinear dynamic analysis, the spatial discretization based on the Extended Galerkin Method (EGM) [45, 70] is implemented. Thus, the discretized nonlinear equations of

motion for wing-store system can be written as

$$[\mathbf{M}+\mathbf{E}]\{\ddot{\mathbf{q}}\}+[\mathbf{K}]\{\mathbf{q}\}+\{\mathbf{N}^2\}+\{\mathbf{N}^3\}+\{\mathbf{E}^2\}+\{\mathbf{E}^3\}+\{\mathcal{O}^4\}=\{\mathbf{Q}\}, \quad (6.11)$$

where

$$\mathbf{q}=\left\{\begin{array}{cccccc}\mathbf{q}_u^T & \mathbf{q}_v^T & \mathbf{q}_w^T & \mathbf{q}_\phi^T & \mathbf{q}_x^T & \mathbf{q}_z^T\end{array}\right\}^T, \quad (6.12)$$

and $\mathbf{M}$, $\mathbf{E}$, $\mathbf{K}$, $\mathbf{Q}$ denote mass matrix of wing, mass matrix of all stores, stiffness matrix and external excitation vector, respectively. Their expressions are shown in appendix A.10. $\mathbf{N}^2$, $\mathbf{N}^3$ are the vectors of wing structure nonlinearities, while $\mathbf{E}^2$ and $\mathbf{E}^3$ are the vectors of nonlinearities induced by all external stores. $\mathcal{O}^4$ stands for the higher order nonlinear terms.

6.3.2 Analytical solution via the multiscale method

We follow the procedure in Ref. [67] and seek a first-order uniform expansion by using the method of multiple scales in the form

$$\mathbf{q}=\varepsilon\mathbf{q_1}(T_0,T_1,...)+\varepsilon^2\mathbf{q_2}(T_0,T_1,...)+\varepsilon^3\mathbf{q_3}(T_0,T_1,...)+\cdots \quad (6.13)$$

where ε is a small, dimensionless parameter related to the amplitudes and $T_n=\varepsilon^n t$. Furthermore, we introduce the external harmonic excitation matrix $\mathbf{F}$ and the Rayleigh damping matrix $\mathbf{C}_R$ [51, 92] into the system. Meanwhile we order these two matrices so that the effects of the external excitation, the damping and the nonlinearity appear in the same perturbation equations. Thus we let

$$\{\mathbf{F}\}=-2\varepsilon^2\{\mathbf{Q}\}\cos\Omega t, \quad [\mathbf{C}_R]=2\varepsilon\mu[\mathbf{M}+\mathbf{E}], \quad (6.14)$$

where Ω denotes the frequency of the external excitation. Substituting Eqs. (6.13) and (6.14) into Eq. (6.11) and collecting all terms of order ε, we obtain
On scale $O(\varepsilon)$

$$[\mathbf{M}+\mathbf{E}]\{\frac{\partial^2\mathbf{q}_1}{\partial T_0^2}\}+[\mathbf{K}]\{\mathbf{q}_1\}=\mathbf{0}, \quad (6.15)$$

On scale $O(\varepsilon^2)$

$$\begin{aligned}[\mathbf{M}+\mathbf{E}]\{\frac{\partial^2\mathbf{q}_2}{\partial T_0^2}\}+[\mathbf{K}]\{\mathbf{q}_2\}=&-2[\mathbf{M}+\mathbf{E}]\{\frac{\partial^2\mathbf{q}_1}{\partial T_0\partial T_1}\}-2\mu[\mathbf{M}+\mathbf{E}]\{\frac{\partial\mathbf{q}_1}{\partial T_0}\}\\&-\{\mathbf{N}^2(\mathbf{q}_1,\mathbf{q}_1)\}-\{\mathbf{E}^2(\dot{\mathbf{q}}_1,\dot{\mathbf{q}}_1)\}-\{\mathbf{E}^2(\mathbf{q}_1,\ddot{\mathbf{q}}_1)\}-2\{\mathbf{Q}\}\cos\Omega t,\end{aligned} \quad (6.16)$$

On scale $O(\varepsilon^3)$

$$\begin{aligned}[\mathbf{M}+\mathbf{E}]\{\frac{\partial^2\mathbf{q}_3}{\partial T_0^2}\}+[\mathbf{K}]\{\mathbf{q}_3\}=&-[\mathbf{M}+\mathbf{E}]\{\frac{2\partial^2\mathbf{q}_1}{\partial T_0\partial T_1}+\frac{\partial^2\mathbf{q}_1}{\partial^2 T_1}\}-[\mathbf{M}+\mathbf{E}]\{\frac{2\partial^2\mathbf{q}_2}{\partial T_0\partial T_1}\}\\&-2\mu[\mathbf{M}+\mathbf{E}]\{\frac{\partial\mathbf{q}_1}{\partial T_1}+\frac{\partial\mathbf{q}_2}{\partial T_0}\}-\{\mathbf{N}^2(\mathbf{q}_1,\mathbf{q}_2)\}\\&-\{\mathbf{N}^3(\mathbf{q}_1,\mathbf{q}_1,\mathbf{q}_1)\}-\{\mathbf{E}^2(\dot{\mathbf{q}}_1,\dot{\mathbf{q}}_2)\}-\{\mathbf{E}^2(\mathbf{q}_1,\ddot{\mathbf{q}}_2)\}\\&-\{\mathbf{E}^2(\ddot{\mathbf{q}}_1,\mathbf{q}_2)\}-\{\mathbf{E}^3(\mathbf{q}_1,\dot{\mathbf{q}}_1,\dot{\mathbf{q}}_1)\}-\{\mathbf{E}^3(\mathbf{q}_1,\mathbf{q}_1,\ddot{\mathbf{q}}_1)\}.\end{aligned} \quad (6.17)$$

The solution to the first-order perturbation Eq. (6.15) can be written in the form [52, 66]:

$$\mathbf{q}_1 = \sum_{n=1}^{\infty} \left\{ A_n(T_1)\mathbf{V}_n e^{i\omega_n T_0} + \bar{A}_n(T_1)\mathbf{V}_n e^{-i\omega_n T_0} \right\}, \tag{6.18}$$

in which, A_n and $\mathbf{V}_n$ denote the amplitude and the eigenvector of the nth mode. Replacing the first-order solution form Eq. (6.18) into Eq. (6.16) leads to

$$\begin{aligned}
[\mathbf{M}+\mathbf{E}]\{\frac{\partial^2 \mathbf{q}_2}{\partial T_0^2}\} + [\mathbf{K}]\{\mathbf{q}_2\} &= -2\{\mathbf{Q}\}\cos\Omega t \\
-2[\mathbf{M}+\mathbf{E}]\sum_{p=1}^{\infty}\mathbf{V}_p(i\omega_p)\Big\{\frac{\partial A_p}{\partial T_1}e^{i\omega_p T_0} - \frac{\partial \bar{A}_p}{\partial T_1}e^{-i\omega_p T_0}\Big\} & \\
-2\mu[\mathbf{M}+\mathbf{E}]\sum_{p=1}^{\infty}\mathbf{V}_p(i\omega_p)\Big\{A_p e^{i\omega_p T_0} - \bar{A}_p e^{-i\omega_p T_0}\Big\} & \\
-\sum_{n=1}^{\infty}\sum_{m=1}^{\infty}[\mathbf{N}_{nm} - {\omega_m}^2\mathbf{E}_{nm}]\Big\{A_n A_m e^{i(\omega_n+\omega_m)T_0} + A_n\bar{A}_m e^{i(\omega_n-\omega_m)T_0} & \\
+\bar{A}_n A_m e^{i(-\omega_n+\omega_m)T_0} + \bar{A}_n\bar{A}_m e^{-i(\omega_n+\omega_m)T_0}\Big\} & \\
-\sum_{n=1}^{\infty}\sum_{m=1}^{\infty}[-\omega_m\omega_n\hat{\mathbf{E}}_{nm}]\Big\{A_n A_m e^{i(\omega_n+\omega_m)T_0} - A_n\bar{A}_m e^{i(\omega_n-\omega_m)T_0} & \\
-\bar{A}_n A_m e^{i(-\omega_n+\omega_m)T_0} + \bar{A}_n\bar{A}_m e^{-i(\omega_n+\omega_m)T_0}\Big\}, &
\end{aligned} \tag{6.19}$$

where the quadratic nonlinear matrices $\mathbf{N}_{nm}$, $\mathbf{E}_{nm}$ and $\hat{\mathbf{E}}_{nm}$ are defined in appendix A.10. For eliminating the possible secular terms in Eq. (6.19), the extra internal resonance link connecting $\mathbf{q}_2$ may exist when $\omega_p \approx \omega_m \pm \omega_n$. Furthermore, if we go to the third scale (related to Eq. (6.17)) to check an internal resonance, on can find an internal resonance combination $\omega_p \approx \omega_m \pm \omega_n \pm \omega_l$. It becomes apparent that $1:1$, $1:2$ and $1:3$ internal resonances are the special cases of the preceding combinations when $n = l$, $m = n$, and $m = n = l$.

6.4 The internal resonance case: $\omega_p \approx 2\omega_m$

At first, modal interactions in the presence of $1:2$ internal resonance for the clean wing structure is investigated, i.e., we consider the internal resonance when $\omega_p \approx 2\omega_m$ as a case study. We introduce the internal and external resonance detuning parameters σ_1 and σ_2 [42, 90]

$$\omega_p = 2\omega_m + \varepsilon\sigma_1, \quad \Omega = \omega_i + \varepsilon\sigma_2, \tag{6.20}$$

where Ω denotes the frequency of the external excitation, while ω denotes the natural frequency of the beam.

6.4.1 When the external energy input from the pth mode, Ω near ω_p.

In such a case, by dropping the terms related to external stores, the solvability conditions of Eq. (6.19) are

$$i\frac{\mathrm{d}\,A_p}{\mathrm{d}\,T_1} + N_p A_m A_m e^{-i\sigma_1 T_1} + i\mu A_p + F_p \cos\Omega t e^{-i\omega_p T_0} = 0, \tag{6.21a}$$

$$i\frac{\mathrm{d}\,A_m}{\mathrm{d}\,T_1} + N_m A_p \bar{A}_m e^{i\sigma_1 T_1} + i\mu A_m = 0, \tag{6.21b}$$

in which the nonlinear coefficients N_p, N_m and the external excitation coefficient F_p (or F_m) are defined as

$$N_p = \frac{(\mathbf{N}_{mm}{}^T)\mathbf{V}_p}{\omega_p \mathbf{V}_p{}^T \mathbf{M}^T \mathbf{V}_p}, \quad N_m = \frac{(\mathbf{N}_{mp}{}^T + \mathbf{N}_{pm}{}^T)\mathbf{V}_m}{2\omega_m \mathbf{V}_m{}^T \mathbf{M}^T \mathbf{V}_m}, \tag{6.22}$$

$$F_p = \frac{\mathbf{Q}^T \mathbf{V}_p}{2\omega_p \mathbf{V}_p{}^T \mathbf{M}^T \mathbf{V}_p}, \quad F_m = \frac{\mathbf{Q}^T \mathbf{V}_m}{2\omega_m \mathbf{V}_m{}^T \mathbf{M}^T \mathbf{V}_m}. \tag{6.23}$$

We introduce the polar notations for the amplitudes as

$$A_p(T_1) = \alpha_p(T_1) e^{i\beta_p(T_1)}, \quad A_m(T_1) = \alpha_m(T_1) e^{i\beta_m(T_1)}, \tag{6.24}$$

substituting Eq. (6.24) into Eqs. (6.21a-b), separating real and imaginary parts of the resulting equations, and after some manipulations, we obtain the following differential equations:

$$\dot{\alpha}_p = -N_p {\alpha_m}^2 \sin\gamma - \mu\alpha_p - F_p \sin\xi, \tag{6.25a}$$

$$\alpha_p \dot{\beta}_p = N_p {\alpha_m}^2 \cos\gamma + F_p \cos\xi, \tag{6.25b}$$

$$\dot{\alpha}_m = N_m \alpha_p \alpha_m \sin\gamma - \mu\alpha_m, \tag{6.25c}$$

$$\alpha_m \dot{\beta}_m = N_m \alpha_p \alpha_m \cos\gamma, \tag{6.25d}$$

where

$$\gamma = 2\beta_m - \sigma_1 T_1 - \beta_p, \quad \xi = \sigma_2 T_1 - \beta_i. \tag{6.26}$$

Steady-state solution

The steady-state motions occur when $\dot{\alpha}_p = \dot{\alpha}_m = 0$, $\dot{\gamma} = 0$ and $\dot{\xi} = 0$, which correspond to the fixed points solution of Eqs. (6.25) and (6.26). It can be found that there are two kinds of fixed points:
(1) $\alpha_p \neq 0$ and $\alpha_m = 0$,

$${\alpha_p}^2 = \frac{{F_p}^2}{\mu^2 + {\sigma_2}^2}, \tag{6.27}$$

(2) $\alpha_p \neq 0$ and $\alpha_m \neq 0$,

$${\alpha_p}^2 = \frac{(\sigma_1 + \sigma_2)^2 + 4\mu^2}{4{N_m}^2}, \tag{6.28}$$

while α_m is the solution of the following equation

$${N_p}^2 {\alpha_m}^4 + \frac{N_p}{N_m}[2\mu^2 - \sigma_2(\sigma_1 + \sigma_2)]{\alpha_m}^2 + {\alpha_p}^2(\mu^2 + {\sigma_2}^2) - {F_p}^2 = 0. \tag{6.29}$$

For solution (1), the primary (external) resonance plays a dominant role and the internal resonance can be ignored. No energy transfer between modes occur and the response of the system is governed by the directly excited pth mode only. This agrees with the solution of the corresponding linear system.

In solution (2), the amplitude of the primary resonance mode α_p is independent of external excitation F_P. For further discussion, at first we define two critical values of F_p, namely, f_p^{c1} and f_p^{c2}

$$\left[f_p^{c1}\right]^2 = \left[\frac{\mu(3\sigma_2+\sigma_1)}{2N_m}\right]^2, \quad \left[f_p^{c2}\right]^2 = \frac{(\sigma_1+\sigma_2)^2+4\mu^2}{4{N_m}^2}\left(\mu^2+{\sigma_2}^2\right). \tag{6.30a}$$

Clearly, $|f_p^{c2}|$ must be greater than $|f_p^{c1}|$. Similarly, we also define two critical values of σ_2, namely, σ_2^{c1} and σ_2^{c2}, which are governed by

$$\left[\mu(3\sigma_2^{c1}+\sigma_1)\right]^2 = \left[2F_pN_m\right]^2, \tag{6.31}$$

and

$$\left[(\sigma_2^{c2}+\sigma_1)^2+4\mu^2\right]\left[(\sigma_2^{c2})^2+\mu^2\right] = \left[2F_pN_m\right]^2. \tag{6.32}$$

Next we determine when the roots ${\alpha_m}^2$ of Eq. (6.29) are real. If the parameter Γ is no less than 0, i.e.,

$$\Gamma = \frac{N_p}{N_m}[2\mu^2-\sigma_2(\sigma_1+\sigma_2)] \geqslant 0, \tag{6.33}$$

one real solution ${\alpha_m}^2$ exists when $|F_P| \geqslant |f_p^{c2}|$. Otherwise there is no real solution. If the parameter Γ is negative, two real solutions ${\alpha_m}^2$ exist when $|F_P| < |f_p^{c2}|$, and one real solution ${\alpha_m}^2$ exists when $|F_P| \geqslant |f_p^{c2}|$. We note that when the detunings of internal and external resonance are both small, the sign of the parameter Γ is just determined by the sign of N_p/N_m.

Stability analysis

The stability of steady-state solutions can be determined by the eigenvalues of the linearized coefficients matrix of the system (Jacobian matrix) near the corresponding steady-state solution. If the real part of each eigenvalue of the coefficient matrix is not positive, then the corresponding steady-state solution is stable, otherwise is unstable. Consequently [66], the stability of steady-state solutions can be summarized as:

1. When $|F_p| < |f_p^{c1}|$, the stable response must be given by (6.27), which agrees with the linear solution of the system.

2. When Γ is negative and $|f_p^{c1}| \leqslant |F_p| \leqslant |f_p^{c2}|$, the response given by the linear system (6.27) and the response given by the greater one of the two possibilities predicted by (6.28) and (6.29) are both stable. Jump phenomenon can be observed in this case.

3. When $|F_p| > |f_p^{c2}|$, the stable response is given by (6.28) and (6.29). Saturation phenomenon can be observed in this case.

6.4.2 When the external energy input from the mth mode, Ω near ω_m.

Similarly to (6.25) and (6.26), we can obtain the following differential equations:

$$\dot{\alpha}_p = -N_p {\alpha_m}^2 \sin\gamma - \mu\alpha_p, \tag{6.34a}$$

$$\alpha_p \dot{\beta}_p = N_p {\alpha_m}^2 \cos\gamma, \tag{6.34b}$$

$$\dot{\alpha}_m = N_m \alpha_p \alpha_m \sin\gamma - \mu\alpha_m - F_m \sin\xi, \tag{6.34c}$$

$$\alpha_m \dot{\beta}_m = N_m \alpha_p \alpha_m \cos\gamma + F_m \cos\xi, \tag{6.34d}$$

where

$$\gamma = 2\beta_m - \sigma_1 T_1 - \beta_p, \quad \xi = \sigma_2 T_1 - \beta_i. \tag{6.35}$$

Steady-state solution

In this case, only one steady-state solution exists ($\alpha_p \neq 0$ and $\alpha_m \neq 0$),

$${\alpha_p}^2 = \frac{{N_p}^2}{\mu^2 + (2\sigma_2 - \sigma_1)^2} {\alpha_m}^4, \tag{6.36}$$

while α_m is the solution of the following equation

$$\frac{{N_m}^2 {N_p}^2 {\alpha_m}^6}{\mu^2 + (2\sigma_2 - \sigma_1)^2} + \frac{2\left[\mu^2 - \sigma_2(2\sigma_2 - \sigma_1)\right] N_m N_p {\alpha_m}^4}{\mu^2 + (2\sigma_2 - \sigma_1)^2} + (\mu^2 + {\sigma_2}^2){\alpha_m}^2 - {F_m}^2 = 0. \tag{6.37}$$

According to the discriminant of the cubic equations, the roots ${\alpha_m}^2$ of Eq. (6.37) may have one or three real solutions. Indeed, only one real solution exists when F_m is beyond a critical value, and normally this critical value is zero, which means three real solutions may rarely exist.

Stability analysis

Similarly, the stability of the steady-state solutions is determined by the eigenvalues of the corresponding Jacobian matrix.Then for the steady-state solution, Jacobian matrix can be simplified as

$$\mathbf{J} = \begin{bmatrix} -\mu & \dfrac{2\mu\alpha_p}{\alpha_m} & -(2\sigma_2 - \sigma_1)\alpha_p & 0 \\ -\dfrac{\mu N_m \alpha_p}{N_p \alpha_m} & -\mu + J_{43} & J_{23} & \alpha_m\sigma_2 - J_{23} \\ J_{31} & -2J_{42} - \dfrac{2(2\sigma_2 - \sigma_1)}{\alpha_m} & -\mu - 2J_{43} & -2J_{43} + 2\mu \\ -\dfrac{J_{23}}{\alpha_m \alpha_p} & J_{42} & J_{43} & -\mu + J_{43} \end{bmatrix}, \tag{6.38}$$

where,

$$J_{23} = \frac{(2\sigma_2 - \sigma_1) N_m {\alpha_p}^2}{N_p \alpha_m}, \quad J_{31} = \frac{2J_{23}}{\alpha_m \alpha_p} + \frac{(2\sigma_2 - \sigma_1)}{\alpha_p},$$

$$J_{42} = \frac{\sigma_2}{\alpha_m} - \frac{(2\sigma_2 - \sigma_1) N_m {\alpha_p}^2}{N_p {\alpha_m}^3}, \quad J_{43} = -\frac{\mu N_m {\alpha_p}^2}{N_p {\alpha_m}^2}.$$

According to the Routh-Hurwitz criterion, it can be proved that when F_m is beyond a critical value, there exists no steady-state in spite of the presence of damping. In this case the energy is continuously exchanged between these two modes without being attenuated. There is no saturation phenomenon.

6.4.3 Further analysis of the internal resonance relationship

The results of the governing equations (6.8) and boundary conditions (6.9)-(6.10) show that the linear part of the system can be split into two independent subsystems, viz., one involving Lateral **B**ending/**E**xtension/Lateral Transverse-shear motions (BE-subsystem $u_0 - v_0 - \theta_z$) and the other involving **T**wist /Vertical **B**ending /Vertical Transverse-shear motions (TB-subsystem $w_0 - \phi - \theta_x$). Thus the eigen-frequencies ω_i and the corresponding eigen-modes can also be split into two parts, ω_i^{BE} in the BE-subsystem and ω_i^{TB} in the TB-subsystem. Therefore, the possible internal resonance relationship $\omega_p \approx 2\omega_m$ can be split into the following 4 cases,

$$(1) \quad \omega_p^{BE} \approx 2\omega_m^{BE}, \quad (2) \quad \omega_p^{BE} \approx 2\omega_m^{TB}, \quad (3) \quad \omega_p^{TB} \approx 2\omega_m^{BE}, \quad (4) \quad \omega_p^{TB} \approx 2\omega_m^{TB}.$$

Because the nonlinear coefficients N_p and N_m are determined by the space of linear system, it is not difficult to determine that the nonlinear coefficients N_p and N_m are both zero for the case (3) and case (4). Indeed for case (4), the nonlinear coefficients N_p and N_m are related to the global stiffness quantities a_{58} that we ignored in the nonlinear terms. As a consequence, there will exist no significant modal interactions for these two internal resonance relationships. In other words, modal interaction may occur only in the following 2 internal resonance relationships:

$$(1) \quad \omega_p^{BE} \approx 2\omega_m^{BE}, \qquad (2) \quad \omega_p^{BE} \approx 2\omega_m^{TB}. \tag{6.39}$$

When the internal resonance relationship $\omega_p^{BE} \approx 2\omega_m^{BE}$ is satisfied, energy just transfers in the BE-subsystem. But when the internal resonance relationship $\omega_p^{BE} \approx 2\omega_m^{TB}$ is satisfied, energy can transfer between the two subsystems, i.e., vertical bending/twist motions may induce lateral bending/extension motions and vice verse. The independent two subsystems are coupled again due to the internal resonance.

6.5 Numerical study for $1:2$ internal resonance

For a concrete study of modal interaction caused by the internal resonance, we consider a composite thin-walled beam with length $L = 2.43m$. The material property and geometric specification of the beam are given in Table 6.1, and the lay-ups are specified in Table 6.2 ($\theta = 45^\circ$). From Table 6.3, a significant relationship for internal resonance can be found: $\omega_3^{BE} \approx 2\omega_3^{TB}$. However it is important to note that, although $\omega_2^{TB} \approx 2\omega_1^{BE}$, this relationship can not induce internal resonance according to the former analysis.

Figures 6.2a and 6.2b give the mode shapes of ω_3^{BE} and ω_3^{TB}, respectively. We can find that v_0 plays a pivotal role in the ω_3^{BE} mode from Fig. 6.2a. While in Fig. 6.2b, each component is important in ω_3^{TB} mode. We make $\omega_p = \omega_3^{BE}$ and $\omega_m = \omega_3^{TB}$, then the nonlinear coefficients can be specified as $N_p = 1906.2$ and $N_m = 138118$. And here we make the damping coefficient as $\mu = 0.5$.

Table 6.1: *Material property and geometric specification of the thin-walled box beam*

Material	Value	Geometric	Value
E_{11}	$206.8 \times 10^9\ N/m^2$	Width ($2b^a$)	0.254 m
$E_{22} = E_{33}$	$5.17 \times 10^9\ N/m^2$	Depth ($2d^a$)	0.0681 m
$G_{13} = G_{23}$	$2.55 \times 10^9\ N/m^2$	Wall thickness (h)	0.0102 m
G_{12}	$3.10 \times 10^9\ N/m^2$	Number of layers (m_l)	6
$\mu_{12} = \mu_{13} = \mu_{23}$	0.25	Layer thickness	0.0017 m
ρ	$1.528 \times 10^3\ Kg/m^3$		

[a] The length is measured on the mid-line contour.

Table 6.2: *Thin-walled box beam with CAS lay-up [unit:deg].*

Flanges		Webs	
Top	Bottom	Left	Right
$[\theta]_6$	$[\theta]_6$	$[\theta/-\theta]_3$	$[\theta/-\theta]_3$

Table 6.3: *The natural frequencies of the thin-walled box beam ($L = 2.432$ m , $\theta = 45°$) [unit:* Hz*]*

Mode$^{\#}$	Theoretical	ABAQUS	Error (%)[a]
ω_1^{BE}	22.701	22.637	0.28
ω_2^{BE}	134.11	134.48	-0.28
ω_3^{BE}	248.07	247.22	0.35
ω_4^{BE}	348.52	350.59	-0.59
ω_1^{TB}	7.1784	7.1379	0.57
ω_2^{TB}	44.672	44.451	0.50
ω_3^{TB}	124.06	123.33	0.59
ω_4^{TB}	149.25	147.93	0.89

[a] Relative error, ([Analytical]-[ABAQUS])/([ABAQUS])$\times 100\%$.

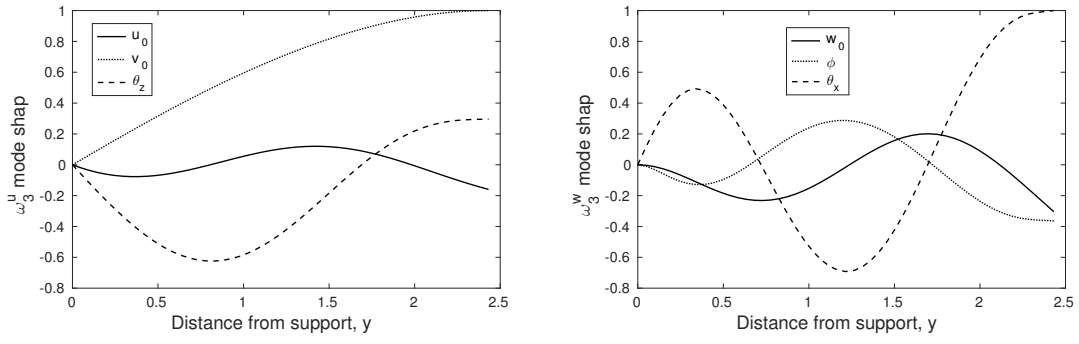

(a) ω_3^{BE} **(b)** ω_3^{TB}

Figure 6.2: *Mode shapes*

6.5.1 Energy is input from the ω_3^{BE} mode, Ω near ω_3^{BE}

In Figs. 6.3a and 6.3b, α_p and α_m are plotted as functions of external excitation F_p, where stable solutions are indicated in solid lines while unstable solutions in dashed lines. In Fig. 6.3a the detunings of the internal and external resonance are both small, the parameter Γ is positive. Thus there is only one real solution for (6.36) when $F_p > f_p^{c2}$. In Fig. 6.3b, $\sigma_1 = \sigma_2 = 1.5$, this combination renders Γ negative. Thus in the region $f_p^{c1} < F_p < f_p^{c2}$, there is a jump phenomenon associated with varying the amplitude of the excitation F_p. The trend of amplitude responses α_p and α_m can be traced from two ways, i.e., from $F_p = 0$ to higher values and vice verse. The jump phenomenon can be traced by tracking the arrows, respectively.

In Figs. 6.3a and 6.3b, one can clearly see the saturation phenomenon. As the external excitation F_p increases from zero, so does the response of α_p. This agrees with the solution of the corresponding linear system (6.27). Beyond the critical value f_p^{c2}, the solution (6.27) loses stability and another branch of solution determined by (6.28) and (6.36) dominates. It is clearly seen that the response α_p is independent of external excitation, though the energy is input from the external resonance mode ω_3^{BE}.

In Figs. 6.4a, 6.4b, and 6.4c, α_p and α_m are plotted as functions of external resonance detuning parameter σ_2, where stable solutions are indicated in solid lines while unstable solutions in dashed lines. In the region between σ_2^{-c2} and σ_2^{c2}, the linear solution (6.27) is unstable. The regions between σ_2^{c2} and σ_2^{c1} and between σ_2^{-c2} and σ_2^{-c1}, where two stable solutions exist, correspond to the parameter $\Gamma < 0$. In Fig. 6.4a, the jump phenomenon associated with varying the frequency Ω of the excitation is indicated by the arrows. The symmetric behavior of the frequency-response curve versus external resonance detuning σ_2 can be seen where the internal resonance detuning σ_1 is zero. The nonzero value of internal resonance detuning parameter σ_1 will cause the unsymmetrical configurations in frequency-response curves which can be seen in Figs. 6.4b and 6.4c.

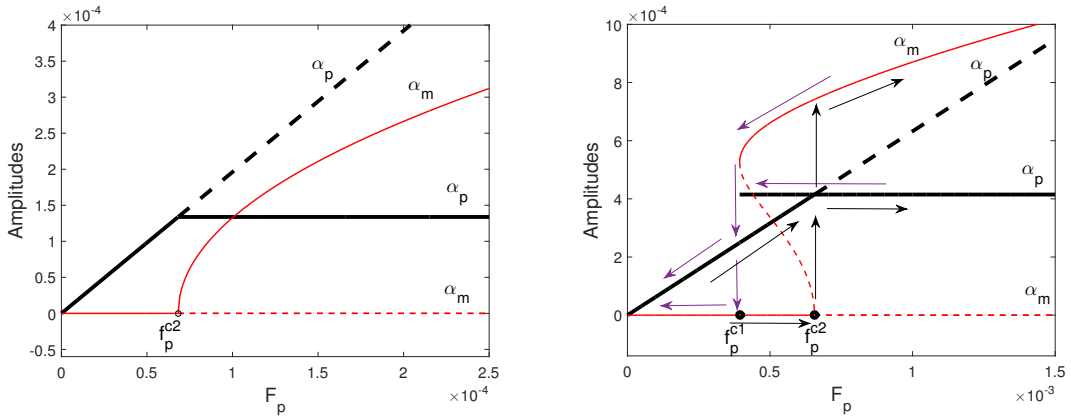

(a) $\sigma_1 = \sigma_2 = 0.1$ **(b)** $\sigma_1 = \sigma_2 = 1.5$

Figure 6.3: *Response amplitudes versus excitation intensity F_p when energy is input from the ω_3^{BE} mode*

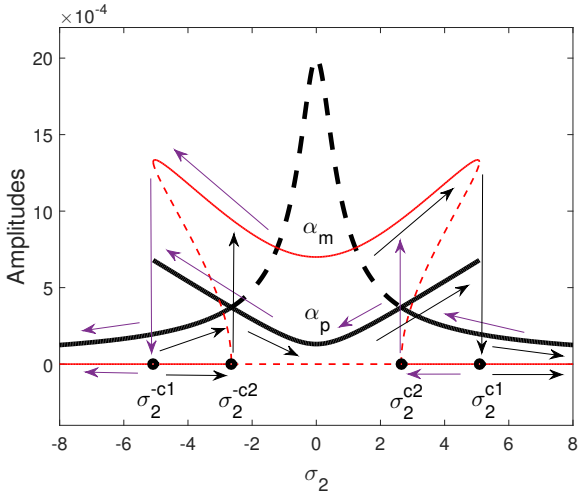

(a) $\sigma_1 = 0$

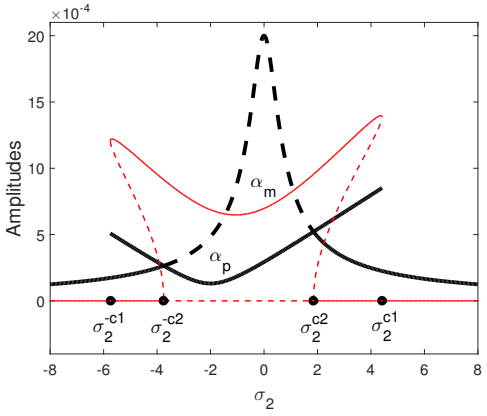

(b) $\sigma_1 = 2$

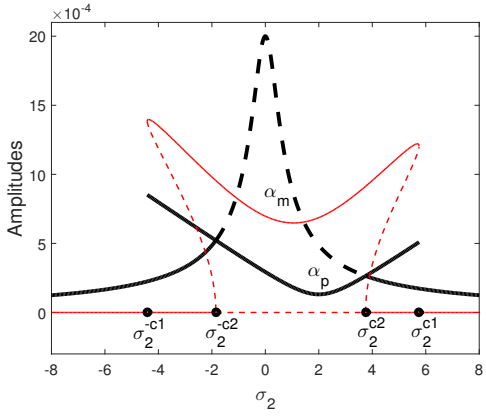

(c) $\sigma_1 = -2$

Figure 6.4: *Response amplitudes versus excitation frequency σ_2 when energy is input from the ω_3^{BE} mode ($F_p = 0.001$).*

6.5.2 Energy is input from the ω_3^{TB} mode, Ω near ω_3^{TB}

In Figs. 6.5a and 6.5b, α_p and α_m are plotted as functions of external excitation F_m, where stable solutions are indicated in solid lines while unstable solutions in dashed lines. Fig. 6.5a shows that when F_m is beyond a critical value, there exists no steady-state solution. In such a case, the energy is continuously exchanged between the two modes without being attenuated. Fig. 6.6 shows a continuous exchange of energy back and forth between the two modes for a large value of time T_1. There no saturation phenomenon exists. When the external resonance detuning σ_2 is large ($\sigma_2 = 3$), jump phenomenon indicated by the arrows can be observed in Fig. 6.5b.

In Figs. 6.7a, 6.7b, and 6.7c, α_p and α_m are plotted as functions of external resonance detuning parameter σ_2. There is a region near the center dip of theses curves where no steady-state solution exists. The regions in which there are two stable solutions correspond to Fig. 6.5b, while the center regions correspond to Fig. 6.5a. As $|\sigma_2|$ increases, α_p tends to zero faster than α_m which is similarly to Figs. 6.4a, 6.4b, and 6.4c.

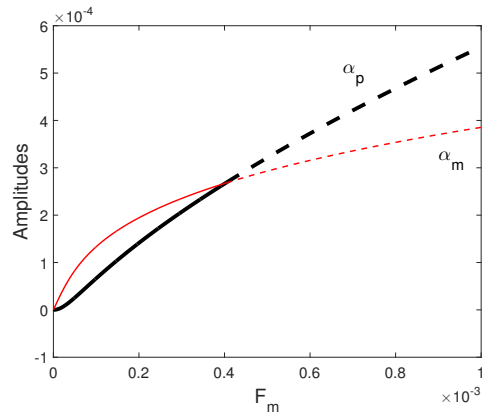

(a) $\sigma_1 = \sigma_2 = 0.1$

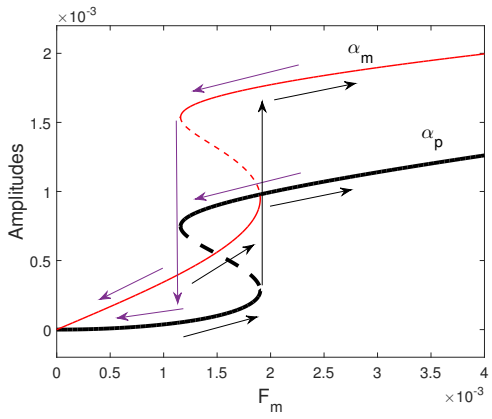

(b) $\sigma_1 = 0.1$ *and* $\sigma_2 = 3$

Figure 6.5: *Response amplitudes versus excitation intensity F_m when energy is input from the ω_3^{TB} mode*

6.5.3 Validation

In oder to test the accuracy of our model and validate our theoretical results on modal interactions, the commercial code ABAQUS [31] is used in simulating the forced nonlinear vibration responses of the thin-walled box beams. A 4-node doubly curved general-purpose shell element type S4 is adopted in the computation. All the responses in validations all come from one note at the tip of the beam. And Fast Fourier Transform (FFT) [99] is used for the corresponding frequency-domain analysis. Material property, geometric specification and lay-ups of the beams we used in the ABAQUS validation are given in Table 6.1 and Table 6.2.

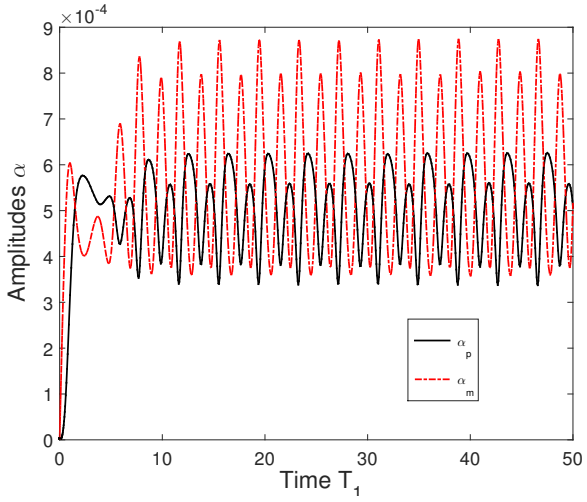

Figure 6.6: *The evolution of the amplitudes α_p and α_m when energy is input from the ω_3^{TB} mode. ($F_m = 0.001$ and $\sigma_1 = \sigma_2 = 0.1$).*

Case 1: $\omega_p^{BE} \approx 2\omega_m^{TB}$

Firstly, the validation for the beam model used in the example is given, where internal resonance relationship $\omega_3^{BE} \approx 2\omega_3^{TB}$ occurs. Theoretical prediction of the natural frequencies and the results from ABAQUS are compared in Table 6.3. In all computed modes, an excellent agreement is observed between the theoretical and numerical results. Because v_0 plays a pivotal role in the ω_3^{BE} mode, in this validation we just focus on the analysis of extension and vertical bending responses of the beam.

Excitation energy is input from the ω_3^{BE} mode The normal uniform shell edge external load distributed on the tip of the beam with magnitude specified as 5000N/m and frequency Ω specified as 247.2Hz is considered in this case. The responses of v and w are displayed in Fig. 6.8a and Fig. 6.8b, respectively. It is readily seen that after a transient process about 0.3 second, the vertical bending response is induced strongly by the extension excitation. And from the results of frequency-domain analysis, it is easy to confirm the induced mode is ω_3^{TB}. Moreover, the response amplitude of mode ω_3^{TB} is nearly twice that of the response amplitude of mode ω_3^{BE}. Extension excitation induces high-amplitude low-frequency vertical bending response, which agrees with our theoretical prediction.

Excitation energy is input from the ω_3^{TB} mode The normal vertical pressure distributed uniformly on the top and bottom walls of the beam with magnitude specified as 10Kpa and frequency specified as 123.3Hz is considered in this case. The responses of w and v are displayed in Fig. 6.9a and Fig. 6.9b, respectively. The mode ω_3^{BE} is significantly excited, which can been seen in Fig. 6.9b.

When we increase the magnitude of the pressure to 100Kpa, significant noise can be seen in Fig. 6.10a and Fig. 6.10b. According to the preceding theoretical analyses, when the external excitation is large enough, there will be no steady-state solution. Thus these noise may come from the energy exchange between ω_3^{TB} mode and ω_3^{BE} mode, which is similar to that in Fig. 6.6.

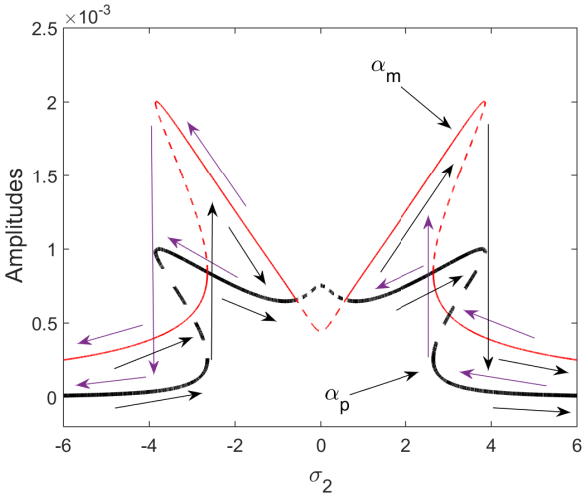

(a) $\sigma_1 = 0$

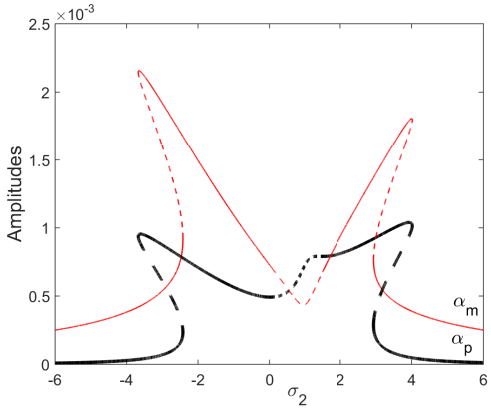

(b) $\sigma_1 = 2$

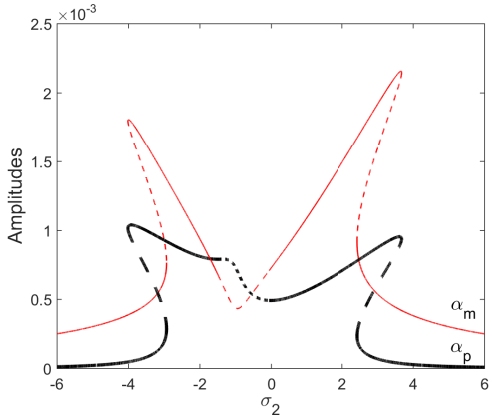

(c) $\sigma_1 = -2$

Figure 6.7: *Response amplitudes versus excitation frequency σ_2 when energy is input from the ω_3^{TB} mode ($F_m = 0.0015$)*

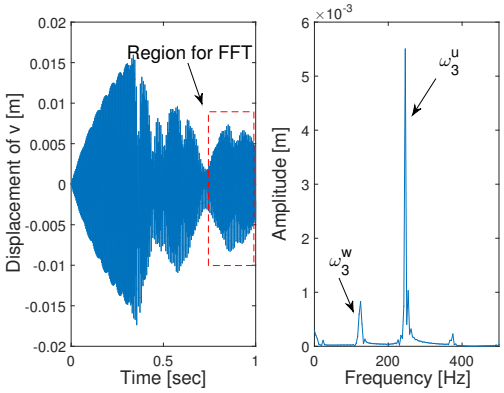

(a) *Extension response v*

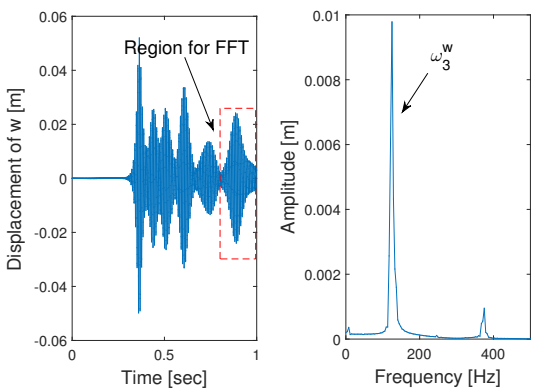

(b) *Vertical bending response w*

Figure 6.8: *The responses and the corresponding frequency-domain analysis when the excitation energy is input from the ω_3^{BE} mode.*

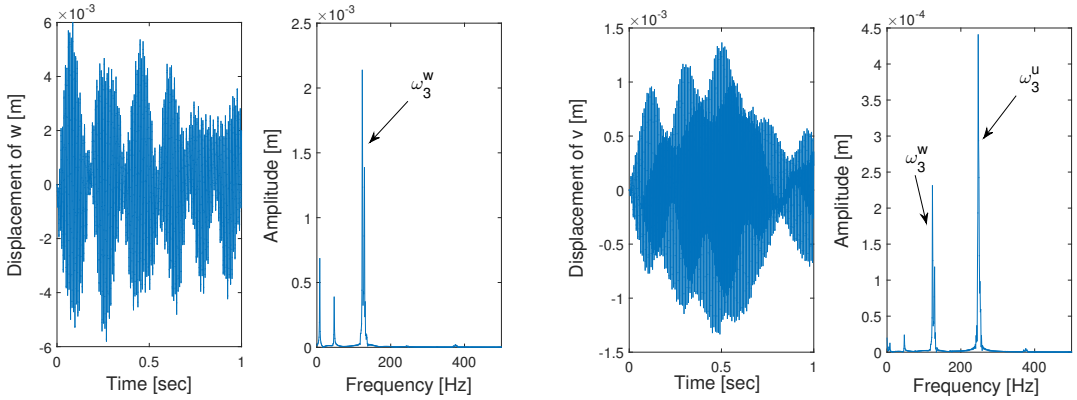

(a) *The vertical bending response w* **(b)** *The extension response v*

Figure 6.9: *The responses and the corresponding frequency-domain analysis when the excitation energy is input from the ω_3^{TB} mode.*

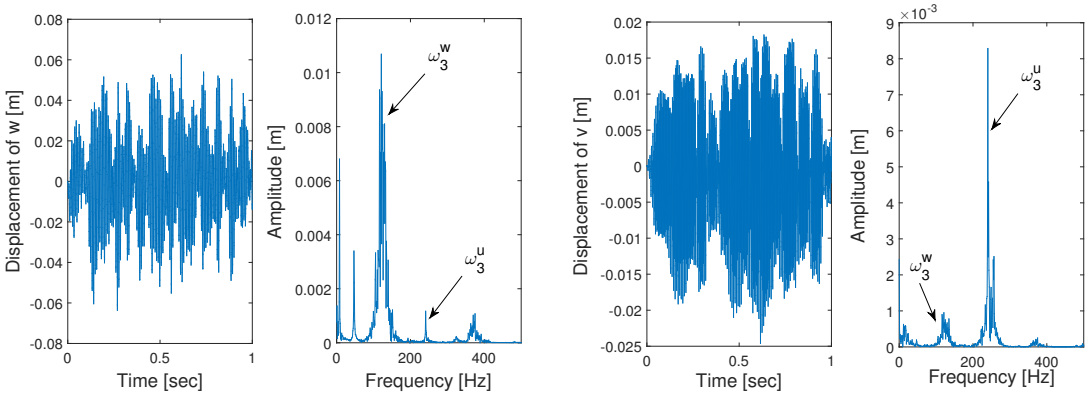

(a) *The vertical bending response w* **(b)** *The extension response v*

Figure 6.10: *The responses and the corresponding frequency-domain analysis when the excitation energy is input from the ω_3^{TB} mode.*

Table 6.4: *The natural frequencies of the thin-walled box beam by ABAQUS ($Length = 2.665$ m, $\theta = 45°$) [unit: Hz]*

Mode$^{\#}$	1st	2nd	3nd	4th
ω^{BE}	18.835	112.89	224.78	300.22
ω^{TB}	5.9334	36.995	102.94	135.11

Case 2: $\omega_p^{TB} \approx 2\omega_m^{BE}$

In the example model, whose frequencies are listed in Table 6.3, there exists another internal resonance relationship $\omega_2^{TB} \approx 2\omega_1^{BE}$. But there will be no significant modal interactions according to the theoretical analysis. Because u_0 plays a pivotal role in the ω_1^{BE} mode, we focus on the analysis of lateral bending and vertical bending responses.

Excitation energy is input from ω_2^{TB} The normal vertical pressure distributed uniformly on the top and bottom walls of the beam with magnitude specified as 10Kpa and frequency specified as 44.5Hz is considered in this case. The responses of w and u are displayed in Fig. 6.11a and Fig. 6.11b, respectively. No ω_1^{BE} mode exists in the frequency-domain analysis. And the induced lateral bending response u is tiny compared with the vertical bending response w.

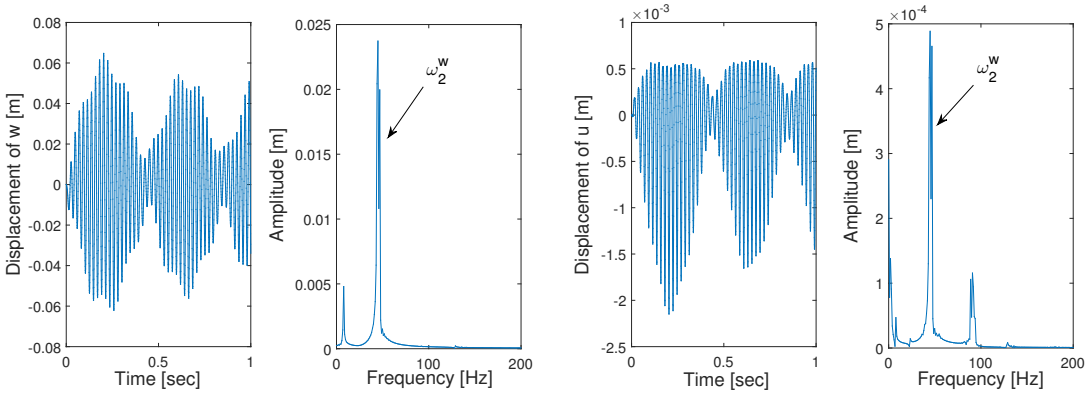

(a) *The vertical bending response w*

(b) *The lateral bending response u*

Figure 6.11: *The responses and the corresponding frequency-domain analysis when the excitation energy is input from the ω_2^{TB} mode.*

Excitation energy is input from ω_1^{BE} The normal lateral pressure distributed uniformly on the left and right walls of the beam with magnitude specified as 10Kpa and frequency specified as 22.6Hz is considered in this case. The responses of u and w are displayed in Figs. 6.12a and 6.12b, respectively. Although ω_2^{TB} mode is excited and can been seen in Fig. 6.12b, the induced vertical bending response is extremely tiny compared with the lateral bending response (nearly 3000 times), which can be neglected. There is no significant modal interactions when the internal relationship $\omega_p^{TB} \approx 2\omega_m^{BE}$ occurs.

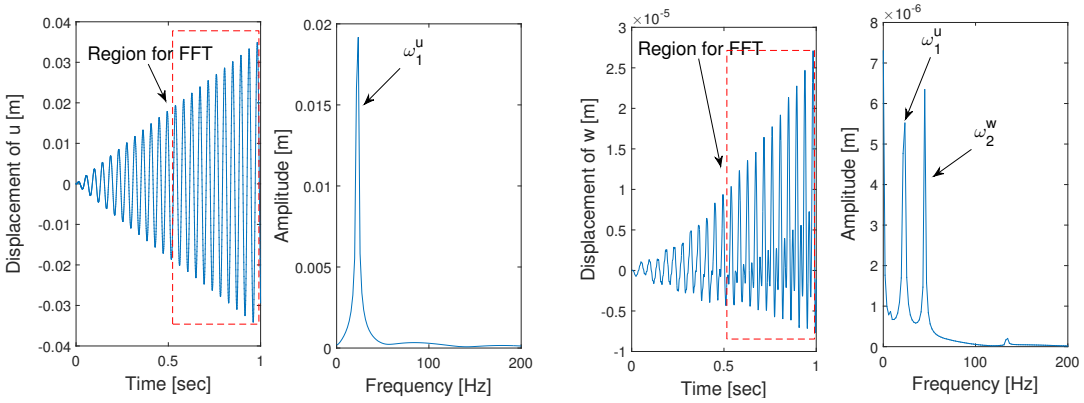

(a) *The lateral bending response u*

(b) *The vertical bending response w*

Figure 6.12: *The responses and the corresponding frequency-domain analysis when the excitation energy is input from the ω_1^{BE} mode.*

Case 3: $\omega_p^{BE} \approx 2\omega_m^{BE}$

Here we consider a thin-walled beam with length $L = 2.665$m whose frequencies by ABAQUS are given in Table. 6.4, where a significant internal resonance relationship $\omega_3^{BE} \approx 2\omega_2^{BE}$ can be found. According the theoretical prediction, significant modal interactions will occur when excitation energy is input from ω_2^{BE} mode or ω_3^{BE} mode. We note that u_0 plays a pivotal role in the ω_2^{BE} mode, however v_0 plays a pivotal role in the ω_3^{BE} mode.

Excitation energy is input from ω_3^{BE} The normal uniform shell edge external load distributed on the tip of the beam with magnitude is specified as 5000N/m and frequency Ω specified as 224.8Hz is considered in this case. The responses of v and u are displayed in Fig. 6.13a and Fig. 6.13b, respectively. It is readily seen that after a transient process about 0.6 second, the lateral bending response is induced strongly by the extension excitation, i.e. ω_2^{BE} mode is excited when excitation energy is input from ω_3^{BE} mode. The response amplitude of mode ω_2^{BE} is over thrice than that of mode ω_3^{BE}, which may be the result of the saturation phenomenon.

Excitation energy is input from ω_2^{BE} The normal lateral pressure distributed uniformly on the left and right walls of the beam with magnitude is specified as 40Kpa and frequency specified as 112.9Hz is considered in this case. The responses of u and v are displayed in Fig. 6.14a and Fig. 6.14b, respectively. ω_3^{BE} mode is excited due to modal interaction when excitation energy is input from ω_2^{BE} mode.

Case 4: $\omega_p^{TB} \approx 2\omega_m^{TB}$

In order to validate that there will be no significant modal interactions with the internal resonance relationship $\omega_p^{TB} \approx 2\omega_m^{TB}$, a thin-walled beam with length $L = 2.98$m is considered here. The frequencies by ABAQUS are given in Table. 6.5, where $\omega_7^{TB} \approx 2\omega_5^{TB}$ can be found.

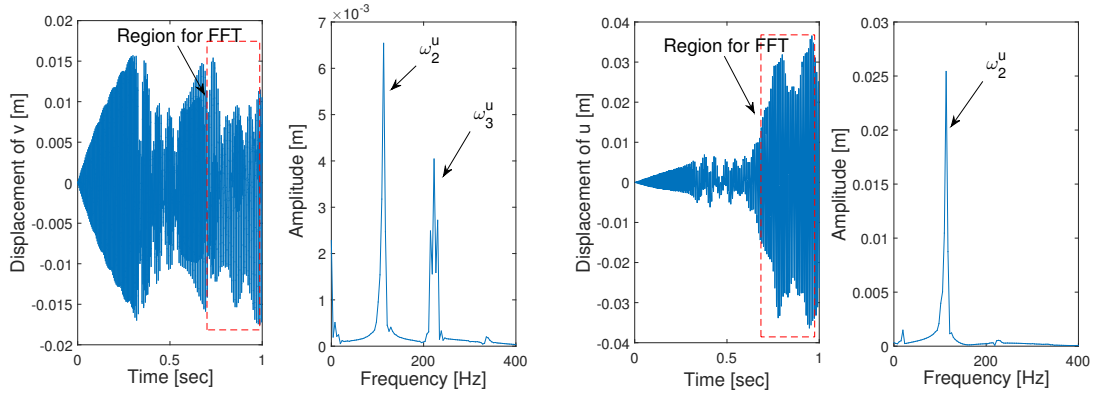

(a) *The extension response v* **(b)** *The lateral bending response u*

Figure 6.13: *The responses and the corresponding frequency-domain analysis when the excitation energy is input from the ω_3^{BE} mode.*

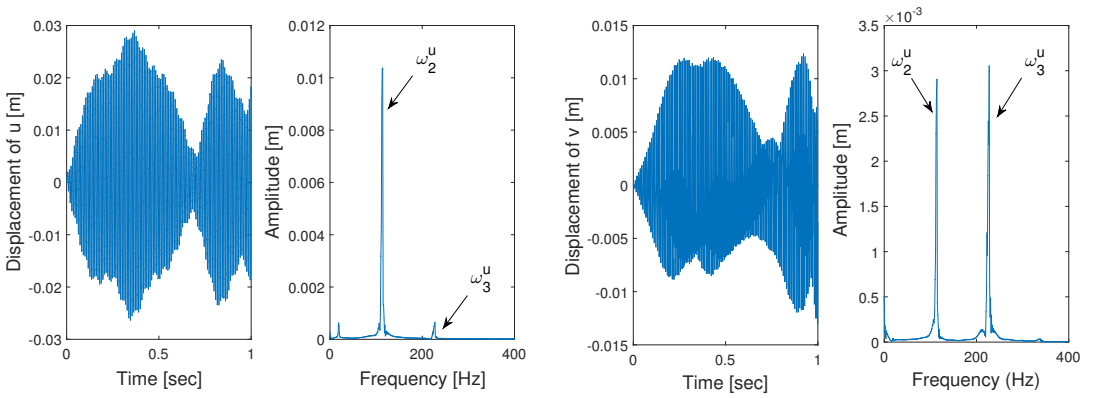

(a) *The lateral bending response u* **(b)** *The extension response v*

Figure 6.14: *The responses and the corresponding frequency-domain analysis when the excitation energy is input from the ω_2^{BE} mode.*

Table 6.5: *The natural frequencies of the thin-walled box beam by ABAQUS ($Length = 2.98$ m, $\theta = 45°$) [unit: Hz]*

Mode$^{\#}$	**1st**	**2nd**	**3nd**	**4th**	**5th**	**6th**	**7th**	**8th**
ω^{TB}	4.7354	29.560	82.441	120.91	160.57	258.25	320.54	367.84

Excitation energy is input from ω_7^{TB} The normal vertical pressure distributed uniformly on the top and bottom walls of the beam with magnitude specified as 600Kpa and frequency specified as 320.5Hz is considered in this case. The response of w is displayed in Fig. 6.15a. Although ω_5^{BE} mode component can be found in the frequency-domain analysis, it is extremely small so that it can be ignored.

Excitation energy is input from ω_5^{TB} For the external excitation in this case, We just change the excitation frequency from 320.5Hz to 160.6Hz. From Fig. 6.15b, there is no noticeable ω_7^{TB} mode component in the frequency-domain analysis. There is no significant modal interactions when the internal relationship $\omega_p^{TB} \approx 2\omega_m^{TB}$ occurs.

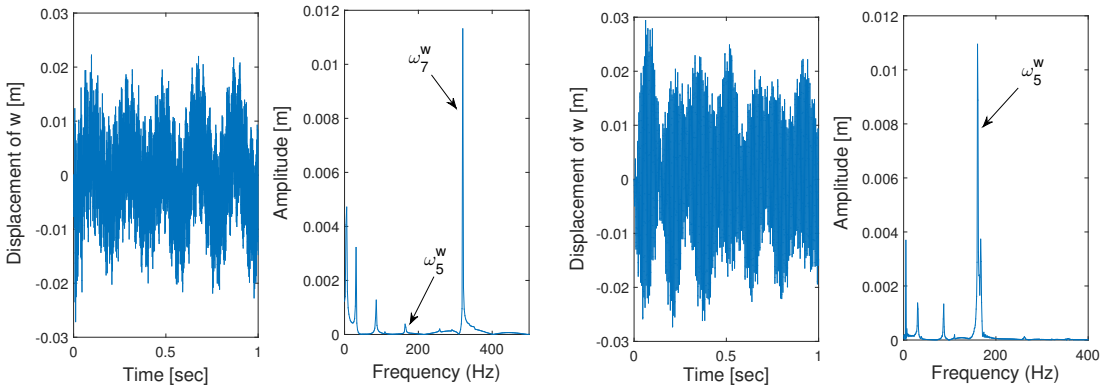

(a) *The excitation energy is input from the ω_7^{TB} mode*

(b) *The excitation energy is input from the ω_5^{TB} mode*

Figure 6.15: *The vertical bending response w and the corresponding frequency-domain analysis*

6.6 The internal resonance case: $\omega_p \approx \omega_m + \omega_n$

Next, based on the $1:2$ internal resonance discussion in the previous sections, a more general frequency relationship is investigated for the wing with external stores, i.e.,

$$\omega_p = \omega_m + \omega_n + \varepsilon\sigma_1, \quad \Omega_i = \omega_i + \varepsilon\sigma_2. \tag{6.40}$$

6.6.1 When the external energy is input from the pth mode

In such a case, in order to allow solvability of Eq. (6.19) [67], the following amplitude modulation equations can be obtained

$$i\frac{\mathrm{d}\,A_p}{\mathrm{d}\,T_1} + N_p A_m A_n e^{-i\sigma_1 T_1} + i\mu A_p + F_p \cos(\Omega_p t) e^{-i\omega_p T_0} = 0, \tag{6.41a}$$

$$i\frac{\mathrm{d}\,A_m}{\mathrm{d}\,T_1} + N_m A_p \bar{A}_n e^{i\sigma_1 T_1} + i\mu A_m = 0, \tag{6.41b}$$

$$i\frac{\mathrm{d}\,A_n}{\mathrm{d}\,T_1} + N_n A_p \bar{A}_m e^{i\sigma_1 T_1} + i\mu A_n = 0, \tag{6.41c}$$

in which the nonlinear coefficients N_p, N_m, N_n are defined as

$$N_p = \frac{[(\mathbf{N}_{nm}{}^T + \mathbf{N}_{mn}{}^T) - (\omega_m{}^2\mathbf{E}_{nm}{}^T + \omega_n{}^2\mathbf{E}_{mn}{}^T) - \omega_m\omega_n(\hat{\mathbf{E}}_{nm}^T + \hat{\mathbf{E}}_{mn}^T)]\mathbf{V}_p}{2\omega_p\mathbf{V}_p{}^T[\mathbf{M}+\mathbf{E}]^T\mathbf{V}_p}, \tag{6.42a}$$

$$N_m = \frac{[(\mathbf{N}_{np}{}^T + \mathbf{N}_{pn}{}^T) - (\omega_p{}^2\mathbf{E}_{np}{}^T + \omega_n{}^2\mathbf{E}_{pn}{}^T) + \omega_n\omega_p(\hat{\mathbf{E}}_{np}^T + \hat{\mathbf{E}}_{pn}^T)]\mathbf{V}_m}{2\omega_m\mathbf{V}_m{}^T[\mathbf{M}+\mathbf{E}]^T\mathbf{V}_m}, \tag{6.42b}$$

$$N_n = \frac{[(\mathbf{N}_{mp}{}^T + \mathbf{N}_{pm}{}^T) - (\omega_m{}^2\mathbf{E}_{pm}{}^T + \omega_p{}^2\mathbf{E}_{mp}{}^T) + \omega_m\omega_p(\hat{\mathbf{E}}_{mp}^T + \hat{\mathbf{E}}_{pm}^T)]\mathbf{V}_n}{2\omega_n\mathbf{V}_n{}^T[\mathbf{M}+\mathbf{E}]^T\mathbf{V}_n}, \tag{6.42c}$$

and the external excitation parameter F_p is defined as

$$F_p = \frac{\mathbf{Q}^T\mathbf{V}_p}{2\omega_p\mathbf{V}_p{}^T[\mathbf{M}+\mathbf{E}]^T\mathbf{V}_p}. \tag{6.43}$$

The amplitude modulation equations (6.41) can be put in real form by introducing the polar notations for the amplitudes

$$A_k(T_1) = \alpha_k(T_1)e^{i\beta_k(T_1)}, \quad k = p, m, n, \tag{6.44}$$

where α_k and β_k are real amplitudes and phases, respectively. By substituting Eq. (6.44) into Eqs. (6.41) and separating the real and imaginary parts, it follows that

$$\dot{\alpha}_p = -N_p\alpha_m\alpha_n\sin\gamma - \mu\alpha_p - F_p\sin\xi_p, \tag{6.45a}$$

$$\alpha_p\dot{\beta}_p = N_p\alpha_m\alpha_n\cos\gamma + F_p\cos\xi_p, \tag{6.45b}$$

$$\dot{\alpha}_m = N_m\alpha_p\alpha_n\sin\gamma - \mu\alpha_m, \tag{6.45c}$$

$$\alpha_m\dot{\beta}_m = N_m\alpha_p\alpha_n\cos\gamma, \tag{6.45d}$$

$$\dot{\alpha}_n = N_n\alpha_p\alpha_m\sin\gamma - \mu\alpha_n, \tag{6.45e}$$

$$\alpha_n\dot{\beta}_n = N_n\alpha_p\alpha_m\cos\gamma, \tag{6.45f}$$

where

$$\gamma = \beta_m + \beta_n - \sigma_1 T_1 - \beta_p, \qquad \xi_p = \sigma_2 T_1 - \beta_p. \tag{6.46}$$

The steady-state motions occur when $\dot{\alpha}_p = \dot{\alpha}_m = \dot{\alpha}_n = \dot{\gamma} = \dot{\xi}_p = 0$, that correspond to the fixed points solution of amplitudes and phases equations (6.45) and (6.46). It can be found that there are two kinds of fixed points.

1. The first kind fixed point is

$$\alpha_p{}^2 = \frac{F_p{}^2}{\mu^2 + \sigma_2{}^2}, \quad \alpha_m = \alpha_n = 0. \tag{6.47}$$

The first kind fixed point is actually the solution of the corresponding linear system.

2. The second kind fixed point is

$$\alpha_p{}^2 = \frac{(\sigma_1+\sigma_2)^2 + 4\mu^2}{4N_mN_n}, \quad \alpha_m{}^2 = \sqrt{\frac{N_m}{N_n}}X_p, \quad \alpha_n{}^2 = \sqrt{\frac{N_n}{N_m}}X_p, \tag{6.48a}$$

where X_p is the positive real root of the following equation,

$$N_p{}^2 X_p{}^2 + \frac{N_p N_m}{\sqrt{N_m{}^3 N_n}}[2\mu^2 - \sigma_2(\sigma_1+\sigma_2)]X_p + \alpha_p{}^2(\mu^2+\sigma_2{}^2) - F_p{}^2 = 0. \quad (6.49)$$

α_p, α_m and α_n will have real solutions for the second kind fixed point only when the condition $N_m N_n > 0$ is satisfied. Eq. (6.48a) shows that the amplitude of the external resonance mode α_p is independent of external excitation F_P. This may lead to a saturation phenomenon [66] and result in energy transfer to lower frequency modes ω_m and ω_n.

According to the solution cases of Eq. (6.49), the domain of the steady-state solutions can be split into three parts. i.e., subdomain **I**, **II** and **III**.

Subdomain I In this subdomain, the second kind fixed point has no real solution. Thus the system only has the first kind fixed point. This implies that in subdomain **I** there is no modal interactions and the external resonance plays the dominant role.

Subdomain II When the parameters combination satisfies

$$[(\sigma_1+\sigma_2)^2 + 4\mu^2](\mu^2+\sigma_2{}^2) - 4N_m N_n F_p{}^2 < 0, \quad (6.50)$$

Eq. (6.49) has only one positive real solution. In this subdomain, the system exhibits the first kind fixed point and one second kind fixed point at the same time. The stability of these two fixed points can be determined by the eigenvalues of the system's Jacobian matrix near the corresponding steady-state solution [22]. If the real part of each eigenvalue is not positive, then the corresponding steady-state solution is stable, otherwise is unstable.

Subdomain III When the parameters combination satisfies

$$\begin{cases} N_m[2\mu^2 - \sigma_2(\sigma_1+\sigma_2)] < 0, \\ \mu^2(\sigma_1+3\sigma_2)^2 < 4N_m N_n F_p{}^2, \\ 4N_m N_n F_p{}^2 < [(\sigma_1+\sigma_2)^2 + 4\mu^2](\mu^2+\sigma_2{}^2), \end{cases} \quad (6.51)$$

Eq. (6.49) has two positive real solutions. Thus subdomain **III** consists of the first kind fixed point plus two second kind fixed points.

6.6.2 When the external energy is input from the mth or nth mode.

Since the mth mode and nth mode can be exchanged with each other in the solvability conditions, we just consider the case when external energy is input from the mth mode. Similarly to Eqs. (6.45) and (6.46), we can obtain the following amplitudes and phases

equations:

$$\dot{\alpha}_p = -N_p\alpha_m\alpha_n \sin\gamma - \mu\alpha_p, \tag{6.52a}$$

$$\alpha_p\dot{\beta}_p = N_p\alpha_m\alpha_n \cos\gamma \tag{6.52b}$$

$$\dot{\alpha}_m = N_m\alpha_p\alpha_n \sin\gamma - \mu\alpha_m - F_m \sin\xi_m, \tag{6.52c}$$

$$\alpha_m\dot{\beta}_m = N_m\alpha_p\alpha_n \cos\gamma + F_m \cos\xi_m, \tag{6.52d}$$

$$\dot{\alpha}_n = N_n\alpha_p\alpha_m \sin\gamma - \mu\alpha_n, \tag{6.52e}$$

$$\alpha_n\dot{\beta}_n = N_n\alpha_p\alpha_m \cos\gamma, \tag{6.52f}$$

where

$$F_m = \frac{\mathbf{Q}^T\mathbf{V}_m}{2\omega_m {\mathbf{V}_m}^T[\mathbf{M}+\mathbf{E}]^T\mathbf{V}_m}, \quad \xi_m = \sigma_2 T_1 - \beta_m. \tag{6.53}$$

For steady-state motions, similarly, two kinds of fixed points can be found.

1. The first kind fixed point is

$$ {\alpha_m}^2 = \frac{{F_m}^2}{\mu^2 + {\sigma_2}^2}, \quad \alpha_p = \alpha_n = 0. \tag{6.54}$$

2. The second kind fixed point is

$$ {\alpha_m}^2 = \frac{(\sigma_1-\sigma_2)^2 + 4\mu^2}{-4N_pN_n}, \quad {\alpha_p}^2 = \sqrt{-\frac{N_p}{N_n}}X_m, \quad {\alpha_n}^2 = \sqrt{-\frac{N_n}{N_p}}X_m, \tag{6.55a}$$

where X_m is the positive root of the following equation,

$$ {N_m}^2{X_m}^2 + \frac{N_m}{\sqrt{-N_pN_n}}[2\mu^2 - \sigma_2(\sigma_1-\sigma_2)]X_m + {\alpha_m}^2(\mu^2+{\sigma_2}^2) - {F_m}^2 = 0. \tag{6.56}$$

One essential condition for that α_p, α_m and α_n have real solutions for the second kind fixed point is $N_pN_n < 0$.

According to the solution cases of Eq. (6.56), similarly, subdomains **I**, **II** and **III** can be defined in the steady-sate solution domain.

Subdomain I Eq. (6.56) has no positive real solution. The solution of the linear system dominates the system.

Subdomain II When the parameters combination satisfies

$$[(\sigma_1-\sigma_2)^2 + 4\mu^2](\mu^2+{\sigma_2}^2) + 4N_pN_n{F_m}^2 < 0, \tag{6.57}$$

Eq. (6.56) has one positive real solution.

Subdomain III Eq. (6.56) has two positive real solutions when the parameters combination satisfies

$$\begin{cases} N_m[2\mu^2 - \sigma_2(\sigma_1-\sigma_2)] < 0, \\ [(\sigma_1-\sigma_2)^2 + 4\mu^2](\mu^2+{\sigma_2}^2) < 4N_pN_n{F_m}^2, \\ 4N_pN_n{F_m}^2 < \mu^2(\sigma_1+\sigma_2)^2. \end{cases} \tag{6.58}$$

6.6.3 Discussion for internal resonance conditions and energy flow criterion

Similar in section 6.4.3, eigen-frequencies of the wing-store system can also be split into two independent parts, ω_i^{BE} in the BE-subsystem and ω_i^{TB} in the TB-subsystem. Therefore, the possible internal resonance relationship $\omega_p \approx \omega_m + \omega_n$ can be split into the following 6 cases,

$$(1)\quad \omega_p^{BE} \approx \omega_m^{BE} + \omega_n^{BE}, \quad (2)\quad \omega_p^{BE} \approx \omega_m^{TB} + \omega_n^{TB}, \quad (3)\quad \omega_p^{TB} \approx \omega_m^{BE} + \omega_n^{TB},$$
$$(4)\quad \omega_p^{TB} \approx \omega_m^{BE} + \omega_n^{BE}, \quad (5)\quad \omega_p^{BE} \approx \omega_m^{TB} + \omega_n^{BE}, \quad (6)\quad \omega_p^{TB} \approx \omega_m^{TB} + \omega_n^{TB}.$$

It can be determined that the nonlinear coefficients N_p N_m and N_n in Eqs. (6.42) are all zero for the last three cases (4-6). In other words, the existence of the efficient internal resonances is only related to the first three (cases 1-3) eigenfrequencies combinations.

When the relationship $\omega_p^{BE} \approx \omega_m^{BE} + \omega_n^{BE}$ is satisfied, energy flows inside the BE-subsystem. However when the relationship $\omega_p^{BE} \approx \omega_m^{TB} + \omega_n^{TB}$ or $\omega_p^{TB} \approx \omega_m^{BE} + \omega_n^{TB}$ is satisfied, energy can be transferred between the two subsystems, i.e., flapping-twist motions may induce lagging-extension motions and vice versa. Because of modal interactions, the independent two subsystems are nonlinearly coupled again.

Energy flow criterion

Based on the discussions in sections 6.6.1 and 6.6.2, the conditions for existence of the second kind fixed point can offer a criterion to estimate the direction of energy flow during the internal resonance. Based on the convention $N_p > 0$, the other two nonlinear parameters N_m and N_n leads to the relation conditions:

1. $N_m > 0 \ \ \& \ \ N_n > 0$. In this case, the second kind fixed point exists only when external energy is input from ω_p mode. Energy can only be transferred from higher to lower modes when the internal resonance exists.

2. $N_m > 0 \ \ \& \ \ N_n < 0$ (or $N_m < 0 \ \ \& \ \ N_n > 0$). Only when energy is input from ω_m (or ω_n) mode, the system may have the second kind fixed point. As a result, the energy can be transferred only from ω_m (or ω_n) mode to the other two during the internal resonance.

3. $N_m < 0 \ \& \ N_n < 0$. In this case, Eqs. (6.48) and (6.55) can both have positive real solutions. This means that energy can be freely transferred among the three modes via the internal resonance. Moreover, when energy is transferred from mode A to modes B and C, mode B or C will serve as a new energy source, passing energy to the other two modes and looping infinitely. As a result, in this case there will be no stable steady-sate solutions during the internal resonance process.

6.7 Numerical study for wings with external stores

6.7.1 Frequency study

The material property and geometric specification of the wing structure of Fig. 6.1a are given in Table 6.6. The CAS lay-up configuration is given in Table 6.7. In the numerical study, only one rigid homogeneous cylinder with geometric specification as diameter 0.127 m and height 0.508 m is considered as the external store.

Table 6.6: *Material property and geometric specification of the thin-walled box beam*

Material	Value	Geometric	Value
E_{11}	206.8×10^9 N/m^2	Width ($2b^a$)	0.254 m
$E_{22} = E_{33}$	5.17×10^9 N/m^2	Depth ($2d^a$)	0.0681 m
$G_{13} = G_{23}$	2.55×10^9 N/m^2	Wall thickness (h)	0.0102 m
G_{12}	3.10×10^9 N/m^2	Number of layers	6
$\mu_{12} = \mu_{13} = \mu_{23}$	0.25	Length (L)	2.540 m
ρ	1.528×10^3 Kg/m^3	Layer thickness	0.0017 m

[a] The length is measured on the mid-line contour.

Table 6.7: *Lay-up configuration for wing structure (deg)*

Flanges		Webs	
Top	Bottom	Left	Right
$[45]_6$	$[45]_6$	$[45/-45]_3$	$[45/-45]_3$

Influence of span distributed store Three nondimensional parameters are defined to describe the span distributed store, viz., span and chord locations η_Y and η_r, and mass parameter η_M

$$\eta_Y = \frac{Y_j}{L}, \quad \eta_r = \frac{r_j}{2b}, \quad \eta_M = \frac{M_s}{M_b}. \tag{6.59}$$

Figure 6.16a shows the variation of the frequencies against the span location of the external store. It can be found that both the fundamental frequencies ω_1^{TB} and ω_1^{BE} decrease when the store moves from the root to the tip of the wing. For higher modes, the frequencies are sensitive to the span location. As for the influence of the chord location, it is significant only on ω_3^{TB}, in which the twist component ϕ dominates the mode shape, see Fig. 6.16b.

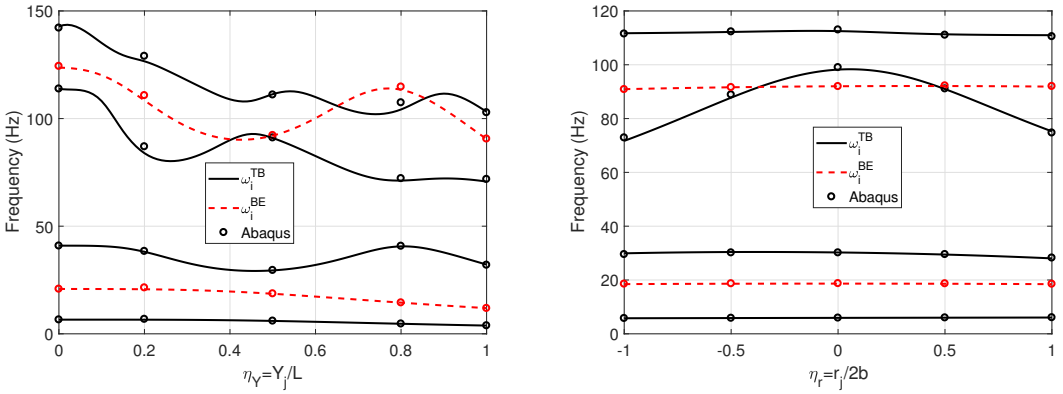

(a) *Span location Y_j*

(b) *Chord location η_r*

Figure 6.16: *Variation of the frequencies as a function of the span and chord locations ($\eta_r = 0.5$, $\eta_M = 0.5$, $\Lambda = 30°$)*

Influence of the tip store The other two nondimensional parameters of the tip store, viz., the chord and span offsets parameters η_{Tx} and η_{Ty} are defined as

$$\eta_{Tx} = \frac{x_T}{2b}, \quad \eta_{Ty} = \frac{y_T}{L}. \tag{6.60}$$

Figure 6.17 shows the variation of the frequencies against the mass of the tip store. As the mass parameter η_M increases, the frequencies of the wing-store system decrease. Moreover, it can be seen that the gradient of the frequencies also decrease. The influ-

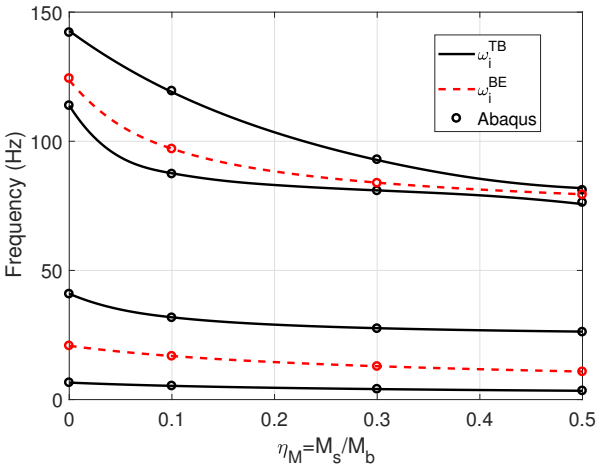

Figure 6.17: *Variation of the frequencies as a function of the mass of the tip store* η_M. *(* $\eta_{Tx} = 0$, $\eta_{Ty} = 0.1$, $\Lambda = 30°$*)*

ences of the chord and span offsets on frequencies are highlighted in Figs. 6.18a and 6.18b, respectively. It can be seen that the fundamental frequencies, ω_1^{TB} and ω_1^{BE}, are slightly sensitive to the tip store location. Fig. 6.19 further depicts the frequency as a function of the sweep angle Λ. The result shows that the sweep angle Λ only has an obvious effect on the high mode frequencies.

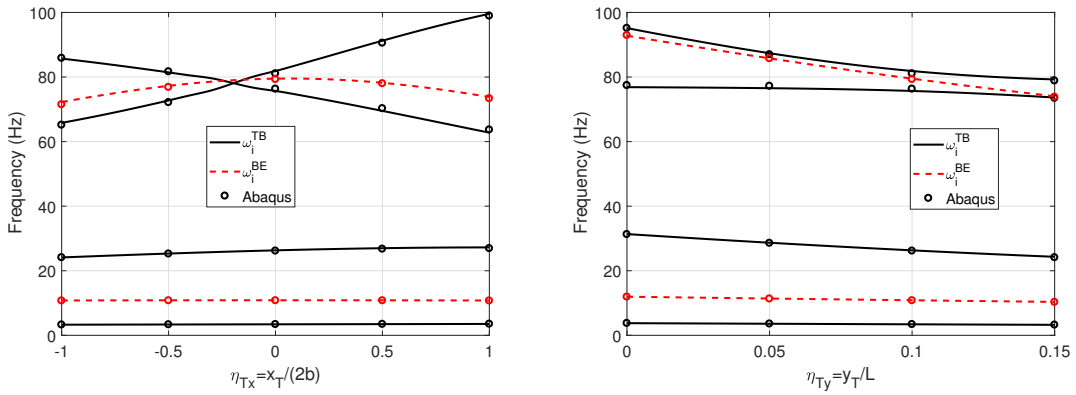

(a) *Chord offest (* $\eta_{Ty} = 0.1$*)*

(b) *Span offset (*$\eta_{Tx} = 0$*)*

Figure 6.18: *Variation of the frequencies as a function of the chord and span offsets of the tip store* η_{Tx} *(* $\eta_M = 0.5$, $\Lambda = 30°$ *)*

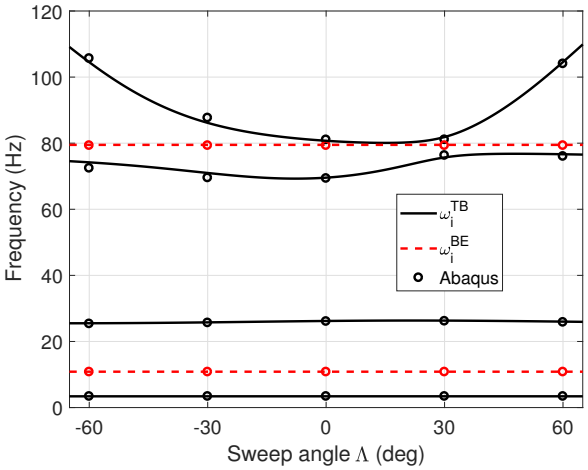

Figure 6.19: *Variation of the frequencies as a function of sweep angle* Λ. *(* $\eta_M = 0.5$, $\eta_{Tx} = 0$, $\eta_{Ty} = 0.1$

6.7.2 Nonlinear modal interactions

For a concrete study of modal interaction in the presence of internal resonance, the case that the aircraft wing carrying a heavy tip store is considered here. The mass and location parameters of the tip store are given as $\eta_M = 0.326$, $\eta_{Tx} = 0$, and $\eta_{Ty} = 0.07$. The frequencies of the wing-store system are listed in Table 6.8. Two significant relationships for internal resonance can be found, i.e., $\omega_4^{TB} \approx \omega_2^{BE} + \omega_1^{TB}$ and $\omega_2^{BE} \approx \omega_3^{TB} + \omega_1^{TB}$. According to the internal resonance conditions in section 6.6.3, these two relationships are both efficient, i.e., can both yield modal interactions.

Table 6.8: *Frequencies of the wing-tip store system* ($\eta_M = 0.326$, $\eta_{Tx} = 0$, $\eta_{Ty} = 0.07$, $\Lambda = 30°$) *[unit:* Hz*]*

Mode$^{\#}$	Theoretical	Abaqus	Error (%)^a	Mode$^{\#}$	Theoretical	Abaqus	Error (%)^a
ω_1^{BE}	12.903	12.820	0.646	ω_1^{TB}	4.0570	4.0344	0.560
ω_2^{BE}	87.000	86.955	0.051	ω_2^{TB}	28.798	28.668	0.454
ω_3^{BE}	180.66	179.40	0.705	ω_3^{TB}	83.795	84.268	-0.561
ω_4^{BE}	240.16	242.14	-0.816	ω_4^{TB}	91.072	90.879	0.213

^{a} Relative error: ([Theoretical]-[Abaqus])/([Abaqus])$\times 100\%$.

Internal resonance: $\omega_4^{TB} \approx \omega_2^{BE} + \omega_1^{TB}$

The internal resonance relationship $\omega_4^{TB} \approx \omega_2^{BE} + \omega_1^{TB}$ is firstly discussed. Letting $\omega_p = \omega_4^{TB}$, $\omega_m = \omega_2^{BE}$ and $\omega_n = \omega_1^{TB}$, then the nonlinear parameters N_p, N_m and N_n can be identified from Eqs. (6.42). Their values are given in Table 6.9, i.e., $N_p = 0.6609$, $N_m = 0.7271$ and $N_n = -14.59$. [1] Recalling the energy flow criterion in section 6.6.3, the condition ($N_m > 0$, $N_n < 0$) implies that only when energy is input from ω_2^{BE} mode, the modal interaction phenomenon will occur. Note that, a different energy flow direction will exhibit if we ignore the nonlinearities induced by the external stores (see

[1] Here we make the convention $N_p > 0$

Table 6.9), i.e., condition ($N_m > 0$, $N_n > 0$) means energy can only be transferred from ω_4^{TB} mode to ω_2^{BE} and ω_1^{TB} modes.

Table 6.9: *Comparison of nonlinear parameters N_p, N_m and N_n*

	$\omega_4^{TB} \approx \omega_2^{BE} + \omega_1^{TB}$			$\omega_2^{BE} \approx \omega_3^{TB} + \omega_1^{TB}$		
	N_p	N_m	N_n	N_p	N_m	N_n
	-0.6609	-0.7271	14.59	3.590	3.518	72.82
[a]	8.247	9.134	187.4	6.202	6.160	127.2
[b]	-9.008	-9.861	-172.8	-2.711	-2.641	-54.42

[a] Component induced by the wing structure.
[b] Component induced by the external store.

When energy is input from ω_2^{BE} mode, the steady-state solutions of the wing-store system will be governed by Eqs. (6.54) and (6.55). Figs. 6.20a and 6.20b present two typical types of steady-state solutions domain. Specifically, when the absolute value of the internal resonance detuning parameter σ_1 is small, the solution domain just consists of subdomain **I** and **II**, see Fig. 6.20a. However, if the absolute value of σ_1 is greater than a critical value ($|\sigma_1| > 2\sqrt{2}\mu$), the solution domain will involve the subdomain **III**, see Fig. 6.20b. Both Figs 6.20a and 6.20b show that only when external excitation F_m is beyond a minimal extreme value, the steady-state solution may locate in subdomain **II** or **III**.

One can see this conclusion more clearly in Figs. 6.21a and 6.21b, which depict the amplitudes as a function of external excitation parameter F_m for two different combinations of $\sigma 1$ and $\sigma 2$. Note that in Figs. 6.21a and 6.21b, stable solutions are indicated in solid lines while unstable solutions are in dashed lines. In Fig. 6.21a, with the in-

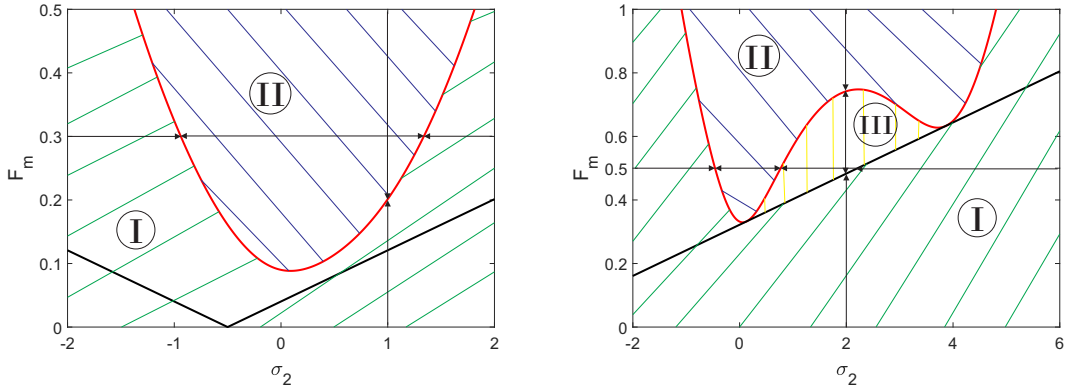

(a) $\sigma_1 = 0.5$, $\mu = 0.5$ **(b)** $\sigma_1 = 4$, $\mu = 0.5$

Figure 6.20: *Steady-state solution domain*

creasing F_m, the steady-state solution will shift to subdomain **II** from **I** (also indicated in Fig. 6.20a). In subdomain **II**, the second kind fixed point will replace the first kind fixed point as the system stable solutions with the presence of ω_2^{BE} mode saturation phenomenon [66]. In Fig. 6.21b, the increasing F_m leads the steady-state solution from subdomain **I**, crossing subdomian **III**, and then into subdomain **II** (also indicated in Fig. 6.20b). It can be seen that the first kind fixed point and one of the second kind

fixed points are both stable in subdomain **III**. As a result, a jump phenomenon indicated by the arrows in Fig. 6.21b can be observed on the boundary of subdomain **III**.

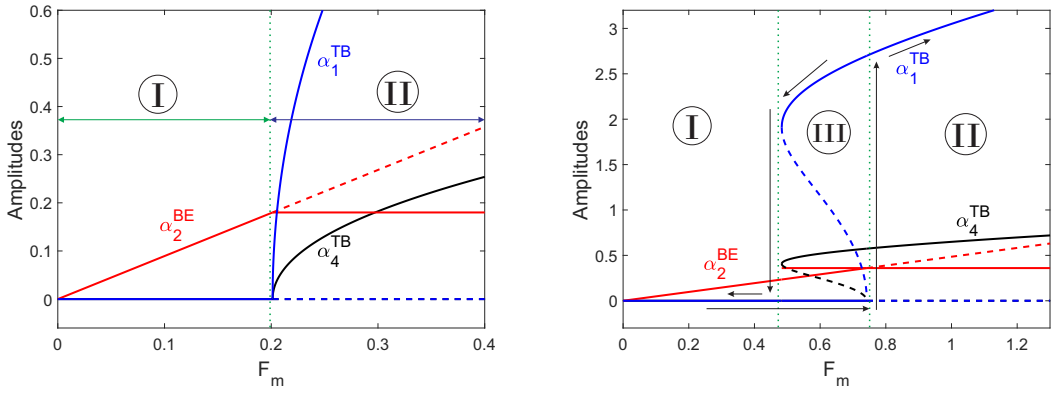

(a) $\sigma_1 = 0.5$, $\sigma_2 = 1$, $\mu = 0.5$ **(b)** $\sigma_1 = 4$, $\sigma_2 = 2$, $\mu = 0.5$

Figure 6.21: *Response amplitudes versus excitation parameter F_m when energy is input from ω_2^{BE} mode*

Figures 6.22a and 6.22b depict the amplitudes in the steady-state solution as a function of external resonance detuning parameter σ_2 for selected two combinations of $\sigma 1$ and F_m. Similarly, on the boundary of subdomain **III**, the jump phenomenon indicated by the arrows in Fig. 6.22b can be observed. In addition, it can been seen that for $\sigma_1 \neq 0$ cases, suitable external resonance detuning may contribute to the modal interactions.

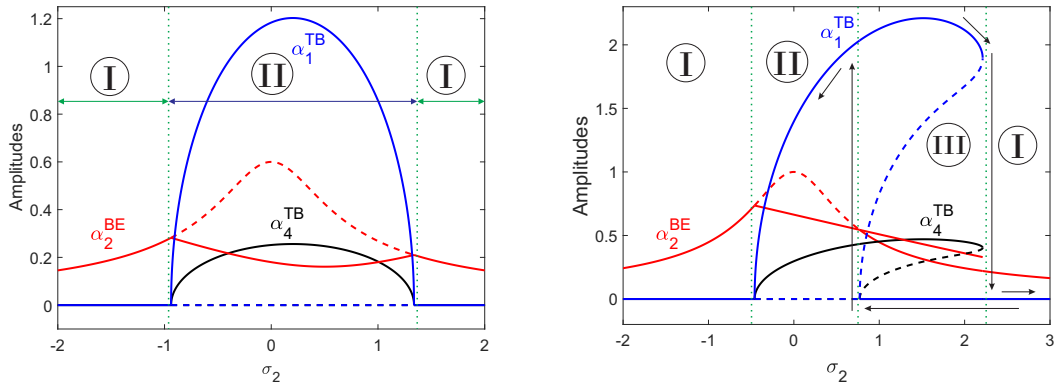

(a) $\sigma_1 = 0.5$, $F_m = 0.3$, $\mu = 0.5$ **(b)** $\sigma_1 = 4$, $F_m = 0.5$, $\mu = 0.5$

Figure 6.22: *Response amplitudes versus external resonance detuning parameter σ_2 when energy is input from ω_2^{BE} mode*

Internal resonance: $\omega_2^{BE} \approx \omega_3^{TB} + \omega_1^{TB}$

Next, the internal resonance relationship $\omega_2^{BE} \approx \omega_3^{TB} + \omega_1^{TB}$ is investigated. The parameters $\omega_p = \omega_2^{BE}$, $\omega_m = \omega_3^{TB}$ and $\omega_n = \omega_1^{TB}$ are defined in Eqs. (6.41). Then the nonlinear parameters $N_p = 3.590$, $N_m = 3.518$ and $N_n = 72.82$ can be obtained. $(N_m > 0, N_n > 0)$ means that the system will exhibit an apparent internal resonance

only when energy is input from ω_2^{BE} mode. By comparing the nonlinearity components in Table 6.9, nonlinearities induced by the tip store present a negative effect on the modal interactions in this case.

The typical steady-state solution domain determined by Eqs (6.47) and (6.48) is presented in Fig. 6.23a. Unlike Fig. 6.20b that just contains a negligible closed subdomain **III**, Fig. 6.23a has two significant open subdomain **III**. This difference can also be clearly seen in Fig. 6.23b, which depicts the amplitudes as a function of external resonance detuning parameter σ_2. From the result of Fig. 6.23b, one can see that the critical modal interaction occurs at the boundary of subdomain **III**.

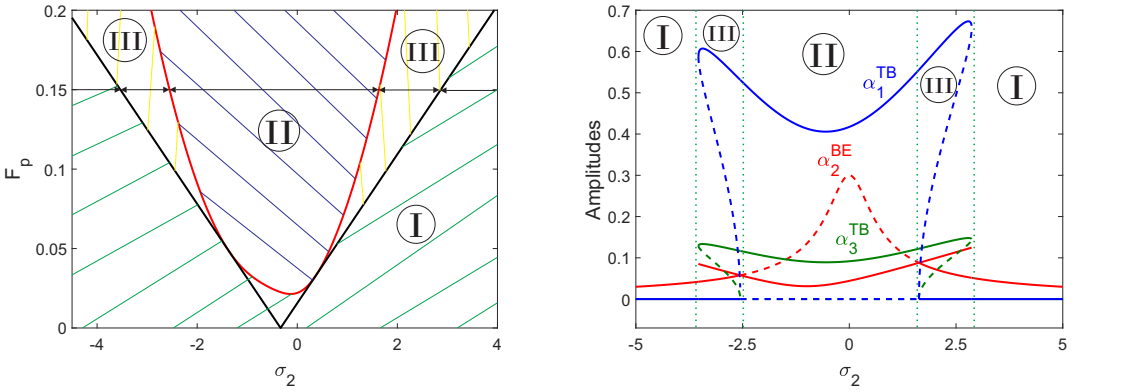

(a) *Steady-state solution domain*

(b) *Response amplitudes versus external resonance detuning parameter σ_2 when energy is input from ω_2^{BE} mode*

Figure 6.23: *Internal resonance: $\omega_2^{BE} \approx \omega_3^{TB} + \omega_1^{TB}$ ($\sigma_1 = 1$, $F_p = 0.15$, $\mu = 0.5$)*

6.7.3 Validation

For the purpose of validating the results showed in the numerical section, the commercial code Abaqus [31] is used for direct numerical simulations. In the computation, the 4-node doubly curved general-purpose shell element type $S4$ is adopted.

For frequency validation, good agreements between theoretical results and Abaqus results are achieved, as shown in Figs. 6.16a-6.19. Table 6.8 compares the eigenfrequencies from our theoretical analysis with the results from Abaqus, showing excellent agreement.

For the nonlinear forced vibration simulation, we note that the external excitations loading on the wing structure are all strong enough to induce the possible internal resonance. All the results presented in the time-domain are directly obtained by tracing responses of the nodes on the 80% beam span during the simulation time of 2 second. Actually 80% is a balanced choice according to the mode shapes (ω_2^{BE}, ω_1^{TB}, ω_3^{TB}, ω_4^{TB}) that involved in the internal resonances. In addition, fast Fourier transform (FFT) [99] is applied for the corresponding frequency-domain analysis.

When energy is input from ω_2^{BE} mode

According to the numerical study in section 6.7, we know that when energy is input from ω_2^{BE} mode, energy will be transferred to lower frequency modes ω_1^{TB}, ω_3^{TB} and

higher frequency mode ω_4^{TB} via the internal resonances at the same time.

In order to simulate the case when energy is input from ω_2^{BE} mode, the normal lateral pressure distributed uniformly on the left and right walls of the wing structure with magnitude specified as 5 kpa and frequency specified as 87 Hz is considered. Figs. 6.24a, 6.24b and 6.24c depict the response components u, w and ϕ during the simulation time 2 second, respectively.

In Fig. 6.24a, the displayed time-domain result reveals that after an external resonance process about 0.8 second, the response of lateral bending u decreases significantly. Taking into account the results of Figs. 6.24b and 6.24c, it can be seen that energy is transferred from BE-subsystem to TB-subsystem, and ω_1^{TB}, ω_3^{TB}, ω_4^{TB} these three modes are induced significantly. The simulation results agree with our theoretical predictions excellently.

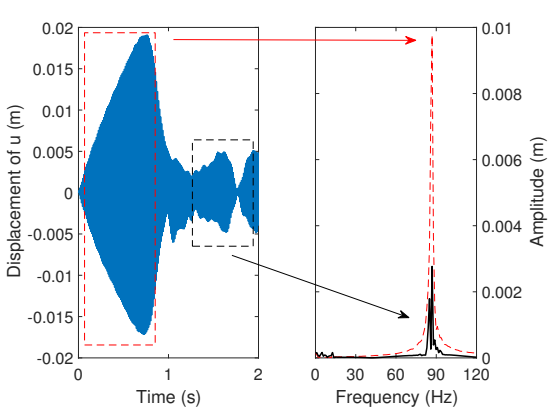

(a) *The lateral bending* u_0

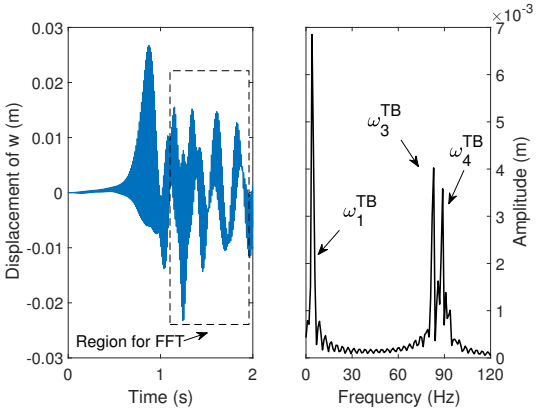

(b) *The vertical bending* w_0

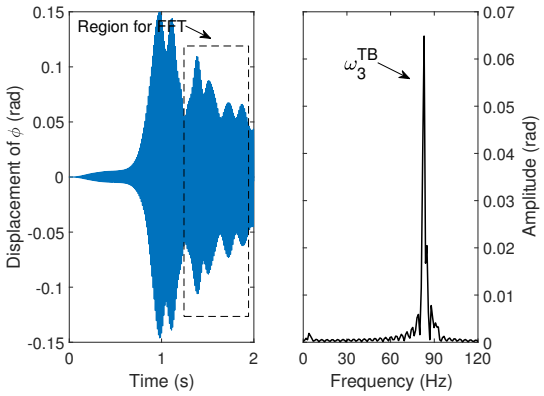

(c) *The twist* ϕ

Figure 6.24: *The responses at the* 80% *span and the corresponding frequency-domain analysis when energy is input from* ω_2^{BE} *mode*

When energy is input from ω_4^{TB}, ω_3^{TB} or ω_1^{TB} mode

The numerical study in section 6.7 points out that when energy is input from ω_4^{TB}, ω_3^{TB} or ω_1^{TB} mode, there will be no modal interactions. As a result, the external resonance will dominate the primary resonance and the internal resonance can be ignored.

First of all, for the case when energy is input from ω_4^{TB} mode, the normal vertical pressure distributed uniformly on the top and bottom walls of the wing structure with magnitude specified as 5 kpa and frequency specified as 91.0 Hz is considered as the external excitation. Based on the previous theoretical study, ω_4^{TB} mode involves in the internal resonance $\omega_4^{TB} \approx \omega_w^{BE} + \omega_1^{TB}$. However, neither apparent ω_2^{BE} frequency component in the lateral bending response in Fig. 6.25a nor ω_1^{TB} frequency component in the vertical bending response in Fig. 6.25b or in the twist response in Fig. 6.25c can be found. In addition, compared with the vertical bending amplitude in Fig. 6.25b, the lateral bending amplitude in Fig. 6.25a is negligible. Thus, we can conclude that when energy is input from ω_4^{TB} mode, the external resonance dominates the system and the responses of BE-subsystem can be ignored. This conclusion agrees with our theoretical prediction.

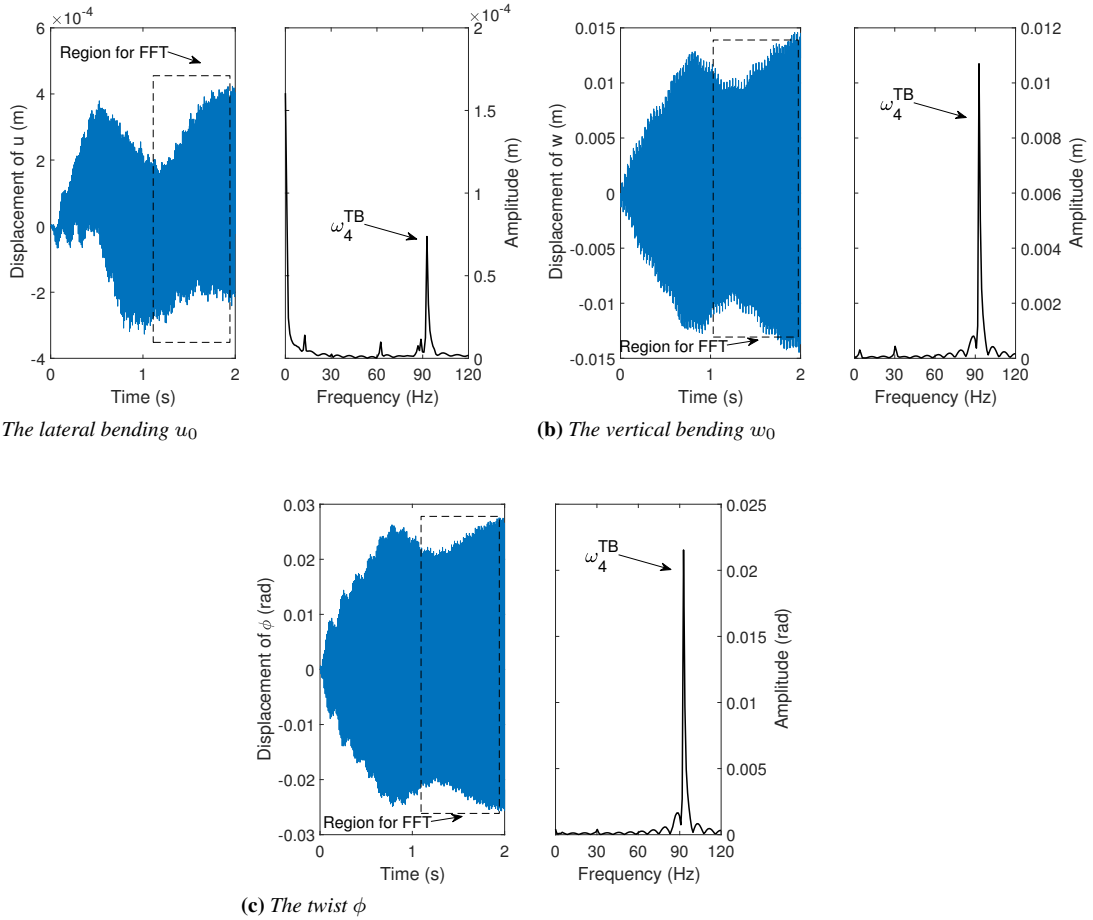

(a) *The lateral bending* u_0

(b) *The vertical bending* w_0

(c) *The twist* ϕ

Figure 6.25: *The responses at the* 80% *span and the corresponding frequency-domain analysis when energy is input from* ω_4^{TB} *mode*

For the case when energy is input from ω_3^{TB} mode, similar conclusion can be obtained from the results of Figs. 6.26a, 6.26b and 6.26c. In this case, frequency of the external excitation is specified as 84.5 Hz.

At last, when energy is input from ω_1^{TB} mode, the vertical pressure distributed uniformly on the top and bottom walls of the wing with magnitude specified as 0.5 kpa and

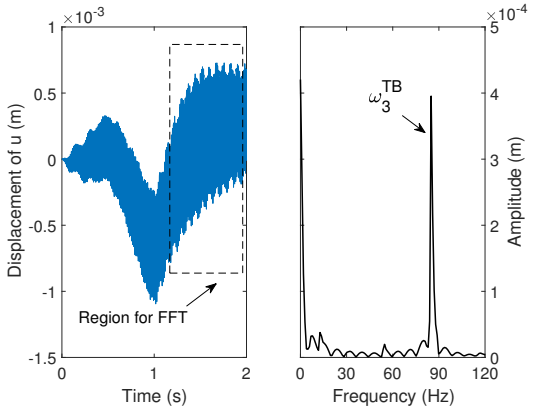

(a) *The lateral bending* u_0

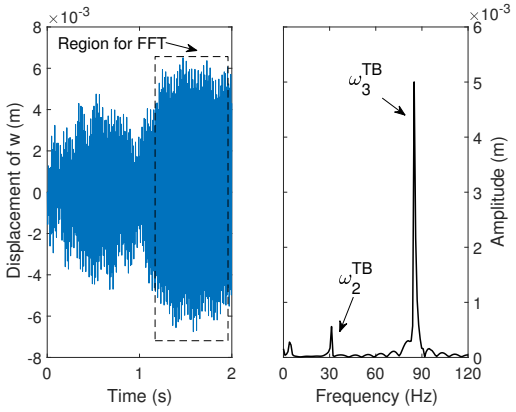

(b) *The vertical bending* w_0

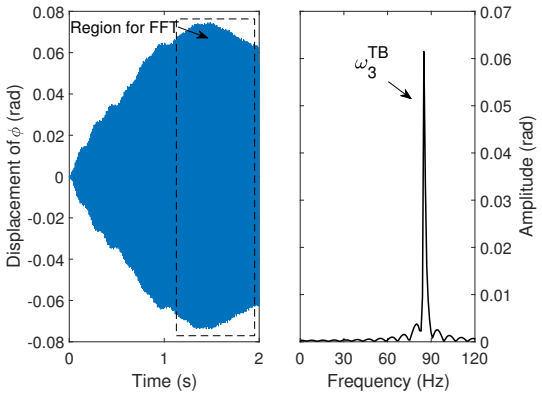

(c) *The twist* ϕ

Figure 6.26: *The responses at the* 80% *span and the corresponding frequency-domain analysis when energy is input from* ω_3^{TB} *mode*

frequency specified as $4.0\,\mathrm{Hz}$ is considered. From the responses of the system depicted in Figs. 6.27a, 6.27b and 6.27c, no evidence for internal resonance $\omega_4^{TB} \approx \omega_2^{BE} + \omega_1^{TB}$ or $\omega_2^{BE} \approx \omega_3^{TB} + \omega_1^{TB}$ can be found.

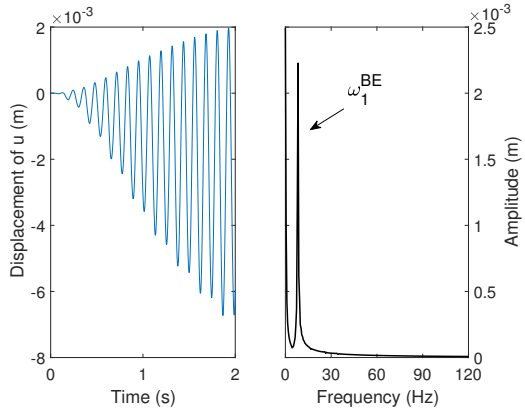

(a) *The lateral bending* u_0

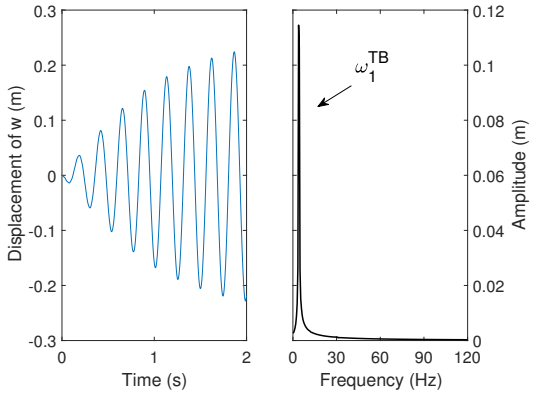

(b) *The vertical bending* w_0

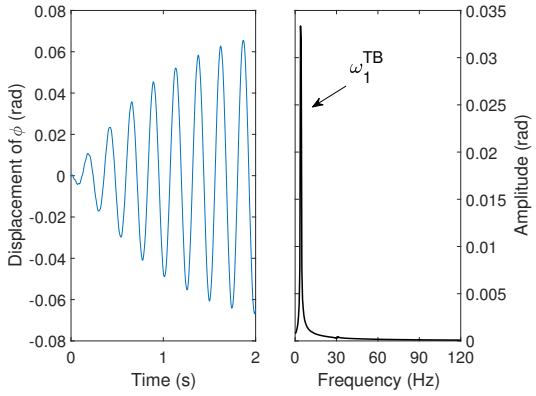

(c) *The twist* ϕ

Figure 6.27: *The responses at the* 80% *span and the corresponding frequency-domain analysis when energy is input from* ω_1^{TB} *mode*

CHAPTER 7

Aeroelasticity Control of Adaptive Aircraft Wings

7.1 Introduction

In this chapter, active control of swept smart aircraft wings in an incompressible flow and exposed to gust loads are examined. The wing structure is modeled as a composite thin-walled beam featuring fiber-reinforced host structure and piezo-composite actuators. The nonclassical effects, such as twist-bending elastic coupling, warping inhibition, transverse shear and rotatory inertia are incorporated. The unsteady incompressible aerodynamics are derived based on the concept of indicial functions, applicable to arbitrary small motion in the time domain. The influence of directionality property both of the host structure and piezo-actuators on improving aeroelastic performance are specifically investigated. A number of conclusions are outlined at the end.

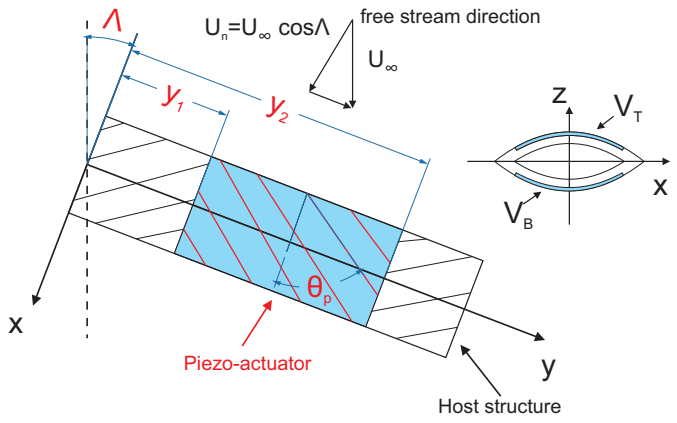

Figure 7.1: *Aircraft wing structure*

7.2 3-D unsteady aerodynamic loads in incompressible flow

Based on the two-dimensional incompressible unsteady strip theory aerodynamics, the aerodynamic lift L_{ae} and twist moment T_{ae} about the beam coordinate system $oxyz$ in Fig. 7.1 can be expressed in the time domain [76]

$$L_{ae}(y,t) = \underline{-\pi\rho_\infty b^2 \left[\dot{w}_{c/2}(y,t)\right]} - L_C(y,t), \tag{7.1a}$$

$$T_{ae}(y,t) = \underline{-\pi\rho_\infty b^3 \left[\frac{1}{2}U_n\dot{\phi}(y,t) + \frac{1}{8}b\ddot{\phi}(y,y)\right]} - \frac{1}{2}bL_C(y,t). \tag{7.1b}$$

In these equations, the underscored terms are associated with non-circulatory part of aerodynamic loads (e.g., see Ref. [39]); U_n is the freestream speed normal to the leading edge (see Fig. 7.1); $w_{c/2}$ denotes the downwash at the middle chord points measured from the leading edge of the airfoil; Λ denotes the sweep angle (positive backward, see Fig. 7.1); and the circulatory lift force L_C can be written as [76]

$$L_C(y,t) = 2\pi\rho_\infty U_n b \left\{ w_{3c/4}(y,t)\phi_w\left(\frac{U_n}{b}t\right) + \int_0^t \frac{\mathrm{d}\, w_{3c/4}(y,\tau)}{\mathrm{d}\,\tau}\phi_w\left[\frac{U_n}{b}(t-\tau)\right]\mathrm{d}\,\tau \right\}, \tag{7.2}$$

where ϕ_w is Wagner's function, which is related to Theodoresn's lift deficiency function through a Fourier transform; $w_{3c/4}$ denotes the downwash at the three quarters chord point.

Actually, the previous results are valid for two-dimensional cross-section wings. In order to extend the 2-D aerodynamics to 3-D one, the modified strip theory for a finite-span wing is used [15, 83]. Taking into account the sweep angle Λ, the lift curve slope 2π and the downwash boundary condition for the 2-D aerodynamics model are modified partially to account for the finite-span effects [9]:

$$2\pi \to C_{L\phi} \equiv \frac{\mathrm{d}\, C_L}{\mathrm{d}\,\phi} = \frac{L}{L + 2b\cos\Lambda}2\pi, \quad \frac{1}{2}b \to \left[\frac{C_{L\phi}}{2\pi} - \frac{1}{2}\right]b. \tag{7.3}$$

Note that only circulatory lift L_C in Eq. (7.2) should be modified.

In connection with the geometric transformations, the downwash velocities at middle and three quarters chord points of the profile related to the rotated chordwise coordinate system are

$$w_{c/2}(y,t) = \dot{w}_0(y,t) - U_n\phi(y,t) + U_n\tan\Lambda\frac{\partial w_0(y,t)}{\partial y}, \tag{7.4a}$$

$$\begin{aligned} w_{3c/4}(y,t) =& \dot{w}_0(y,t) - U_n\phi(y,t) + U_n\tan\Lambda\frac{\partial w_0(y,t)}{\partial y} \\ & - \frac{b}{2}\left[\frac{\partial\phi(y,t)}{\partial t} + U_n\frac{\partial\phi(y,t)}{\partial y}\tan\Lambda\right]\left[\frac{C_{L\phi}}{\pi} - 1\right]. \end{aligned} \tag{7.4b}$$

7.2.1 State space form

To cast L_{ae} and T_{ae} into state space form, a general two term exponentially growing indicial function ϕ_w in Eq. (7.2) is assumed such that [8, 37]

$$\begin{aligned}\phi_w(t) &= 1.0 - \alpha_1 e^{-\beta_1 \frac{U_n}{b} t} - \alpha_2 e^{-\beta_2 \frac{U_n}{b} t} \\ &= 1.0 - 0.165 e^{-0.0455 \frac{U_n}{b} t} - 0.355 e^{-0.3 \frac{U_n}{b} t}.\end{aligned} \tag{7.5}$$

By denoting

$$\begin{aligned}D(y,t) &= w_{3c/4}(y,0)\phi_w(t) + \int_0^t \frac{\mathrm{d}\, w_{3c/4}(y,\tau)}{\mathrm{d}\,\tau}\phi_w(t-\tau)\,\mathrm{d}\,\tau \\ &\approx w_{3c/4}(y,t) - \alpha_1 B_1(y,t) - \alpha_2 B_2(y,t),\end{aligned} \tag{7.6}$$

where $B_i(y,t)$ satisfies the condition [76]

$$\dot{B}_i(y,t) + \left(\frac{U_n}{b}\beta_i\right) B_i(y,t) = \dot{w}_{3c/4}(y,t), \quad i = 1,\, 2. \tag{7.7}$$

Thus the unsteady aerodynamic lift and twist moment can be expressed in state space form as

$$\begin{aligned}L_{ae}(y,t) = -\pi\rho_\infty b^2 \left[\ddot{w}_0 + U_n \dot{w}_0' \tan\Lambda - U_n\dot{\phi}\right] - C_{L\phi}\rho_\infty U_n b \Bigg[\dot{w}_0 - U_n\phi \\ + U_n w_0' \tan\Lambda - \frac{b}{2}\left(\frac{C_{L\phi}}{\pi} - 1\right)\left(\dot{\phi} + U_n\phi'\tan\Lambda\right) - \alpha_1 B_1 - \alpha_2 B_2\Bigg],\end{aligned} \tag{7.8a}$$

$$\begin{aligned}T_{ae}(y,t) = -\pi\rho_\infty b^3 \Bigg\{ \left[\frac{1}{2}\left(\frac{C_{L\phi}}{\pi} - 1\right)\left(U_n\dot{\phi} + {U_n}^2\phi'\tan\Lambda\right)\right] \\ + \frac{1}{8}b\left[\ddot{\phi} + U_n\dot{\phi}'\tan\Lambda\right]\Bigg\} - \frac{1}{2}C_{L\phi}\rho_\infty U_n b^2 \Bigg\{\dot{w}_0 - U_n\phi + U_n w_0'\tan\Lambda \\ - \frac{b}{2}\left(\frac{C_{L\phi}}{\pi} - 1\right)\left(\dot{\phi} + U_n\phi'\tan\Lambda\right) - \alpha_1 B_1 - \alpha_2 B_2\Bigg\}.\end{aligned} \tag{7.8b}$$

7.2.2 Gust Loads

Based on Duhamel's convolution integral and the indicial function for an arbitrary gust $w_G(t)$, the induced aerodynamic lift is expressed as [9]

$$L_g(t) = C_{L\phi} b U_n \left[w_G(0)\psi_K(t) + \int_0^t \frac{\partial w_G(\tau)}{\partial\tau}\psi_K(t-\tau)\,\mathrm{d}\,\tau\right], \tag{7.9}$$

where in the practical calculation, the Kussner's Function ψ_K can be approximated by the following exponential form

$$\psi_K(t) = 1 - 0.500 e^{-0.130 \frac{U_n}{b} t} - 0.500 e^{-1.00 \frac{U_n}{b} t}, \quad t > 0. \tag{7.10}$$

As proved by von Kármán and Sears [95], the gust embedded in the atmosphere and flowing with the atmosphere always acts at the quarter chord position, even when the aerodynamic load is not completely circulatory. For simplicity, it is assumed that the gust is not affected by the penetration of the wing. Thus, the aerodynamic moment about the reference axis due to the gust can be expressed as

$$T_g(t) = \frac{1}{2} b L_g(t) = \frac{1}{2} C_{L\phi} b^2 U_n \left[w_G(0)\psi_K(t) + \int_0^t \frac{\partial w_G(\tau)}{\partial \tau} \psi_K(t-\tau)\,\mathrm{d}\,\tau \right]. \quad (7.11)$$

In general, a gust can be specified by the gust intensity, gradient and its profile. Here, with the assumption the gust intensity is uniformly distributed along the span, the following Sharp-edged gust is used in the present study

$$w_G(\tau) = H(\tau) U_g, \quad (7.12)$$

where U_g is the peak gust velocity.

7.3 Dynamical model

The structure model of the adaptive aircraft wing is based on the thin-walled beam model we developed in Chapter 2. Indicated in Chapter 5, the beam system will decoupled into two subsystems, viz., one governing vertical bending-twist coupling motion and the the other governing extension-lateral bending couping motion, when applying circumferentially asymmetric stiffness (CAS) lay-up configuration. Taking into account the aerodynamic model in section 7.2, the governing equations and the associated boundary conditions of the aeroelastic system can be derived from Hamilton's principle [75]. After a lengthy variation process and collecting the terms associated with the same variations (δw_0, $\delta\phi$ and $\delta\theta_x$), the linear governing equations of the bending-twist subsystem that are of interest for the present problem are

$$\delta w_0 : \ \bar{Q}_z' + \tilde{Q}_z' + L_{ae} + L_g - b_1 \ddot{w}_0 = 0, \quad (7.13a)$$

$$\delta\phi : \ \bar{M}_y' + \tilde{M}_y' - \bar{B}_w'' - \tilde{B}_w'' + T_{ae} + T_g - (b_4 + b_5)\ddot{\phi} + (b_{10} + b_{18})\ddot{\phi}'' = 0, \quad (7.13b)$$

$$\delta\theta_x : \ \bar{M}_x' + \tilde{M}_x' - \bar{Q}_z - \tilde{Q}_z - (b_4 + b_{14})\ddot{\theta}_x = 0, \quad (7.13c)$$

the associated boundary conditions at the beam root are

$$w_0(0) = \phi(0) = \phi'(0) = \theta_x(0) = 0, \quad (7.14)$$

and at the beam tip are

$$\delta w_0 : \ \bar{Q}_z(L) + \tilde{Q}_z(L) = 0, \quad (7.15a)$$

$$\delta\phi : \ \bar{M}_y(L) + \tilde{M}_y(L) - B_w'(L) - \tilde{B}_w'(L) + (b_{10} + b_{18})\ddot{\phi}'(L) = 0, \quad (7.15b)$$

$$\delta\phi' : \ \bar{B}_w(L) + \tilde{B}_w(L) = 0, \quad (7.15c)$$

$$\delta\theta_x : \ M_x(L) + \tilde{M}_x(L) = 0. \quad (7.15d)$$

The above aeroelastic model is valid for the thin-walled beam with an arbitrary closed cross-section, however we will consider rectangular and biconvex these two typical cross-section cases in the following discussions.

7.3.1 Rectangular cross-section

Based on the thin-walled box beam theory in section 5.2, the governing equations (7.13) for the rectangular cross-section can be simplified as

$$\delta w_0 \ : \ a_{55}(w_0'' + \theta_x') - b_1\ddot{w}_0 + L_{ae} + L_g + \delta_p \mathcal{A}_4^{Qz} V_4 R'(y) = 0, \tag{7.16a}$$

$$\begin{aligned}\delta\phi \ : a_{37}\theta_x'' + a_{77}\phi'' - a_{66}\phi^{(iv)} - (b_4 + b_5)\ddot{\phi} + (b_{10} + b_{18})\ddot{\phi}'' \\ + T_{ae} + T_g + \delta_p \mathcal{A}_1^{My} V_1 R'(y) + \delta_p \mathcal{A}_3^{My} V_3 R'(y) = 0,\end{aligned} \tag{7.16b}$$

$$\begin{aligned}\delta\theta_x \ : a_{33}\theta_x'' + a_{37}\phi'' - a_{55}(w_0' + \theta_x) - (b_4 + b_{14})\ddot{\theta}_x + \delta_p \mathcal{A}_1^{Mx} V_1 R'(y) \\ 5 - (\delta_p + \delta_s)\mathcal{A}_4^{Qz} V_4 R(y) = 0.\end{aligned} \tag{7.16c}$$

The associated boundary conditions are
at $y = 0$:

$$w_0 = \phi = \phi' = \theta_x = 0, \tag{7.17}$$

and at $y = L$:

$$\delta w_0 \ : a_{55}(w_0' + \theta_x) + \delta_s \mathcal{A}_4^{Qz} V_4 = 0, \tag{7.18a}$$

$$\delta\phi \ : a_{37}\theta_x' + a_{77}\phi' - a_{66}'''\phi + (b_{10} + b_{18})\ddot{\phi}' + \delta_s \mathcal{A}_1^{My} V_1 + \delta_s \mathcal{A}_3^{My} V_3 = 0, \tag{7.18b}$$

$$\delta\phi' \ : \ a_{66}\phi'' = 0, \tag{7.18c}$$

$$\delta\theta_x \ : a_{33}\theta_x' + a_{37}\phi' + \delta_s \mathcal{A}_1^{Mx} V_1 = 0, \tag{7.18d}$$

7.3.2 Biconvex cross-section

For the biconvex cross-section, the stiffness matrix $[a_{ij}]$ in Eq. (2.33) can be decoupled into four parts when applying the circumferential asymmetric stiffness (CAS) lay-up configuration, viz., extension-chordwise transverse shear coupling

$$\begin{Bmatrix} \hat{T}_y \\ \hat{Q}_x \\ \hat{\Gamma}_t \end{Bmatrix} = \begin{bmatrix} a_{11} & a_{14} & a_{18} \\ a_{14} & a_{44} & a_{48} \\ a_{18} & a_{48} & a_{88} \end{bmatrix} \begin{Bmatrix} v_0' + \frac{1}{2}(u_0')^2 + \frac{1}{2}(w_0')^2 \\ \theta_z + u_0' \cos\phi - w_0' \sin\phi \\ \frac{1}{2}(\phi')^2 \end{Bmatrix}, \tag{7.19a}$$

chordwise bending

$$\left\{\hat{M}_z\right\} = \left[a_{22}\right]\left\{\theta_z' - w_0'\phi' \cos\phi - u_0'\phi' \sin\phi\right\}, \tag{7.19b}$$

twist-flapwise bending coupling

$$\begin{Bmatrix} \hat{M}_x \\ \hat{M}_y \end{Bmatrix} = \begin{bmatrix} a_{33} & a_{37} \\ a_{37} & a_{77} \end{bmatrix} \begin{Bmatrix} \theta_x' + u_0'\phi' \cos\phi - w_0'\phi' \sin\phi \\ \phi' \end{Bmatrix}, \tag{7.19c}$$

and flapwise transvser shear-bimoment coupling

$$\begin{Bmatrix} \hat{Q}_z \\ \hat{B}_w \end{Bmatrix} = \begin{bmatrix} a_{55} & a_{56} \\ a_{56} & a_{66} \end{bmatrix} \begin{Bmatrix} \theta_x + u_0' \sin\phi + w_0' \cos\phi \\ \phi'' \end{Bmatrix}. \tag{7.19d}$$

As for the piezo-actuators of Fig. 7.1, Eq. (2.35) can also be decoupled into two actuation couplings, viz., twist-flapwise bending coupling

$$\begin{Bmatrix} \tilde{M}_x(y,t) \\ \tilde{M}_y(y,t) \end{Bmatrix} = \begin{bmatrix} \mathcal{A}_1^{Mx} \\ \mathcal{A}_1^{My} \end{bmatrix} V_1(t)P(y), \tag{7.20a}$$

extension-chordwise transverse shear coupling

$$\begin{Bmatrix} \tilde{T}_y(y,t) \\ \tilde{Q}_x(y,t) \\ \tilde{\Gamma}_t \end{Bmatrix} = \begin{bmatrix} \mathcal{A}_2^{My} \\ \mathcal{A}_2^{Mx} \\ \mathcal{A}_2^{\Gamma_t} \end{bmatrix} V_2(t)P(y). \tag{7.20b}$$

As for the piezoelectrically induced flapwise transverse shear $\tilde{Q}_z$, chordwise bending $\tilde{M}_z$ and bimoment $\tilde{B}_w$, they are immaterial.

Taking Eqs. (7.19) and (7.20) into governing equations (7.13), as a result, the linear governing equations of the thin-walled beam with a biconvex cross-section expressed in terms of the basic unknowns are

$$\delta w_0 \ : \ a_{55}(w_0'' + \theta_x') + a_{56}\phi''' - b_1\ddot{w}_0 + L_{ae} + L_g = 0, \tag{7.21a}$$

$$\begin{aligned} \delta\phi \ : a_{37}\theta_x'' + a_{77}\phi'' - a_{66}\phi^{(iv)} - a_{56}(w_0''' + \theta_x'') - (b_4 + b_5)\ddot{\phi} + (b_{10} + b_{18})\ddot{\phi}'' \\ + T_{ae} + T_g + \delta_p\mathcal{A}_1^{My}V_1R'(y) = 0, \end{aligned} \tag{7.21b}$$

$$\delta\theta_x \ : a_{33}\theta_x'' + a_{37}\phi'' - a_{55}(w_0' + \theta_x) - a_{56}\phi'' - (b_4 + b_{14})\ddot{\theta}_x + \delta_p\mathcal{A}_1^{Mx}V_1R'(y) = 0, \tag{7.21c}$$

the associated boundary conditions are
at $y = 0$:

$$w_0 = \phi = \phi' = \theta_x = 0, \tag{7.22}$$

and at $y = L$:

$$\delta w_0 \ : a_{55}(w_0' + \theta_x) + a_{56}\phi'' = 0, \tag{7.23a}$$

$$\delta\phi \ : a_{37}\theta_x' + a_{77}\phi' - a_{66}'''\phi - a_{56}(w_0'' + \theta_x') + (b_{10} + b_{18})\ddot{\phi}'' + \delta_s\mathcal{A}_1^{My}V_1 = 0, \tag{7.23b}$$

$$\delta\phi' \ : \ -a_{56}(w_0' + \theta_x) - a_{66}\phi'' = 0, \tag{7.23c}$$

$$\delta\theta_x \ : a_{33}\theta_x' + a_{37}\phi' + \delta_s\mathcal{A}_1^{Mx}V_1 = 0. \tag{7.23d}$$

Note that the traces are $\delta_p = 0$ and $\delta_s = 1$ for the case the actuator is spread over the entire beam span, otherwise their values are assumed as $\delta_p = 1$ and $\delta_s = 0$. In the previous case the bending moment piezo-coefficient $\mathcal{A}_1^{Mx}$ and torque piezo-coefficient $\mathcal{A}_1^{My}$ appear in the governing equations; while in the later case they appear solely in the boundary conditions at $y = L$, their contribution in the governing equations being immaterial. The whole aeroelastic system is controlled solely by the voltage parameter V_1.

Note that, unless other states, we solely consider the aircraft wing with a biconvex cross-section in the following discussions.

7.4 Solution methodology

7.4.1 State-space solution

Due to the high complexity arising from the elastic couplings and the boundary conditions, the spatial discretization via the extended Galerkin's method [45, 70] is implemented to cast the governing equations in state-space form. Thus the following spatial semi-discretization is introduced:

$$w_0(y,t) = \boldsymbol{\Psi}_w{}^T(y)\mathbf{q}_w(t), \quad \phi(y,t) = \boldsymbol{\Psi}_\phi{}^T(y)\mathbf{q}_\phi(t), \quad \theta_x(y,t) = \boldsymbol{\Psi}_x{}^T(y)\mathbf{q}_x(t), \tag{7.24}$$

where the $1 \times N$ shape functions $\boldsymbol{\Psi}_w{}^T(y)$, $\boldsymbol{\Psi}_\phi{}^T(y)$ and $\boldsymbol{\Psi}_x{}^T(y)$ are required to fulfill only the geometric boundary conditions. In Eq. 7.24, $\mathbf{q}_w(t)$, $\mathbf{q}_\phi(t)$ and $\mathbf{q}_x(t)$ are $N \times 1$ generalized displacement vectors, which, by the modal expansion theorem (e.g., see [58, pp. 171-178]), can be further expressed as:

$$\mathbf{q}_w(t) = \boldsymbol{\Theta}_w\xi_s(t), \quad \mathbf{q}_\phi(t) = \boldsymbol{\Theta}_\phi\xi_s(t), \quad \mathbf{q}_x(t) = \boldsymbol{\Theta}_x\xi_s(t), \tag{7.25}$$

$\boldsymbol{\Theta}_w$, $\boldsymbol{\Theta}_\phi$ and $\boldsymbol{\Theta}_x$ are $N \times m$ matrices consisting of the first m eigenmodes; ξ_s are the modal coordinates (e.g., see [58, p. 199]). Thus the state-space form of the aeroelastic governing equations are obtained as

$$\begin{Bmatrix} \dot{\mathbf{x}}_s \\ \dot{\mathbf{x}}_a \end{Bmatrix} = \begin{bmatrix} \mathbf{A}_s & \mathbf{B}_s \\ \mathbf{B}_a\mathbf{A}_s & \mathbf{A}_a + \mathbf{B}_a\mathbf{B}_s \end{bmatrix} \begin{Bmatrix} \mathbf{x}_s \\ \mathbf{x}_a \end{Bmatrix} + \begin{Bmatrix} \mathbf{0}_{m\times m} \\ \mathbf{M}^{-1} \\ \mathbf{D}_2\mathbf{M}^{-1} \\ \mathbf{D}_2\mathbf{M}^{-1} \end{Bmatrix} \left[\mathbf{Q}_g + \mathcal{A}V_1(t)\right]. \tag{7.26}$$

In Eq. (7.26), $\mathbf{x}_s$ and $\mathbf{x}_a$ are $2m \times 1$ vectors that describe the motion of the wing and unsteady aerodynamic loads on the wing, respectively. The expression of the matrices in Eq. (7.26) are

$$[\mathbf{A}_s]_{2m\times 2m} = \begin{bmatrix} \mathbf{0}_{m\times m} & \mathbf{I}_{m\times m} \\ -\mathbf{M}^{-1}\mathbf{K} & -\mathbf{M}^{-1}\mathbf{C} \end{bmatrix}, \tag{7.27a}$$

$$[\mathbf{B}_s]_{2m\times 2m} = \begin{bmatrix} \mathbf{0}_{m\times 2m} \\ -(C_{L\phi}\rho_\infty bU_n)\mathbf{M}^{-1}\begin{bmatrix}\alpha_1\mathbf{I}_{m\times m} & \alpha_2\mathbf{I}_{m\times m}\end{bmatrix} \end{bmatrix}, \tag{7.27b}$$

$$[\mathbf{A}_a]_{2m\times 2m} = \begin{bmatrix} -\beta_1\mathbf{I}_{m\times m} & \mathbf{0}_{m\times m} \\ \mathbf{0}_{m\times m} & -\beta_2\mathbf{I}_{m\times m} \end{bmatrix}, \tag{7.27c}$$

$$[\mathbf{B}_a]_{2m\times 2m} = \begin{bmatrix} \mathbf{I}_{m\times m} \\ \mathbf{I}_{m\times m} \end{bmatrix} \begin{bmatrix} \mathbf{D}_1 & \mathbf{D}_2 \end{bmatrix}_{m\times 2m}, \tag{7.27d}$$

$$\mathbf{D}_1 = \int_0^L \Big(\boldsymbol{\Theta}_w{}^T\boldsymbol{\Psi}_w + \frac{1}{2}b\boldsymbol{\Theta}_\phi{}^T\boldsymbol{\Psi}_\phi\Big)U_n\Big[\boldsymbol{\Psi}'_w{}^T\boldsymbol{\Theta}_w\dot{\xi}_s\tan\Lambda - \boldsymbol{\Psi}'_\phi{}^T\boldsymbol{\Theta}_\phi\dot{\xi}_s - \frac{1}{2}b\boldsymbol{\Psi}'_\phi{}^T\boldsymbol{\Theta}_\phi\dot{\xi}_s\tan\Lambda\Big(\frac{C_{L\phi}}{\pi} - 1\Big)\Big]\,\mathrm{d}\,y, \tag{7.27e}$$

$$\mathbf{D}_2 = \int_0^L \Big(\boldsymbol{\Theta}_w{}^T\boldsymbol{\Psi}_w + \frac{1}{2}b\boldsymbol{\Theta}_\phi{}^T\boldsymbol{\Psi}_\phi\Big)\Big[\boldsymbol{\Psi}_w{}^T\boldsymbol{\Theta}_w\ddot{\xi}_s - \frac{1}{2}b\boldsymbol{\Psi}_\phi{}^T\boldsymbol{\Theta}_\phi\ddot{\xi}_s\Big(\frac{C_{L\phi}}{\pi} - 1\Big)\Big]\,\mathrm{d}\,y, \tag{7.27f}$$

$$\mathbf{Q}_g = \frac{1}{2}C_{L\phi}b^2U_n\left[w_G(0)\psi_K(t) + \int_0^t \frac{\partial w_G(\tau)}{\partial\tau}\psi_K(t-\tau)\,\mathrm{d}\,\tau\right] \times \int_0^L \left[\boldsymbol{\Theta}_w{}^T\boldsymbol{\Psi}_w + \frac{b}{2}\boldsymbol{\Theta}_\phi{}^T\boldsymbol{\Psi}_\phi\right]\mathrm{d}\,y, \tag{7.27g}$$

$$\mathcal{A} = \int_0^L \left[\mathcal{A}_1^{My} \mathbf{\Theta}_\phi{}^T \mathbf{\Psi}_\phi + \mathcal{A}_1^{Mx} \mathbf{\Theta}_x{}^T \mathbf{\Psi}_x \right] P'(y)\, \mathrm{d}\, y. \tag{7.27h}$$

In the above equations, $\mathbf{M}$ and $\mathbf{K}$ are the mass and stiffness matrices of the wing structure; $\mathbf{C}$ is the pneumatic damping matrix; $\mathbf{Q}_g$ denotes the external gust loads; $\mathcal{A}$ is the actuating matrix; $\mathbf{D}_1$ and $\mathbf{D}_2$ are related to Wagner's function.

7.4.2 Velocity feedback control

In order to study the influence of anisotropic characteristics of the piezo-composite layer on control authority, a negative velocity feedback control algorithm is applied. Recalling governing equations (7.21), the ply-angle θ_p of piezo-actuator just affects the piezoelectric bending moment and twist actuations. Thus the actuating voltage $V_1(t)$ can be computed as two cases [97], viz., Bending Control Methodology

$$V_1(t) = k_B \dot{\theta}_x(Y_s, t) = k_B \mathbf{\Psi}_x{}^T(Y_s) \mathbf{\Theta}_x \dot{\xi}_s(t), \tag{7.28}$$

and Twist Control Methodology

$$V_1(t) = k_T \dot{\phi}(Y_s, t) = k_T \mathbf{\Psi}_\phi{}^T(Y_s) \mathbf{\Theta}_\phi \dot{\xi}_s(t), \tag{7.29}$$

where k_B and k_T are the control gains; Y_s is span location of the sensor offering the velocity information. Note that the sensor is assumed at the wing tip ($Y_s = L$) unless explicitly stated. Thus the closed-loop system Eq. (7.26) becomes

$$\begin{Bmatrix} \dot{\mathbf{x}}_s \\ \dot{\mathbf{x}}_a \end{Bmatrix} = \begin{bmatrix} \hat{\mathbf{A}}_s & \mathbf{B}_s \\ \mathbf{B}_a \hat{\mathbf{A}}_s & \mathbf{A}_a + \mathbf{B}_a \mathbf{B}_s \end{bmatrix} \begin{Bmatrix} \mathbf{x}_s \\ \mathbf{x}_a \end{Bmatrix} + \begin{Bmatrix} \mathbf{0}_{m\times m} \\ \mathbf{M}^{-1} \\ \mathbf{D}_2 \mathbf{M}^{-1} \\ \mathbf{D}_2 \mathbf{M}^{-1} \end{Bmatrix} \mathbf{Q}_g, \tag{7.30}$$

where

$$[\hat{\mathbf{A}}_s]_{2m\times 2m} = \begin{bmatrix} \mathbf{0}_{m\times m} & \mathbf{I}_{m\times m} \\ -\mathbf{M}^{-1}\mathbf{K} & -\mathbf{M}^{-1}(\mathbf{C} + \mathbf{P}_{T/B}) \end{bmatrix}, \tag{7.31}$$

$$\mathbf{P}_T = k_T \mathcal{A} \mathbf{\Psi}_x{}^T(Y_s) \mathbf{\Theta}_x, \quad \mathbf{P}_B = k_B \mathcal{A} \mathbf{\Psi}_\phi{}^T(Y_s) \mathbf{\Theta}_\phi. \tag{7.32}$$

7.5 Validation

In order to validate our aeroelastic model, the wing structure model in Ref. [49] is used for validation. The material properties and geometric specification of the wing structure are shown in Table 7.1. The CAS lay-up configuration is given in Table 7.2.

Figures 7.2a and 7.2b plot the first five frequencies and the associated damping ratios as functions of freestream speed U_∞, respectively. It can been seen that the lowest flutter speed in Fig. 7.2b and the eigen-frequencies near the onset of flutter in Fig. 7.2a predicted by our approach all show excellent agreements with those in Ref. [49] (see also Table 7.3).

Figure 7.3 further highlights the influence of elastic tailoring on instability boundaries for selected swept wings. When in the domain $0^o < \theta_h < 90^o$, host structure ply-angle θ_h produces a negative elastic bending-twist couping, leading to a very low

Table 7.1: *Material property and geometric specification of the thin-walled beam with a biconvex cross-section [49]*

Material	Value	Geometric	Value
E_{11}	206.8×10^9 N $\cdot$ m^{-2}	Width ($2b^a$)	0.757 m
$E_{22} = E_{33}$	5.17×10^9 N $\cdot$ m^{-2}	Depth ($2d^a$)	0.100 m
$G_{13} = G_{23}$	2.55×10^9 N $\cdot$ m^{-2}	Wall thickness (h)	0.03 m
G_{12}	3.10×10^9 N $\cdot$ m^{-2}	Number of layers (m_h)	6
$\mu_{12} = \mu_{13} = \mu_{23}$	0.25	Aspect ratio	16
ρ	1528 Kg $\cdot$ m^{-3}	Length (L)	6.058 m

[a] The length is measured on the mid-line contour.

Table 7.2: *CAS lay-up configurations for the thin-walled beam[a] of Fig. 7.1 (deg).*

Host structure	Top	Bottom	Piezo-actuator	Top	Bottom
Graphite-Epoxy	$[\theta_h]_6$	$[\theta_h]_6$	MFC	$[\theta_p]$	$[\theta_p]$

[a] The piezo-actuator is positioned of the outer side of the laminate.

divergence speed (indicated by $-\mathrm{o}-$ lines), especially for forward-swept wings. However, when in the domain $95^o < \theta_h < 125^o$, the strong positive elastic bending-twist couping leads to a higher divergence speed. Instead, flutter speed (indicated by $- \times -$ lines) becomes the lowest instability speed.

7.6 Numerical study

7.6.1 Piezo-coefficients study

We assume the piezo-actuator manufactured by MFC [100] is distributed over the entire beam span. The lay-up configuration and material properties are presented in Tables 7.2 and 7.4, respectively.

Figure 7.4 plots the bending moment piezo-coefficient $\mathcal{A}_1^{Mx}$ and torque piezo-coefficient $\mathcal{A}_1^{My}$ as a function of piezo-actuator ply-angle θ_p for selected host structure cases. It can be seen that stiffness of the host structure has a significant effect on piezo-coefficients. In general, centered around $\theta_p = 90^o$, the curves of $\mathcal{A}_1^{Mx}$ and $\mathcal{A}_1^{My}$ exhibit a symmetric and an antisymmetric behavior, respectively. Furthermore, $\theta_p = 90^o$ yields the maximum piezoelectric bending moment while the piezoelectric torque is immaterial.

7.6.2 Damping ratio study for wing structure

In order to focus on the wing structure, we assume the freestream speed $U_\infty = 0$ m $\cdot$ s^{-1} in the aeroelastic system of Eq. (7.30). Recalling the instability boundaries in Fig. 7.3, two typical host structure cases are chosen for specific investigation, i.e., $\theta_h = 105^o$

Table 7.3: *Frequencies of the system near onset of flutter (Hz)*

	Mode 1	Mode 2	Mode 3	Mode 4
Ref. [49]	14.449	15.842	32.205	53.399
Present	14.920	15.688	32.735	52.358

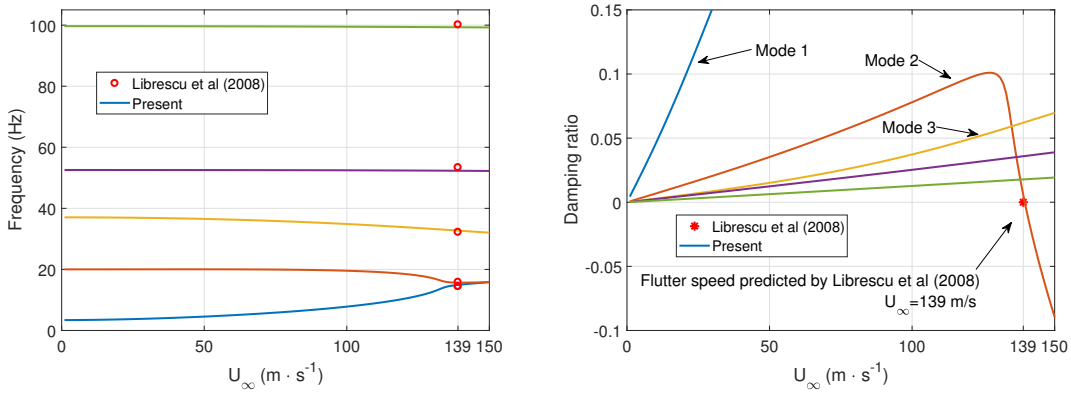

(a) *Frequency* **(b)** *Damping ratio*

Figure 7.2: *Frequencies and damping ratios vs. freestream speed U_∞; $\theta_h = 105^0$, $\Lambda = 0^o$.*

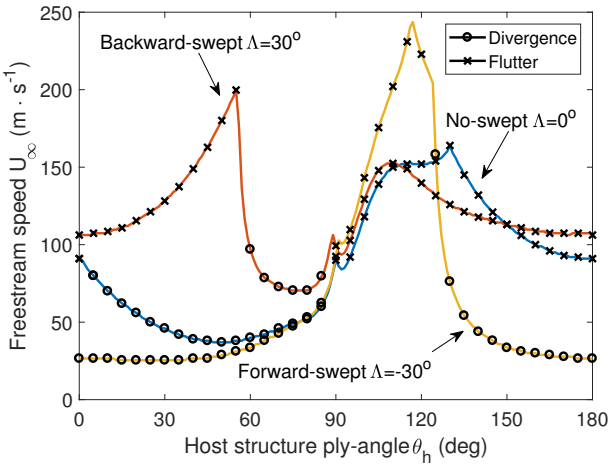

Figure 7.3: *Flutter and divergence velocities vs. host structure ply-angle θ_h.*

Table 7.4: *Material properties of piezo-actuator manufactured by MFC [71]*

E_{11}	$31.2.8 \times 10^9$ N $\cdot$ m^{-2}	d_{11}	386.63×10^{-12} m $\cdot$ V^{-1}
$E_{22} = E_{33}{}^*$	17.05×10^9 N $\cdot$ m^{-2}	$d_{12} = d_{13}{}^*$	-175.50×10^{-12} m $\cdot$ V^{-1}
$G_{12} = G_{13}{}^* = G_{23}{}^*$	5.12×10^9 N $\cdot$ m^{-2}	ρ	5115.9 Kg $\cdot$ m^{-3}
$\mu_{12} = \mu_{13}{}^* = \mu_{23}{}^*$	0.303	m_p	1
Electrode spacing	0.005 m	Thickness	0.005 m

* The value is assumed by the author.

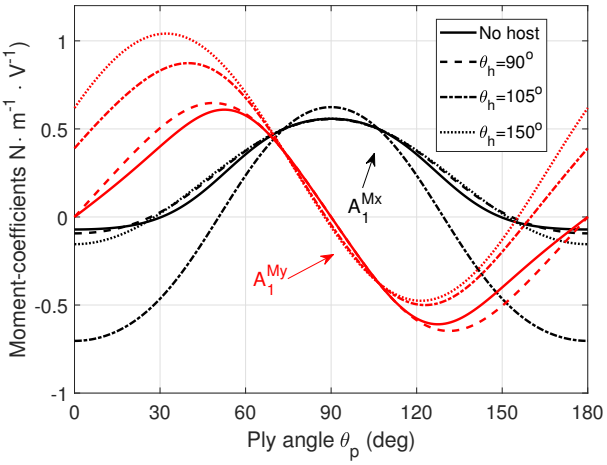

Figure 7.4: *Piezo-coefficients vs. piezo-actuator ply-angle θ_p.*

characterizing strong bending-twist elastic coupling and $\theta_h = 150^o$ characterizing weaker elastic coupling.

For the excellent aeroleastic behavior [43] even for forward-swept wings, the structure with strong elastic coupling case $\theta_h = 105^o$ is investigated firstly. Fig. 7.5 depicts damping ratios of the first four modes as functions of piezo-actuator ply-angle θ_p. It can be found that no matter implementing the bending or the twist control methodology, the trends of all damping ratio curves show a similarity with that of torque piezo-coefficient $\mathcal{A}_1^{My}$ in Fig. 7.4. This implies that piezoelectric torque actuation plays a dominant role in the structure incorporating strong bending-twist elastic couping. Based on the mode shape study, it can be identified that the bending motion is more significant than the twist motion in the first two modes, while the twist motion dominates the third mode. Thus the result of Fig. 7.5 reveals that the twist control will even be more efficient than the direct bending control for bending motions. Note that for the third mode, bending control methodology produces a negative damping ratio while makes the first two modes exhibiting positive damping ratios. On the other hand, twist control methodology shows an extremely large positive damping ratio of the third mode when $\theta_p \approx 45^o$.

For the wing structure ($\theta_h = 150^o$) characterizing weak elastic coupling case, Fig. 7.6 compares damping ratios of the first four modes between twist and control methodologies. It can be found that depending on the mode shape dominated by bending and twist component, bending and twist control methodologies have the better control authority, respectively.

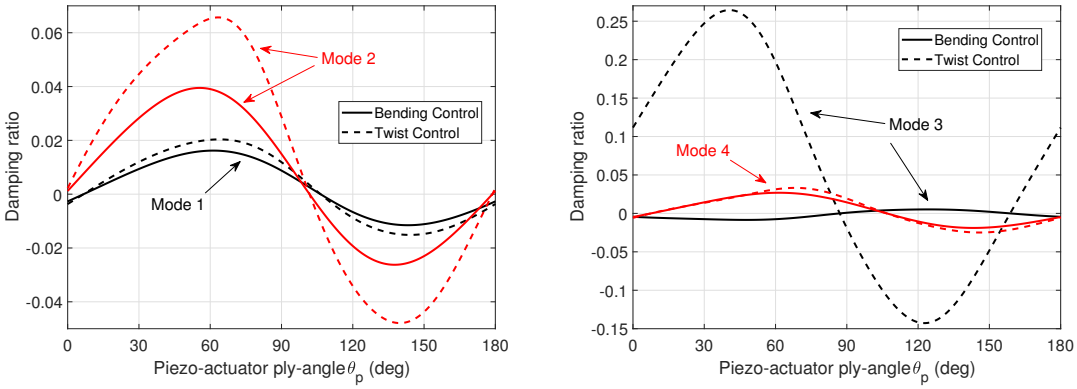

Figure 7.5: *Damping ratios of the first four modes vs. piezo-actuator ply-angle* θ_p*;* $k_B = k_T = 200\ \mathrm{V}\cdot\mathrm{s}$*,* $\theta_h = 105^o$*,* $U_\infty = 0\ \mathrm{m}\cdot\mathrm{s}^{-1}$.

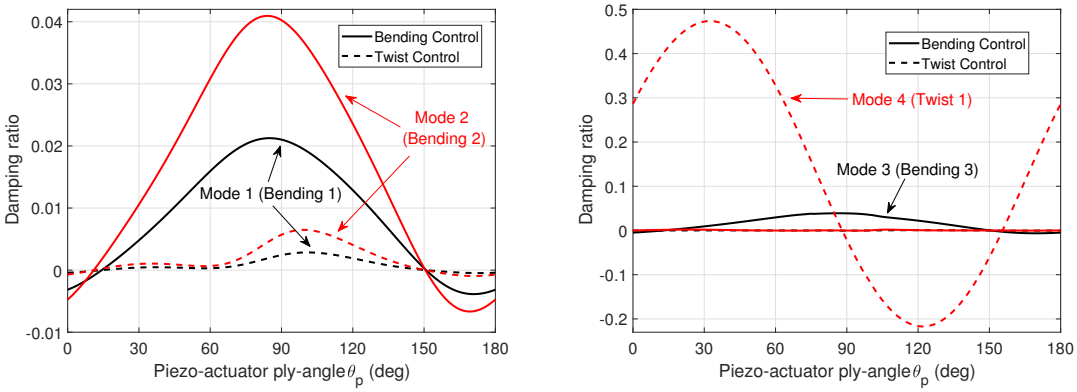

Figure 7.6: *Damping ratios of the first four modes vs. piezo-actuator ply-angle* θ_p*;* $k_B = k_T = 200\ \mathrm{V}\cdot\mathrm{s}$*,* $\theta_h = 150^o$*,* $U_\infty = 0\ \mathrm{m}\cdot\mathrm{s}^{-1}$.

7.6.3 Damping ratio study for aeroelastic system

Figure 7.7 plots damping ratios of the first three modes as functions of piezo-actuator ply-angle θ_p for an unswept wing ($\Lambda = 0^o$) with strong elastic coupling ($\theta_h = 105^o$) at freestream speed $U_\infty = 50\ \mathrm{m \cdot s^{-1}}$. There is no doubt twist control methodology has significantly better control performance. Actually, the aerodynamic load induced damping ratio (indicated by dotted lines) is large enough on the first mode in Fig. 7.7. Thus in order to improve the flight stability, more attention should be focused on the higher modes, especially the mode dominated by twist motion. In summary, twist control with $\theta_p \approx 60^o$ can offer a balanced control performance for the first three modes.

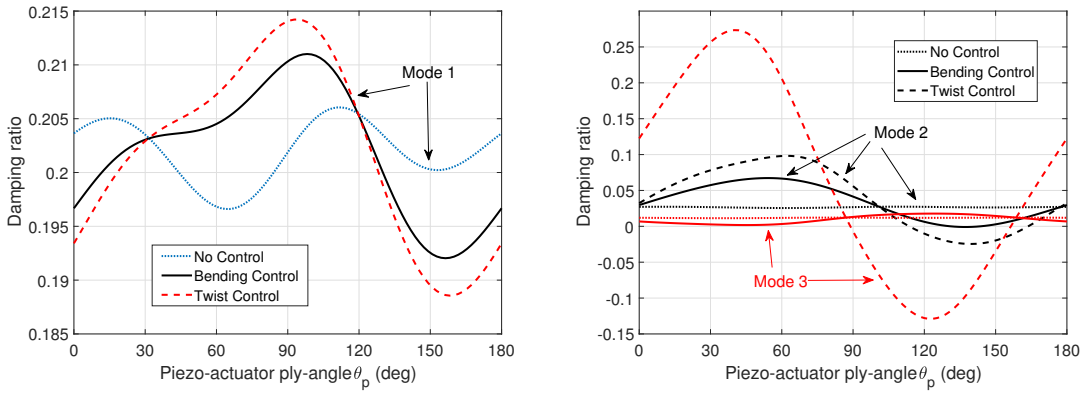

Figure 7.7: *Damping ratio of the first three modes vs. piezo-actuator ply-angle* θ_p*;* $k_B = k_T = 200\ \mathrm{V \cdot s}$, $\theta_h = 105^o$, $U_\infty = 50\ \mathrm{m \cdot s^{-1}}$, $\Lambda = 0^o$.

Damping ratios of the aeroelastic system with weak bending-twist elastic coupling ($\theta_h = 150^o$) are reported in Fig. 7.8. In view of physical evidence that on the one hand aerodynamic lift and twist loads may enhance the coupling of twist-bending motion, on the other hand the aerodynamic load induced damping is already strong enough on bending motion, the twist control seems more essential than the bending control. Thus twist control with $\theta_p \approx 30^o$ is suggested for the aeroelastic system of $\theta_h = 150^o$.

7.6.4 Post-flutter study

One important target of active aeroelastic control is preventing or delaying the occurrence of flutter. Fig. 7.9 highlights the influence of additional piezo-composite layers on the lowest flutter speed. In Fig. 7.9, compared with the predicted flutter speed when ignoring the piezo-actuator plotted as solid lines, the additional mass and stiffness of piezo-composite layers have a significant effect on flutter speed, which are indicated by dashed lines. Specifically, ignoring the effect of mass and stiffness of the piezo-actuator in the modeling process may induce a maximum error over 30%.

Firstly, an unswept wing ($\Lambda = 0^o$) with weak bending-twist elastic couping ($\theta_h = 150^o$) is considered to study the active control near the onset of flutter. In Fig. 7.9, it can be found that the lowest flutter speed varies from $130\ \mathrm{m \cdot s^{-1}}$ to $149\ \mathrm{m \cdot s^{-1}}$ with the change of piezo-actuator ply-angle θ_p. Thus a freestream speed $U_\infty = 151\ \mathrm{m \cdot s^{-1}}$ is applied to investigate the post-flutter control performance. Based on the associated

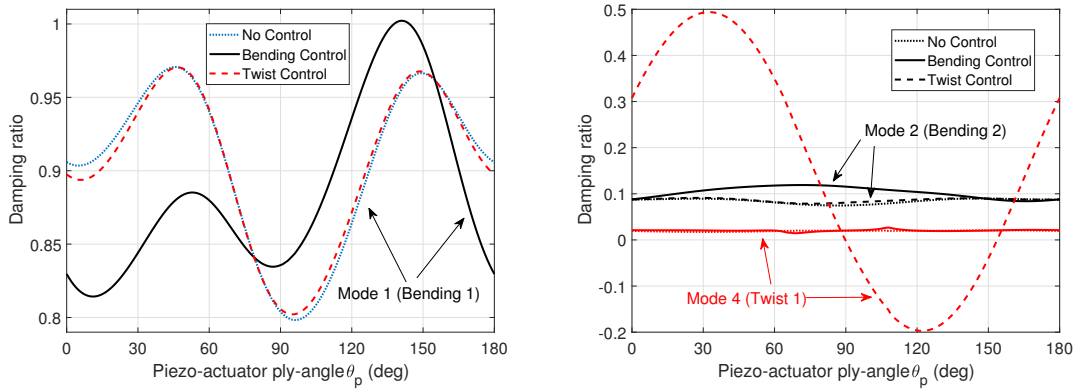

Figure 7.8: *Damping ratios vs. piezo-actuator ply-angle* θ_p*;* $k_B = k_T = 200$ V · s, $\theta_h = 150^o$, $U_\infty = 50$ m · s^{-1}, $\Lambda = 0^o$.

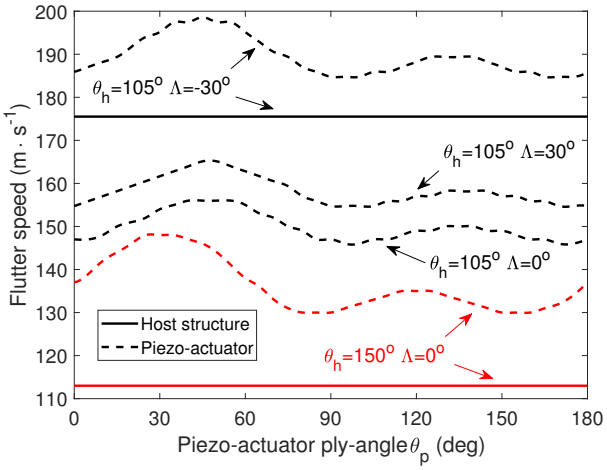

Figure 7.9: *Lowest flutter speed vs. piezo-actuator ply-angle* θ_p *for selected host structure and sweep angle combinations.*

eigenvalue and eigenvector study, it can be verified that the twist component dominates the unstable mode shape, viz., the lowest flutter is dominated by the twist motion.

Figure 7.10a depicts damping ratio of the unstable mode as a function of piezo-actuator ply-angle θ_p for controlled and uncontrolled cases. Without control, the aerodynamic load will produce a negative damping ratio of the lowest twist mode which is indicated by the dotted line. When applying the twist control, the flutter mode will be stable when $0^o < \theta_p < 70^o$. On the contrary, bending control will make the flutter instability even worse. Note that, the damping ratio curves in Fig. 7.10a may present a sudden change (non-smooth) during the mode cross point (see, e.g. [97]).

In order to further investigate the influence of these two control methodologies on flutter speed, piezo-actuator with ply-angle $\theta_p = 30^o$ is selected to demonstrate the damping ratios near the onset of flutter in Fig. 7.10b. Since the flutter mode is dominated by twist motion (in dotted line), bending control (in solid line) will decrease the lowest flutter speed. On the contrary, twist control (in dashed line) will improve the

stability of the lowest twist mode and increase the lowest flutter speed significantly. Note that the lowest bending mode will become the flutter mode instead of the lowest twist mode when the aeroelastic system is under twist control.

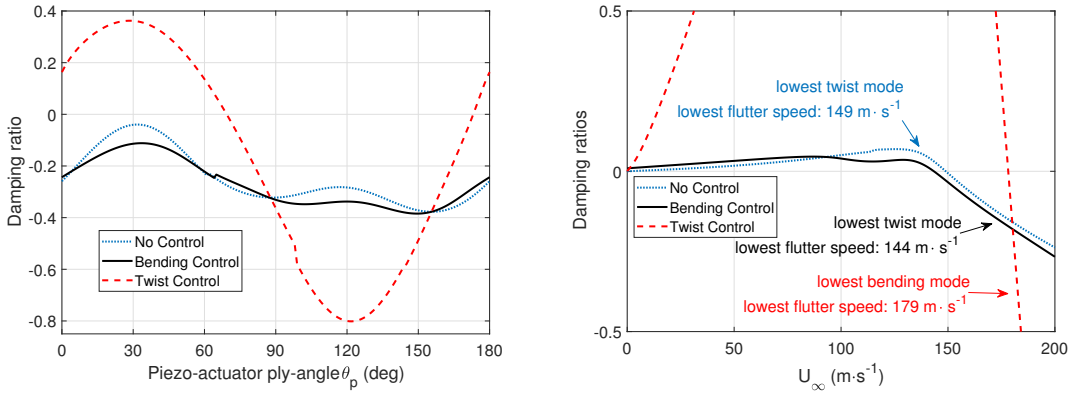

(a) *Damping ratio of the lowest twist mode vs. piezo-actuator ply-angle;* $U_\infty = 151\ \mathrm{m \cdot s^{-1}}$

(b) *Damping ratio of the unstable flutter mode vs. freestream speed;* $\theta_p = 30^o$

Figure 7.10: *Damping ratio study;* $k_B = k_T = 200\ \mathrm{V \cdot s}$, $\theta_h = 150^o$, $\Lambda = 0^o$

Next, the aeroelastic system characterizing strong twist-bending elastic coupling ($\theta_h = 105^o$) is investigated. Figs. 7.11a and 7.11b show damping ratios of the unstable flutter mode of an unswept ($\Lambda = 0^o$) and a backward-swept ($\Lambda = 30^o$) wing cases, respectively. The results of Figs. 7.11a and 7.11b show that bending and twist control methodologies both present a negative control effect near the onset of flutter. This is because, although the velocity feedback control improve the stability of $Mode\,2$, it makes $Mode\,1$ unstable even before the flutter speed. Thus, an optimal effective control strategy, e.g., bang-bang control, sliding mode control, should be applied instead of the simple velocity feedback control.

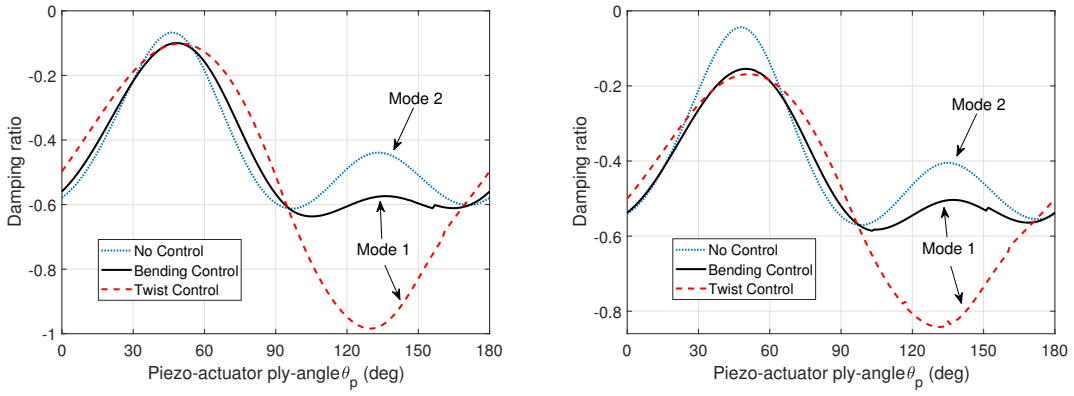

(a) *Noswept wing;* $\Lambda = 0^o$, $U_\infty = 158\ \mathrm{m \cdot s^{-1}}$

(b) *Backward-swept wing;* $\Lambda = 30^o$, $U_\infty = 166\ \mathrm{m \cdot s^{-1}}$

Figure 7.11: *Damping ratio of the unstable flutter mode vs. piezo-actuator ply-angle* θ_p*;* $k_B = k_T = 200\ \mathrm{V \cdot s}$, $\theta_h = 105^o$

However for the forward-swept wing ($\Lambda = -30^o$) case in Fig. 7.12, the simple ve-

locity feedback control can keep $Mode\,1$ stable while improving the stability of $Mode\,2$ near the onset of flutter when piezo-actuator ply-angle around $\theta_p \approx 45^o$. This can be

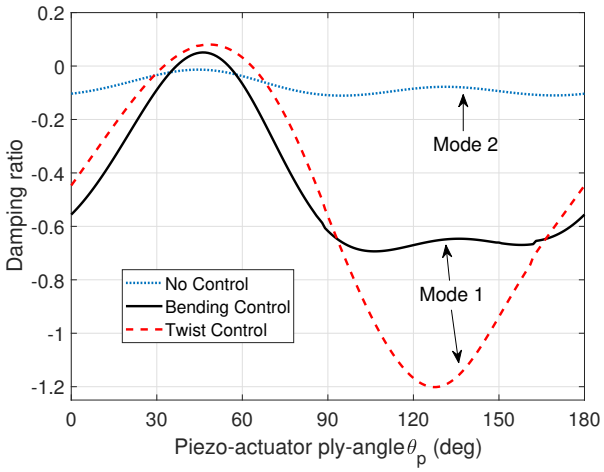

Figure 7.12: *Damping ratio of the unstable mode vs. piezo-actuator ply-angle θ_p; $k_B = k_T = 200$ V · s, $\theta_h = 105^o$, $\Lambda = -30^o$, $U_\infty = 201$ m · s^{-1}.*

seen more clearly in the numerical simulations of the forward-swept wing exposed to a sharp gust in Figs. 7.13a and 7.13b. Figs. 7.13a and 7.13b display the tip bending and twist responses under a twist control for selected ply-angles θ_p, respectively. Note that only the first five structural modes are used in the actual simulations. And the results are simulated based on zero initial conditions. It can be found that twist control with $\theta_p = 45^o$ can significantly prevent the occurrence of the flutter instability penalties when the flight speed is slightly over the flutter speed. Fig. 7.14 further gives the associated voltage time-history applied on the actuator.

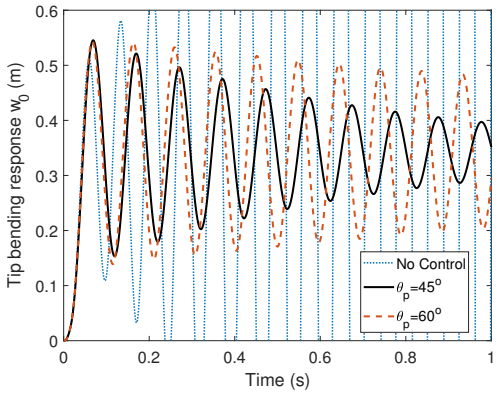

(a) *Bending $w_0(L,t)$*

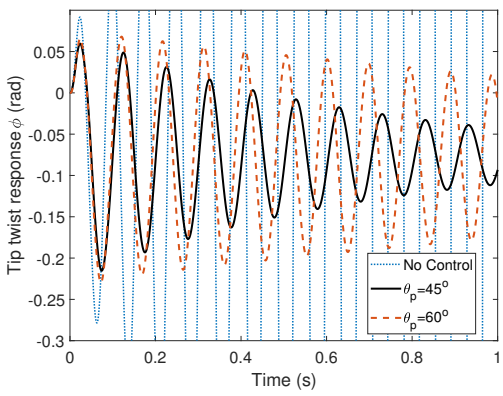

(b) *Twist $\phi(L,t)$*

Figure 7.13: *Tip responses of a forward-swept wing subject to a sharp-edged gust near the onset of flutter under twist control methodology; $k_T = 200$ V · s, $\Lambda = -30^o$, $U_g = 10$ m · s^{-1}, $U_\infty = 201$ m · s^{-1}*

.

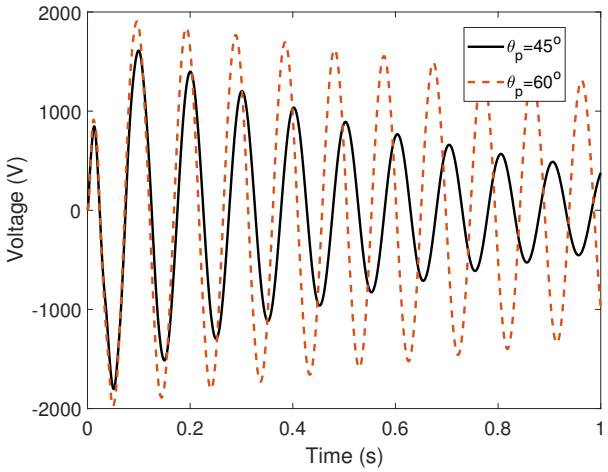

Figure 7.14: *Voltage V_1 applied on the actuators of a forward-swept wing subject to a sharp-edged gust near the onset of flutter under twist control methodology; $k_T = 200\ \mathrm{V \cdot s}$, $\Lambda = -30^o$, $U_g = 10\ \mathrm{m \cdot s^{-1}}$, $U_\infty = 201\ \mathrm{m \cdot s^{-1}}$.*

CHAPTER 8

Conclusion

A Geometrically nonlinear fiber-reinforced composite rotary thin-walled beam theory incorporating piezo-composite actuators is developed. Some non-classical effects, e.g., anisotropy, transverse shear, warping inhibitions and three-dimensional strain are accounted for in the beam model. The strong and synergistic effect played by the directionality property of advanced composite materials, considered in conjunction with that of piezoelectric actuation, on their dynamic response characteristics was highlighted. This one dimensional beam model can serve as the basic model of rotating blade, spacecraft and aircraft wing, offering a simple way for engineers to design and study the structure meeting the particular operating environment condition. Generally speaking, engineers can use elastic tailoring for passive control of the system. And at same time, they can implement an effective active control via designing an optimal piezo-actuator configuration.

In this dissertation, two special lay-up configurations, i.e., circumferentially uniform stiffness (CUS) and circumferentially asymmetric stiffness (CAS) configurations are adopted. Applying CUS lay-up configuration, the linear system will decouple into two independent subsystems, viz., chordwise bending-spanwise bending coupled BB-subsystem and twist-extension coupled TE-subsystem. As for the CAS lay-up configuration, the linear system can be similarly split into two parts, chordwise bending-extension coupled BE-subsystem and twist-spanwise bending coupled TB-subsystem. Although BE-subsystem and TB-subsystem are piezo-actuated coupled, they can be treated as independent subsystems in most cases. However, based on the nonlinear dynamics analysis, these two subsystems appear to be coupled via modal interactions, i.e., energy can be transferred between these two subsystems.

Considering that structure elastic couplings and active control strategy both have significant effects on active control efficiency, designers are suggested to implement

elastic tailoring and determine the appropriate control strategy firstly, then to optimize configuration factors of piezo-actuators, such as fiber orientations, lay-ups, sizes and positions.

APPENDIX $\mathcal{A}$

Appendix

A.1 The modified local stiffness coefficients K_{ij}

$$K_{11} = A_{22} - \frac{A_{12}^2}{A_{11}}, \quad K_{12} = A_{26} - \frac{A_{12}A_{16}}{A_{11}} = K_{21}, \tag{A-1a}$$

$$K_{13} = \left(A_{26} - \frac{A_{12}A_{16}}{A_{11}}\right)\psi(s) + 2\left(B_{26} - \frac{A_{12}B_{16}}{A_{11}}\right), \tag{A-1b}$$

$$K_{14} = B_{22} - \frac{A_{12}B_{12}}{A_{11}} = K_{41}, \quad K_{22} = A_{66} - \frac{A_{16}^2}{A_{11}}, \tag{A-1c}$$

$$K_{23} = \left(A_{66} - \frac{A_{16}^2}{A_{11}}\right)\psi(s) + 2\left(B_{66} - \frac{A_{16}B_{16}}{A_{11}}\right), \tag{A-1d}$$

$$K_{24} = B_{26} - \frac{A_{16}B_{12}}{A_{11}} = K_{42}, \tag{A-1e}$$

$$K_{43} = \left(B_{26} - \frac{B_{12}A_{16}}{A_{11}}\right)\psi(s) + 2\left(D_{26} - \frac{B_{12}B_{16}}{A_{11}}\right), \tag{A-1f}$$

$$K_{44} = D_{22} - \frac{B_{12}^2}{A_{11}}, \quad K_{51} = B_{26} - \frac{B_{16}A_{12}}{A_{11}}, \tag{A-1g}$$

$$K_{52} = B_{66} - \frac{B_{16}A_{16}}{A_{11}}, \quad K_{54} = D_{26} - \frac{B_{12}B_{16}}{A_{11}}, \tag{A-1h}$$

$$K_{53} = \left(B_{66} - \frac{B_{16}A_{16}}{A_{11}}\right)\psi(s) + 2\left(D_{66} - \frac{{B_{16}}^2}{A_{11}}\right). \tag{A-1i}$$

A.2 Inertial coefficients b_{ij}

$$(b_1, b_4, b_5, b_{10}) = \oint_C (1, z^2, x^2, F_w(s)^2) \left[\sum_{k=1}^{N_{hp}} \int_{h_{(k-)}}^{h_{(k+)}} \rho(k) \, \mathrm{d}\, n \right] \mathrm{d}\, s, \tag{A-2}$$

$$(b_{14}, b_{15}, b_{18}) = \oint_C (\left(\frac{\mathrm{d}\, x}{\mathrm{d}\, s} \right)^2, \left(\frac{\mathrm{d}\, z}{\mathrm{d}\, s} \right)^2, a(s)^2) \left[\sum_{k=1}^{N_{hp}} \int_{h_{(k-)}}^{h_{(k+)}} \rho(k) n^2 \, \mathrm{d}\, n \right] \mathrm{d}\, s. \tag{A-3}$$

A.3 The cross-section stiffness quantities a_{ij}

$$a_{11} = \oint_C K_{11} \, \mathrm{d}\, s, \quad a_{12} = \oint_C \left(K_{11} x - K_{14} \frac{\mathrm{d}\, z}{\mathrm{d}\, s} \right) \mathrm{d}\, s, \tag{A-4a}$$

$$a_{13} = \oint_C \left(z K_{11} + K_{14} \frac{\mathrm{d}\, x}{\mathrm{d}\, s} \right) \mathrm{d}\, s, \quad a_{14} = \oint_C K_{12} \frac{\mathrm{d}\, x}{\mathrm{d}\, s} \, \mathrm{d}\, s, \tag{A-4b}$$

$$a_{15} = \oint_C K_{12} \frac{\mathrm{d}\, z}{\mathrm{d}\, s} \, \mathrm{d}\, s, \quad a_{16} = - \oint_C \left[F_w K_{11} + K_{14} a(s) \right] \mathrm{d}\, s, \tag{A-4c}$$

$$a_{17} = \oint_C K_{13} \, \mathrm{d}\, s, \quad a_{18} = \oint_C \left[K_{11} (x^2 + z^2) + 2 r_n K_{41} \right] \mathrm{d}\, s, \tag{A-4d}$$

$$a_{22} = \oint_C \left[x^2 K_{11} - 2x \frac{\mathrm{d}\, z}{\mathrm{d}\, s} K_{14} + \left(\frac{\mathrm{d}\, z}{\mathrm{d}\, s} \right)^2 K_{44} \right] \mathrm{d}\, s, \tag{A-5a}$$

$$a_{23} = \oint_C \left[x z K_{11} + x \frac{\mathrm{d}\, x}{\mathrm{d}\, s} K_{14} \right] \mathrm{d}\, s - \oint_C \left[z \frac{\mathrm{d}\, z}{\mathrm{d}\, s} K_{14} + \frac{\mathrm{d}\, z}{\mathrm{d}\, s} \frac{\mathrm{d}\, x}{\mathrm{d}\, s} K_{44} \right] \mathrm{d}\, s, \tag{A-5b}$$

$$a_{24} = \oint_C \left[x \frac{\mathrm{d}\, x}{\mathrm{d}\, s} K_{12} - \frac{\mathrm{d}\, z}{\mathrm{d}\, s} \frac{\mathrm{d}\, x}{\mathrm{d}\, s} K_{42} \right] \mathrm{d}\, s, \quad a_{25} = \oint_C \left[x \frac{\mathrm{d}\, z}{\mathrm{d}\, s} K_{12} - \left(\frac{\mathrm{d}\, z}{\mathrm{d}\, s} \right)^2 K_{42} \right] \mathrm{d}\, s \tag{A-5c}$$

$$a_{26} = \oint_C \left[-x F_w K_{11} - x a(s) K_{14} \right] \mathrm{d}\, s + \oint_C \left[K_{41} \frac{\mathrm{d}\, z}{\mathrm{d}\, s} F_w + a(s) \frac{\mathrm{d}\, z}{\mathrm{d}\, s} K_{44} \right] \mathrm{d}\, s, \tag{A-5d}$$

$$a_{27} = \oint_C \left[x K_{13} - \frac{\mathrm{d}\, z}{\mathrm{d}\, s} K_{43} \right] \mathrm{d}\, s, \tag{A-5e}$$

$$a_{28} = \oint_C \left\{ x \left[K_{11} (x^2 + z^2) + 2 r_n K_{41} \right] \right\} \mathrm{d}\, s - \oint_C \left\{ \frac{\mathrm{d}\, z}{\mathrm{d}\, s} \left[K_{14} (x^2 + z^2) + 2 r_n K_{44} \right] \right\} \mathrm{d}\, s, \tag{A-5f}$$

$$a_{33} = \oint_C \left[z^2 K_{11} + 2 z \frac{\mathrm{d}\, x}{\mathrm{d}\, s} K_{14} + \left(\frac{\mathrm{d}\, x}{\mathrm{d}\, s} \right)^2 K_{44} \right] \mathrm{d}\, s, \tag{A-6a}$$

$$a_{34} = \oint_C \left[z \frac{\mathrm{d}\, x}{\mathrm{d}\, s} K_{12} + \left(\frac{\mathrm{d}\, x}{\mathrm{d}\, s} \right)^2 K_{42} \right] \mathrm{d}\, s, \quad a_{35} = \oint_C \left[z \frac{\mathrm{d}\, z}{\mathrm{d}\, s} K_{12} + \frac{\mathrm{d}\, x}{\mathrm{d}\, s} \frac{\mathrm{d}\, z}{\mathrm{d}\, s} K_{42} \right] \mathrm{d}\, s, \tag{A-6b}$$

$$a_{36} = \oint_C [-zF_wK_{11} - a(s)zK_{14}]\,\mathrm{d}\,s - \oint_C \left[\frac{\mathrm{d}\,x}{\mathrm{d}\,s}F_wK_{41} + a(s)\frac{\mathrm{d}\,x}{\mathrm{d}\,s}K_{44}\right]\mathrm{d}\,s, \quad \text{(A-6c)}$$

$$a_{37} = \oint_C \left[zK_{13} + \frac{\mathrm{d}\,x}{\mathrm{d}\,s}K_{43}\right]\mathrm{d}\,s, \quad \text{(A-6d)}$$

$$a_{38} = \oint_C \left\{z[K_{11}(x^2+z^2) + 2r_nK_{41}]\right\}\mathrm{d}\,s + \oint_C \left\{\frac{\mathrm{d}\,x}{\mathrm{d}\,s}[K_{14}(x^2+z^2) + 2r_nK_{44}]\right\}\mathrm{d}\,s, \quad \text{(A-6e)}$$

$$a_{44} = \oint_C \left[\left(\frac{\mathrm{d}\,x}{\mathrm{d}\,s}\right)^2 K_{22} + \left(\frac{\mathrm{d}\,z}{\mathrm{d}\,s}\right)^2 \bar{A}_{44}\right]\mathrm{d}\,s, \quad a_{45} = \oint_C \left[\frac{\mathrm{d}\,x}{\mathrm{d}\,s}\frac{\mathrm{d}\,z}{\mathrm{d}\,s}K_{22} - \frac{\mathrm{d}\,x}{\mathrm{d}\,s}\frac{\mathrm{d}\,z}{\mathrm{d}\,s}A_{44}\right]\mathrm{d}\,s, \quad \text{(A-7a)}$$

$$a_{46} = \oint_C \left[-F_w\frac{\mathrm{d}\,x}{\mathrm{d}\,s}K_{21} - a(s)\frac{\mathrm{d}\,x}{\mathrm{d}\,s}K_{24}\right]\mathrm{d}\,s, \quad a_{47} = \oint_C K_{23}\frac{\mathrm{d}\,x}{\mathrm{d}\,s}\,\mathrm{d}\,s, \quad \text{(A-7b)}$$

$$a_{48} = \oint_C \frac{\mathrm{d}\,x}{\mathrm{d}\,s}[K_{12}(x^2+z^2) + 2r_nK_{42}]\,\mathrm{d}\,s, \quad \text{(A-7c)}$$

$$a_{55} = \oint_C \left[\left(\frac{\mathrm{d}\,z}{\mathrm{d}\,s}\right)^2 K_{22} + \left(\frac{\mathrm{d}\,x}{\mathrm{d}\,s}\right)^2 \bar{A}_{44}\right]\mathrm{d}\,s, \quad \text{(A-8a)}$$

$$a_{56} = \oint_C \left[-F_w\frac{\mathrm{d}\,z}{\mathrm{d}\,s}K_{21} - a(s)\frac{\mathrm{d}\,z}{\mathrm{d}\,s}K_{24}\right]\mathrm{d}\,s, \quad a_{57} = \oint_C K_{23}\frac{\mathrm{d}\,z}{\mathrm{d}\,s}, \quad \text{(A-8b)}$$

$$a_{58} = \oint_C \frac{\mathrm{d}\,z}{\mathrm{d}\,s}[K_{12}(x^2+z^2) + 2r_nK_{42}]\,\mathrm{d}\,s, \quad \text{(A-8c)}$$

$$a_{66} = \oint_C \left[F_w^2K_{11} + 2F_wa(s)K_{14} + a(s)^2K_{44}\right]\mathrm{d}\,s, \quad \text{(A-8d)}$$

$$a_{67} = -\oint_C [F_wK_{13} + a(s)K_{43}]\,\mathrm{d}\,s, \quad \text{(A-8e)}$$

$$a_{68} = -\oint_C \left\{F_w[K_{11}(x^2+z^2) + 2r_nK_{41}]\right\}\mathrm{d}\,s - \oint_C \left\{a[K_{14}(x^2+z^2) + 2r_nK_{44}]\right\}\mathrm{d}\,s, \quad \text{(A-8f)}$$

$$a_{77} = \oint_C (\psi(s)K_{23} + 2K_{53})\,\mathrm{d}\,s, \quad a_{78} = \oint_C [K_{13}(x^2+z^2) + 2r_nK_{43}]\,\mathrm{d}\,s, \quad \text{(A-8g)}$$

$$a_{88} = \oint_C \left\{(x^2+z^2)[K_{11}(x^2+z^2) + 2r_nK_{41}]\right\}\mathrm{d}\,s + \oint_C \left\{2r_n[K_{14}(x^2+z^2) + 2r_nK_{44}]\right\}\mathrm{d}\,s, \quad \text{(A-8h)}$$

where

$$\bar{A}_{44} = A_{44} - \frac{A_{45}^2}{A_{55}}. \quad \text{(A-9)}$$

A.4 The cross-section piezo-actuator coefficients $\mathcal{A}_i^X$

The subscript $i = 1, 2, 3, 4$ of piezo-actuator coefficients $\mathcal{A}_i^X$ denote the operation

$$\mathcal{A}_1^X = \int_T \mathcal{A}_T^X \,\mathrm{d}\, s - \int_B \mathcal{A}_B^X \,\mathrm{d}\, s, \quad \mathcal{A}_2^X = \int_T \mathcal{A}_T^X \,\mathrm{d}\, s + \int_B \mathcal{A}_B^X \,\mathrm{d}\, s, \tag{A-10a}$$

$$\mathcal{A}_3^X = \int_L \mathcal{A}_L^X \,\mathrm{d}\, s - \int_R \mathcal{A}_R^X \,\mathrm{d}\, s, \quad \mathcal{A}_4^X = \int_L \mathcal{A}_L^X \,\mathrm{d}\, s + \int_R \mathcal{A}_R^X \,\mathrm{d}\, s, \tag{A-10b}$$

where the definition of $\mathcal{A}^X$ are given as

$$\mathcal{A}^{Ty} = \sum_{k=1}^{m} \left(e_{yy} - \frac{A_{12}}{A_{11}} e_{ss} \right) \frac{(n_2 - n_1)}{\hat{h}} R_{(k)}(s), \tag{A-11a}$$

$$\mathcal{A}^{Mz} = \sum_{k=1}^{m} \left\{ x \left(e_{yy} - \frac{A_{12}}{A_{11}} e_{ss} \right) \frac{(n_2 - n_1)}{\hat{h}} R_{(k)}(s) - \frac{\mathrm{d}\, z}{\mathrm{d}\, s} \left[\frac{1}{2} e_{yy}(n_1 + n_2) - \frac{B_{12}}{A_{11}} e_{ss} \right] \frac{(n_2 - n_1)}{\hat{h}} R_{(k)}(s) \right\}, \tag{A-11b}$$

$$\mathcal{A}^{Mx} = \sum_{k=1}^{m} \left\{ z \left(e_{yy} - \frac{A_{12}}{A_{11}} e_{ss} \right) \frac{(n_2 - n_1)}{\hat{h}} R_{(k)}(s) + \frac{\mathrm{d}\, x}{\mathrm{d}\, s} \left[\frac{1}{2} e_{yy}(n_1 + n_2) - \frac{B_{12}}{A_{11}} e_{ss} \right] \frac{(n_2 - n_1)}{\hat{h}} R_{(k)}(s) \right\}, \tag{A-11c}$$

$$\mathcal{A}^{Qx} = \sum_{k=1}^{m} \frac{\mathrm{d}\, x}{\mathrm{d}\, s} \left(e_{sy} - \frac{A_{16}}{A_{11}} e_{ss} \right) \frac{(n_2 - n_1)}{\hat{h}} R_{(k)}(s), \tag{A-11d}$$

$$\mathcal{A}^{Qz} = \sum_{k=1}^{m} \frac{\mathrm{d}\, z}{\mathrm{d}\, s} \left(e_{sy} - \frac{A_{16}}{A_{11}} e_{ss} \right) \frac{(n_2 - n_1)}{\hat{h}} R_{(k)}(s), \tag{A-11e}$$

$$\mathcal{A}^{Bw} = -\sum_{k=1}^{m} \left\{ F_w \left(e_{yy} - \frac{A_{12}}{A_{11}} e_{ss} \right) \frac{(n_2 - n_1)}{\hat{h}} R_{(k)}(s) + a \left[\frac{1}{2} e_{yy}(n_1 + n_2) - \frac{B_{12}}{A_{11}} e_{ss} \right] \frac{(n_2 - n_1)}{\hat{h}} R_{(k)}(s) \right\}, \tag{A-11f}$$

$$\mathcal{A}^{My} = \sum_{k=1}^{m} \left\{ \psi(s) \left(e_{sy} - \frac{A_{16}}{A_{11}} e_{ss} \right) \frac{(n_2 - n_1)}{\hat{h}} R_{(k)}(s) + 2 \left[\frac{1}{2} e_{sy}(n_1 + n_2) - \frac{B_{16}}{A_{11}} e_{ss} \right] E_k (n_2 - n_1) R_{(k)}(s) \right\}, \tag{A-11g}$$

$$\mathcal{A}^{\Gamma t} = \sum_{k=1}^{m} \left\{ (x^2 + z^2) \left(e_{yy} - \frac{A_{12}}{A_{11}} e_{ss} \right) \frac{(n_2 - n_1)}{\hat{h}} R_{(k)}(s) + 2 r_n \left[\frac{1}{2} e_{yy}(n_1 + n_2) - \frac{B_{12}}{A_{11}} e_{ss} \right] \frac{(n_2 - n_1)}{\hat{h}} R_{(k)}(s) \right\}. \tag{A-11h}$$

A.5 Global stiffness quantities a_{ij}

$$a_{11} = a_{11}^p, \quad a_{16} = a_{16}^p, \quad a_{17} = a_{17}^p, \quad a_{18} = a_{18}^p, \tag{A-12a}$$

$$a_{28} = a_{28}^p, \quad a_{66} = a_{66}^p, \quad a_{67} = a_{67}^p, \quad a_{68} = a_{68}^p, \tag{A-12b}$$

$$a_{77} = a_{77}^p, \quad a_{78} = a_{78}^p, \quad a_{88} = a_{88}^p. \tag{A-12c}$$

$$a_{12} = a_{12}^p \cos\beta + a_{13}^p \sin\beta, \quad a_{13} = a_{13}^P \cos\beta - a_{12}^p \sin\beta, \tag{A-13}$$
$$a_{14} = a_{14}^p \cos\beta + a_{15}^p \sin\beta, \quad a_{15} = a_{15}^p \cos\beta - a_{14}^p \sin\beta, \tag{A-14}$$
$$a_{26} = a_{26}^p \cos\beta + a_{36}^p \sin\beta, \quad a_{27} = a_{27}^p \cos\beta + a_{37}^p \sin\beta, \tag{A-15}$$
$$a_{36} = a_{36}^p \cos\beta - a_{26}^p \sin\beta, \quad a_{37} = a_{37}^p \cos\beta - a_{27}^p \sin\beta, \tag{A-16}$$
$$a_{38} = a_{38}^p \cos\beta - a_{28}^p \sin\beta, \quad a_{46} = a_{46}^p \cos\beta + a_{56}^p \sin\beta, \tag{A-17}$$
$$a_{47} = a_{47}^p \cos\beta + a_{57}^p \sin\beta, \quad a_{48} = a_{48}^p \cos\beta + a_{58}^p \sin\beta, \tag{A-18}$$
$$a_{56} = a_{56}^p \cos\beta - a_{46}^p \sin\beta, \quad a_{57} = a_{57}^p \cos\beta - a_{47}^p \sin\beta, \tag{A-19}$$
$$a_{58} = a_{58}^p \cos\beta - a_{48}^p \sin\beta. \tag{A-20}$$

$$a_{22} = a_{22}^p \cos^2\beta + a_{33}^p \sin^2\beta + 2a_{23}^p \cos\beta \sin\beta, \tag{A-21}$$
$$a_{23} = a_{23}^p(\cos^2\beta - \sin^2\beta) + (a_{33}^p - a_{22}^p)\cos\beta \sin\beta, \tag{A-22}$$
$$a_{24} = a_{24}^p \cos^2\beta + a_{35}^p \sin^2\beta + (a_{25}^p + a_{34}^p)\cos\beta \sin\beta, \tag{A-23}$$
$$a_{25} = a_{25}^p \cos^2\beta - a_{34}^p \sin^2\beta + (a_{35}^p - a_{24}^p)\cos\beta \sin\beta, \tag{A-24}$$
$$a_{33} = a_{33}^p \cos^2\beta + a_{22}^p \sin^2\beta - 2a_{23}^p \cos\beta \sin\beta, \tag{A-25}$$
$$a_{34} = a_{34}^p \cos^2\beta - a_{25}^p \sin^2\beta + (a_{35}^p - a_{24}^p)\cos\beta \sin\beta, \tag{A-26}$$
$$a_{35} = a_{35}^P \cos^2\beta + a_{24}^p \sin^2\beta - (a_{34}^p + a_{25}^p)\cos\beta \sin\beta, \tag{A-27}$$
$$a_{44} = a_{44}^p \cos^2\beta + a_{55}^p \sin^2\beta + 2a_{45}^p \cos\beta \sin\beta, \tag{A-28}$$
$$a_{45} = a_{45}^p(\cos^2\beta - \sin^2\beta) + (a_{55}^p - a_{44}^p)\cos\beta \sin\beta, \tag{A-29}$$
$$a_{55} = a_{55}^p \cos^2\beta + a_{44}^p \sin^2\beta - 2a_{45}^p \cos\beta \sin\beta. \tag{A-30}$$

A.6 Matrix via the Extended Galerkin's Method in CUS lay-ups

Mass matrix

$$\mathbf{M}_B = \int_0^L \begin{bmatrix} b_1 \boldsymbol{\Psi}_u \boldsymbol{\Psi}_u^T & 0 & 0 & 0 \\ 0 & b_1 \boldsymbol{\Psi}_w \boldsymbol{\Psi}_w^T & 0 & 0 \\ 0 & 0 & b_4 \boldsymbol{\Psi}_x \boldsymbol{\Psi}_x^T & b_6 \boldsymbol{\Psi}_x \boldsymbol{\Psi}_z^T \\ 0 & 0 & b_6 \boldsymbol{\Psi}_z \boldsymbol{\Psi}_x^T & b_5 \boldsymbol{\Psi}_z \boldsymbol{\Psi}_z^T \end{bmatrix} \mathrm{d}\, y. \tag{A-31}$$

$$\mathbf{M}_T = \int_0^L \begin{bmatrix} b_1 \boldsymbol{\Psi}_v \boldsymbol{\Psi}_v^T & 0 \\ 0 & (b_4 + b_5)\boldsymbol{\Psi}_\phi \boldsymbol{\Psi}_\phi^T + b_{10} \boldsymbol{\Psi'}_\phi \boldsymbol{\Psi'}_\phi^T \end{bmatrix} \mathrm{d}\, y. \tag{A-32}$$

Stiffness matrix

$$\mathbf{K}_B = \int_0^L \begin{bmatrix} a_{44}\boldsymbol{\Psi}'_u \boldsymbol{\Psi}'^T_u & a_{45}\boldsymbol{\Psi}'_u \boldsymbol{\Psi}'^T_w & a_{34}\boldsymbol{\Psi}'_u \boldsymbol{\Psi}'^T_x + a_{45}\boldsymbol{\Psi}'_u \boldsymbol{\Psi}_x^T & a_{24}\boldsymbol{\Psi}'_u \boldsymbol{\Psi}'^T_z + a_{44}\boldsymbol{\Psi}'_u \boldsymbol{\Psi}_z^T \\ & a_{55}\boldsymbol{\Psi}'_w \boldsymbol{\Psi}'^T_w & a_{35}\boldsymbol{\Psi}'_w \boldsymbol{\Psi}'^T_x + a_{55}\boldsymbol{\Psi}'_w \boldsymbol{\Psi}_x^T & a_{25}\boldsymbol{\Psi}'_w \boldsymbol{\Psi}'^T_z + a_{45}\boldsymbol{\Psi}'_w \boldsymbol{\Psi}_z^T \\ & & \mathbf{K}_{55} & \mathbf{K}_{56} \\ \text{Symm} & & & \mathbf{K}_{66} \end{bmatrix} \mathrm{d}\, y, \tag{A-33}$$

with

$$\begin{cases} \mathbf{K}_{55} = a_{33}\boldsymbol{\Psi}'_x{\boldsymbol{\Psi}'_x}^T + a_{35}\boldsymbol{\Psi}'_x{\boldsymbol{\Psi}_x}^T + a_{35}\boldsymbol{\Psi}_x{\boldsymbol{\Psi}'_x}^T + a_{55}\boldsymbol{\Psi}_x{\boldsymbol{\Psi}_x}^T, \\ \mathbf{K}_{56} = a_{23}\boldsymbol{\Psi}'_x{\boldsymbol{\Psi}'_z}^T + a_{34}\boldsymbol{\Psi}'_x{\boldsymbol{\Psi}_z}^T + a_{25}\boldsymbol{\Psi}_x{\boldsymbol{\Psi}'_z}^T + a_{45}\boldsymbol{\Psi}_x{\boldsymbol{\Psi}_z}^T, \\ \mathbf{K}_{66} = a_{22}\boldsymbol{\Psi}'_z{\boldsymbol{\Psi}'_z}^T + a_{24}\boldsymbol{\Psi}'_z{\boldsymbol{\Psi}_z}^T + a_{24}\boldsymbol{\Psi}_z{\boldsymbol{\Psi}'_z}^T + a_{44}\boldsymbol{\Psi}_z{\boldsymbol{\Psi}_z}^T. \end{cases} \tag{A-34}$$

$$\mathbf{K}_T = \int_0^L \begin{bmatrix} a_{11}\boldsymbol{\Psi}'_v{\boldsymbol{\Psi}'_v}^T & a_{17}\boldsymbol{\Psi}'_v{\boldsymbol{\Psi}'_\phi}^T \\ a_{17}\boldsymbol{\Psi}'_\phi{\boldsymbol{\Psi}'_v}^T & a_{77}\boldsymbol{\Psi}'_\phi{\boldsymbol{\Psi}'_\phi}^T + a_{66}\boldsymbol{\Psi}''_\phi{\boldsymbol{\Psi}''_\phi}^T \end{bmatrix} \mathrm{d}\, y. \tag{A-35}$$

Additional stiffness matrix

$$\hat{\mathbf{K}}_B = \int_0^L \begin{bmatrix} b_1 R(y)\boldsymbol{\Psi}'_u{\boldsymbol{\Psi}'_u}^T - b_1\boldsymbol{\Psi}_u{\boldsymbol{\Psi}_u}^T & 0 & 0 & 0 \\ 0 & b_1 R(y)\boldsymbol{\Psi}'_w{\boldsymbol{\Psi}'_w}^T & 0 & 0 \\ 0 & 0 & -b_4\boldsymbol{\Psi}_x{\boldsymbol{\Psi}_x}^T & -b_6\boldsymbol{\Psi}_x{\boldsymbol{\Psi}_z}^T \\ 0 & 0 & -b_6\boldsymbol{\Psi}_z{\boldsymbol{\Psi}_x}^T & -b_5\boldsymbol{\Psi}_z{\boldsymbol{\Psi}_z}^T \end{bmatrix} \mathrm{d}\, y, \tag{A-36}$$

$$\hat{\mathbf{K}}_T = \int_0^L \begin{bmatrix} -b_1\boldsymbol{\Psi}_v{\boldsymbol{\Psi}_v}^T & 0 \\ 0 & -(b_4 - b_5 - b_6)\boldsymbol{\Psi}_\phi{\boldsymbol{\Psi}_\phi}^T + (b_4 + b_5)R(y)\boldsymbol{\Psi}'_\phi{\boldsymbol{\Psi}'_\phi}^T - b_{10}\boldsymbol{\Psi}'_\phi{\boldsymbol{\Psi}'_\phi}^T \end{bmatrix} \mathrm{d}\, y. \tag{A-37}$$

Actuating matrix

$$\mathcal{A}_B = \int_0^L \begin{bmatrix} \mathcal{A}_1^{Qx}\boldsymbol{\Psi}'_u\cos\beta & \mathcal{A}_3^{Qz}\boldsymbol{\Psi}'_u\sin\beta \\ -\mathcal{A}_1^{Qx}\boldsymbol{\Psi}'_u\sin\beta & \mathcal{A}_3^{Qz}\boldsymbol{\Psi}'_w\cos\beta \\ \mathcal{A}_1^{Mx}\boldsymbol{\Psi}'_x\cos\beta - \mathcal{A}_1^{Qx}\boldsymbol{\Psi}_x\sin\beta & -\mathcal{A}_3^{Mz}\boldsymbol{\Psi}'_x\sin\beta + \mathcal{A}_3^{Qz}\boldsymbol{\Psi}_x\cos\beta \\ \mathcal{A}_1^{Mx}\boldsymbol{\Psi}'_z\sin\beta + \mathcal{A}_1^{Qx}\boldsymbol{\Psi}_z\cos\beta & \mathcal{A}_3^{Mz}\boldsymbol{\Psi}'_z\cos\beta + \mathcal{A}_3^{Qz}\boldsymbol{\Psi}_x\sin\beta \end{bmatrix} P(y)\,\mathrm{d}\, y. \tag{A-38}$$

$$\mathcal{A}_T = \int_0^L \begin{bmatrix} \mathcal{A}_2^{Ty}\boldsymbol{\Psi}'_v & \mathcal{A}_4^{Ty}\boldsymbol{\Psi}'_v \\ \mathcal{A}_2^{My}\boldsymbol{\Psi}'_\phi & \mathcal{A}_4^{My}\boldsymbol{\Psi}'_\phi \end{bmatrix} P(y)\,\mathrm{d}\, y. \tag{A-39}$$

External forces vector

$$\mathbf{Q}_B = \begin{Bmatrix} \int_0^L p_x\boldsymbol{\Psi}_u\,\mathrm{d}\, y + \bar{Q}_x\boldsymbol{\Psi}_u(L) \\ \int_0^L p_z\boldsymbol{\Psi}_w\,\mathrm{d}\, y + \bar{Q}_z\boldsymbol{\Psi}_w(L) \\ \int_0^L m_x\boldsymbol{\Psi}_x\,\mathrm{d}\, y + \bar{M}_x\boldsymbol{\Psi}_x(L) \\ \int_0^L m_z\boldsymbol{\Psi}_z\,\mathrm{d}\, y + \bar{M}_z\boldsymbol{\Psi}_z(L) \end{Bmatrix}. \tag{A-40}$$

$$\mathbf{Q}_T = \begin{Bmatrix} \int_0^L [\Omega^2(R_0 + y) + p_y]\boldsymbol{\Psi}_v\,\mathrm{d}\, y + \bar{T}_y\boldsymbol{\Psi}_v(L) \\ \int_0^L (\Omega^2 b_6 + m_y + b'_w)\boldsymbol{\Psi}_\phi\,\mathrm{d}\, y + [\bar{M}_y\boldsymbol{\Psi}_\phi(L) + \bar{B}_w\boldsymbol{\Psi}'_\phi(L)] \end{Bmatrix}. \tag{A-41}$$

Control matrix

$$\mathbf{P}_B = \begin{bmatrix} 0 & 0 & k_1 \cos\beta(Y_s)\boldsymbol{\Psi}_x{}^T(Y_s) & k_1 \sin\beta(Y_s)\boldsymbol{\Psi}_z{}^T(Y_s) \\ 0 & 0 & k_3 \sin\beta(Y_s)\boldsymbol{\Psi}_x{}^T(Y_s) & -k_3 \cos\beta(Y_s)\boldsymbol{\Psi}_z{}^T(Y_s) \end{bmatrix}, \tag{A-42}$$

$$\mathbf{P}_T = \begin{bmatrix} 0 & -k_2\boldsymbol{\Psi}_\phi{}^T(Y_s) \\ 0 & -k_4\boldsymbol{\Psi}_\phi{}^T(Y_s) \end{bmatrix}. \tag{A-43}$$

A.7 Matrix via the Extended Galerkin's Method in CAS lay-ups

Mass matrix

$$\mathbf{M}_B = \int_0^L \begin{bmatrix} b_1\boldsymbol{\Psi}_u\boldsymbol{\Psi}_u^T & 0 & 0 \\ & b_1\boldsymbol{\Psi}_v\boldsymbol{\Psi}_v^T & 0 \\ \text{Symm} & & (b_5+b_{15})\boldsymbol{\Psi}_z\boldsymbol{\Psi}_z^T \end{bmatrix} \mathrm{d}\, y, \tag{A-44}$$

$$\mathbf{M}_T = \int_0^L \begin{bmatrix} b_1\boldsymbol{\Psi}_w\boldsymbol{\Psi}_w^T & 0 & 0 \\ & (b_4+b_5)\boldsymbol{\Psi}_\phi\boldsymbol{\Psi}_\phi^T + (b_{10}+b_{18})\boldsymbol{\Psi'}_\phi\boldsymbol{\Psi'}_\phi^T & 0 \\ \text{Symm} & & (b_4+b_{14})\boldsymbol{\Psi}_x\boldsymbol{\Psi}_x^T \end{bmatrix} \mathrm{d}\, y. \tag{A-45}$$

Stiffness matrix

$$\mathbf{K}_B = \int_0^L \begin{bmatrix} a_{44}\boldsymbol{\Psi'}_u\boldsymbol{\Psi'}_u{}^T & a_{14}\boldsymbol{\Psi'}_u\boldsymbol{\Psi'}_v{}^T & a_{44}\boldsymbol{\Psi'}_u\boldsymbol{\Psi}_z{}^T \\ & a_{11}\boldsymbol{\Psi'}_v\boldsymbol{\Psi'}_v{}^T & a_{14}\boldsymbol{\Psi'}_v\boldsymbol{\Psi}_z{}^T \\ \text{Symm} & & a_{22}\boldsymbol{\Psi'}_z\boldsymbol{\Psi'}_z{}^T + a_{44}\boldsymbol{\Psi}_z\boldsymbol{\Psi}_z{}^T \end{bmatrix} \mathrm{d}\, y, \tag{A-46}$$

$$\mathbf{K}_T = \int_0^L \begin{bmatrix} a_{55}\boldsymbol{\Psi'}_w\boldsymbol{\Psi'}_w{}^T & 0 & a_{55}\boldsymbol{\Psi'}_w\boldsymbol{\Psi'}_x{}^T \\ & a_{77}\boldsymbol{\Psi'}_\phi\boldsymbol{\Psi'}_\phi{}^T + a_{66}\boldsymbol{\Psi''}_\phi\boldsymbol{\Psi''}_\phi{}^T & a_{37}\boldsymbol{\Psi'}_\phi\boldsymbol{\Psi'}_x{}^T \\ \text{Symm} & & a_{33}\boldsymbol{\Psi'}_x\boldsymbol{\Psi'}_x{}^T + a_{55}\boldsymbol{\Psi}_x\boldsymbol{\Psi}_x{}^T \end{bmatrix} \mathrm{d}\, y. \tag{A-47}$$

Piezo-actuator Matrix

$$\mathcal{A}_B = \int_0^L \begin{bmatrix} \mathcal{A}_2^{Qx}\boldsymbol{\Psi}_u R'(y) & 0 & 0 \\ \mathcal{A}_2^{Ty}\boldsymbol{\Psi}_v R'(y) & 0 & \mathcal{A}_4^{Ty}\boldsymbol{\Psi}_v R'(y) \\ -\mathcal{A}_2^{Qx}\boldsymbol{\Psi}_z R(y) & \mathcal{A}_3^{Qz}\boldsymbol{\Psi}_z R'(y) & 0 \end{bmatrix} \mathrm{d}\, y, \tag{A-48}$$

$$\mathcal{A}_T = \int_0^L \begin{bmatrix} 0 & 0 & \mathcal{A}_4^{Qz}\boldsymbol{\Psi}_w R'(y) \\ \mathcal{A}_1^{My}\boldsymbol{\Psi}_\phi R'(y) & \mathcal{A}_3^{My}\boldsymbol{\Psi}_\phi R'(y) & 0 \\ \mathcal{A}_1^{Mx}\boldsymbol{\Psi}_x R'(y) & 0 & -\mathcal{A}_4^{Qz}\boldsymbol{\Psi}_x R(y) \end{bmatrix} \mathrm{d}\, y, \tag{A-49}$$

External forces vector

$$\mathbf{Q}_B = \begin{Bmatrix} \int_0^L p_x\boldsymbol{\Psi}_u \,\mathrm{d}\, y + \bar{Q}_x\boldsymbol{\Psi}_u(L) \\ \int_0^L p_y\boldsymbol{\Psi}_v \,\mathrm{d}\, y + \bar{T}_y\boldsymbol{\Psi}_v(L) \\ \int_0^L m_z\boldsymbol{\Psi}_z \,\mathrm{d}\, y + \bar{M}_z\boldsymbol{\Psi}_z(L) \end{Bmatrix}, \tag{A-50}$$

$$\mathbf{Q}_T = \left\{ \begin{array}{c} \int_0^L p_z \mathbf{\Psi}_w \,\mathrm{d}\, y + \bar{Q}_z \mathbf{\Psi}_w(L) \\ \int_0^L (m_y + b'_w)\mathbf{\Psi}_\phi \,\mathrm{d}\, y + [\bar{M}_y \mathbf{\Psi}_\phi(L) + \bar{B}_w \mathbf{\Psi}'_\phi(L)] \\ \int_0^L m_x \mathbf{\Psi}_x \,\mathrm{d}\, y + \bar{M}_x \mathbf{\Psi}_x(L) \end{array} \right\}. \tag{A-51}$$

Control matrix $\mathbf{P}$ in Eq. (5.11)

$$\mathbf{P} = \begin{bmatrix} \mathbf{0} & -k_1 \alpha_1^k {\mathbf{\Psi}_\phi}^T(Y_s) & -k_1 \beta_1^k {\mathbf{\Psi}_x}^T(Y_s) \\ \mathbf{0} & -k_3 {\mathbf{\Psi}_\phi}^T(Y_s) & \mathbf{0} \\ -k_4 \alpha_4^k \dfrac{\mathbf{\Psi}_w(Y_s)^T}{2b} & \mathbf{0} & -k_4 \beta_4^k {\mathbf{\Psi}_x}^T(Y_s) \end{bmatrix} \tag{A-52}$$

A.8 Matrix in the hub-beam multibody system

$$\mathbf{M} = \int_0^L \begin{bmatrix} b_1 \mathbf{\Psi}_u \mathbf{\Psi}_u^T & 0 & 0 \\ & b_1 \mathbf{\Psi}_v \mathbf{\Psi}_v^T & 0 \\ \text{Symm} & & (b_5 + b_{15}) \mathbf{\Psi}_z \mathbf{\Psi}_z^T \end{bmatrix} \mathrm{d}\, y, \tag{A-53}$$

$$\mathbf{M}_{\Lambda \mathbf{q}} = \int_0^L \begin{bmatrix} -b_1(R_0 + y)\mathbf{\Psi}_u^T & \mathbf{0} & \mathbf{0} & \mathbf{0} & \mathbf{0} & (b_5 + b_{15})\mathbf{\Psi}_z^T \end{bmatrix} \mathrm{d}\, y \tag{A-54}$$

$$\mathbf{K} = \int_0^L \begin{bmatrix} a_{44} \mathbf{\Psi}'_u {\mathbf{\Psi}'_u}^T & a_{14} \mathbf{\Psi}'_u {\mathbf{\Psi}'_v}^T & a_{44} \mathbf{\Psi}'_u {\mathbf{\Psi}_z}^T \\ & a_{11} \mathbf{\Psi}'_v {\mathbf{\Psi}'_v}^T & a_{14} \mathbf{\Psi}'_v {\mathbf{\Psi}_z}^T \\ \text{Symm} & & a_{22} \mathbf{\Psi}'_z {\mathbf{\Psi}'_z}^T + a_{44} \mathbf{\Psi}_z {\mathbf{\Psi}_z}^T \end{bmatrix} \mathrm{d}\, y, \tag{A-55}$$

$$\mathbf{G}_{\Lambda q} = \int_0^L \begin{bmatrix} \mathbf{0} & b_1(R_0 + y)\mathbf{\Psi}_v^T & \mathbf{0} & \mathbf{0} & \mathbf{0} & \mathbf{0} & \mathbf{0} \end{bmatrix} \mathrm{d}\, y \tag{A-56}$$

$$\mathbf{G} = \int_0^L \begin{bmatrix} -b_1 \mathbf{\Psi}_u \mathbf{\Psi}_v^T & \mathbf{0} & \mathbf{0} \\ \mathbf{0} & -b_1 \mathbf{\Psi}_v \mathbf{\Psi}_u^T & \mathbf{0} \\ \mathbf{0} & \mathbf{0} & \mathbf{0} \end{bmatrix} \mathrm{d}\, y \tag{A-57}$$

$$\mathcal{C} = \int_0^L \begin{bmatrix} b_1 R(y) \mathbf{\Psi}'_u {\mathbf{\Psi}'_u}^T - b_1 \mathbf{\Psi}_u {\mathbf{\Psi}_u}^T & 0 & 0 \\ 0 & -b_1 \mathbf{\Psi}_v {\mathbf{\Psi}_v}^T & 0 \\ 0 & 0 & -(b_5 + b_{15}) \mathbf{\Psi}_z {\mathbf{\Psi}_z}^T \end{bmatrix} \mathrm{d}\, y, \tag{A-58}$$

$$\mathcal{A} = \begin{bmatrix} \mathcal{A}_2 & \mathcal{A}_3 & \mathcal{A}_4 \end{bmatrix} = \int_0^L \begin{bmatrix} \mathcal{A}_2^{Qx} \mathbf{\Psi}_u P'(y) & 0 & 0 \\ \mathcal{A}_2^{Ty} \mathbf{\Psi}_v P'(y) & 0 & \mathcal{A}_4^{Ty} \mathbf{\Psi}_v P'(y) \\ -\mathcal{A}_2^{Qx} \mathbf{\Psi}_z P(y) & \mathcal{A}_3^{Qz} \mathbf{\Psi}_z P'(y) & 0 \end{bmatrix} \mathrm{d}\, y, \tag{A-59}$$

$$\mathbf{Q} = \int_0^L \left\{ \begin{array}{c} p_x \mathbf{\Psi}_u \\ [\dot{\Lambda}^2 (R_0 + y) + p_y] \mathbf{\Psi}_v \\ m_z \mathbf{\Psi}_z \end{array} \right\} \mathrm{d}\, y. \tag{A-60}$$

A.9 Nonlinear terms in Eqs. (6.8) and (6.10)

Quadratic nonlinear terms of wing structure

$$N_u^2 : a_{11}v_0'u_0' + a_{14}\theta_z u_0' + a_{55}\theta_x\phi + (a_{55}-a_{44})w_0'\phi + a_{14}\left[\frac{3}{2}(u_0')^2 + \frac{1}{2}(w_0')^2\right] + a_{33}\theta_x'\phi' + a_{37}(\phi')^2 + a_{48}\frac{1}{2}(\phi')^2, \tag{A-61a}$$

$$N_v^2 : a_{11}\left[\frac{1}{2}(u_0')^2 + \frac{1}{2}(w_0')^2\right] - a_{14}w_0'\phi + a_{18}\frac{1}{2}(\phi')^2, \tag{A-61b}$$

$$N_w^2 : a_{11}v_0'w_0' + a_{14}\theta_z w_0' - a_{14}v_0'\phi - a_{44}\theta_z\phi + a_{14}u_0'w_0' - a_{22}\theta_z'\phi' + (a_{55}-a_{44})u_0'\phi, \tag{A-61c}$$

$$N_\phi^2 : a_{18}v_0'\phi' + a_{48}\phi'\theta_z + 2a_{37}u_0'\phi' + a_{33}u_0'\theta_x' - a_{22}w_0'\theta_z' + a_{48}u_0'\phi', \tag{A-61d}$$

$$\bar{N}_\phi^2 : a_{14}v_0'w_0' + a_{44}w_0'\theta_z - a_{55}u_0'\theta_x + (a_{44}-a_{55})u_0'w_0', \tag{A-61e}$$

$$N_x^2 : a_{33}u_0'\phi', \quad \bar{N}_x^2 : -a_{55}u_0'\phi, \quad N_z^2 : -a_{22}w_0'\phi', \tag{A-61f}$$

$$\bar{N}_z^2 : -a_{14}\left[\frac{1}{2}(u_0')^2 + \frac{1}{2}(w_0')^2\right] + a_{44}w_0'\phi - a_{48}\frac{1}{2}(\phi')^2. \tag{A-61g}$$

Quadratic nonlinear terms induced by the span distributed stores

$$\bar{E}_u^2 = \sum_{j=1}^{J}\delta_D(y-Y_j)m_j r_j\Big[-\theta_z\ddot{\theta}_z - \phi\ddot{\phi} - \dot{\theta}_z^2 - \dot{\phi}^2\Big] \tag{A-62a}$$

$$\bar{E}_v^2 = \sum_{j=1}^{J}\delta_D(y-Y_j)m_j r_j\Big[-\frac{1}{2}\phi\ddot{\theta}_x - \frac{1}{2}\theta_x\ddot{\phi} - \dot{\phi}\dot{\theta}_x\Big], \tag{A-62b}$$

$$\bar{E}_w^2 = \sum_{j=1}^{J}\delta_D(y-Y_j)m_j r_j\Big[-\frac{1}{2}\theta_x\ddot{\theta}_z - \frac{1}{2}\theta_z\ddot{\theta}_x - \dot{\theta}_x\dot{\theta}_z\Big], \tag{A-62c}$$

$$\begin{aligned}\bar{E}_\phi^2 = \sum_{j=1}^{J}\delta_D(y-Y_j)\Big\{&m_j\Big[r_j(-\phi\ddot{u}_0 - \frac{1}{2}\theta_x\ddot{v}_0) + {r_j}^2(\frac{1}{2}\theta_x\ddot{\theta}_x + \dot{\theta}_x\dot{\theta}_z)\Big]\\ &+\frac{1}{2}\Big[I_j^{11}\cos^2\Lambda + I_j^{22}\sin^2\Lambda\Big]\Big[2\dot{\theta}_x\dot{\theta}_z + \theta_z\ddot{\theta}_x\Big] + \frac{1}{2}\Big[I_j^{11}\sin^2\Lambda + I_j^{22}\cos^2\Lambda\Big]\Big[\theta_x\ddot{\theta}_z - \theta_z\ddot{\theta}_x\Big]\\ &+\frac{1}{2}\sin\Lambda\cos\Lambda\Big[I_j^{22} - I_j^{11}\Big]\Big[2\dot{\phi}\dot{\theta}_z + 2\theta_z\ddot{\phi} - \phi\ddot{\theta}_z\Big] + \frac{1}{2}I_j^{33}\Big[-2\dot{\theta}_x\dot{\theta}_z - \theta_x\ddot{\theta}_z\Big]\Big\},\end{aligned} \tag{A-62d}$$

$$\begin{aligned}\bar{E}_x^2 = \sum_{j=1}^{J}\delta_D(y-Y_j)\Big\{&m_j\Big[-\frac{1}{2}r_j(\theta_z\ddot{w}_0 + \phi\ddot{v}_0) + \frac{1}{2}{r_j}^2(\theta_z\ddot{\phi} - \phi\ddot{\theta}_z)\Big]\\ &+\frac{1}{2}\Big[I_j^{11}\cos^2\Lambda + I_j^{22}\sin^2\Lambda\Big]\Big[\theta_z\ddot{\phi} - \phi\ddot{\theta}_z\Big] + \frac{1}{2}\Big[I_j^{11}\sin^2\Lambda + I_j^{22}\cos^2\Lambda\Big]\Big[-2\dot{\phi}\dot{\theta}_z - \theta_z\ddot{\phi}\Big]\\ &+\frac{1}{2}\sin\Lambda\cos\Lambda\Big[I_j^{22} - I_j^{11}\Big]\Big[-2\dot{\theta}_x\dot{\theta}_z + \theta_x\ddot{\theta}_z - 2\theta_z\ddot{\theta}_x\Big] + \frac{1}{2}I_j^{33}\Big[2\dot{\phi}\dot{\theta}_z + \phi\ddot{\theta}_z\Big]\Big\},\end{aligned} \tag{A-62e}$$

$$\begin{aligned}\bar{E}_z^2 =&\sum_{j=1}^{J}\delta_D(y-Y_j)\Big\{m_j\Big[-r_j(\theta_z\ddot{u}_0+\frac{1}{2}\theta_x\ddot{w}_0)-{r_j}^2(\frac{1}{2}\phi\ddot{\theta}_x+\dot{\phi}\dot{\theta}_x)\Big]\\&+\frac{1}{2}\Big[I_j^{11}\cos^2\Lambda+I_j^{22}\sin^2\Lambda\Big]\Big[-2\dot{\theta}_x\dot{\phi}-\phi\ddot{\theta}_x\Big]+\frac{1}{2}\Big[I_j^{11}\sin^2\Lambda+I_j^{22}\cos^2\Lambda\Big]\Big[2\dot{\phi}\dot{\theta}_x+\theta_x\ddot{\phi}\Big]\\&+\frac{1}{2}\sin\Lambda\cos\Lambda\Big[I_j^{22}-I_j^{11}\Big]\Big[-2\dot{\phi}^2+2\dot{\theta}_x^2-\phi\ddot{\phi}+\theta_x\ddot{\theta}_x\Big]+\frac{1}{2}I_j^{33}\Big[-\theta_x\ddot{\phi}+\phi\ddot{\theta}_x\Big]\Big\}.\end{aligned} \tag{A-62f}$$

Quadratic nonlinear terms induced by the tip store

$$E_u^2 =m_T\Big[-x_T(\theta_z\ddot{\theta}_z+\phi\ddot{\phi}+\dot{\theta}_z^2+\dot{\phi}^2)-y_T(\frac{1}{2}\phi\ddot{\theta}_x+\frac{1}{2}\theta_x\ddot{\phi}+\dot{\theta}_x\dot{\phi})\Big], \tag{A-63a}$$

$$E_v^2 =m_T\Big[-x_T(\frac{1}{2}\phi\ddot{\theta}_x+\frac{1}{2}\theta_x\ddot{\phi}+\dot{\phi}\dot{\theta}_x)-y_T(\theta_x\ddot{\theta}_x+\theta_z\ddot{\theta}_z+\dot{\theta}_x^2+\dot{\theta}_z^2)\Big], \tag{A-63b}$$

$$E_w^2 =m_T\Big[-x_T(\frac{1}{2}\theta_x\ddot{\theta}_z+\frac{1}{2}\theta_z\ddot{\theta}_x+\dot{\theta}_x\dot{\theta}_z)+y_T(\frac{1}{2}\phi\ddot{\theta}_z+\frac{1}{2}\theta_z\ddot{\phi}+\dot{\phi}\dot{\theta}_z)\Big], \tag{A-63c}$$

$$\begin{aligned}E_\phi^2 =&m_T\Big[x_T(-\frac{1}{2}\theta_x\ddot{v}_0-\phi\ddot{u}_0)+\frac{1}{2}y_T(-\theta_x\ddot{u}_0+\theta_z\ddot{w}_0)+x_Ty_T(\frac{1}{2}\phi\ddot{\theta}_z-\theta_z\ddot{\phi}-\dot{\phi}\dot{\theta}_z)\\&+{x_T}^2(\frac{1}{2}\theta_z\ddot{\theta}_x+\dot{\theta}_x\dot{\theta}_z)+\frac{1}{2}{y_T}^2(-\theta_z\ddot{\theta}_x+\theta_x\ddot{\theta}_z)\Big]+\frac{1}{2}\Big[I_T^{11}\cos^2\Lambda+I_T^{22}\sin^2\Lambda\Big]\\&\Big[2\dot{\theta}_x\dot{\theta}_z+\theta_z\ddot{\theta}_x\Big]+\frac{1}{2}\Big[I_T^{11}\sin^2\Lambda+I_T^{22}\cos^2\Lambda\Big]\Big[\theta_x\ddot{\theta}_z-\theta_z\ddot{\theta}_x\Big]\\&+\frac{1}{2}\sin\Lambda\cos\Lambda\Big[I_T^{22}-I_T^{11}\Big]\Big[2\dot{\phi}\dot{\theta}_z+2\theta_z\ddot{\phi}-\phi\ddot{\theta}_z\Big]+\frac{1}{2}I_T^{33}\Big[-2\dot{\theta}_x\dot{\theta}_z-\theta_x\ddot{\theta}_z\Big],\end{aligned} \tag{A-63d}$$

$$\begin{aligned}E_x^2 =&m_T\Big[\frac{1}{2}x_T(-\theta_z\ddot{w}_0-\phi\ddot{v}_0)+y_T(-\theta_x\ddot{v}_0-\frac{1}{2}\phi\ddot{u}_0)+x_Ty_T(\theta_z\ddot{\theta}_x-\frac{1}{2}\theta_x\ddot{\theta}_z+\dot{\theta}_x\dot{\theta}_z)\\&+\frac{1}{2}{x_T}^2(-\phi\ddot{\theta}_z+\theta_z\ddot{\phi})+{y_T}^2(-\frac{1}{2}\theta_z\ddot{\phi}-\dot{\theta}_z\dot{\phi})\Big]+\frac{1}{2}\Big[I_T^{11}\cos^2\Lambda+I_T^{22}\sin^2\Lambda\Big]\Big[\theta_z\ddot{\phi}-\phi\ddot{\theta}_z\Big]\\&+\frac{1}{2}\Big[I_T^{11}\sin^2\Lambda+I_T^{22}\cos^2\Lambda\Big]\Big[-2\dot{\phi}\dot{\theta}_z-\theta_z\ddot{\phi}\Big]\\&+\frac{1}{2}\sin\Lambda\cos\Lambda\Big[I_T^{22}-I_T^{11}\Big]\Big[-2\dot{\theta}_x\dot{\theta}_z+\theta_x\ddot{\theta}_z-2\theta_z\ddot{\theta}_x\Big]\\&+\frac{1}{2}I_T^{33}\Big[2\dot{\phi}\dot{\theta}_z+\phi\ddot{\theta}_z\Big],\end{aligned} \tag{A-63e}$$

$$\begin{aligned}E_z^2 =&m_T\Big[x_T(-\frac{1}{2}\theta_x\ddot{w}_0-\theta_z\ddot{u}_0)+y_T(-\theta_z\ddot{v}_0+\frac{1}{2}\phi\ddot{w}_0)+x_Ty_T(\frac{1}{2}\phi\ddot{\phi}-\frac{1}{2}\theta_x\ddot{\theta}_x+\dot{\phi}^2-\dot{\theta}_x^2)\\&+{x_T}^2(-\frac{1}{2}\phi\ddot{\theta}_x-\dot{\phi}\dot{\theta}_x)+{y_T}^2(\frac{1}{2}\theta_x\ddot{\phi}+\dot{\phi}\dot{\theta}_x)\Big]+\frac{1}{2}\Big[I_T^{11}\cos^2\Lambda+I_T^{22}\sin^2\Lambda\Big]\Big[-2\dot{\theta}_x\dot{\phi}-\phi\ddot{\theta}_x\Big]\\&+\frac{1}{2}\Big[I_T^{11}\sin^2\Lambda+I_T^{22}\cos^2\Lambda\Big]\Big[2\dot{\phi}\dot{\theta}_x+\theta_x\ddot{\phi}\Big]+\frac{1}{2}I_T^{33}\Big[-\theta_x\ddot{\phi}+\phi\ddot{\theta}_x\Big]\\&+\frac{1}{2}\sin\Lambda\cos\Lambda\Big[I_T^{22}-I_T^{11}\Big]\Big[-2\dot{\phi}^2+2\dot{\theta}_x^2-\phi\ddot{\phi}+\theta_x\ddot{\theta}_x\Big].\end{aligned} \tag{A-63f}$$

A.10 Matrixes in Eq. 6.11 and Eq. 6.19

Mass matrix

$$\mathbf{M}=\int_0^L \begin{bmatrix} b_1\boldsymbol{\Psi}_u\boldsymbol{\Psi}_u^T & 0 & 0 & 0 & 0 & 0 \\ & b_1\boldsymbol{\Psi}_v\boldsymbol{\Psi}_v^T & 0 & 0 & 0 & 0 \\ & & b_1\boldsymbol{\Psi}_w\boldsymbol{\Psi}_w^T & 0 & 0 & 0 \\ & & & (b_4+b_5)\boldsymbol{\Psi}_\phi\boldsymbol{\Psi}_\phi^T+(b_{10}+b_{18})\boldsymbol{\Psi}'_\phi\boldsymbol{\Psi}'^T_\phi & 0 & 0 \\ & \text{Symm} & & & (b_4+b_{14})\boldsymbol{\Psi}_x\boldsymbol{\Psi}_x^T & 0 \\ & & & & & (b_5+b_{15})\boldsymbol{\Psi}_z\boldsymbol{\Psi}_z^T \end{bmatrix}\mathrm{d}\,y. \tag{A-64}$$

Mass matrix of external stores $\mathbf{E}$

$$\mathbf{E}=\sum_{j=1}^{J}\begin{bmatrix} m_j\boldsymbol{\Psi}_u{\boldsymbol{\Psi}_u}^T & 0 & 0 & 0 & 0 & 0 \\ & m_j\boldsymbol{\Psi}_v{\boldsymbol{\Psi}_v}^T & 0 & 0 & 0 & r_jm_j\boldsymbol{\Psi}_v{\boldsymbol{\Psi}_z}^T \\ & & m_j\boldsymbol{\Psi}_w{\boldsymbol{\Psi}_w}^T & -r_jm_j\boldsymbol{\Psi}_w{\boldsymbol{\Psi}_\phi}^T & 0 & 0 \\ & & & \left[{r_j}^2m_j+I_j^{11}\sin^2\Lambda+I_j^{22}\cos^2\Lambda\right]\boldsymbol{\Psi}_\phi{\boldsymbol{\Psi}_\phi}^T & (I_j^{22}-I_j^{11})\sin\Lambda\cos\Lambda\boldsymbol{\Psi}_\phi{\boldsymbol{\Psi}_x}^T & 0 \\ & \text{Symm} & & & \left[I_j^{11}\cos^2\Lambda+I_j^{22}\sin^2\Lambda\right]\boldsymbol{\Psi}_x{\boldsymbol{\Psi}_x}^T & 0 \\ & & & & & \left[{r_j}^2m_j+I_j^{33}\right]\boldsymbol{\Psi}_z{\boldsymbol{\Psi}_z}^T \end{bmatrix}\Bigg|_{y=Y_j}$$

$$+\begin{bmatrix} m_T\boldsymbol{\Psi}_u{\boldsymbol{\Psi}_u}^T & 0 & 0 & 0 & 0 & -y_Tm_T\boldsymbol{\Psi}_u{\boldsymbol{\Psi}_z}^T \\ & m_T\boldsymbol{\Psi}_v{\boldsymbol{\Psi}_v}^T & 0 & 0 & 0 & x_Tm_T\boldsymbol{\Psi}_v{\boldsymbol{\Psi}_z}^T \\ & & m_T\boldsymbol{\Psi}_w{\boldsymbol{\Psi}_w}^T & -x_Tm_T\boldsymbol{\Psi}_w{\boldsymbol{\Psi}_\phi}^T & -y_Tm_T\boldsymbol{\Psi}_w{\boldsymbol{\Psi}_x}^T & 0 \\ & & & \left[I_T^{11}\sin^2\Lambda+I_T^{22}\cos^2\Lambda+{x_T}^2m_T\right]\boldsymbol{\Psi}_\phi{\boldsymbol{\Psi}_\phi}^T & \left[(I_T^{22}-I_T^{11})\sin\Lambda\cos\Lambda+x_Ty_Tm_T\right]\boldsymbol{\Psi}_\phi{\boldsymbol{\Psi}_x}^T & 0 \\ & \text{Symm} & & & \left[I_T^{11}\cos^2\Lambda+I_T^{22}\sin^2\Lambda+{y_T}^2m_T\right]\boldsymbol{\Psi}_x{\boldsymbol{\Psi}_x}^T & 0 \\ & & & & & \left[I_T^{33}+{y_T}^2m_T\right]\boldsymbol{\Psi}_z{\boldsymbol{\Psi}_z}^T \end{bmatrix}\Bigg|_{y=L} \tag{A-65}$$

Stiffness matrix

$$\mathbf{K}=\int_0^L \begin{bmatrix} a_{44}\boldsymbol{\Psi}'_u{\boldsymbol{\Psi}'_u}^T & a_{14}\boldsymbol{\Psi}'_u{\boldsymbol{\Psi}'_v}^T & 0 & 0 & 0 & a_{44}\boldsymbol{\Psi}'_u{\boldsymbol{\Psi}_z}^T \\ & a_{11}\boldsymbol{\Psi}'_v{\boldsymbol{\Psi}'_v}^T & a_{15}\boldsymbol{\Psi}'_v{\boldsymbol{\Psi}'_w}^T & 0 & a_{15}\boldsymbol{\Psi}'_v{\boldsymbol{\Psi}'_x}^T & a_{14}\boldsymbol{\Psi}'_v{\boldsymbol{\Psi}_z}^T \\ & & a_{55}\boldsymbol{\Psi}'_w{\boldsymbol{\Psi}'_w}^T & 0 & a_{55}\boldsymbol{\Psi}'_w{\boldsymbol{\Psi}'_x}^T & 0 \\ & & & a_{77}\boldsymbol{\Psi}'_\phi{\boldsymbol{\Psi}'_\phi}^T+a_{66}\boldsymbol{\Psi}''_\phi\boldsymbol{\Psi}''^T_\phi & a_{37}\boldsymbol{\Psi}'_\phi{\boldsymbol{\Psi}'_x}^T & a_{27}\boldsymbol{\Psi}'_\phi{\boldsymbol{\Psi}'_z}^T \\ & \text{Symm} & & & a_{33}\boldsymbol{\Psi}'_x{\boldsymbol{\Psi}'_x}^T+a_{55}\boldsymbol{\Psi}_x{\boldsymbol{\Psi}_x}^T & 0 \\ & & & & & a_{22}\boldsymbol{\Psi}'_z{\boldsymbol{\Psi}'_z}^T+a_{44}\boldsymbol{\Psi}_z{\boldsymbol{\Psi}_z}^T \end{bmatrix}\mathrm{d}\,y. \tag{A-66}$$

External forces vector $\mathbf{Q}$

$$\mathbf{Q}=\int_0^L\left\{p_x\boldsymbol{\Psi}_u \quad p_y\boldsymbol{\Psi}_v \quad p_z\boldsymbol{\Psi}_w \quad (m_y+b'_w)\boldsymbol{\Psi}_\phi \quad m_x\boldsymbol{\Psi}_x \quad m_z\boldsymbol{\Psi}_z\right\}^T\mathrm{d}\,y. \tag{A-67}$$

Nonlinear terms related to wing structure $\mathbf{N}_{nm}$

$$\mathbf{N}_{nm}=\int_0^L\left\{\boldsymbol{\Psi}'_uN_u^2 \quad \boldsymbol{\Psi}'_vN_v^2 \quad \boldsymbol{\Psi}'_wN_w^2 \quad (\boldsymbol{\Psi}'_\phi N_\phi^2-\boldsymbol{\Psi}_\phi\bar{N}_\phi^2) \quad (\boldsymbol{\Psi}'_xN_\phi^2-\boldsymbol{\Psi}_x\bar{N}_x^2) \quad (\boldsymbol{\Psi}'_zN_\phi^2-\boldsymbol{\Psi}_z\bar{N}_z^2)\right\}^T\mathrm{d}\,y \tag{A-68}$$

Nonlinear terms induced by external stores $\mathbf{E}_{nm}$ and $\hat{\mathbf{E}}_{nm}$. First of all, we define a vector $\mathring{\mathbf{E}}_{nm}$

$$\begin{aligned}\mathring{\mathbf{E}}_{nm}=&\int_0^L\left\{\boldsymbol{\Psi}_u\bar{E}_u^2 \quad \boldsymbol{\Psi}_v\bar{E}_v^2 \quad \boldsymbol{\Psi}_w\bar{E}_w^2 \quad \boldsymbol{\Psi}_\phi\bar{E}_\phi^2 \quad \boldsymbol{\Psi}_x\bar{E}_x^2 \quad \boldsymbol{\Psi}_z\bar{E}_z^2\right\}^T\mathrm{d}\,y\\ &+\left\{\boldsymbol{\Psi}_u(L)E_u^2(L) \quad \boldsymbol{\Psi}_v(L)E_v^2(L) \quad \boldsymbol{\Psi}_w(L)E_w^2(L) \quad \boldsymbol{\Psi}_\phi(L)E_\phi^2(L) \quad \boldsymbol{\Psi}_x(L)E_x^2(L) \quad \boldsymbol{\Psi}_z(L)E_z^2(L)\right\}^T\end{aligned} \tag{A-69}$$

Then $\mathbf{E}_{nm}$ and $\hat{\mathbf{E}}_{nm}$ equal to $\mathring{\mathbf{E}}_{nm}$ only when $(A_n\ddot{B}_m)$ and $(\dot{A}_n\dot{B}_m)$ $(A,B=u_0,v_0,w_0,\phi,\theta_x,\theta_z)$ terms are retained in $\mathring{\mathbf{E}}_{nm}$, respectively.

Bibliography

[1] Edward C . Smith and Inderjit Chopra. Aeroelastic response, loads, and stability of a composite rotor in forward flight. *AIAA journal*, 31(7):1265–1273, 1993.

[2] H NAYFEH Ali and LACARBONARA Walter. On the discretization of spatially continuous systems with quadratic and cubic nonlinearities. *JSME Int J., Ser. C*, 41(3):510–531, 1998.

[3] John Argyris. An excursion into large rotations. *Computer methods in applied mechanics and engineering*, 32(1):85–155, 1982.

[4] Erian A Armanios and Ashraf M Badir. Free vibration analysis of anisotropic thin-walled closed-section beams. *AIAA journal*, 33(10):1905–1910, 1995.

[5] W Keith Belvin and KC Park. Structural tailoring and feedback control synthesis-an interdisciplinary approach. *Journal of Guidance, Control, and Dynamics*, 13(3):424–429, 1990.

[6] Aaron Alton Bent. *Active fiber composites for structural actuation*. PhD thesis, Massachusetts Institute of Technology, 1997.

[7] K. Bhaskar and L. Librescu. A geometrically non-linear theory for laminated anisotropic thin-walled beams. *Int. J. Eng. Sci.*, 33(9):1331–1344, 1995.

[8] Richard L Bielawa. *Rotary wing structural dynamics and aeroelasticity*. Amer Inst of Aeronautics &, 2006.

[9] Raymond L Bisplinghoff, Holt Ashley, and Robert L Halfman. *Aeroelasticity*. Courier Corporation, 2013.

[10] Claudio Brillante, Marco Morandini, and Paolo Mantegazza. Characterization of beam stiffness matrix with embedded piezoelectric devices via generalized eigenvectors. *International Journal of Solids and Structures*, 59:37–45, May 2015.

[11] Claudio Brillante, Marco Morandini, and Paolo Mantegazza. Periodic controllers for vibration reduction using actively twisted blades. *The Aeronautical Journal*, 120(1233):1763–1784, November 2016.

[12] Povl Brøndsted, Hans Lilholt, and Aage Lystrup. Composite materials for wind power turbine blades. *Annu. Rev. Mater. Res.*, 35:505–538, 2005.

[13] Erasmo Carrera, Matteo Filippi, Prashanta KR Mahato, and Alfonso Pagani. Advanced models for free vibration analysis of laminated beams with compact and thin-walled open/closed sections. *J. Compos. Mater.*, page 0021998314541570, 2014.

[14] Erasmo Carrera, Matteo Filippi, and Enrico Zappino. Free vibration analysis of rotating composite blades via carrera unified formulation. *Composite Structures*, 106:317–325, 2013.

[15] E Carson. Calculation of flutter characteristics for finite-span. 1958.

[16] Seok-Ju Cha, Ji-Seok Song, Hwan-Hee Lee, Sungsoo Na, Jae-Hong Shim, and Piergiovanni Marzocca. Dynamic response control of rotating thin-walled composite blade exposed to external excitations. *J. Aerosp. Eng.*, 27(5):04014025, 2014.

[17] Ramesh Chandra and Inderjit Chopra. Experimental-theoretical investigation of the vibration characteristics of rotating composite box beams. *Journal of Aircraft*, 29(4):657–664, 1992.

[18] Ramesh Chandra, Alan D Stemple, and Inderjit Chopra. Thin-walled composite beams under bending torsional and externsional loads. *J. Aircraft*, 27(7):619–26, 1990.

[19] Seung-Chan Choi, Jae-Sang Park, and Ji-Hwan Kim. Vibration control of pre-twisted rotating composite thin-walled beams with piezoelectric fiber composites. *J. Sound Vib.*, 300(1):176–196, 2007.

[20] V.H. Cortinez and M.T. Piovan. Vibration and buckling of composite thin-walled beams with shear deformability. *J. Sound Vib.*, 258:701–723, 2002.

[21] F. Demoures, F. Gay-Balmaz, S. Leyendecker, S. Ober-Blöbaum, T. S. Ratiu, and Y. Weinand. Discrete variational lie group formulation of geometrically exact beam dynamics. *Numerische Mathematik*, 130(1):73–123, 2015.

[22] Richard C Dorf and Robert H Bishop. Modern control systems. 1998.

[23] Andries J Du Plessis. *Modeling and experimental testing of twist actuated single cell composite beams for helicopter blade control*. PhD thesis, Massachusetts Institute of Technology, 1996.

[24] DJ Ewins and R Henry. Structural dynamic characteristics of individual blades. *Lecture series-van Kareman Institute for fluid dynamics*, 6:B1–B28, 1992.

[25] Daining Fang and Jinxi Liu. *Fracture Mechanics of Piezoelectric and Ferroelectric Solids*. Springer, 2013.

[26] Edwin Forster, Stephen Clay, Richard Holzwarth, and Donald Paul. Flight vehicle composite structures. In *The 26th Congress of ICAS and 8th AIAA ATIO*, page 8976, 2008.

[27] Gian Luca Ghiringhelli, Pierangelo Masarati, Marco Morandini, and Davide Muffo. Integrated aeroservoelastic analysis of induced strain rotor blades. *Mechanics of Advanced Materials and Structures*, 15(3-4):291–306, 2008.

[28] V. Giavotto, M. Borri, P. Mantegazza, G. Ghiringhelli, V. Carmaschi, G.C. Maffioli, and F. Mussi. Anisotropic beam theory and applications. *Computers & Structures*, 16(1-4):403–413, 1983.

[29] S Glukhikh, E Barkanov, A Kovalev, Pierangelo Masarati, Marco Morandini, Johannes Riemenschneider, and Peter Wierach. Design of helicopter rotor blades with actuators made of a piezomacrofiber composite. *Mechanics of Composite Materials*, 44(1):57–64, 2008.

[30] C.E. Harris, Jr. J.H. Starnes, and M.J. Shuart. Design and manufacturing of aerospace composite structures, state-of-the-art assessment. *J. Aircraft*, 39(4):545–560, Jul.-Aug. 2002.

[31] Hibbitt, Karlsson, and Sorensen. *ABAQUS/standard user's Manual*, volume 1. Hibbitt, Karlsson & Sorensen, 2001.

[32] Dewey H Hodges. Review of composite rotor blade modeling. *AIAA journal*, 28(3):561–565, 1990.

[33] D.H. Hodges. Geometrically exact, intrinsic theory for dynamics of curved and twisted anisotropic beams. *AIAA J.*, 41(6):1131–1137, 2003.

[34] Gerhard A Holzapfel. *Nonlinear solid mechanics*, volume 24. Wiley Chichester, 2000.

[35] S.M. Ibrahim, E. Carrera, M. Petrolo, and E. Zappino. Buckling of composite thin walled beams by refined theory. *Compos. Struct.*, 94:563–570, 2012.

[36] Robert M Jones. *Mechanics of composite materials*. CRC press, 1998.

[37] Robert T Jones. The unsteady lift of a wing of finite aspect ratio. 1940.

[38] Sung Nam Jung, VT Nagaraj, and Inderjit Chopra. Refined structural dynamics model for composite rotor blades. *AIAA journal*, 39(2):339–348, 2001.

[39] TH Von Karman. Airfoil theory for non-uniform motion. *Journal of the Aeronautical Sciences*, 5(10):379–390, 1938.

[40] RE Kielb. Effects of warping and pretwist on torsional vibration of rotating beams. *Journal of applied mechanics*, 51:913, 1984.

[41] W Lacarbonara, G Rega, and AH Nayfeh. Resonant non-linear normal modes. part i: analytical treatment for structural one-dimensional systems. *Int. J. Non Linear Mech.*, 38(6):851–872, 2003.

[42] Christopher L Lee and Noel C Perkins. Nonlinear oscillations of suspended cables containing a two-to-one internal resonance. *Nonlinear Dyn.*, 3(6):465–490, 1992.

[43] L Librescu and A Khdeir. Aeroelastic divergence of swept-forward composite wings including warping restraint effect. *AIAA journal*, 26(11):1373–1377, 1988.

[44] L Librescu, L Meirovitch, and Sung Soo Na. Control of cantilever vibration via structural tailoring and adaptive materials. *AIAA journal*, 35(8):1309–1315, 1997.

[45] L. Librescu and S.S. Na. Dyanmic response of cantilevered thin-wlled beams to blast and sonic-boom loadings. *Shock. Vib.*, 5(1):23–33, 1998.

[46] L. Librescu and O. Song. Behavior of thin-walled beams made of advanced composite materials and incorporating non-classical effects. *Appl. Mech. Rev.*, 44(11):S174–80, 1991.

[47] L. Librescu and O. Song. *Thin-Walled Composite Beams: Theory and Application*. Springer, New York, 2006. Chap.8, pp. 213-232.

[48] Liviu Librescu and Sung Soo Na. Dynamic response of cantilevered thin-walled beams to blast and sonic-boom loadings. *Shock and Vibration*, 5(1):23–33, 1998.

[49] Liviu Librescu, Sungsoo Na, Zhanming Qin, and Bokhee Lee. Active aeroelastic control of aircraft composite wings impacted by explosive blasts. *J. Sound Vib.*, 318(1):74–92, 2008.

[50] Liviu Librescu and SUROT THANGJITHAM. Analytical studies on static aeroelastic behavior of forward-swept composite wing structures. *Journal of aircraft*, 28(2):151–157, 1991.

[51] Man Liu and DG Gorman. Formulation of Rayleigh damping and its extensions. *Computers & structures*, 57(2):277–285, 1995.

[52] Angelo Luongo, Angelo Di Egidio, and Achille Paolone. On the proper form of the amplitude modulation equations for resonant systems. *Nonlinear Dynam.*, 27(3):237–254, 2002.

[53] Angelo Luongo, Achille Paolone, and Angelo Di Egidio. Multiple timescales analysis for 1: 2 and 1: 3 resonant hopf bifurcations. *Nonlinear Dynam.*, 34(3-4):269–291, 2003.

[54] Angelo Luongo and Giuseppe Piccardo. Non-linear galloping of sagged cables in 1: 2 internal resonance. *J. Sound Vib.*, 214(5):915–940, 1998.

[55] Angelo Luongo and Giuseppe Piccardo. A continuous approach to the aeroelastic stability of suspended cables in 1: 2 internal resonance. *J. Vib. Control*, 14(1-2):135–157, 2008.

[56] Angelo Luongo, Daniele Zulli, and Giuseppe Piccardo. Analytical and numerical approaches to nonlinear galloping of internally resonant suspended cables. *J. Sound Vib.*, 315(3):375–393, 2008.

[57] Pierangelo Masarati and Gian Luca Ghiringhelli. Characterization of anisotropic, non-homogeneous plates with piezoelectric inclusions. *Computers & Structures*, 83(15-16):1171–1190, June 2005.

[58] Leonard Meirovitch. *Principles and Techniques of Vibrations*. Prentice Hall, Upper Saddle River, New Jersey, 1997.

[59] Teodoro Merlini and Marco Morandini. On successive differentiations of the rotation tensor: An application to nonlinear beam elements. *Journal of Mechanics of Materials and Structures*, 8(5):305–340, 2013.

[60] Marco Morandini, Maria Chierichetti, and Paolo Mantegazza. Characteristic behavior of prismatic anisotropic beam via generalized eigenvectors. *International Journal of Solids and Structures*, 47(10):1327–1337, May 2010.

[61] Sungsoo Na and Liviu Librescu. Oscillation control of cantilevers via smart materials technology and optimal feedback control: actuator location and power consumption issues. *Smart Materials and Structures*, 7(6):833, 1998.

[62] Sungsoo Na, Liviu Librescu, Myung-Hyun Kim, In-Joo Jeong, and Pier Marzocca. Robust aeroelastic control of flapped wing systems using a sliding mode observer. *Aerosp. Sci. Technol.*, 10(2):120–126, 2006.

[63] Sungsoo Na, Liviu Librescu, and Jae Kyung Shim. Modeling and bending vibration control of nonuniform thin-walled rotating beams incorporating adaptive capabilities. *International Journal of Mechanical Sciences*, 45(8):1347–1367, 2003.

[64] A.H. Nayfeh. *Introduction to Perturbation Techniques*. John Wiley & Sons, Inc, N.Y, 1981.

[65] A.H. Nayfeh. *Nonlinear interactions: Analytical, computational, and experimental methods*. Wiley Series in Nonlinear Science. John Wiley & Sons, Inc., New York, 2000.

[66] A.H. Nayfeh and D.T. Mook. *Nonlinear Oscillations*. John Wiley & Sons, Inc, N.Y, 1979.

[67] Ali H Nayfeh. *Perturbation methods*. John Wiley & Sons, 2008.

[68] S-Y Oh, L Librescu, and O Song. Modelling and vibration of composite thin-walled rotating blades featuring extension-twist elastic coupling. *Aeronautical Journal*, 109(1095):233–246, 2005.

[69] S-Y Oh, O Song, and L Librescu. Effects of pretwist and presetting on coupled bending vibrations of rotating thin-walled composite beams. *Int. J. Solids Struct.*, 40(5):1203–1224, 2003.

[70] A.N. Palazotto and P.E. Linnemann. Vibration and buckling characteristics of com-posite cylindrical panels incorporating the effects of a higher order shear theory. *Int. J. Solids Struct.*, 28(3):341–361, 1991.

[71] Jae-Sang Park and Ji-Hwan Kim. Analytical development of single crystal macro fiber composite actuators for active twist rotor blades. *Smart Mater. Struct.*, 14(4):745, 2005.

[72] M.J. Patil and D.H. Hodges. Flight dynamics of highly flexible flying wings. *J. Aircraft*, 43(6):1790–1799, 2006.

[73] Yong Lin Pi and Nicholas Snowden Trahair. Nonlinear inelastic analysis of steel beam-columns. i: Theory. *Journal of Structural Engineering*, 120(7):2041–2061, 1994.

[74] Wojciech Pietraszkiewicz and Janusz Badur. Finite rotations in the description of continuum deformation. *Int. J. Eng. Sci.*, 21(9):1097–1115, 1983.

[75] Z. Qin and L. Librescu. On a shear-deformable theory of anisotropic thin-walled beams: further contribution and validation. *Compos. Struct.*, 56(4):345–358, 2002.

[76] Zhanming Qin and Liviu Librescu. Dynamic aeroelastic response of aircraft wings modeled as anisotropic thin-walled beams. *Journal of Aircraft*, 40(3):532–543, 2003.

[77] Zhanming Qin, Liviu Librescu, and Piergiovanni Marzocca. Aeroelasticity of composite aerovehicle wings in supersonic flows. *Journal of spacecraft and rockets*, 40(2):162–173, 2003.

[78] M Rafiee, F Nitzsche, and M Labrosse. Dynamics, vibration and control of rotating composite beams and blades: A critical review. *Thin-Walled Structures*, 119:795–819, 2017.

[79] Omri Rand. Analysis of composite rotor blades. In *Numerical Analysis and Modelling of Composite Materials*, pages 1–26. Springer, 1996.

[80] M.E. Raville and C.E.S. Ueng. Determination of natural frequencies of vibration of a sandwich plate. *Exp. Mech.*, 7:490–493, 1967.

[81] Lawrence W Rehfield and Ali R Atilgan. Toward understanding the tailoring mechanisms for thin-walled composite tubular beams. In *Proceedings of the First USSR-US Symposium on Mechanics of Composite Materials, Riga, Latvia, May*, pages 23–26, 1989.

[82] Lawrence W Rehfield, Ali R Atilgan, and Dewey H Hodges. Nonclassical behavior of thin-walled composite beams with closed cross sections. *Journal of the American Helicopter Society*, 35(2):42–50, 1990.

[83] WILLIAM P RODDEN and BERNHARD STAHL. A strip method for prediction of damping in subsonic wind tunnel andflight flutter tests. *Journal of Aircraft*, 6(1):9–17, 1969.

[84] Juan C Simo and Loc Vu-Quoc. A geometrically-exact rod model incorporating shear and torsion-warping deformation. *Int. J. Solids Struct.*, 27(3):371–393, 1991.

[85] Gurkirpal Singh, Pierre T Kabamba, and N Harris McClamroch. Planar, time-optimal, rest-to-rest slewing maneuvers of flexible spacecraft. *Journal of Guidance, Control, and Dynamics*, 12(1):71–81, 1989.

[86] Ji-Seok Song, Jeonghwan Choo, Seog-Ju Cha, Sungsoo Na, and Zhanming Qin. Robust aeroelastic instability suppression of an advanced wing with model uncertainty in subsonic compressible flow field. *Aerosp. Sci. Technol.*, 25(1):242–252, 2013.

[87] O Song, N-H Jeong, and L Librescu. Vibration and stability of pretwisted spinning thin-walled composite beams featuring bending–bending elastic coupling. *Journal of Sound and Vibration*, 237(3):513–533, 2000.

[88] O Song and L Librescu. Structural modeling and free vibration analysis of rotating composite thin-walled beams. *Journal of the American Helicopter Society*, 42(4):358–369, 1997.

[89] Ohseop Song, Liviu Librescu, and Sang-Yong Oh. Vibration of pretwisted adaptive rotating blades modeled as anisotropic thin-walled beams. *AIAA journal*, 39(2):285–295, 2001.

[90] Narakorn Srinil, Giuseppe Rega, and Somchai Chucheepsakul. Two-to-one resonant multi-modal dynamics of horizontal/inclined cables. part i: Theoretical formulation and model validation. *Nonlinear Dyn.*, 48(3):231–252, 2007.

[91] Alan D Stemple and Sung W Lee. A finite element model for composite beams undergoing large deflection with arbitrary cross-sectional warping. *Int. J. Numer. Methods Eng.*, 28(9):2143–2160, 1989.

[92] T Trombetti and S Silvestri. On the modal damping ratios of shear-type structures equipped with Rayleigh damping systems. *J. Sound Vib.*, 292(1):21–58, 2006.

[93] Alberto Varello and Erasmo Carrera. Free vibration response of thin and thick nonhomogeneous shells by refined one-dimensional analysis. *J. Vib. Acoust.*, 136(6):061001, 2014.

[94] T. P. Vo and J. Lee. Flexural-torsional behavior of thin-walled composite box beams using shear-deformable beam theory. *Eng. Struct.*, 30:1958–1968, 2008.

[95] T Von Karman and WR Sears. Airfoil theory for non-uniform motion. *AIAA Journal*, 41(7):5–16, 2003.

[96] Xiao Wang, Marco Morandini, and Pierangelo Masarati. Modeling and control for rotating pretwisted thin-walled beams with piezo-composite. *Composite Structures*, 180:647 – 663, 2017.

[97] Xiao Wang, Marco Morandini, and Pierangelo Masarati. Velocity feedback damping of piezo-actuated wings. *Composite Structures*, 174:221 – 232, 2017.

[98] Xiao Wang and Zhanming Qin. Nonlinear modal interactions in composite thin-walled beam structures with simultaneous 1:2 internal and 1:1 external resonances. *Nonlinear Dynamics*, 86(2):1381–1405, 2016.

[99] Peter D Welch. The use of fast fourier transform for the estimation of power spectra: A method based on time averaging over short, modified periodograms. *IEEE Trans. Audio Electroacoust.*, 15(2):70–73, 1967.

[100] William K Wilkie, Robert G Bryant, James W High, Robert L Fox, Richard F Hellbaum, Anthony Jalink Jr, Bruce D Little, and Paul H Mirick. Low-cost piezocomposite actuator for structural control applications. In *SPIE's 7th Annual International Symposium on Smart Structures and Materials*, pages 323–334. International Society for Optics and Photonics, 2000.

[101] Jiashi Yang. *An introduction to the theory of piezoelectricity*, volume 9. Springer Science & Business Media, 2004.

[102] W. Yu, D.H. Hodges, and J.C. Ho. Variational asymptotic beam sectional analysis-an updated version. *Int. J. Eng. Sci.*, 59:40–64, 2012.